In situ Diagnostics of Damage Accumulation in Ni-Based Superalloy



Koji Kageyama

St Anne's College
University of Oxford

A thesis submitted for the degree of Doctor of Philosophy

Michaelmas Term 2020

I would like to dedicate this thesis to my wife, Mayuko, my daughter, Ayame, and my son, Aoto ...

Abstract

There have been a significant interest in capturing how the damage is initiated and accumulated in polycrystalline Ni-based superalloys while applied thermal and mechanical impact – tensile and creep loading at 800°C. This is because the turbine component in jet propulsion or power generation these materials applied can experience such environments while in service and need to avoid unexpected degradation and failure causing severe accidents. *In situ* damage observation techniques required to be developed to understand the sequential mechanisms of damage growth even in such complicated environment.

In this work, for the first time in this field, a design and operation of laboratory-scale X-ray computed tomography (XCT) arrangement is developed for the purpose of *in situ* damage observation. The *in situ* XCT technique covers high temperature mechanical testing and improvements of tomography image processing for high resolution enables to capture the sequential damage growth during tensile or creep loading at 800°C, in examples of polycrystalline Ni-based superalloys, Inconel 718 and Nimonic 80A. Furthermore, laser-based Acoustic Emission (AE) techniques are combined with the system to determine whether the object is damaged to be captured by XCT.

The developed *in situ* observation technique was applied to high temperature tensile and creep testing. Our results indicated that the damage growth can be captured with the resolution of 30 μm at 800°C, and can be compared not only with strain rate and loading condition but with stress state of the deformed testpiece, and that AE technique can be the damage indicator of the object by observing the change of AE energy and frequency.

Research contents in this thesis have been published and prepared for publication as follows:

- K. Kageyama, F. Adziman, E. Alabort, T. Sui, A.M. Korsunsky, R.C. Reed, *In situ Diagnostics of Damage Accumulation in Ni-based Superalloys using High Temperature Computed Tomography*, Metallurgical and Materials Transactions A 49A (2018), pp. 4274-4289, doi:10.1007/s11661-018-4737-6

- K. Kageyama, F. Adziman, Y. Tang, Y. Gong, T. Sui, A.A.A. Németh, A.M. Korsunsky, R.C. Reed, *Damage Accumulation during High Temperature Deformation of a Superalloy Analysed by in situ Computed Tomography*, In manuscript.

- K. Kageyama, F. Adziman, D. Barba, S. Sulzer, T. Tang, T. Sui, A.M. Korsunsky, R.C. Reed, *In situ XCT and Acoustic Emission Diagnostics of High Temperature Deformation of Nickel-based Superalloy*, In manuscript.

Acknowledgements

My doctorate studying at the University of Oxford has provided me with the precious opportunity to experience many lessons and obstacles, without which I could not have written this thesis. Most of those opprotunities are linked to the generous support of a number of people who I wish to acknowledge.

I am deeply grateful to my academic advisors, **Professor Roger Reed** and **Professor Alexander Korsunsky**. I would like to express my appreciation for their advice, encouragement, patience, and inspiring me to produce new ideas throughout my research. I would also like to thank the generous financial support provided by Nippon Steel Corporation and many helpful advices by **Dr. Manabu Takahashi** (Nippon Steel Corporation).

I am greatly indebted to the assistance by **Dr. Tan Sui** and **Dr. Fauzan Adziman**, who supported and encouraged me throughout designing the *in situ* XCT setup and image reconstructing algorithm. I would like to express my gratitude to the technical team at the University of Oxford, **Stuart Carter** and **Jeffrey Fullerton**, for their assistance and skillful performance.

I would also like to deeply thank all of my colleagues in Professor Reed's research group: **Karen Bamford**, **Dr. Andre Nemeth**, **Dr. Sabin Sulzer**, **Dr. Tony Tang**, **Dr. Enrique Alabort**, **Dr. Daniel Barba**, **Dr. David Crudden**, **Dr. Chinnapat Panwisawas**, **Dr. Heather Wilson**, and my colleagues in Professor Korsunsky's research group: **Dr. Enrico Salvati**, **Dr. Joris Everaerts**, **Dr. Hong Ji Zhang**, **Dr. Chryssa Papadaki**. This research could not have been conducted without any parts of their support. I wish to thank my closest friends in Oxford **Arthur Moya**, **Daniel Gregory**, **William Kurdahl Larsen**, **Jim Yang Xu**, **Fumiaki Sagisaka**, **Koichi Sakai**, **Moeko Hayashi**, **Chiara Comastri**, **Martin Nicolle**, **Atsushi Shimada**, **Keisuke Kishi**, **Fudie Zhao**, **Yusuke Sakuyama**, **Toshihiro Iio**, and **Shota Miura**, and **Yutaro Mochida**. Thank you for exciting discussions over sleepless nights and sharing the stimulating time in Oxford.

I wish to thank you to my family, my parents **Shogo Kageyama** and **Mitsuko Kageyama**, my grandmother **Eiko Kageyama**, my brother **Masayuki Kageyama**,

and my sister **Rie Kageyama** for their generous support. Most importantly, thank you to my wife, **Mayuko Kageyama** for your unconditional love and huge support, and thank you my daughter, **Ayame Kageyama**, and my son, **Aoto Kageyama**.

Table of contents

Preface **vi**

1 Introduction **1**
1.1 The Importance of *In situ* Damage observation in Ni-based Superalloy . 1
1.2 *In situ* Damage observation techniques 2
1.3 Aim of Research and Thesis Structure 3

2 Literature Review **7**
2.1 Ni-based superalloys 7
2.1.1 Metallurgy of superalloys in general 7
2.1.2 Plastic deformation at high temperature 11
2.1.3 Failure 18
2.1.4 Metallurgy and mechanical properties of superalloys chosen in this thesis 23
2.2 Testing methods 27
2.2.1 X-ray computed tomography (XCT) 27
2.2.2 Acoustic Emission (AE) 37
2.2.3 High temperature tensile/creep testing 44
2.3 Key research questions for this thesis 47

3 *In situ* Diagnostics of Damage Accumulation in Ni-based Superalloys using High Temperature Computed Tomography **51**
3.1 Introduction 52
3.2 Preparation for Experiment 53
3.3 Experimental Methods 67
3.3.1 *In situ* XCT system: source and detector 67
3.3.2 Rotary and displacement control 68
3.3.3 XCT analysis 71

3.3.4 Testing materials . . . 72
3.4 Results . . . 72
3.4.1 Rotary control for XCT imaging . . . 72
3.4.2 True stress - true strain curves, and mapping of local thinning of cross-sections . . . 74
3.4.3 XCT results . . . 80
3.5 Discussion . . . 96
3.5.1 On the spatial resolution achieved in the high temperature XCT system . . . 96
3.5.2 On internal voids in Inconel 718 . . . 99
3.5.3 On surface cracks in Nimonic 80A . . . 102
3.5.4 On the advantage and limitation of the devised system . . . 104
3.6 Summary and Conclusions . . . 108

4 Damage Accumulation during High Temperature Deformation of a Superalloy Analysed by *In Situ* Computed Tomography 111
4.1 Introduction . . . 112
4.2 Experimental Methods . . . 113
4.2.1 Testing machine operation . . . 113
4.2.2 XCT post processing . . . 116
4.2.3 Stress triaxiality during necking . . . 120
4.2.4 Testing material . . . 121
4.2.5 Scanning electron microscopy analyses . . . 122
4.3 Results . . . 123
4.3.1 High temperature tensile experiment for *in situ* XCT . . . 123
4.3.2 SEM analyses of the interrupted testpieces . . . 125
4.3.3 *In situ* XCT observation . . . 126
4.4 Discussion . . . 138
4.4.1 Post-processing method for *in situ* XCT images . . . 138
4.4.2 Damage during the tensile deformation . . . 139
4.4.3 Damage generated due to XCT operation . . . 143
4.5 Summary and Conclusions . . . 143

5 *In situ* XCT and Acoustic Emission Diagnostics of High Temperature Deformation of Nickel-based Superalloy 147
5.1 Introduction . . . 148
5.2 Experimental Methods . . . 150

5.2.1 Preparation for experiment 150
5.2.2 Testing system 152
5.2.3 Testing materials 156
5.3 Results 157
5.3.1 AE and XCT analyses during high temperature tensile deformation 157
5.3.2 AE and XCT analyses during high temperature creep loading . 164
5.3.3 Defect volume effect on AE parameters 167
5.4 Discussion 167
5.4.1 Plastic deformation and AE parameters 167
5.4.2 Damage effect on AE parameters 171
5.4.3 AE signals as fracture indicators 172
5.5 Summary and Conclusions 173

6 Conclusions and Future Work **175**
6.1 Conclusion 175
6.2 Future Work 179

References **183**

Chapter 1

Introduction

1.1 The Importance of *In situ* Damage observation in Ni-based Superalloy

Ni-based superalloys are ubiquitous for the use in high-temperature systems in jet propulsion or power generation. The turbine components in such system experience centrifugal cyclic loading at high temperature, which requires high creep strength and high fatigue strength. The recent improvements in fuel economy and CO_2 emissions have been accelerating the development of their mechanical performances [1].

The failure of turbine components is a rare occurrence, since the designs or requirements in such parts must be very conservative and account for significant safety factors. Nonetheless, aviation accident is inevitable due to the unexpected failure of these components. For example, the in-flight engine failure of a Boeing 737 in Tasmania on 13 October 2000 occurred due to the loss of a segment from the trailing edge of a single high-pressure (HP) turbine blade [2]. The radial crack shape observed in the segment was attributed to severe thermal cycling, high thermal gradient, and thermal

fatigue. The oxidation and corrosion affected the crack growth in the failed blade during service, which finally lead to fatigue failure near a repaired weld. Another example is the uncontained engine failure during take-off of another Boeing 737 in Manchester on 22 August 1985, which caused losing 55 fatalities [3]. In the previous inspection of engine parts in 1983, a cracked part was repaired by fusion welding but solutioning and weld stress-relief heat treatments had not been applied, which is likely a major reason for that failure.

As introduced in these tragic incidents, defects generated during manufacturing or accumulated damage during service can lead to catastrophic failure, therefore it is critical to fabricate the components with the highest quality and have a meticulous regular inspection of these damage or defects before repaired [4]. Furthermore, it is very important to capture how the damage was initiated and accumulated, simulate the thermal or mechanical failure, and estimate remained lifetime of components. Ideally, measurements of damage accumulation would be carried out by *in situ*. A significant advantage would then arise: a direct determination of the dynamics of damage accumulation, which would lead to a better understanding of detailed responses against applied mechanical or thermal conditions, which can be used for calibrating modeling.

1.2 *In situ* Damage observation techniques

Superalloys designed in the turbine part can experience higher temperature than 800°C due to the efficiency requirements of higher turbine entry temperature (TET), which is the temperature of the hot gases entering the turbine arrangement. Since the mechanical work inside the turbine is extracted from the gas stream heat energy, further improvements of the engine efficiency demand increasing the TET. To understand

the damage mechanisms in such severe and complicated environments, accurately estimating damaged status or the remaining life, and improving the lifetime of the turbine component, it is critical to conduct *in situ* experimental analyses and studies while simulating the thermal and mechanical conditions.

X-ray computed tomography (XCT) [5] can provide visual analysis measures during high temperature mechanical testing. Since the tomography images can offer a sufficient resolution, from submicron-scale to meso-scale [6] [7], it could capture the cavitation, void growth or cracking behaviour in Ni-based superalloys during experiment. However, there are some reasons why only few attempts have been made so far. First, XCT is a three dimensional visual analyses, which requires projection images from all angles. Thus, for *in situ* XCT observation, the testpiece, or a set of X-ray source and detector need to be mechanically rotated along with applying the load to the testpiece. Obtaining one tomography requires a long duration depending on its target resolution. Especially, the rotational operation under high temperature might induce further untargeted damage in a more complicated manner. Second, XCT arrangements for high temperature testing can lead to obstacles for capturing images, for example electric furnace or induction heating coils. This could hinder the control of image uncertainties [8]. Furthermore, it is difficult to detect the target damage in a timely manner. Deciding when to commence XCT operation requires an indicator of the damage or certain type of microstructural changes. This can be tackled by means of acoustic signals [9] [10].

1.3 Aim of Research and Thesis Structure

In this thesis, a laboratory-scale XCT setup is developed for the purpose of *in situ* damage observation. The *in situ* XCT procedure for high temperature mechanical

testing and improvements of tomography image processing for high resolution will be investigated. The studied materials include Inconel 718 and Nimonic 80A as typical examples of polycrystalline Ni-based superalloys. Furthermore, novel contactless Acoustic Emission (AE) techniques are combined with the XCT system to determine precisely when CT images of the deformed or damaged object should be captured.

Chapter 2 begins with an overview of the physical metallurgy of Ni-based superalloys. The deformation, damage growth and failure mechanisms at high temperature are reviewed. Then, the development of XCT and AE testing techniques as *in situ* damage observation measures are presented. Finally, possible difficulties of combining these measures with mechanical testing are discussed, since developing a new *in situ* observation system for high temperature mechanical testing is the main focus of this thesis.

Chapter 3 will present the development of a novel *in situ* XCT arrangement to capture the deformation, internal cracks and voids generated during loading at 800°C. The system is optimised for the sequential acquisition of 3D backprojection images recorded during tensile deformation at strain rates between 10^{-4} and 10^{-2} [s^{-1}]. The polycrystalline Ni-based superalloys, Nimonic 80A and Inconel 718, which exhibit lesser and greater ductility, are studied. The tomography images can be resolved to within 30 to 50 μm, thus providing the time- and spatially-resolved data for the growth of internal cracks and voids.

In Chapter 4, post-processing methods including beam-hardening correction and spot artefact removal will be proposed to improve the tomography image resolution to around 30 μm to allow more quantitative damage analysis. In addition, a robust method for XCT rotation is developed to prevent unintentional damage and focus on the effects of necking on internal void growth. The investigated visualised relations

between void growth and necking behaviours during tensile or creep loading at 800°C offer new insights of stress triaxiality effects on cavity growth.

In Chapter 5, a novel system combining XCT and AE techniques will be introduced. This devised system investigate the effect of damage growth or plastic deformation at high temperatures on the characteristics of generated elastic waves. The newly combined XCT and AE techniques succeeded in detecting AE signals and comparing them with *in situ* 3D damage analyses at 800°C during the tensile and creep deformation of a Ni-based superalloy. The quantitative 3D XCT and AE analyses of the deformation status or damage growth reveal that the plastic strain rate correlates with the amplitude or the energy of generated elastic waves, while the growth of internal defects affects the AE median frequency. These findings will provide new insights on when to capture the internal damage by *in situ* XCT.

Finally, in Chapter 6 the key outcomes from this research are summarised. Suggestions for the future work are given regarding the investigation of the complicated mechanical/thermal damage accumulation in polycrystalline Ni-based superalloys by means of the newly devised *in situ* XCT system.

Chapter 2

Literature Review

2.1 Ni-based superalloys

2.1.1 Metallurgy of superalloys in general

Ni-based superalloys are widely used for high temperature applications within jet engines for civil aeroplanes. Since the introduction of jet engines, the turbine entry temperature has drastically increased from 800°C to approximately 1500°C [4, 11]. It is estimated to reach 1700°C considering ongoing fuel efficiency demands and the constant need to reduce emissions [12, 13]. Increasing the turbine entry temperature is a major driving force for the continued development of new Ni-based superalloys. For regular use at these high temperatures, the material properties require a high temperature strength, improved fatigue, and creep life. Today, these high-temperature materials are one of the most chemically complex alloy systems, often containing up to eleven different alloying elements.

The alloy chemical composition affects the equilibrium microstructure, which is substantially composed of a (i) Ni-base face centred cubic (FCC) austenitic matrix phase, γ-phase, (ii) Ni_3Al, a cubic $L1_2$-type ordered strengthening precipitate called $\gamma^{'}$-phase, and (iii) body-centred tetragonal (BCT) $D0_{22}$-type precipitate called $\gamma^{''}$-phase (Ni_3Nb). Minor phases such as carbides, borides, and topological closed packed (TCP) phases are also included and often located at the grain boundaries (see Figure 2.1). Of the alloying elements, Al and Ti help in the precipitation of $\gamma^{'}$-phase. Nb and Ta promote the precipitation of $\gamma^{''}$-phase. Cr and Mo help in the carbide precipitation of $M_{23}C_6$ and M_6C, respectively. Excessive quantities of Cr, Mo, W, and Re promote the precipitation of TCP phases.

The γ-phase usually contains Cr, Co, Mo, and W. Cr is included to form a protective Cr_2O_3 oxide layer [14], Co exists for enhancing the processing ability [15], Mo and W are employed for solid solution strengthening and creep resistance [16]. Figure 2.2 shows the preference of the partition for each element. The γ'-precipitate is an intermetallic compound mainly responsible for the high temperature strength of Ni-based superalloys. Curbing the cross-slip of dislocations in the γ'-phase causes the yield stress to increase under the temperature up to approximately 800°C [17]. Advanced polycrystalline Ni-based superalloys contains γ'-phase for 40 to 60% in volume fraction [18].

The typical γ'-precipitates is Ni_3Al with a lattice parameter of $a_{\gamma'} = 0.3570$ nm, which is 1.5% larger than the lattice parameter of pure fcc Ni with $a_{\gamma} = 0.3517$ nm [4]. Therefore the phase boundary between the γ-matrix and the γ'-precipitate is regarded to be coherent, and the interfacial energy remains low. The orientation relationship between the γ-matrix and the γ'-precipitates is a cube-cube orientation, which can be described by $\{100\}_{\gamma}/\{100\}_{\gamma'}$ with $\langle 010\rangle_{\gamma}/\langle 010\rangle_{\gamma'}$. The γ'-precipitates often align along the $\langle 100\rangle_{\gamma}$ direction [4].

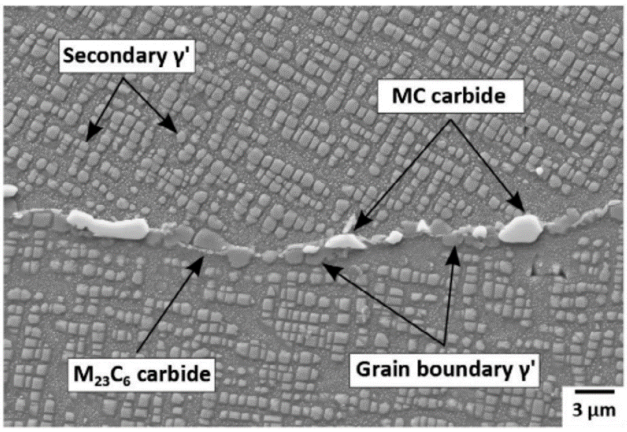


Fig. 2.1 Secondary Scanning Electron Microscope image of $M_{23}C_6$ carbides at a γ-grain boundary in a γ/γ'-phase strengthened Ni-based superalloy. Adapted from reference [19].

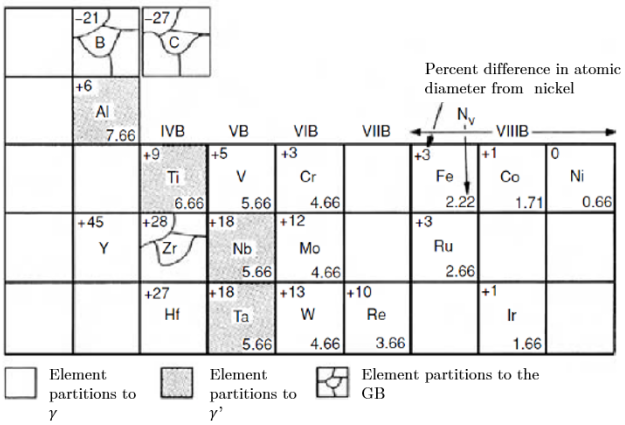


Fig. 2.2 Essntial solute elements in Ni-based superalloys and their position in the periodic table of elements. Adapted from reference [20].

The lattice parameters, a_γ and $a_{\gamma'}$, are increased or decreased by solute atoms in each phase, which is consistent with Vegard's law : $a_\gamma = a_\gamma^0 + \Sigma_i\ \Gamma_i^\gamma\ x_i^\gamma$ and $a_{\gamma'} = a_{\gamma'}^0 + \Sigma_i\ \Gamma_i^{\gamma'}\ x_i^{\gamma'}$, where x_i^γ and $x_i^{\gamma'}$ are the mole fractions of added solutes (i) in each phase. The misfit between the γ-matrix and the γ'-precipitate is a function of the lattice parameters a_γ and $a_{\gamma'}$ which can be mathematically defined as [4]:

$$\delta = 2 \cdot \frac{a_{\gamma'} - a_\gamma}{a_{\gamma'} + a_\gamma} \quad . \tag{2.1}$$

The γ' precipitates grow in the sequence of spheres, cubes, arrays of cubes, and dendrites as the increasing degree of ageing [21]. The lattice misfit, δ, affects the γ' particle size starting as the spherical morphology and sensitivity of the heat treatment to form the cuboidal arrays. In superalloys which contain Nb – such as Inconel 706 and 718 –, instead of the γ' phase, the meta-stable γ''-precipitate can occur as the primary strengthening precipitate [4].

At the grain boundaries of polycrystalline Ni-based superalloys, various carbide and boride species can be formed depending on the alloy composition and the processing method. Common carbides and borides are MC, $M_{23}C_6$ and M_6C, M_3B_2 and M_5B_3, where M represents a metal atom such as Cr, Mo, Ti, Ta, and Hf. The MC carbide can decompose into the γ'-precipitate and $M_{23}C_6$ as following transformation: $MC + \gamma \rightarrow M_{23}C_6 + \gamma'$ [22]. The MC carbide can also decay into the M_6C carbide: $MC + \gamma \rightarrow M_6C + \gamma'$ [23]. These are usually found to precipitate on the γ grain boundaries. Borides such as M_3B_2 and M_5B_3 can also be found at the grain boundaries. These phases potentially play a role in strengthening the alloy through inhibiting movement of dislocations, prohibiting grain boundary sliding and cavitation [24]. However, the role

of grain boundary phases is still controversial since they can enhance brittle fracture as nucleation sites for cracks [25].

After being exposed to high temperature conditions for a long time, topologically close-packed (TCP) phases like the σ-, μ-, η- and laves-phases can be generated with the sufficient amounts of Cr, W, Co, and Mo in the alloy. One of the most common TCP phases is the σ-phase. This phase consists of (Cr, Mo)$_x$(Ni, Co)$_y$ where x and y can be from one to seven [20]. TCP phases are often composed in a complex crystal structure, thus exhibiting a limited number of slip planes. Thus these phases enhance brittle rupture and limit tensile ductility leading to a short stress rupture life.

2.1.2 Plastic deformation at high temperature

Static deformation

Plastic deformation in Ni-based superalloys in the mid-temperature range at intermediate and fast deformation rates is affected by interactions of dislocations with (i) solute atoms in the γ-matrix, (ii) γ-grain boundaries, and (iii) the γ'-precipitates.

Additions of Co, Cr, Mo, and W can strengthen the γ-matrix. When a different size atom is introduced to the Ni site within the crystal structure, the internal strain fields inhibit dislocation movement, which causes a strengthening effect. In addition, for example, adding Co element in the γ-matrix can lower the stacking fault energy, and changing the *ABC ABC ABC* sequence can make dislocation movement more difficult. At lower than 750°C, dislocations can move on the $a/2\ \langle 1\bar{1}0\rangle\ \{111\}$ slip system and be divided into two dislocations known as Shockley partials [4]:

$$a/2\ \langle 1\bar{1}0\rangle\ \{111\} \rightarrow a/6\ \langle 211\rangle\ \{\bar{1}11\} + a/6\ \langle 12\bar{1}\rangle\ \{\bar{1}11\} \tag{2.2}$$

The distance between the partial dislocations is known to be inversely proportional to the stacking fault energy [4]. Lowering this energy has an important role in the resistance to dislocation climb. The steady-state creep rate decreases with the stacking fault energy decrease for high temperature applications. In polycrystalline Ni-based superalloys, grain boundaries can curb the dislocation movement in yield. But in creep, since a small grain size increases dislocation density and enhances diffusion processes, large grain size is preferable for increasing creep resistance. This will be explained in detail in the next section.

The Ni_3Al phase within the γ-matrix strongly affects the strengthening behaviour of Ni-based superalloys. Since two superlattice partial dislocations are needed to produce a dislocation in the ordered γ'-phase, shearing over γ'-precipitates is hindered. When the superlattice partial dislocation in the γ-matrix enters the precipitate during deformation, it forms a planar fault, which is called anti-phase boundary (APB). The γ'-phase $L1_2$ crystal structure order is then restored by forcing Ni-Ni and Ni-Al bonds as first neighbour bonds rather than Ni-Al bonds; a following superlattice partial dislocation is then able to recover the ordered $L1_2$ structure. Therefore, precipitate shearing could occur only if the shear stress is sufficiently large to force the partial dislocation to prevent the γ'-particle from creating an APB. The dislocation of a γ'-precipitate can be coupled either 'strongly' or 'weakly' depending on the γ' fraction [4].

Both 'strongly' and 'weakly' indicate the attractive force between the leading dislocations and the trailing dislocation when they pass through the γ'-precipitate particles. 'Weakly' coupled dislocations are generated in cases when the distance between the leading and the trailing dislocation is huge compared to the γ'-precipitate radius, which often occurs when the microstructure is not in fully-aged condition. In an over-aged condition, the dislocations can be 'strongly' coupled. Figure 2.3 depicts an

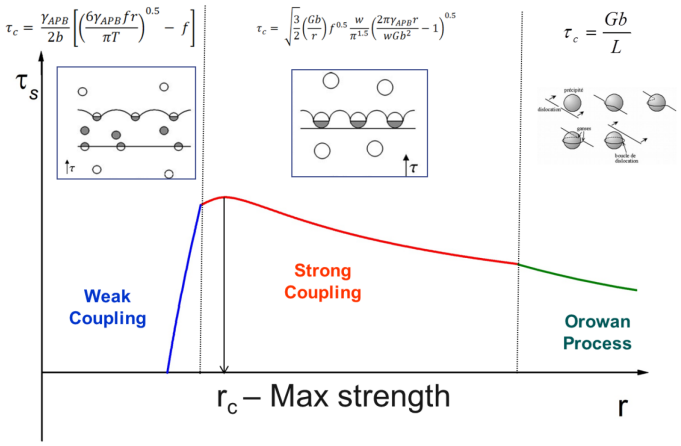


Fig. 2.3 An overview of how dislocation couplings can vary over the γ'-precipitate in Ni-based superalloys. Adapted from reference [11].

overview of the γ'-particle shearing mechanisms variations. The γ'-phase strengthening becomes maximum where dislocation shearing changes from the weakly to strongly coupled pairs [26].

At this critical γ'-precipitate radius (r_c) the strength of the precipitate can be calculated to $1/2{\cdot}\gamma_{APB}\ f^{1/2}/b$ [27], where γ_{APB} is the anti-phase boundary energy, f is the volume fraction of the γ'-phase and b is the Burger's vector. It is thus clear that strengthening in Ni-based superalloys is strongly affected by the precipitate volume fraction and the fault energy.

Time-dependent deformation

At sufficiently low deformation rates, thermally activated time-dependent creep behaviours are attributed to plastic deformation in intermediate and high temperatures. In polycrystalline Ni-based superalloys, the creep mechanism depends significantly upon the microstructure. Especially grain size has a significant effect on creep rates. The deformation mechanism map (Ashby map) [28] is commonly used to represent the creep deformation mechanism map with regards to temperature and stress. An

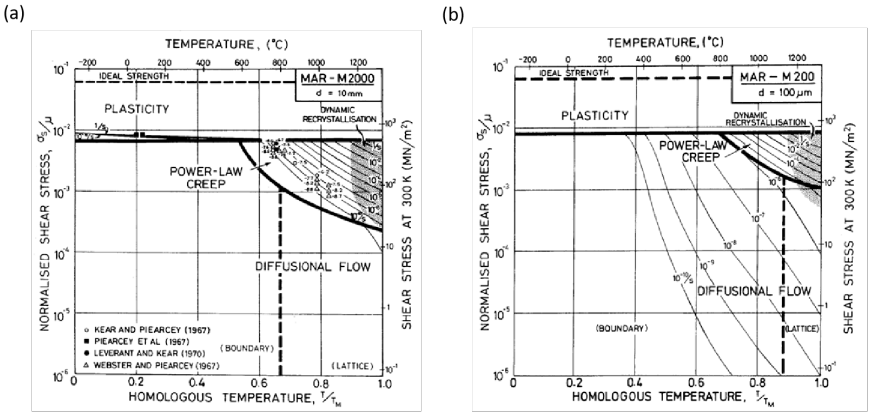


Fig. 2.4 Ashby map for MAR-M200 (a) with a grain size of 10 mm, as cast, and (b) with a grain size of 100 μm, as cast [28].

example of the grain size effect in Mar M200 is illustrated in the Ashby maps shown in Figure 2.4. As shown in the maps, larger grains suppress diffusional flow. Although bulk diffusional flow is not affected as much as grain-boundary diffusional flow in smaller grains, the bulk flow becomes relatively more important when the grain size is increased.

In practice, creep by self-diffusion through the matrix is the predominant mechanism only when the stress is low and the temperature is very close to the melting point. Coble [29] pointed out that the activation energy for self-diffusion along grain boundaries was considerably less than that for self-diffusion through the bulk of the grain. Coble creep is the process whereby atoms are transported around the grain boundaries by stress-induced diffusion to allow grains to extend in the direction of tensile stress. At temperatures 100 °C or more below the melting point, the transport of the matter along the grain boundaries will be more rapid than that through the bulk. At higher temperatures, atoms are transported through the grain, which is called Herring-Nabarro creep.

Figure 2.5 illustrates the general creep curve under the constant true stress. The evolution of creep strain follows three stages. In a period of primary creep, a rapid

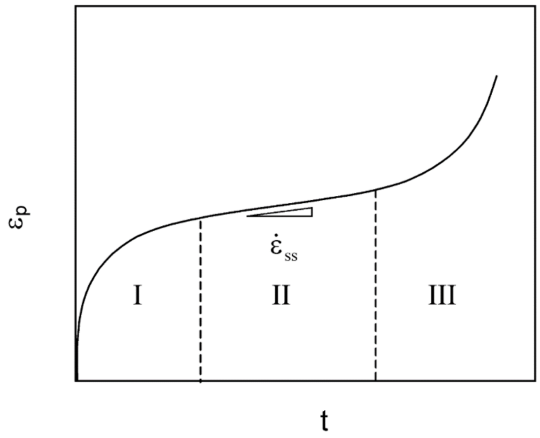


Fig. 2.5 Constant true stress creep behaviour. (I) primary creep stage, (II) secondary or steady-state creep stage, and (III) tertiary creep stage. Adopted from [30].

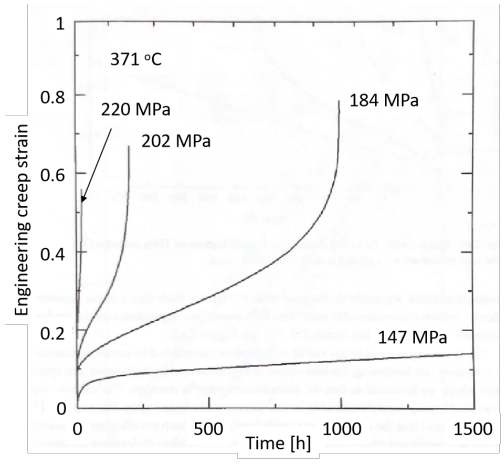


Fig. 2.6 Creep curves (constant load conditions) for pure nickel tested at 371 °C [31].

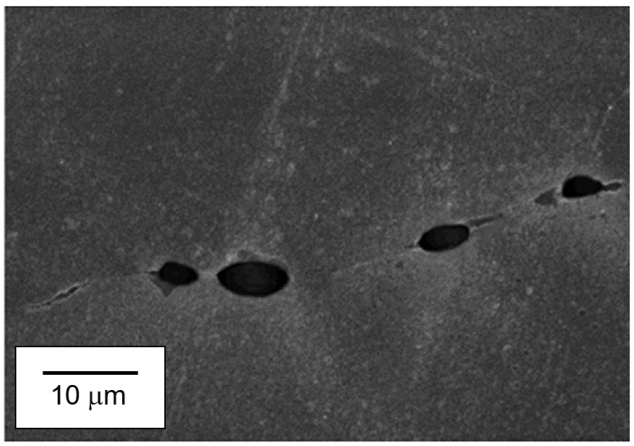


Fig. 2.7 Creep cavities along grain boundary generated under 500 MPa at 650 °C (Adopted from [32]).

initial transient gives way to the next regime, where the creep strain rate is constant. This steady-state regime is called secondary creep. The onset of failure is related to a divergence from the steady-state behaviour. This is the tertiary stage where the creep strain rate increases with the strain increment until the final fracture. Figure 2.6 shows the examples of creep curves of pure nickel subjected to constant load conditions at 371°C and stresses between 147 and 220 MPa. This figure indicates that the tertiary creep stage starts earlier under higher stress conditions. During the secondary stage, creep cavities are formed, and the onset of the tertiary creep stage often accompanies the growth of such damages. Figure 2.7 is the example of creep cavities along grain boundaries in Inconel 718 generated during the steady-state creep stage show the size of less than 10 μm [32].

Strain rate and tensile deformation

During the tensile loading experiment of Ni-based superalloys at elevated temperatures, the strain rate can affect their ductility. This superalloy shows ductile fracture at a higher temperature, while at the medium temperature, it can rupture mainly from

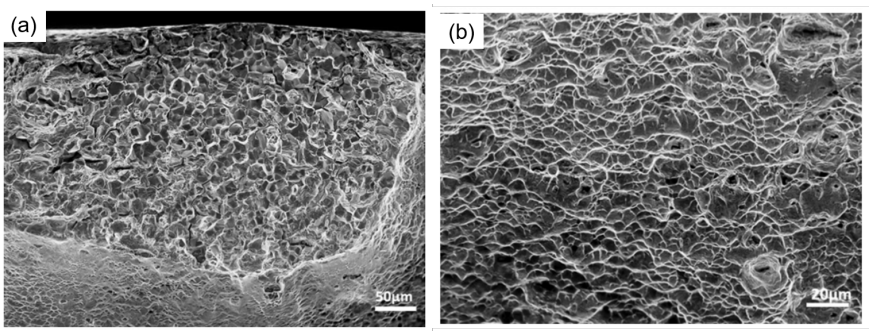


Fig. 2.8 Fractured surface of the testpiece subjected to tensile loading at 600 °C, showing (a) intergranular fracture (3.2 x 10^{-4} s^{-1}), and (b) transgranular fracture (10^{-3} s^{-1}) (Adopted from [35]).

grain boundaries (intergranular fracture) or fracture by ignoring grains (transgranular fracture) depending on strain rate. For example, Inconel 718 shows ductile fracture at 800°C or higher [33], [34] , while at 300 - 700 °C it shows intergranular and transgranular fracture depending on strain rate [35], [36]. This latter behaviour at the medium temperature is due to the dynamic strain ageing (DSA) phenomenon in which dynamic interactions occur between mobile solute atoms and the moving dislocations. Depending on applied temperature and strain rate, plastic instabilities which lead to serrations in stress-strain curves occur from the onset of plastic deformation to fracture [37]. This is called Portevin-Le Chatelier (PLC) effect, which leads to the transgranular fracture at the temperature range. Figure 2.8 exhibits the intergranular fractured surface obtained in DSA condition and the transgranular rupture surface fractured in PLC condition. Intergranular fracture surface shows grain facets that used to be grain boundaries, whilst transgranular fracture surface exhibits dimple shapes that are not originated from grain-based microstructure. At higher temperatures, strain rate can affect the time for energy accumulation, which leads to the difference of tensile stress [38].

2.1.3 Failure

Cavitation and void growth

Alloy materials can form microscopic voids or cavities when sufficient strain is applied during tensile loading. These microscopic cavitations primarily occur in the grain boundaries during high-temperature deformation. Cavitation is a critical phenomenon under high temperatures because it may lead to premature failure during forming and also yield inferior properties before fracture [39]. Thus, primarily for the tensile test, it has been studied extensively.

Cavitation occurs via three stages during tensile deformation: cavity nucleation, void growth, and void coalescence. For cavity nucleation, several mechanisms have been established, such as (a) intragranular slip intersections with second phase particles and grain boundaries, (b) grain boundary sliding, and (c) vacancy concentration on grain boundaries [40], [41], [30]. A cavity-nucleation criterion based on stress equilibrium at the interface is:

$$r_c = 2(\gamma + \gamma_p - \gamma_i)/\sigma \tag{2.3}$$

In which r_c is the critical cavity radius above which a cavity could be stable, and γ, γ_p, and γ_i are the surface energies of the void, the particle, and the particle-matrix interface, respectively; and σ denotes the applied stress. Since such interfacial-energy considerations require extremely high stresses for initiation and early growth of cavities, other approaches based on nucleation and development due to increased local stress triaxiality have also been undertaken [39].

Void growth mechanisms can be classified into diffusional growth and plasticity-controlled growth. Diffusional growth primarily occurs while the cavity is tiny. As the

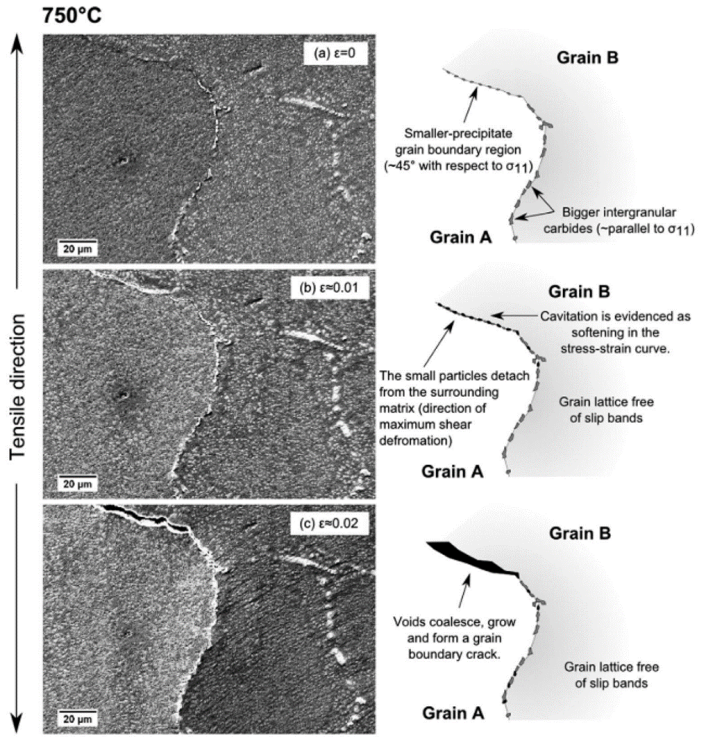


Fig. 2.9 Sequential SEM images of void coalescence in grain boundary in a polycrystalline Ni-based superalloy (STAL-15) during tensile loading at 2 x 10^{-5} s^{-1} at 750°C. (Adopted from [19]).

cavity becomes enlarged, diffusional growth decreases very quickly, and instead, plastic flow in the vicinity of cavities dominates the growth mechanism [39]. Void coalescence is the interlinkage of neighbouring cavities because of the microscopic flow-localisation process in the internal ligament. Coalescence can occur when the width of the material ligament reaches a critical distance which is affected by initial cavity spacing and the strain-rate sensitivity. Coalescence occurs along with both the longitudinal and transverse directions, leading to failure.

Summer *et al.* challenged to observe the void coalescence during tensile loading at 750 °C by *in situ* SEM (Figure 2.9). Small cavities with less than 10 μm in grain boundary were coalesced to induce intergranular cracks leading to failure [19]. Coalesced grown voids were observed as large as 50 μm as shown in fig.2.9. The grown

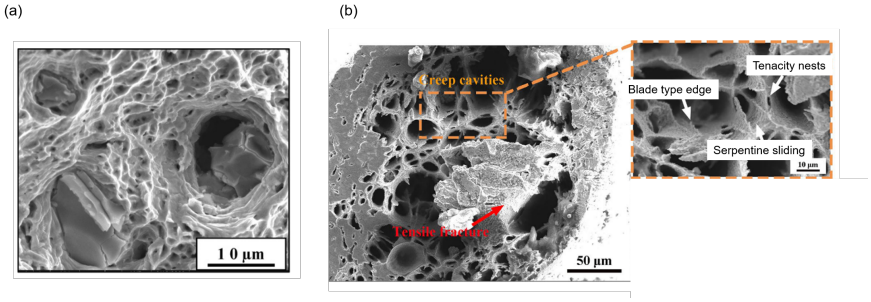


Fig. 2.10 (a) Fractured surface after tensile loading at 3.3 x 10^{-4} s^{-1} at 550 °C (Adopted from [42]). (b) The fracture surface of Inconel 718 after subjected to creep loading of 150 MPa at 800°C (Adopted from [43]).

voids can be also observed from the fractured surface subjected both to tensile loading (fig.2.10(a)) and to creep loading (fig.2.10(b)). The void growth can be affected by applied loading conditions, but larger than 10 μm grown voids can be observed after or during the experiments.

Stress triaxiality

Using the three principle stresses, σ_1, σ_2, and σ_3, the mean stress (σ_m) and the equivalent stress (σ_e) can be expressed as follows (*e.g.* [44], [45]),

$$\sigma_m = \frac{\sigma_1 + \sigma_2 + \sigma_3}{3} \tag{2.4}$$

$$\sigma_e = \sqrt{\frac{1}{2}((\sigma_1 - \sigma_2)^2 + (\sigma_2 - \sigma_3)^2 + (\sigma_3 - \sigma_1)^2)} \tag{2.5}$$

Stress triaxiality (T) is defined by using the above two parameters,

$$T = \frac{\sigma_m}{\sigma_e} \tag{2.6}$$

Although T can be calculated as 1/3 in uniaxial tension case ($\sigma_m = \frac{1}{3}(\sigma_1 + 0 + 0 = \frac{1}{3}\sigma_1$, $\sigma_e = \sqrt{\frac{1}{2}((\sigma_1 - 0)^2 + (0 - 0)^2 + (0 - \sigma_1)^2)} = \sigma_1$), this is not constant during testpiece profile changes due to necking in tensile test. For a round bar tensile testing, Bridgeman [46] calculated radial, hoop, and axial stresses (σ_{rr}, $\sigma_{\theta\theta}$, and σ_{zz}, respectively) for the necked part as follows with radial coordinate r, minimum cross-sectional radius a and necking curvature R (fig.2.11).

$$\sigma_{zz} = \sigma_e\Big(1 + ln(\frac{a^2 + 2aR - r^2}{2aR})\Big) \tag{2.7}$$

$$\sigma_{rr} = \sigma_{\theta\theta} = \sigma_e\Big(ln(\frac{a^2 + 2aR - r^2}{2aR})\Big) \tag{2.8}$$

Therefore, stress triaxiality T can be expressed as follows,

$$T = \frac{\sigma_m}{\sigma_e} = \frac{1}{3} + ln(\frac{a^2 + 2aR - r^2}{2aR}) \tag{2.9}$$

Figure 2.12 shows the empirical data plots of the equivalent strain to fracture against the stress triaxiality [48]. Bao and Wierzbicki demonstrated the fracture differences of an aluminium alloy (2024-T351) with stress triaxiality changes. Different triaxiality states were intentionally prepared with compressive loading mode (-0.33 $\leq$ T $\leq$ -0.12), shear loading mode (0 $\leq$ T $\leq$ 0.02), tensile loading with smooth round bars (0.33 $\leq$ T $\leq$ 0.5) and tensile loading with large-notched (0.6 $\leq$ T $\leq$ 0.7) to small-notched round bars (0.9 $\leq$ T $\leq$ 1). Even in the same tensile loading mode, they exhibited different ductile fracturing behaviour with the stress triaxiality due to the notch sizes. Other works reported the stress triaxiality effect not only on the fracture strain [45], but also on void growth and coalescence behaviour [49]. During the ductile tensile deformation,

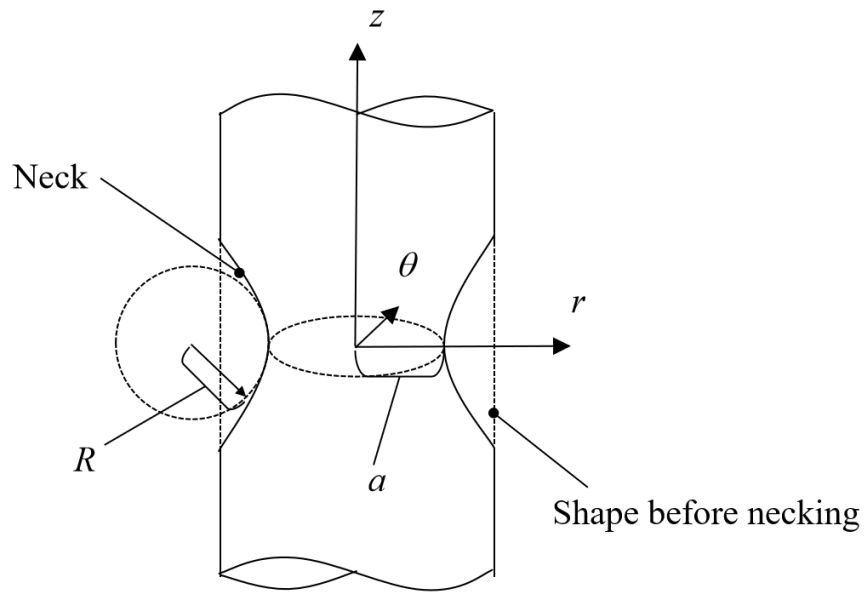


Fig. 2.11 Tensile necking in a round bar (Adopted from [47]).

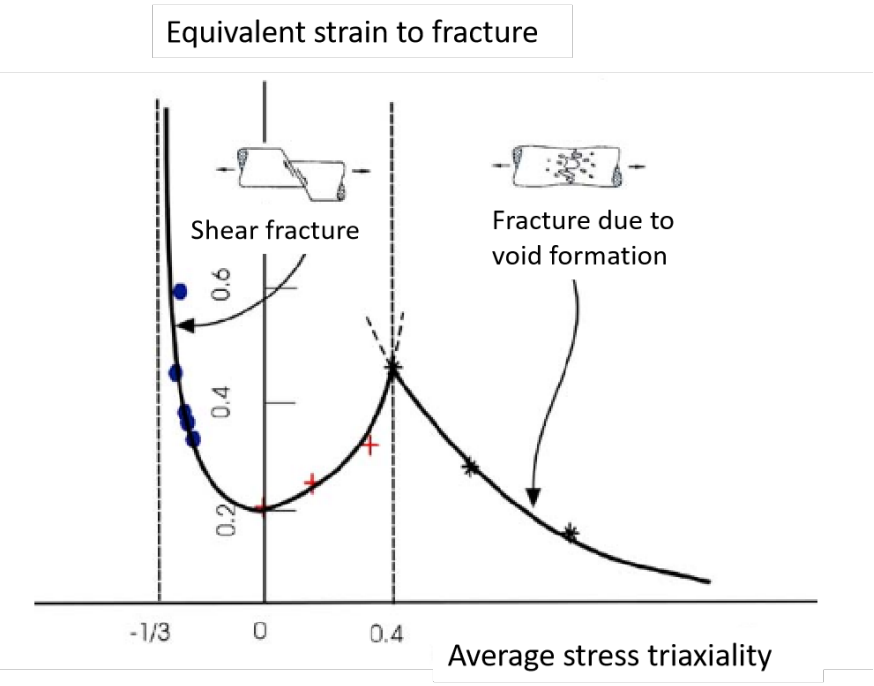


Fig. 2.12 Effective strain at fracture against the stress triaxiality (Adopted from [48]).

different stress triaxiality due to the necking profile can change the ductile fracturing behaviour.

2.1.4 Metallurgy and mechanical properties of superalloys chosen in this thesis

This thesis chooses Nimonic 80A and Inconel 718 as the testing materials. These superalloys exhibit different mechanical behaviours at high temperatures, more than 800°C, which can be the target thermal condition in the experimental system.

Nimonic 80A(N80A)

Nimonic 80A, called N80A, was produced in the 1930s by adding Al and Ti to Ni-based FCC alloys. These elements improved the creep resistance of the nickel alloys by creating the coherent γ' phases [50] in it. Al is the primary γ' - former and an important oxidation-resistant element. Nimonic 80A is a wrought-type Ni-based superalloy that is suitable for applications under high stress under high temperatures up to 750°C. It is widely employed in mechanical joining parts used in high-temperature conditions, such as in the combustion chamber of the gas turbine unit, which can operate at less than 650°C. The chemical composition of Nimonic 80A is defined as described in Table 2.1 in ASTM B637 standard. The standard heat treatment consists of solution annealing at 1079°C for 8 hours, cooling in air to room temperature.

Gibbons and Hopkins [51] have studied the creep behaviour of a series of Nimonic alloys possessing a range of Al and Ti and thus volume fractions of γ' phase. Their work indicates that if the stress level is not so high, the creep performance is improved significantly by increasing the γ' phase. This strong precipitation-hardening effect was

applied to a series of wrought superalloys used for the turbine blading of jet engines produced in the 1940s and 1950s. These were strengthened by increasing the γ' phase. Gibbons and Hopkins [51] also found that the γ' strengthening effect was substantial in the case that the grain size was large. γ' solvus temperature in Nimonic 80A is reported around 1000°C [52]. Above the service temperature range, under higher than 750°C, the elongation during tensile loading is limited, which leads to brittle intergranular fracture [53]. But at higher temperatures, such as more than 850°C, as being close to the γ' solvus temperature, the elongation increases again and ductile behaviour can become present.

Inconel 718(IN718)

Inconel 718, or referred to as IN718, is one of the popular alloys in Nickel-Iron-base superalloys, which contributes to nearly 35% of the world's wrought superalloy production [54]. This alloy was invented by adding Nb to produce γ'' precipitation phase in the late 1950s [50]. Inconel 718 is well known for its high strength due to the γ'' precipitation phase and has good weldability that has good post-weld cracking resistance. It also possesses good corrosion and oxidation resistance and good creep properties. Inconel 718 is commonly used under high temperature and high pressure, for example, turbine blades, rotors, and combustors, in aerospace and nuclear industries.

The γ'' precipitate (Ni_3Nb) is the main hardening phase in Inconel 718. When subjected to an over-ageing condition, the γ'' phase will be transformed to the δ phase. Compared to the γ' phase, γ'' has the lower solvus temperature (around 920°C[55]), which will cause a remarkable strength decrease. Exposed to a temperature higher than 650°C, the γ'' phase can start the transformation into δ phase. This transformation depends strongly upon temperature. It is reported that the creep ductility relates to the amount of intergranular δ precipitation because it leads to the grain boundary

softening [56]. Grain boundary δ phase can be formed in 10 hours at around 800°C and faster at the higher temperature [34]. It means that at higher than 800°C, Inconel 718 exhibits less strength and more ductile behaviour [57]. The chemical composition of Inconel 718 is defined in ASTM B670 standard as described in Table 2.1.

Table 2.1 Chemical compositions of Nimonic 80A and Inconel 718 in wt.-%

Name	Ni	Cr	Al	Ti	Fe	Nb	Co	Mn	Cu	Si	C	B	S
Nimonic 80A	Balance	18.0-21.0	1.0-1.8	1.8-2.7	0-3.0	-	0-2.0	0-1.0	0-0.20	0-1.0	0-0.10	0-0.008	0-0.015
Inconel 718	50.0-55.0	17-21	0.2-0.8	0.65-1.15	Balance	4.75-5.50	0-1.0	0-0.35	0-0.30	0-0.35	0-0.08	0-0.006	0-0.015

2.2 Testing methods

2.2.1 X-ray computed tomography (XCT)

XCT method

In 1917, Radon established the mathematics for X-ray computed tomography (XCT) method [58]. With the aid of the development of digital computers, finally in the 1970s, a commercial computed tomography system was introduced for medical purposes [59]. For developing new products, controlling manufacturing processes, or predicting material performance and failure, the XCT has been gradually introduced in the field of material science since the 1980s (*e.g.* [60]).

As discovered by Röntgen, the intensity of X-rays is attenuated with the coefficient μ by the following equation,

$$I/I_0 = exp(-\mu x) \tag{2.10}$$

where I_0 is the unattenuated X-ray beam, and I is the beam intensity attenuated after travelling through a material thickness x. Based on this attenuating behaviour, XCT can reconstruct the object through which the X-ray beam travelled as follows.

When an X-ray beam L_j passes through a testpiece which has the mass density $f(x, y)$, the X-ray energy should be attenuated. If the energy at the source is $E_{j,0}$, the detected energy $E_{j,1}$ through the specimen is [61]

$$E_{j,1} = E_{j,0} e^{-\int_{L_j} f(x,y)\mathrm{d}s} \tag{2.11}$$

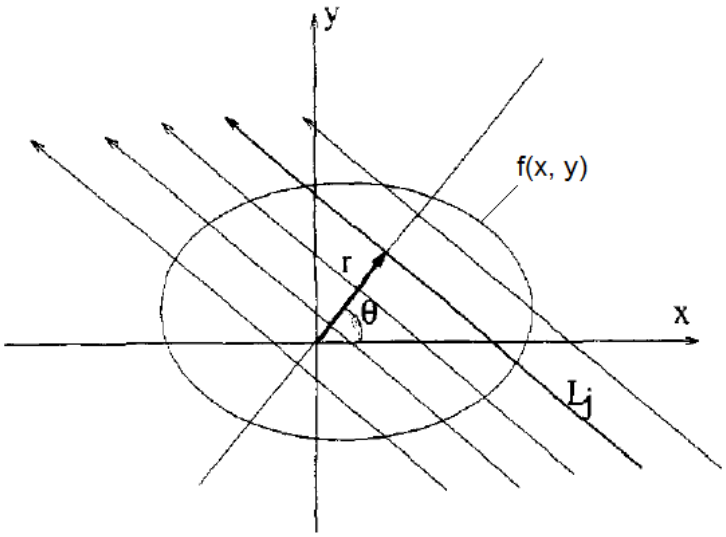


Fig. 2.13 Polar coordinate system r, θ. (adapted from [61])

where ds denotes the path increment along the line L_j. If we set $p_j = ln(E_{j,0}/E_{j,1})$ as measured intensity information detected from the X-ray L_j,

$$\int_{L_j} f(x,y)\mathrm{d}s = p_j \tag{2.12}$$

If we consider the multiple parallel X-ray beams, introducing a polar coordinate system (r,θ), the detected value $p(r,\theta)$ can be expressed as,

$$p(r,\theta) = \int_{-\infty}^{\infty}\int_{-\infty}^{\infty} f(x,y)\delta(x\cos\theta + y\sin\theta - r)\mathrm{d}x\mathrm{d}y \tag{2.13}$$

where $\delta(x)$ is the Dirac's delta-function. The right hand side of Eq.(2.13) is the Radon transform, $\mathcal{R}$. Assuming that $p(r,\theta)$ has already been observed,

$$\begin{aligned} f(x,y) &= \mathcal{R}^{-1}p(r,\theta) \\ &= \frac{1}{2\pi}\int_0^{\pi}\int_{-\infty}^{\infty} \frac{\frac{\partial p}{\partial r}}{x\cos\theta + y\sin\theta - r}\mathrm{d}x\mathrm{d}y \end{aligned} \tag{2.14}$$

Eq.(2.14) is known as the inverse Radon transform, which was given by Radon [58]. Since the obtained values for $p(r,\theta)$ are a finite number of points, f(x,y) needs to be calculated with the discretised integral form. The computing methods for this discretised inverse Radon transform has been proposed, such as the algebraic reconstruction method (e.g. [62]), direct Fourier methods and the filtered back-projection method [61]. The filtered back-projection method offers the image $f(x,y)$ as follows. Here we define the Fourier transform of $p(r,\theta)$ with respect to r by,

$$\hat{p}(\omega,\theta) = \int_{-\infty}^{\infty} p(r,\theta)e^{-i2\pi\omega r}\mathrm{d}r \tag{2.15}$$

where ω is the Fourier variable. Using Eq.(2.15), Eq.(2.14) can be calculated by,

$$f(x,y) = \int_{0}^{\pi}\int_{-\infty}^{\infty} \hat{p}(\omega,\theta)|\omega|e^{i2\pi\omega r}\mathrm{d}\omega\mathrm{d}\theta \tag{2.16}$$

The calculated $f(x,y)$ in Eq.(2.16) is the reconstructed original image. Thus, XCT image reconstruction requires the following steps [61]: (1) Fourier transform of p with respect to r, (2) Multiplied by the filtering function $|\omega|$, (3) Inverse Fourier transform of $\hat{p}|\omega|$, and (4) Integrate $\hat{p}$ with respect to θ. $|\omega|$ is called Ram-Lak filter, which can be replaced with other filtering functions, such as Shepp-Logan, Cosine, Hamming [63]. As inverse Radon transform requires the integrating step described above, the attenuated beam intensity information ($p(r,\theta)$, or 'back projection image') need to be collected from 0 ° to 180°. Sometimes it is collected up to 360° for more precise calculation [64]. In any case, the object testpiece needs to be rotated to capture this back projection images for 3D XCT reconstruction.

As the attenuate coefficient (μ) varies depending on the number of atoms encountered by the X-ray beam [59], the beam intensity $p(r,\theta)$ is affected by the material where the beam traversed. Thus the heavier samples with the large atomic number

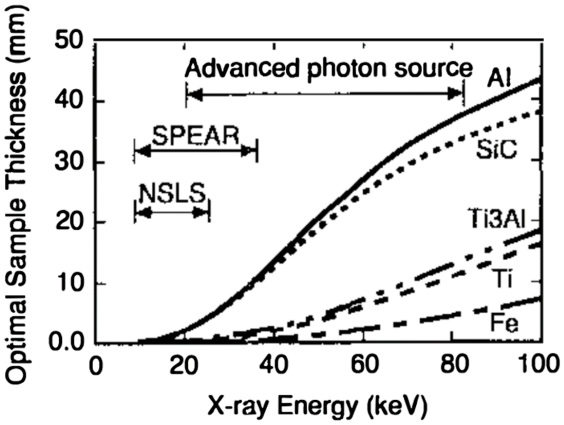


Fig. 2.14 The optimal sample thickness as a function of X-ray energy (Adoped from [65]. NSLS: National Synchrotron Light Source, SPEAR: Stanford Synchrotron Radiation Laboratory, and Advanced photon source exhibits the approximate energy ranges in each X-ray source.

attenuate X-ray beam energy severely, which can hinder capturing the clear XCT images for the large object (Figure.2.14). The heavy materials such as iron or Ni-based superalloys are supposed to be limited in sample size within a few millimetres, in case using the laboratory X-ray source with 10 to 100 [keV] [65].

As the X-ray spectrum does not include any characteristic peaks in the synchrotron source, the X-ray energy can be continuously tuned using single-crystal monochromators over the whole range of the X-ray source [65]. Therefore, it is possible to select the ideal monochromatic X-ray energy for a specific tomographic imaging purpose. However, in the case of polychromatic X-ray beam from the laboratory conical X-ray source, the low-energy X-ray photons are severely attenuated while transporting through the testpiece, which causes "beam hardening" [66, 67]. Hence the attenuation produced by a testpiece, which would be used in Eq.(2.11),(2.12), is not strictly proportional to its thickness or the path where it traverses. For the beam hardening correction with the polychromatic X-ray source, pre-filter with alloy foil (*e.g.* [68]) and post-processing measures [69] for beam hardening are required to obtain the tomography image with the sufficiently high resolution.

XCT techniques

Based on the reconstructing method introduced in the previous section, several experimental arrangements have been developed for capturing backprojections and reconstructing tomography images [59]. Figure 2.15(a) shows the pencil beam systems which employed a pinhole collimator C to produce pencil-like X-ray beam scanning the object O along x_1 to produce each view. Successive views are obtained by rotating the x-axis. The X-ray detector D captures the zero-dimensional attenuated information. This method requires long scan times, but can obtain very accurate linear attenuation coefficients [60],[70]. Fan beam systems (Figure 2.15(b)) use a rotating operation. A flat fan of X-rays collimated by C passes through the object, scatter shield S, and is collected by the one-dimensional X-ray detector. The detector D, in this case, consists of a sufficient number of discrete elements to collect the entire view simultaneously. The fan beam method can detect the attenuated information much more rapidly than pencil-beam systems [59], but normalising the detector response is required. Using a spatially-wide, parallel X-ray beam would allow to collect of multiple slices straightforwardly and rapidly as volume data. This method is available in synchrotron X-ray source [65], [71]. The conical beam geometry (Figure 2.15) with a three-dimensional setup is a fourth option. This is well suited for volumetric computed tomography with microfocus tube sources [72]. This method can also obtain the attenuation data simultaneously as backprojection images, although some blurring artefacts need to be corrected.

Since XCT has been introduced to material science, a wide range of arrangements have challenged to observe by *in situ* damage accumulation or microstructural time-dependent variation in alloy materials (Table 2.2), for example, for the microstructural evolution during solidification ([73], [74], [75], [76], [77], [7]), acid corrosion([78], [79]),

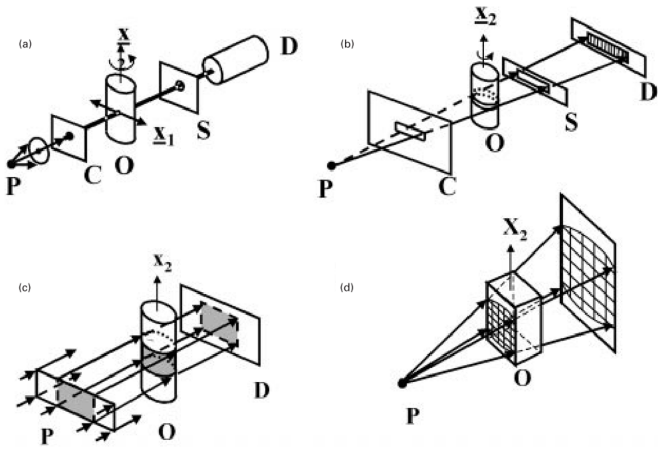


Fig. 2.15 Illustration of experimental systems for XCT observation (Adoped from [59]. P: X-ray source, C: collimater, x_2: the object testpiece, S: slit, and D: detector.

void or crack growth under mechanical loading at ambient temperature ([80], [81], [82], [83], [84], [85]), at high temperature using induction heating ([86], [87], [88], [89]), and recently high temperature tensile test for SiC-SiC composites using the Halogen lamp chamber [90]. Most of these observations were conducted with the X-ray source in the synchrotron facilities because of its fine focal beam with the high flux energy and monochromatic X-ray beam.

The resolution of images using synchrotron X-ray source has been improved from 10 - 20 μm in early 1990's ([60], [91]) to less than 1 μm in 2010's [92] in the aid of developing the refined detector [93] and developing post-processing for removing artefacts (e.g. [94], [95]).

Table 2.2 Examples of *in situ* XCT observations for alloys

Year	Author	X-ray source	Materials	Max Temp.	Max Load	Observed features
1995	Hirano et al. [96]	KEK, Japan	SiC/Al alloy	-	2000N	Reinforced fibre breakage in tensile tests
1997	Guvenilir et al. [71]	Lab source	Al-Li alloy	-	1000N	Small load frame, 360° visible
1998	Guvenilir et al. [97]	CHESS, USA	Al-Li alloy	-	1000N	Small portable load frame, fatigue crack
1999	Buffiere et al. [98]	ESRF ID19, France	SiC/Al alloy	-	1500N	*In situ* tensile test, displacement control
2000	Martin et al. [80]	ESRF ID19, France	Al-Mg alloy	-	-	Cavity growth during superplastic deformation
2003	Nakayama et al. [99]	Spring-8, Japan	Steel	-	-	2D observation during fatigue test
2003	Toda et al. [100]	ESRF ID19, France	Al-Cu-Mg	-	-	Resin tube load frame for *in situ* XCT
2005	Michiel et al. [73]	ESRF ID15A, France	Al-Cu	1000°C	-	Powder sintering, solidification
2006	Toda et al. [101]	Spring-8, Japan	Al alloy	-	2000N	*In situ* compression test for porous materials
2007	Limodin et al. [74]	ESRF ID15, France	Al-Cu alloy	600°C	-	Semi-solid microstructure
2008	Isaac et al. [86]	ESRF ID15A, France	Cu-Zn-Pb	375°C	20N	Induction heating, creep cavities
2008	Eckermann et al. [78]	ANL 2BM, USA	Al alloy	-	-	Acid corrosion behaviour
2009	Limodin et al. [81]	ESRF ID19, France	Al-Cu alloy	600°C	-	Microstructural evolution during solidification
2009	Limodin et al. [75]	Lab source	cast iron	-	200N	Fatigue test for pre-cracked specimen
2009	Zhang et al. [82]	Spring-8, Japan	Al-Mg-Si	-	20N	3 dimensional fatigue crack geometries
2009	Terzi et al. [87]	ESRF ID19, France	Al-Cu alloy	555°C		Induction heating, high temperature tensile test
2010	Terzi et al. [76]	ESRF ID19, France	Al-Cu alloy	570°C	-	Coasening of the dendric microstructure
2010	Knight et al. [79]	ANL 2BM, USA	Al alloy	-	-	Intergranular corrosion
2011	Landron et al. [83]	ESRF ID15, France	DP steel	-	1500N	Void nucleation, interface decohesion
2011	Toda et al. [84]	ESRF ID15A, France	Al alloy	-	400N	Local crack driving force
2011	Maire et al. [102]	ESRF ID15A, France	Al alloy	-	800N	Tensile behaviour and triaxiality
2011	Landron et al. [83]	ESRF ID15A, France	DP steel	-	1500N	Different triaxiality, void growth
2012	Suery et al. [88]	ESRF ID19, France	Al-Cu alloy	555°C		Induction heating, high-temperature tensile test
2012	Tolnai et al. [77]	ESRF ID15A, France	Al-Mg-Si	630°C	-	Solidification, dendritic microstructure
2012	Bale et al. [90]	ALS BL8.3.2, USA	SiC-SiC composite	1750°C	2000N	High-temperature tensile test
2013	Shen et al. [103]	ESRF ID19, France	Al alloy	-	600N	Synchrotron radiation computed laminography
2014	Cai et al. [89]	DLS I12, UK	Al-Cu alloy	555°C	15N	High-temperature compression test in the furnace
2014	Limodin et al. [85]	Lab source	Al-Si alloy	-	500N	Pores, crack initiation in tensile loading
2016	Dezecot et al. [104]	ESRF ID19, France	Al alloy	250°C	300N	High-temperature fatigue test
2016	Saucedo-Mora et al. [105]	DLS I12, UK	SiC-SiC	-	2000N	Room temperature tensile test
2017	Azeem et al. [7]	DLS I12, UK	Ni, Fe, Co alloy	1400°C	-	Solidification in the furnace

In situ XCT system for high temperature experiment

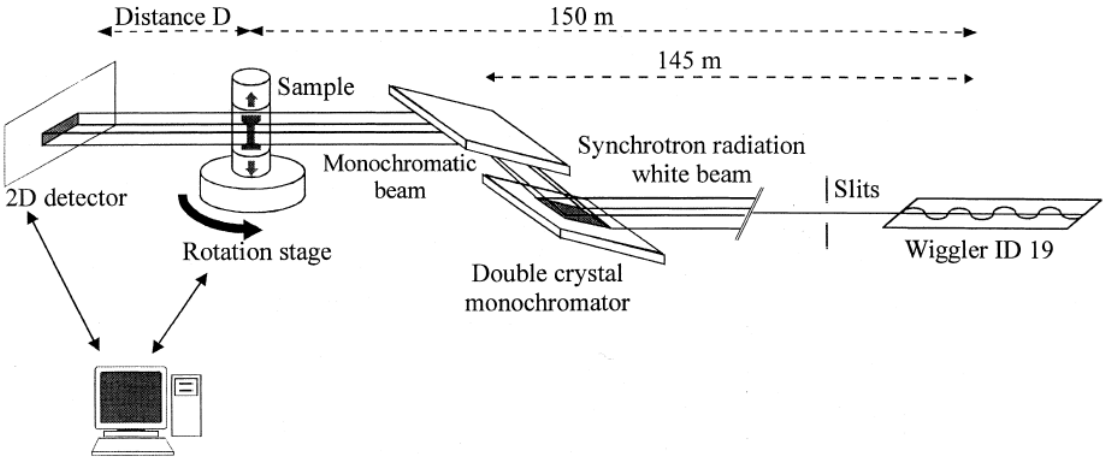


Fig. 2.16 Schematic drawing of the experimental set-up used at ESRF on the ID19 beam line (Adopted from [98]).

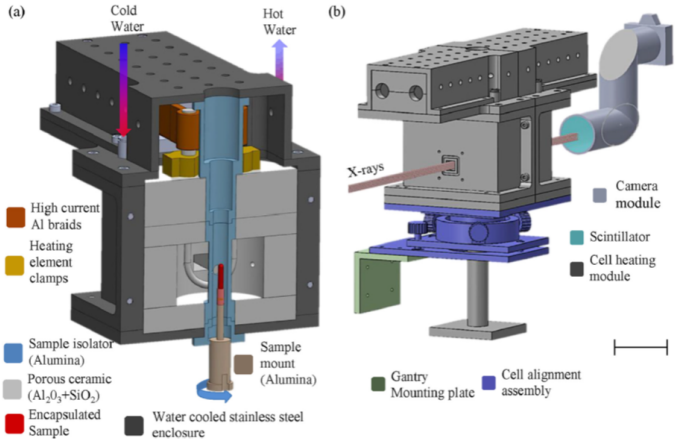


Fig. 2.17 Solidification testing system up to 1400 °C in DLS (Scale bar = 32.5mm) (Adopted from [7]).

During XCT analyses, the testpiece needs to be rotated 180° - 360° on the rotation stage as shown in Figure 2.16, because back projection images from the whole angle are required for tomography reconstruction. For *in situ* observation, testing machines or a heating furnace are also mounted on this stage. In order to avoid any parts of the loading machine obstructing the X-ray beam passing through the sample during the rotation, transparent materials for X-ray, such as PMMA (Polymethyl methacrylate) tube, were

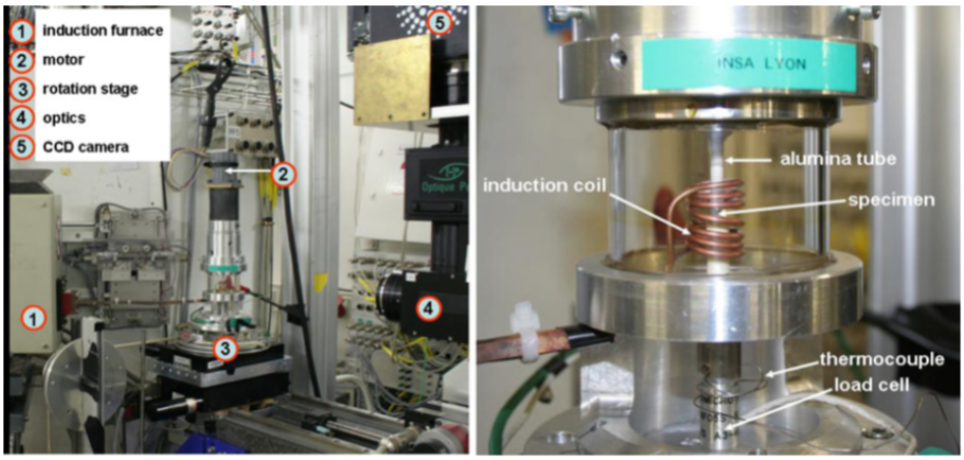


Fig. 2.18 High temperature tensile tests up to 600 °C using induction heating (Adopted from [88]).

employed as the supporting frame [106]. Figure 2.17 and Figure 2.18 illustrate the examples of experimental system for high-temperature solidification experiments and high-temperature mechanical testing [7] [88]. For the high-temperature test, such as the solidification experiment shown in Figure 2.17, the specimen is mounted and fixed on the rotation stage while the furnace is fixed above the stage, which has the window to allow the X-ray beam to penetrate through the sample to capture the back projection images. For high temperature mechanical testing (*e.g.* [98][88]), as shown in fig. 2.18, testing machine and induction heating system are both mounted on the rotation table.

Some of the damage analyses in Ni-based superalloy generated during high temperature, for example, creep void growth and fatigue crack propagation, were conducted by interrupting the experiments and captured XCT at ambient temperature [107], [108]. However, for a better understanding of the damage mechanism under high temperature, this damage requires to be observed by *in situ*, taking a sufficient length of time. However, since the accessibility to the synchrotron facilities is limited, using a synchrotron X-ray source is not suitable. Instead, designing the *in situ* XCT system with a lab-scale X-ray source is preferable for continuously observing the damage

accumulation behaviour for a long time, such as creep and fatigue loading experiments. Moreover, in the case of using the higher power testing machine, the above system with a rotational table (fig. 2.18) is not practical. It would be better to fix the testing machine and rotate the testpiece and tensile loading axis.

2.2.2 Acoustic Emission (AE)

Acoustic emission (AE) testing has been widely employed to detect elastic wave signals generated due to damage initiation or growth. The reported AE signals are related to microstructural information, such as cracking [109], [110], serrated flows [111], or twinning and dislocations ([112], [113]). AE is normally detected non-destructively using piezoelectric sensors attached directly to the testpiece, whilst new Laser interferometer methods [114] enabled to observe the surface vibrations due to AE elastic waves without contacting any sensors to the testpiece.

Acoustic signal analyses

Many efforts on studying non-destructive testings (NDT) have been poured into detecting internal damage generated during mechanical loading, which simulates the actual use. The Acoustic Emission (AE) technique has been used to evaluate the deformation and damaged status, or assess the remained life, while the objective materials are applied to tensile, creep, or fatigue loading (e.g. [115], [116]).

AE is generated when the stored energy is released and dissipated in elastic waves due to the newly induced damage or defects. The AE signals typically have frequencies in the ultrasonic regime depending on the source geometry and the scattering pathways [117]. Since they are directly related to the damage generating behaviours, their inherent characteristics possess plenty of information describing their origin (Table 2.3). Pertinent analyses of these signals would evaluate the dynamic fracturing or deforming status inside materials, which are applicable for the *in situ* damage diagnostics technique.

Table 2.3 Parameters relating to acoustic emission signals (Adopted from [118]).

Emission parameter	Type of information carried
Waveform	Fine structure of source event
Frequency spectrum	Nature of source event
Amplitude	Energy of source event
Amplitude distribution	Type of damage occurring
Rate	Rate of damage occurring
Distribution in time	Type of damage occurring
Relative arrival times at several transducers	Source location

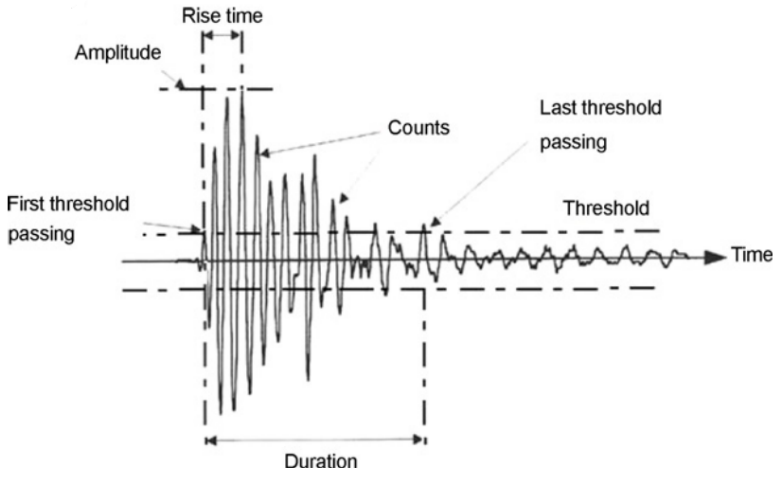


Fig. 2.19 Main acoustic characteristic parameters in a typical waveform signal [119].

Waveform types could be divided in continuous type and burst type, which are affected by different damage sources[120]. Continuous type AE signals are associated with dislocation and grain boundary sliding, whilst the other type shows short rise time and high amplitude (Fig. 5.5) generated by crack advancement, fracture of non-metallic inclusions, twinning, or phase transformation [121] [122]. Besides on the parameters describing wave signals, amplitude, duration, event, count, AE energy (E) and median frequency (f_m) calculated by the following Eq.(5.4) and Eq.(5.5),

$$E = \int_{f_{min}}^{f_{max}} G(f)\mathrm{d}f \tag{2.17}$$

$$\int_0^{f_m} G(f)\mathrm{d}f = \int_{f_{min}}^{\infty} G(f)\mathrm{d}f \tag{2.18}$$

are employed for quantitative analyses of a bunch of AE signals. $G(f)$ in these equations is the power spectral density function, obtained by fast Fourier transformation of the AE data [123] [124] [112]. These parameters have been analysed for alloy or steel materials to correlate AE signals to their fracturing modes and sizes. Some reports indicated that AE amplitude is correlated with the size of deformation band and stress variations within the Portevin - Le Chatelier (PLC) effect [125] in Al-Mg alloys. And in a smaller scale, other works reported a linear relationship with the size of twinning in Mg polycrystals [126]. Frequency has some information about the environment where the dislocations inducing the relevant AE waves were generated. For example, dislocation escaping to a free surface tended to generate low-frequency AE waves[127], and dislocation slip in the gamma phase induced lower frequency AE waves than in the bcc phase[128]. Twinning generated AE waves in a higher frequency range than basal slips in Al-Mg alloys[129] [130]. In more macroscopic research, it was reported that high energy AE transients tended to occur in brittle fracture during the ductile-brittle transition under low temperature in steel pipes [131]. In the case of the brittle fracture during the hydrogen-assisted cracking in Ni-based alloy, step-wise brittle crack induced small energy AE waves, but the final fracture generated AE with the higher energy [132]. These indicate that the released energy is related to the generated AE energy while the crack propagation occurs in the fracturing stage.

In case studying the features of a bunch of AE signals related to the fracturing behaviour, amplitude distribution analyses [133] were applied for various materials [134] [135]. This method investigates damaging and deforming behaviour from the group characteristics of a certain amount of AE signals. Amplitude distribution analyses are

conducted following the Gutenberg-Richter formula [136], replacing the magnitude M in the original power law equation with AE amplitude A:

$$\log_{10} N(A) = a - b \log_{10} A \tag{2.19}$$

where N is the number of cumulative AE signals whose peak amplitudes are more significant than A, and a and b are constants. The parameter b, called "b-value", is known to have some physical implications; when a deformation proceeds with a small number of large steps, a large amount of high-amplitude AE waves are induced, which leads to the small b-value [9].

Experimental setup for AE testing

The piezoelectric sensors were securely mounted on the specimen surface to detect AE signals amplified by a broad-band pre-amplifier. After several smoothing or noise reduction processes, the derived power spectral density $G(f)$ was used to calculate the AE energy E and the median frequency f_m.

Detected AE frequency can include plenty of physical information, such as the source where the AE is generated, the medium properties where the AE propagates, the AE sensor, and the electrical instrument used. These can be expressed by the transfer functions of the source, medium, sensor, and electronics (H_s, H_m, H_t, and H_e). The transfer function of the AE signal, H_{AE}, is given as follows [10]:

$$H_{AE} = H_s \times H_m \times H_t \times H_e \tag{2.20}$$

Ono mentioned in his review [10] that H_m shows the significant effect on the final signal detected. It is essential to determine the time-domain features of AE sources, H_s,

to understand the physical meaning of the original generated AE. We can obtain an inverse-Fourier transform of H functions in the frequency domain and gain their time-domain equivalent (function h) from complete transfer functions. In the time-domain, we need to use convolution integral instead of frequency-domain multiplication:

$$h_3 = h_1 \odot h_2 = \int_o^t h_1(s)h_2(t-s)\ \mathrm{d}s \quad (0 < t < \infty) \tag{2.21}$$

The key step to get H_s from H_{AE} through inverse transformation of convolution, *i.e.* deconvolution processing using known H_m, H_t, and H_e, although it is hardly achieved due to the superimposed noise in H_{AE} or unstable fluctuation in H_m. Some of the deconvolution processes were applied to understand the failure mode analyses [137].

PZT (lead zirconate titanate) transducers are usually employed as piezoelectric sensors. These are some examples of acoustic emission testing systems with these transducers. Scruby et al. [109] showed the AE detecting system with the sensors attached to both ends of the testpiece gripped at the shoulders at either end of the gauge length (Figure 2.20). The emission was detected with a displacement-sensitive damped piezoelectric transducer, attached under constant pressure to the polished flat end of each specimen by a thin layer of vacuum grease. Maire et al. [138] used the setup described in Figure 2.21: piezoelectric sensors were mounted on both ends of the testpiece with a thin layer of vacuum grease. Multiple sensors were attached to the object to determine the location of AE sources.

In these experimental systems, usually AE signals surpassed specific voltage can be detected by certain sampling rate [139], [138]. The background noises are removed by setting the threshold voltages [140] or by eliminating the continuous signals [141]. After detecting signals, fast Fourier transform and several smoothing calculations were conducted for further analyses [142].

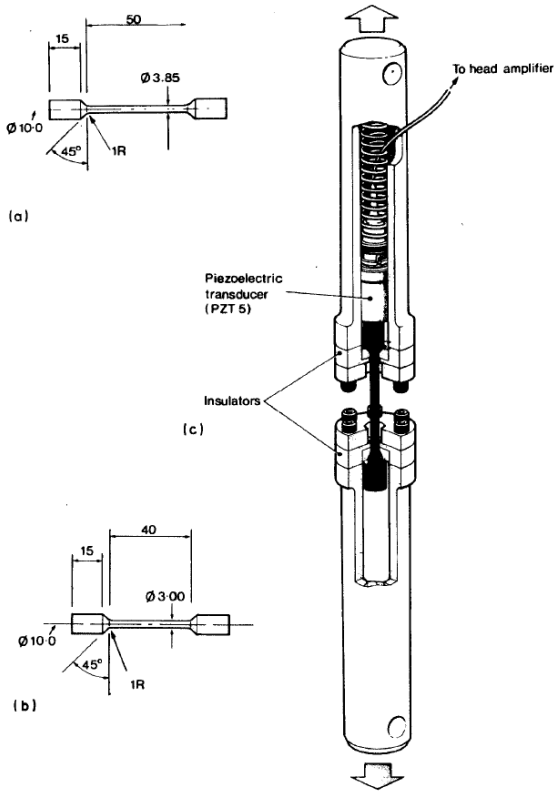


Fig. 2.20 (a)(b) Specimen geometries, together with (c) a sketch of the grips used for the simultaneous measurement of mechanical properties and acoustic emission (dimensions in millimetres)[109]

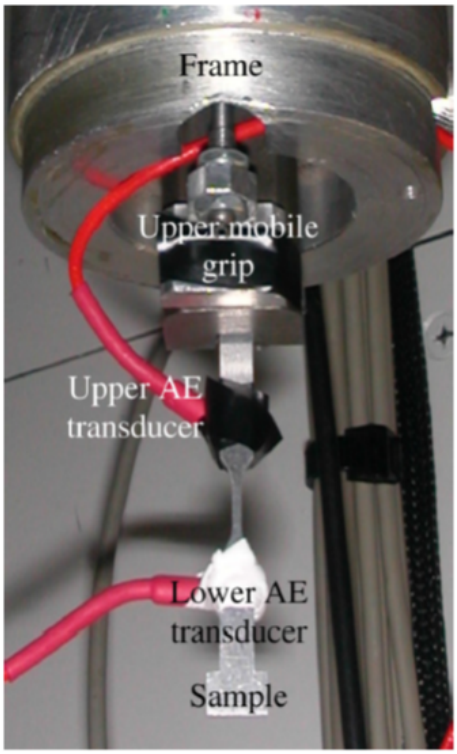


Fig. 2.21 Acoustic emission sensors mounted on the sample[138]

Another measure to detect AE signals is the Laser interferometer using He-Ne Laser. Watanabe et al. [143] introduced this Laser interferometer as the best acoustic emission monitoring method for fracture behaviour, which provides real-time information of the damage process. Some of the advantages of a laser interferometer are non-contact detection, small focused area, and absolute measurement (Table 2.4). Figure 2.22 shows the example of an experimental setup using a Laser interferometer. While the specimen was heated in the air with an infrared image furnace, four laser interferometers were

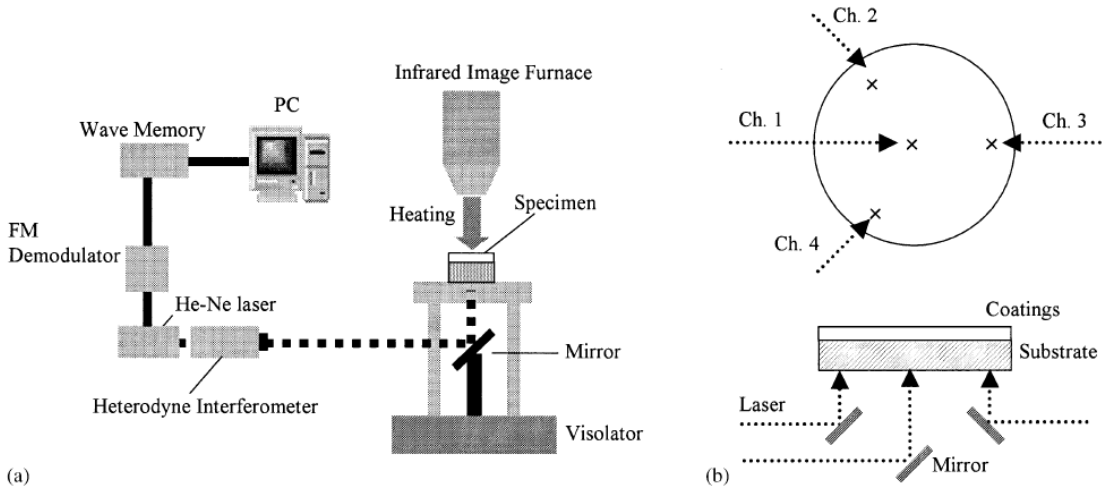


Fig. 2.22 (a) Schematic of the experimental set-up for AE measurement by using a laser interferometer during thermal cycle test, (b) multi-channel AE detection using four laser interferometers. [143]

Table 2.4 Advantages and disadvantages of a laser interferometer and a piezoelectric transducer [143]

	Laser interferometer	PZT sensor
Non-contact detection	Possible	Impossible
Absolute measurement	Possible	Difficult
Focused area	Small (10 μm $\sim$)	Large ($\sim$ PZT size)
Environmental resistance	Good	Not good
Surface preparation	Reflective surface required	As received
Sensitivity	Not high	High

employed to estimate the location of AE signals generated by the internal microfracture of the coating layer.

There are several difficulties in assessing the detected AE waves in the case of using transducers. Since they need to be attached to the testpiece, the transfer functions in Eq.(2.20), especially H_m and H_t, are hardly determined due to many extrinsic factors. Especially in the case of high-temperature experiments, the sensors need to attach the heated object *via* waveguide medium, which protects the sensors from thermal damage. These would make AE analyses more complicated to determine H_s (AE source information). It is essential to prepare the same detecting conditions for the further

interpretation of AE waves on a physical basis and to build the source modelling. On the other hand, the laser interferometer system can assess the AE source information effectively. This is because it detects AE signals without physically attaching the sensors to the object and could remove extrinsic factors (other than H_s in Eq.(2.20)). The laser system is more favourable to obtain the source information, especially for high-temperature experiments.

2.2.3 High temperature tensile/creep testing

In this study, the design and operation of the mechanical testing system were combined with XCT and AE. The testing conditions are aimed at high temperature tensile and creep experiments. In this section, mechanical testing methods and heating systems for the high temperature testing are reviewed to discuss the difficulties of combining the testing system with XCT and AE.

The testpieces are shaped with the gauge section and shoulders for the tensile loading experiment. The cross-sectional area of the gauge section is smaller than other parts so that deformation and failure can be localised in this region. Any observations or measurements regarding this mechanical testing are made within this reduced section. The gauge length should be great enough compared to its diameter to avoid a complicated or unexpected stress state within the gauge. [39]

The shoulders need to be large enough to fix the testpiece during loading applied stably. There are several ways to grip the testpiece (illustrated in Figure 2.23). The end can be shaped like a threaded grip, pinned, or serrated to be held between wedges. The most crucial point to selecting a gripping shape is to ensure that the testpiece can be stably maintained even under the maximum load without the shoulders being slipped or fractured.

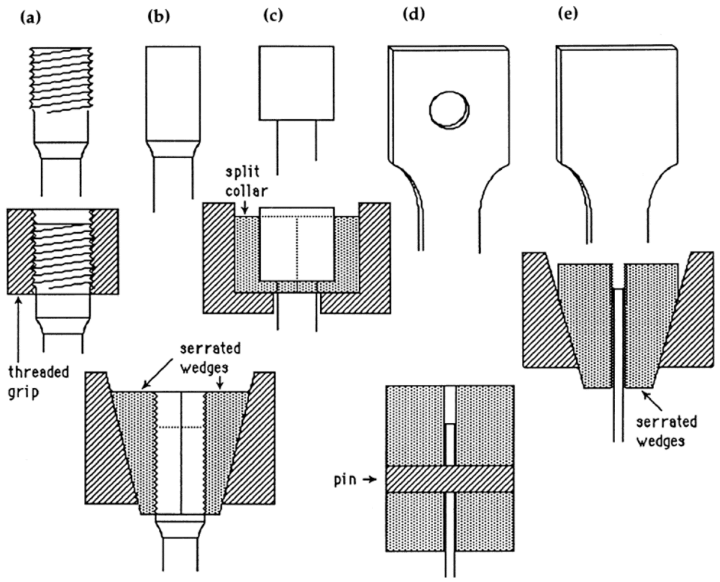


Fig. 2.23 Shoulder designs for gripping testpieces. Threaded grips (a), serrated wedges (b), and butt end shapes constrained by a solid collar (c) for round testpiece. Pin-gripped (d) or serrated wedges (e) for sheet specimens (Adopted from [39]).

Testing machines are either electromechanical or hydraulic. Mechanical loading in these machines can be controlled by strain rate or stress rate. In the elastic region, these controlling methods are identical. However, over the elastic limit, the strain rate increases under a constant stress rate, whilst the stress rate decreases when a constant strain rate is applied [39]. A continual stress rate can be accomplished by a feedback signal from a load cell for automatically adjusting the motion controller of the crosshead. On the other hand, constant strain rate testing can be conducted by extensometers measuring the gauge length change to provide strain data as a function of time. The resulting signal is used to adjust the current strain rate of the crosshead to a stable strain rate.

For high temperature experiments, heating systems with furnace and cooling systems are required. Induction heating (Figure 2.24(a)) allows faster heating rates than other methods, but extra care is required on controlling the temperature inside the testpiece accurately. To avoid nonuniform heating, one should note that induction heating

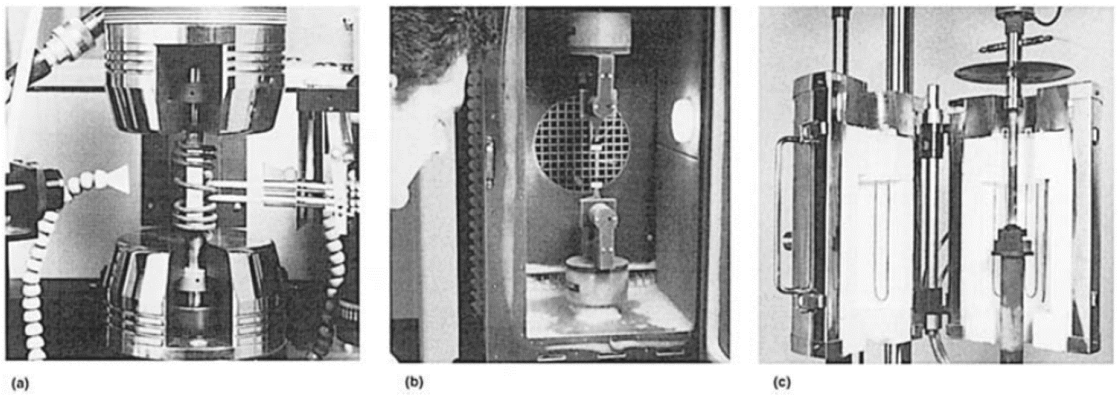


Fig. 2.24 Heating system examples in the load-frame tensile testing. (a) Induction heating, (b) Environmental chamber, (c) Split furnace (Adopted from [39]).

can heat the outer layer of the specimen at first, whilst the interior of the specimen is heated *via* conduction. Indirect-resistance heating in the environmental chamber can be combined with vacuum or a controlled atmosphere (Figure 2.24(b)) As the heating element oxidises easily, the furnace can only be opened after cooling down the temperature. The split furnace shown in Figure 2.24(c) has one or several heating zones. The heating rate can also be programmed. The object testpiece is required to be held in the furnace at a specific temperature for at least 10 to 30 min before the loading is applied [39].

One can notice several difficulties in combining such testing systems with the XCT arrangement. First, the XCT observation needs to limit the focusing object area, the testpiece gauge shape, and arrangements of the detector, object, and X-ray source. Depending on the distance between the object and the detector or the source, the gauge part can be displayed too large to capture the interest of deformation and fracture in the gauge. The gauge length also needs to be carefully shaped so that the detector can observe these changes. The second point is that XCT requires specimen rotating operations. This is for reconstructing tomography images. While rotating the testpiece, if it is fixed along with the tensile axis in the testing machine, unexpected

creep damage or further torque damage must be avoided. Finally, in the case of the high-temperature experiment, the testing system also requires the heating systems as introduced above. For X-ray imaging, the X-ray beam needs to avoid any obstacles, such as induction heating coils, in the vicinity of the testpiece. The furnace requires a pair of transparent windows for the X-ray beam, whilst the X-ray detector or the beam source is approachable by avoiding any radiation lights or heat transfer from the furnace and mobile towards the object testpiece so that they can obtain tomography images with a sufficiently high resolution.

Combining such systems with AE detectors also has several difficulties. In the case of using the PZT sensors, testpiece morphology, sensor size, and methods for attaching sensors need to be carefully designed. If observing the internal damage of the object simultaneously, especially for Ni-based superalloy through which highly attenuate X-ray energy, the testpiece requires to be as small as a few millimetres in diameter. A laser interferometer can be applied for an AE detector to tackle this problem. But in this case, a heating method for the testpiece needs to be considered. For example, induction coil heating might be an obstacle for spotting the laser to the region of interest. Depending on the wavelength of the laser, applicable temperature for high temperature experiments also needs to be considered.

2.3 Key research questions for this thesis

Ni-based superalloys are widely used in thermally and mechanically severe conditions. Their mechanical behaviours, such as tensile ductility and creep failure, can vary depending on the accompanying precipitation phases and the temperature range, as introduced in this chapter with Nimonic 80A and Inconel 718. Understanding how the damage could be generated under the service temperature and loading condition is

essential. *In situ* observation techniques, such as XCT that can detect the internal damage information, can give many indications that relate observed internal damage with the thermal and mechanical conditions applied to the object. But only a few reports engaged on these techniques, especially for the observation under high temperature and loading used. All of these works were conducted in synchrotron facilities with limited time, thermal and mechanical conditions [90, 104, 105], which are insufficient to simulate high temperature tensile, creep, and fatigue behaviour in the service environment for Ni-based superalloys. In this thesis, using two popular polycrystalline Ni-based superalloys, Nimonic 80A and Inconel 718, an *in situ* XCT system for high temperature experimentation will be developed using a lab-scale conical beam X-ray source and a tensile testing machine with a maximum loading force of 10000N. The temperature target is set above 800°C to investigate the different mechanical responses of the two materials under such arduous conditions.

The following points constitute the key research questions for this thesis. Is it possible to capture clear XCT images of Ni-alloy objects during loading at high temperatures? To what extent can damage be observed? What is the detectable damage size? Are there any techniques that allow the experimental setup to start capturing data once the damage growth exceeds a certain limit? Are there any other possibilities to expand or enhance the *in situ* setup and gain more profound information and insights beyond a *post mortem* characterisation?

Without cutting or polishing, to observe the internal damages of the testpieces, the XCT method can be the best technique. It can also offer the 3D-morphological information that relates the generated damage with deformation behaviour. However, since the alignment of the X-ray source and detector can be limited due to the heating system required around the object, such as induction heating or an electric furnace, the visual control for the resolution and magnification can be restricted to some extent.

The XCT reconstruction and post-processing methods for high-resolution images must also be developed for this system. Furthermore, before detecting the stress drop and any other mechanical responses during the loading experiment, it is difficult to capture and assess the period between the initial damage formation to its growth to a substantial size. But as reviewed in this chapter, AE techniques, especially a laser-Doppler vibrometer detector can supply signals which identify damage formation in advance, even at high temperatures.

Thus the experimental set-up requires the following parts. First, a high temperature and loading setup with an electric furnace is needed. An induction coil could be an obstacle to capturing the X-ray images, so that a furnace better suits this system. Second, the X-ray imaging setup requires optimising the resolution of reconstructed XCT images. The imaging calibration needs to be conducted with the object situated in the furnace. Third, the high temperature loading experiment will be conducted with Nimonic 80A and Inconel 718 testpieces to compare their mechanical behaviours at 800°C in terms of ductility and internal damage growth. The next step will be optimising the visual data by eliminating noise and artefacts generated due to the conical beam system. The improved images will be employed in further damage analyses which can be discussed alongside the *in situ*-observed data. The final step will be combining the AE setup with the *in situ* XCT observation to relate AE signals to the object deformation and the internal damage growth.

Chapter 3

In situ Diagnostics of Damage Accumulation in Ni-based Superalloys using High Temperature Computed Tomography

Summary The design, operation and performance of a laboratory-scale X-ray computed tomography (XCT) arrangement is reported, which is capable of elevated temperature deformation studies of superalloys to 800°C and possibly beyond. The system is optimised for the acquisition of 3D backprojection images recorded sequentially during tensile deformation and strain-rates between 10^{-4} and 10^{-2} s^{-1}. These are captured *in situ*. It is used to characterise the evolution of damage – for example, void formation and microcracking – in the superalloys Nimonic 80A and Inconel 718, which are studied as exemplar polycrystalline alloys of lesser and greater ductility, respectively. Our results indicate that such damage can be resolved to within $30 - -50$ μm. The time- and spatially-resolved data collected for the damage evolution during

deformation is proven. Hence the processes leading to creep fracture initiation and final rupture can be quantified in a novel way.

3.1 Introduction

The nickel-based superalloys are ubiquitous in developing the high temperature systems used for jet propulsion and power generation more broadly. The overarching reason for this is their superior properties – both mechanical and chemical – at operating conditions which can approach 800°C or beyond. Significant technical, commercial and legislative pressures exist, which require their high temperature performance to be enhanced. Improvements in fuel economy and thus CO_2 emissions are significant drivers in this.

Due to the nature of the applications, great emphasis is placed on characterising the behaviour of the superalloys under tensile, fatigue, and creep loading conditions. Traditionally, the testing has emphasised the measurement of force and displacement to deduce the fields of stress and strain; this can be regarded as a form of macroscopic characterisation. Microscopic analysis is usually carried out *post mortem* on for example failed [144, 145, 35, 146, 147] or interrupted testpieces [148–151, 107] and then most commonly at ambient temperature. However, a significant difficulty with this approach is that one can never be sure that the damage deduced *post mortem* is truly representative of that driving deformation under the much higher operating conditions. Ideally, better measurements of damage accumulation are needed which are measured *in situ*. A significant advantage would then arise: a direct determination of the dynamics of damage accumulation, which would lead to a better understanding of constitutive response and indeed more e data for calibrating modelling activities.

The research summarised in this chapter was carried out with these ideas in mind. The operation and performance of a laboratory-scale X-ray computed tomography (XCT) arrangement are reported. It is shown that it is capable of *it in situ* characterisation of damage during loading at temperatures of at least 800°C. We describe the design and arrangement of the apparatus, its operational characteristics and its performance during the high temperature testing of two common superalloys: Nimonic 80A and Inconel 718. The advantages and limitations of the new approach are discussed.

3.2 Preparation for Experiment

Considering the main theme of this work for the high-temperature testing system, in this thesis, the X-ray imaging set-up included the electric furnace and the cooling system. As the attenuation of X-ray intensity would behave differently with and without the electric furnace in the X-ray path, through the quartz windows attached in the furnace, this work implemented the intensity calibration for XCT imaging for the high temperature testing system. But all of the following preparation was conducted under the ambient temperature with the furnace off.

Electric Furnace design

For the high temperature experiment, the electric furnace was designed to be monolithic as described in Figure 3.1(a). This monolithic furnace succeeded in obtaining sufficient thermal insulation capacity so that it can heat to as high as 900°C, although the furnace size was limited because the X-ray source and the detector need to be close to the testpiece. However, there were several problems while handling the testpiece and setting up the testing system (Fig. 3.1(b)(c)(d)). With this furnace, the testpiece

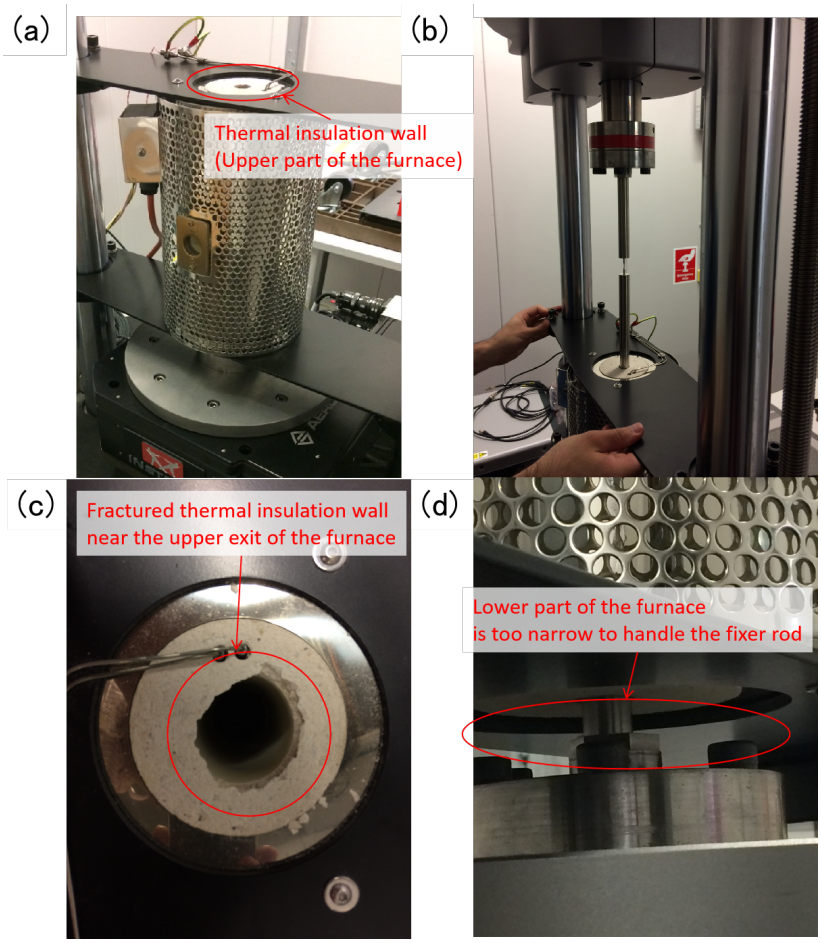


Fig. 3.1 (a) The monolithic furnace employed in the first trial. (b)(c)(d) Revealed problems while using the monolithic furnace.

needs to be removed from the upper exit in the furnace with the testpiece being hung by the fixer rod and moved upward (Fig. 3.1(b)). This method cannot be used in the case that the testpiece was already fractured. The testpiece and fixer rods can touch other parts, which can fracture the thermal insulation wall situated near the upper exit of the furnace (Fig. 3.1(c)). Another problem is that the fixing area for the testpiece is too narrow (lower part of the furnace, Fig. 3.1(d)) and the testpiece cannot be observed while being fixed to the testing machine.

To solve these problems, the split furnace was employed instead in this work (Figure 3.2). The thermal insulation capability is less than the previous furnace, and the maximum temperature in the split furnace is limited to 850°C. The stable maximum testpiece temperature in this furnace is 800°C, but handling the setup, including removing and installing the testpiece became much more manageable.

Cooling design for flange

To avoid heating the flanges of the testing machine during the high-temperature experiment, the flanges required the water cooling system. This needs the hose connected to the flanges as a water circuit even while the rotating procedure for capturing X-ray backprojection images. In the case of the testing machine in torque-free control, as the machine detects a certain amount of torque because of this water hose weight, it can rotate the upper flange to release the detected torque even if the actual torque was not applied to the testpiece at all. This control could cause the hose winding trouble (Figure 3.3(a)) and the testpiece fractured (Fig. 3.3(b)). Therefore torque-free control was not employed in this system. Instead, the rotating algorithm was applied so that the rotating angles of the upper and lower flanges were carefully detected in each angle step to generate the actual torque in the testpiece due to the

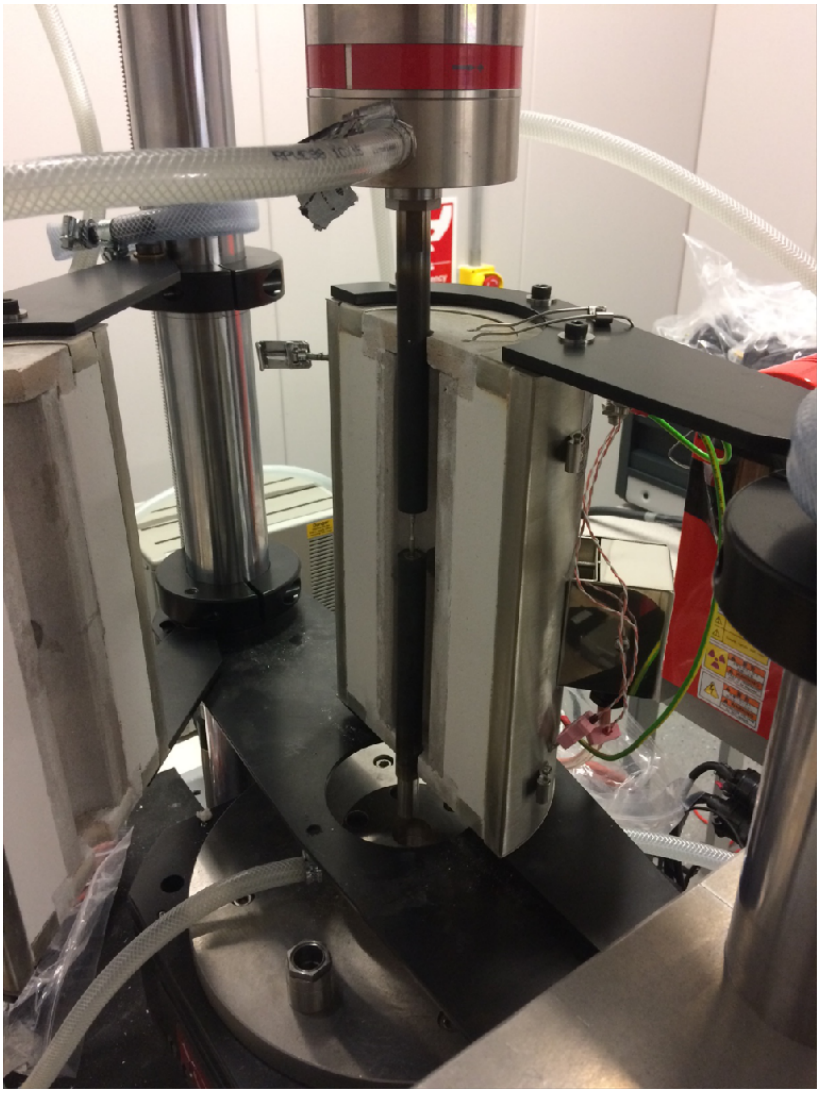


Fig. 3.2 The split furnace employed in this work to solve the problems described in Fig. 3.1.

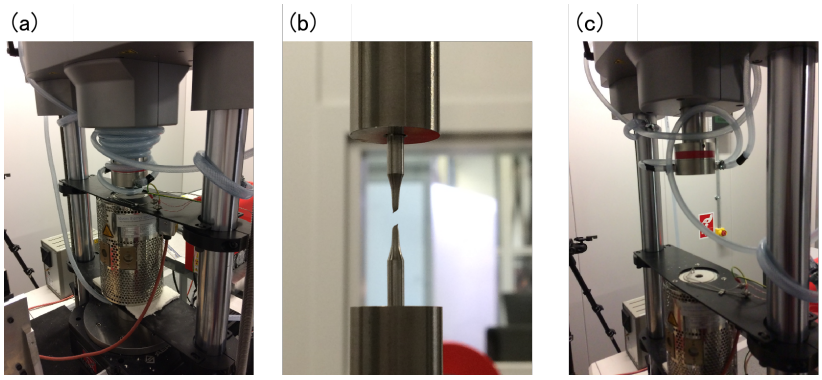


Fig. 3.3 (a) The hose winding trouble due to the torque releasing control of the testing machine. (b) The fractured testpiece after being rotated while the torque-free control. (c) Stopped water circuit due to the bended hose.

angle difference between them. Another problem with using the hose was that the bent hose could stop the water flow (Fig. 3.3(c)). This can also happen during the experiment, which can cause harmful heat damage in the testing machine. To avoid bending the hose, the hose needs to be hung from the upper part of the testing machine and the flanges should not be rotated more than 360°. It is also important to return the angular position to the initial condition before starting the backprojection procedure.

X-ray source and Detector set-up

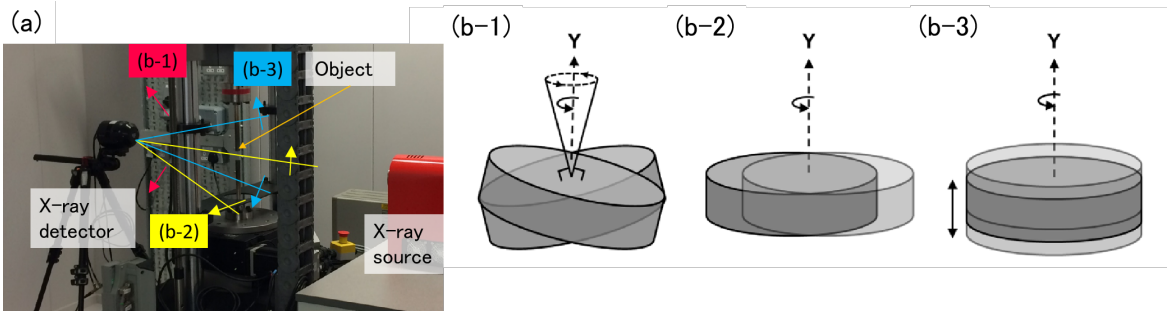


Fig. 3.4 (a) The possible rotary movement of the detector employed in this system related to the XCT imaging instabilities due to tilt error (b-1), radial error (b-2), and axial error motion (b-3). (b-1)-(b-3) are adopted from [152].

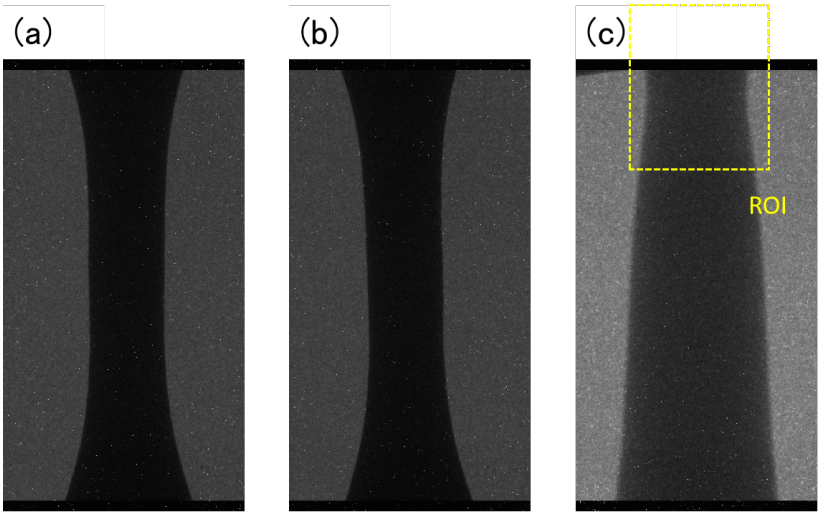


Fig. 3.5 (a) The backprojection image properly captured. (b) The backprojection image with the testpiece tilted. (c) The backprojection image which did not capture the region of interest (ROI).

The backprojection images can be captured by the set of the X-ray source and the detector (Figure 3.4(a)). But due to the rotary movement required for the XCT reconstruction, the image instabilities can be generated by the error motion of the testpiece (Fig. 3.4(b)) [152]. These motions can generate blurred images after the reconstruction, and in many cases, sufficient resolution for observing the internal defects cannot be achieved. In this XCT system, the rotary axis connected to the testpiece is fixed but the instabilities of the detector position can generate the same image instabilities described in Fig. 3.4(b-1)-(b-3). The radial error motion (Fig. 3.4(b-2)) can be avoided by situating the alignment of the X-ray source and the detector right angle to the tensile axis. However, the tilted images and the axial error images can be captured because of the detector movement (Figure 3.5(b) and (c), respectively). To avoid these error movements, the X-ray detecting system employed the tilt angle controllable stage and the axial sliding stage (Figure 3.6(a)). These stages can be controlled from the outside of the XCT room, so that these errors can be fixed while the *in situ* XCT observation. The X-ray detector needs to approach the furnace to

minimise the image unsharpness (as mentioned in the next section), so to protect the detector from the radiation heat through the quartz window, the aluminium sheet (0.1 mm thickness) is placed between the window and the detector. The aluminium sheet does not affect the X-ray imaging in this study.

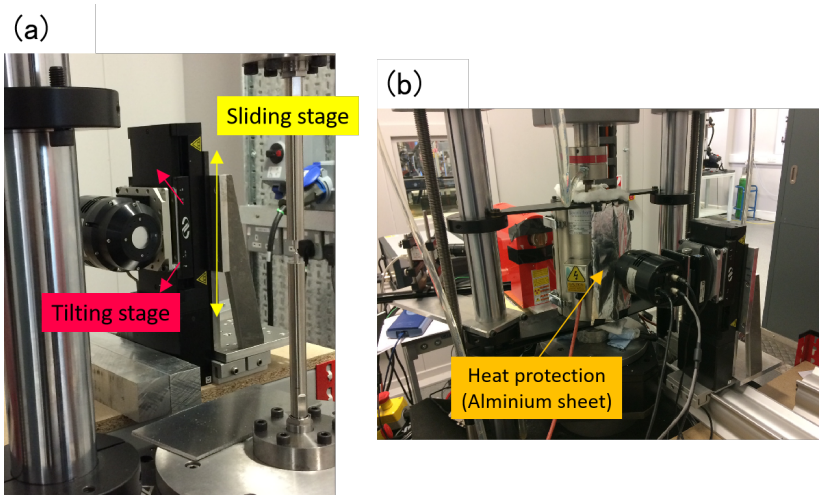


Fig. 3.6 (a) The rotary and axial position controllable rig for the detector. (b) The thermal protect (aluminium sheet) for the detector from the radiation heat through the quartz window.

Flat-field correction and minimising the image unsharpness

Each raw backprojection image was corrected by the flat-field correction method (*e.g.* [94]) prior to the 3D reconstruction process. For depicting the backprojection images, the detector needs to take three kinds of images; the dark-field image (DF), the flat-field image (FF), and the image-field image (IF). DF is the background X-ray noises without the X-ray switched on, whilst FF is the background X-ray intensities with the X-ray switched on. IF is the projected X-ray intensities penetrated through the object with the X-ray switched on. Backprojection images are obtained by considering the X-ray attenuating behaviour against the optical path length L with the following equation,

$$I = I_0 \cdot exp(-\mu L) \tag{3.1}$$

where I and I_0 have attenuated X-ray intensity due to the optical path L through the object and initial X-ray intensity, μ is the attenuation coefficient, and L is sometimes described as $\rho \cdot x$ with the object density ρ and the path length x.

Before processing XCT reconstruction, the flat-field correction was applied using DF, FF and IF in the following equation [94], [61].

$$FFC = ln(\frac{FF - DF}{IF - DF}) \tag{3.2}$$

The flat-field corrected (FFC) image is obtained by Eq.(3.2) for each detector pixel. Flat field correction is essential for the quantitative analysis of images. Averaging over multiple flat field images will reduce the noise, as a Flat field is applied to remove the effect of the pixel-to-pixel sensitivity variation and improve the quality of the projection images for further reconstruction.

Since the X-ray intensity is attenuated when it travels through the object, in eq.3.2, the intensity value $FF - DF$ is higher than $IF - DF$. If the applied X-ray energy is not sufficient and the obtained $FF - DF$ is low, FFC values in eq.3.2 would easily fluctuate. After the flat-field correction, it would be ideal for the next reconstructing process that the averaged intensity of the Ni-alloy part is closed to the maximum and the noise fluctuation is minimised. This is because heavily fluctuated noises can produce low-resolution images and low-intensity artefacts which can be identified as wrong defects. For the purpose of evaluating the intensity roughness and image unsharpness, the intensity value in each pixel (FFC in eq.3.2) was calibrated so that the maximum intensity would be displayed as 65536 to visualise intensity plots in

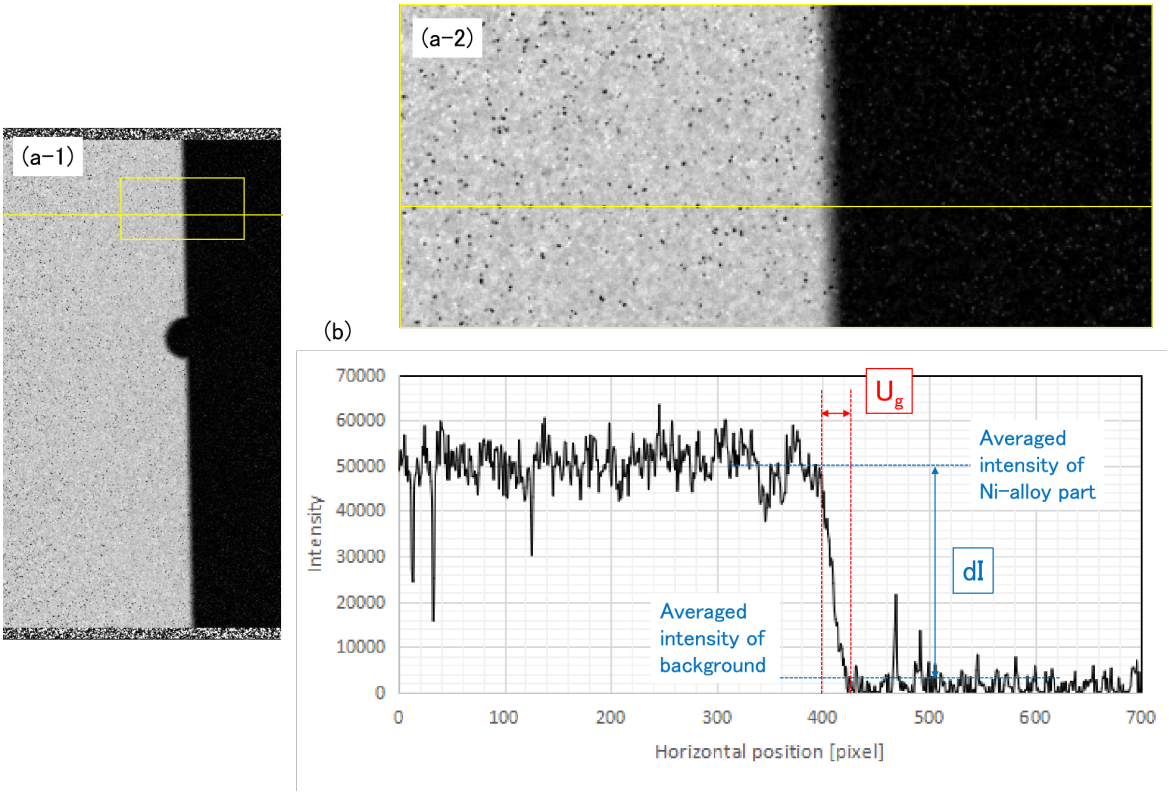


Fig. 3.7 (a-1) An FFC image example captured with the current 500 μA and the exposure time for 500 ms. (a-2) The magnified image from the yellow rectangle part in (a-1). (b) The intensity profile along the yellow line in (a-2).

16-bit white (high intensity) - black (low intensity) images. The intensity roughness, the intensity difference against the averaged background (BG) noises (dI), and image unsharpness (U_g) [153] were evaluated as described in Figure 3.7. The testpiece used for these evaluations was flat-shaped with the semicircle notch (diameter: 400 μm). All the image data is for the averaged data of 4 images captured under the same condition ("exposure time" is the time for taking one picture). Table 3.1 shows dI, averaged BG noises, and U_g calculated from the FFC image data obtained in the different current and exposing time conditions. Compared to case 1 with case 2 and case 3, lower current can create clear images (low U_g) but produce noisy and low-intensity images even for the case of long time exposure. From the following experiments in this work, the current and the exposure time are set to 500 μA and 500 ms, respectively.

Table 3.1 The condition of FFC images captured under different current and time.

	Case 1	Case 2	Case 3
Current [μm]	500	200	50
Exposure time [ms]	500	1250	5000
dI	50000	45000	25000
Averaged BG noises	4900	7100	12400
U_g [pixels]	40	22	26
U_g [μm]	95.2	52.4	61.9

The alignment of the X-ray source and the detector were also examined using the same notch shape testpiece, because the distance between the X-ray source and the object (D_{SO}) and the distance between the object and the detector (D_{OD}) can affect the X-ray image unsharpness [153]. Figure 3.8 shows the FFC images obtained from the different alignments and Table 3.2 is the calculated image data. The FFC images here were also the averaged image data of 4 images captured under the same condition. When the object is close to the detector and far from the X-ray source (Case A), the backprojection image of the notched testpiece showed small and thus the pixel size was large. But conversely situated case (Case F), U_g was large and a very blurred image was produced. In terms of minimising U_g and producing the clear backprojection images, Case C is the best alignment and employed in this study. Thus the resolution of the reconstructed images was optimised by controlling the detector position and adjusting the source-object-detector alignment.

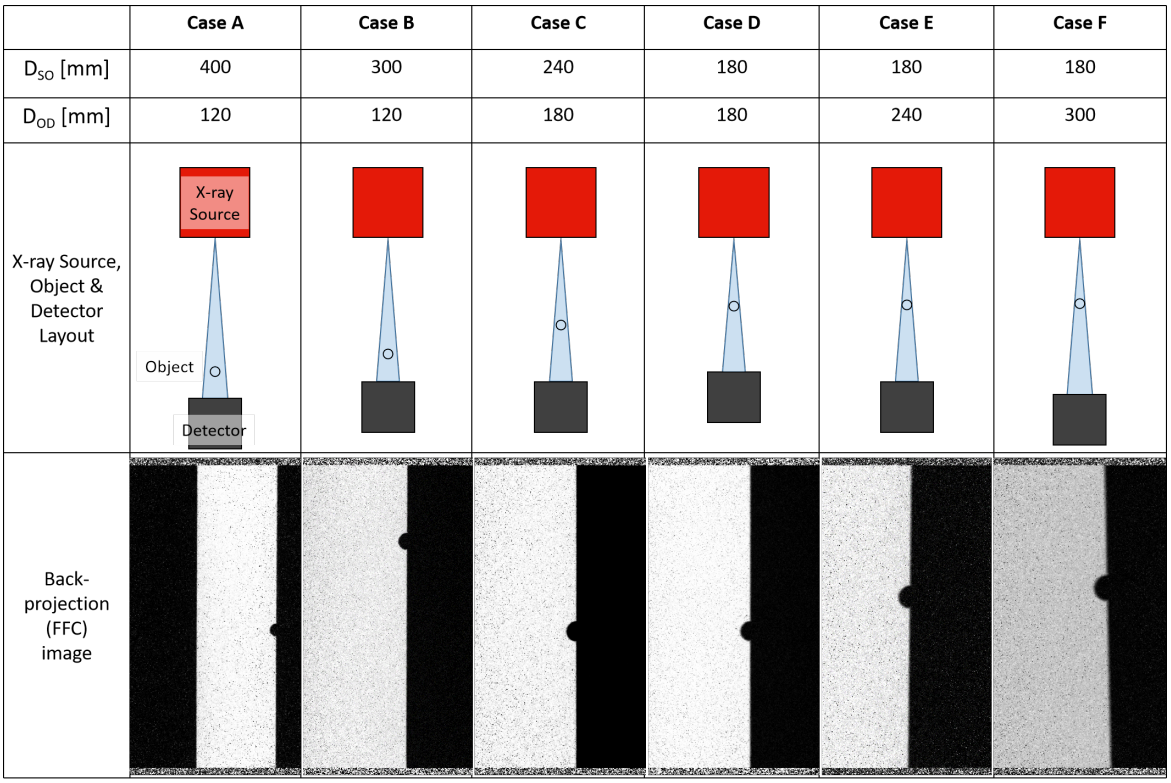


Fig. 3.8 The FFC images obtained under the different alignments of the X-ray source and the detector (Current : 500 μA, Exposure time : 500 ms).

Testpiece design

The gauge diameter was shaped as small as possible in the laboratory machining equipment. This is because that Ni is a kind of heavy metal element and has less permeability for X-ray. The gauge length was selected as larger than the gauge diameter. But it should be less than the length which can be captured by the X-ray detector window and also less than the size that can be fully observed from the furnace window. The curvature from the gauge to the shoulder was designed as loose to make the machining process easier and more productive. In this work, the testpiece shape was designed as follows; the gauge diameter: 1.5 mm, the gauge length: 2 mm, the shoulder diameter: 3 mm, and the curvature to the shoulder: 5.5 mm. The true strain of the

Table 3.2 The condition of FFC images captured under different alignments of the X-ray source and the detector (Current : 500 μA, Exposure time : 500 ms).

	Case A	Case B	Case C	Case D	Case E	Case F
D_{SO} [mm]	400	300	240	180	180	180
D_{OD} [mm]	120	120	180	180	240	300
dI	61000	62000	60000	59000	62000	50000
Averaged BG noises	3300	4100	5100	3200	2900	4900
U_g [pixels]	15	40	11	20	24	40
U_g [μm]	73.2	125	34.9	63.4	65.3	95.2
Pixel size [μm]	4.9	3.1	3.2	3.2	2.7	2.4

testpiece while the experiment can be precisely calculated by measuring the strained gauge diameter from the backprojection images.

Material choice

As the starting material, pure Ni-alloy, such as Nickel201 is chosen for this tensile testing. However, it has low yield stress (148 MPa) that can not endure the stress applied during being machined to the 1.5 mm-diameter round bar. Such low strength materials can be bent during the machining and can not be used in this study. This study employed Inconel 718 and Nimonic 80A, which are widely used Ni-based superalloys. These materials were also selected because the mechanical behaviour at more than 800 °C is expected as different from each other.

Summary of preparation

Once the experiment has started and X-ray beams on, no one can enter the XCT room nor approach this system. It indicates that all of the procedures including X-ray on/off, adjusting the X-ray detector, capturing backprojections, axis rotation, and applying tensile loading needs to be operated remotely from the outside of the X-ray room (the

room where this setup is placed). Therefore, these procedures are incorporated in the algorithm for the testing machine operation so that capturing backprojections and applying the load/displacement can be operated in parallel. The XCT algorithm was programmed to be started after reaching a particular displacement value. The axial rotation for XCT was controlled by detecting the upper/lower flange angles so that the procedure can stop when the angular difference exceeds 0.2°, which is over the error angle difference. The X-ray backprojection was captured four times at every angle step and the averaged data were used for the reconstruction processing.

Figure 3.9 shows the improved *in situ* XCT observation system after improved the problems mentioned above. This system will be employed in work described in the following section and chapters. Table 3.3 describes the number of tested samples in this work (including the following chapter). The data introduced in this thesis does not include the tested data that did not finish the experiment successfully because of unexpected errors, troubles, or the problems described in this section.

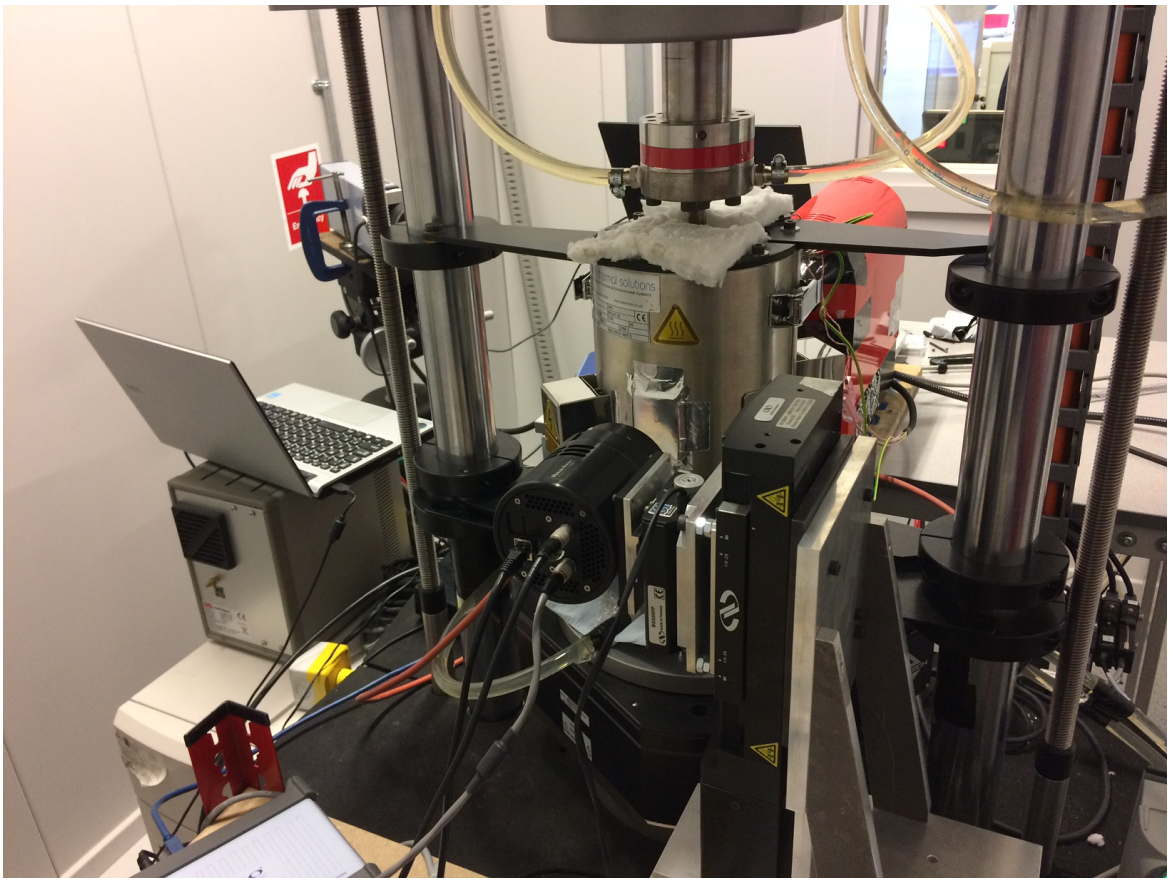


Fig. 3.9 The *in situ* XCT testing system developed in this work.

Table 3.3 The number of tested samples for this work.

	Inconel 718	Nimonic 80A
XCT Set-up	32	24
Room temperature tensile (not for XCT)	10	10
800°C tensile	26	18
800°C creep (Ch.4)	8	-
800°C detecting AE (Ch.5)	16	-

3.3 Experimental Methods

A laboratory-scale X-ray computed tomography (XCT) system is employed which has been developed specifically for *in situ* observations and integrated with a thermo-mechanical testing instrument as described in the previous section. It has been optimised for the acquisition of 3D backprojection images during tensile deformation at temperatures of up to 800°C and strain-rates between 10^{-4} and 10^{-2} s^{-1}. The system, as depicted in Fig. 3.10, consists of (1) an X-ray source (a) and detector (b), (2) an all-electric thermo-mechanical testing instrument (c) including a rotary table (d) and a furnace (e), and (3) integration algorithms for the reconstruction of sequential 3D, or so-called 4D, images by implementing the inverse Radon transformation procedure.

3.3.1 *In situ* XCT system: source and detector

To capture backprojection images, a microfocus X-ray source by Hamamatsu Photonics – of capacity 150kV and 500μA – is paired with an SCMOS X-ray detector by Photonic Science. These were aligned precisely at right angles to the testing specimen's tensile axis. Specimens of circular cross-sections were chosen and gripped at both ends by connecting rods mounted onto a rotary rotor system. The rotor casing was bolted to the lower crosshead and controlled with a closed loop feedback system to maintain a torque-free condition to the specimen during the test. The X-ray source and detector, as well as the testing instrument, were fixed; this has allowed a relatively compact system to be designed to capture uninterrupted multi-angle backprojection images. As reviewed in the previous chapter, this newly proposed system represents an improvement to the conventional method which calls for the testing instrument to be mounted onto and rotated by a rotating floor [7, 98]; such a system is probably impractical for a laboratory setup.

In this chapter, testing at elevated temperatures has been a primary goal. A furnace was chosen for this purpose since temperature stability is essential; this was installed and attached to the testing instrument. The furnace was designed with a set of quartz windows to secure an unobstructed X-ray beam path in passing from the source through the specimen and onto the detector screen. To ensure the system could acquire high-quality backprojection images, the source was positioned as close as practically possible to the specimen while maintaining a sufficient distance to avoid any direct exposure of heat radiated from the furnace to the X-ray source. In addition, a water cooling system has been specifically designed to cool down the clamping flanges of the connecting rods in order to protect the crossheads from an excessive conductive heat transfer.

3.3.2 Rotary and displacement control

Fig. 3.11 illustrates the operating workflow needed for *in situ* XCT observations. Two main steps are executed: (i) the capture of backprojection images by rotating the sample and (ii) the application of tensile load to the sample without rotation. In this procedure, the sample has to be rotated prior to and whilst imposing a displacement-controlled signal. To optimise the rotary setup with the embedded water-flow cooling system, the rotation was controlled to reach 180° angular rotation and then directed back and forth alternately. To avoid specimen damage by the torque generated by the rotating offset between the top and bottom rods, the rotation was operated in a step-wise fashion during which backprojection images of each angle were captured sequentially. After capturing the backprojection images, the displacement was then applied incrementally. This working sequence was continued until the specimen was fractured. In what is reported here, the tensile strain rates ranged from 10^{-4}, 10^{-3}, and 10^{-2} s^{-1} and were applied at 800°C.

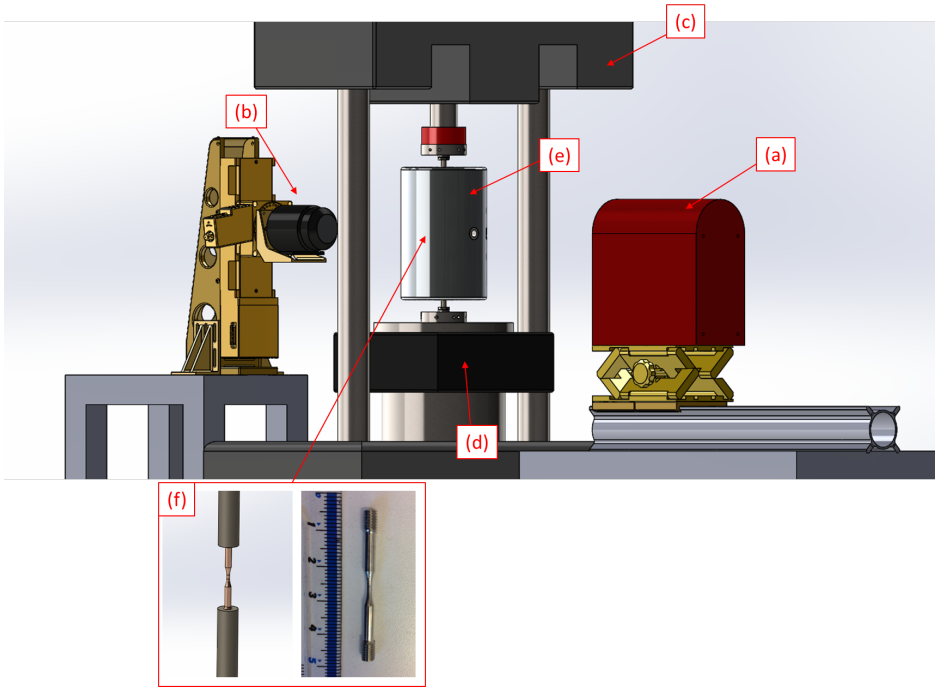


Fig. 3.10 *In situ* XCT setup for high temperature mechanical experiments. (a) X-ray source, (b) X-ray detector, (c) Testing machine, (d) Rotary table, (e) Furnace, (f) Specimen (inside the furnace).

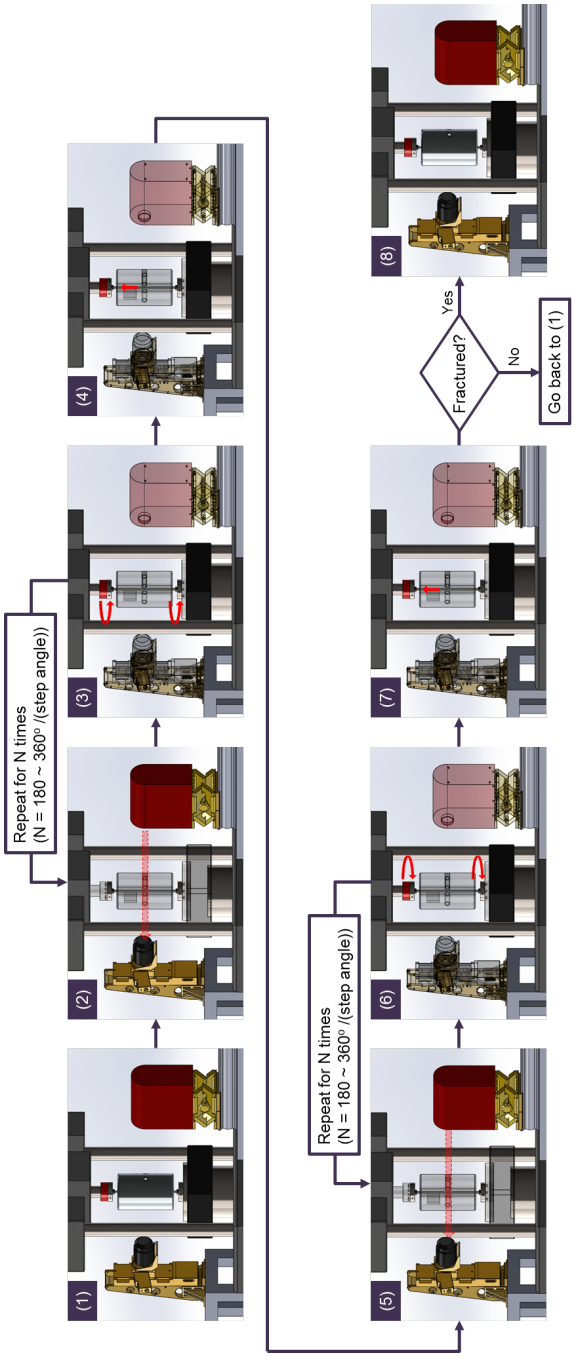


Fig. 3.11 The experimental procedure for *in situ* XCT observation.

3.3.3 XCT analysis

Each backprojection image was then converted to the flat-field corrected image. Sliced images were generated from the flat-field corrected images by employing the inverse Radon transformation procedure. In this case, to produce the Sinogram, we used the Filtered-back Projection method [61] coded in MATLAB. ImageJ [154] was used to render the calculated images and Amira software to reconstruct 3D XCT voxels from those data. Fig. 3.12 illustrates some examples of the raw projection, the flat-field corrected, and the calculated sliced images. The flat-field corrected images were used to observe the 3D profile changes − including the necking behaviour − during high temperature experiments; this method is in line with the optic system as reported in ([155], [156], [157]). Furthermore, the backprojection images were cropped to focus on the gauge area and applied for the 3D reconstruction process. The data acquired in this way included a few pixel size artefacts due to the intensity error while capturing the backprojection. The dark spots were examined whether they are the actual defects or the artefacts by comparing them to the adjacent sliced image data after the reconstruction. If the dark spots were also detected in the adjacent 10 sliced images in the same position (10 pixels connected in the tensile direction), the dark spot was regarded as the actual defects. These visual data were thus examined critically for evidence of void formation and damage evolution. These *in situ* XCT results were also then compared to further data acquired by *ex situ* XCT observations and SEM fractography studies of the traditional type. *Ex situ* XCT analyses were carried out using a North Star Imaging system at 150 kV and a current of 27 μA, which produced a voxel size of 4.9 μm.

3.3.4 Testing materials

For the *in situ* XCT observation, high temperature tensile experiments were conducted for two polycrystalline Ni-based superalloys, Inconel 718 and Nimonic 80A, of composition given in Table 1. These were chosen to demonstrate the capabilities of the experimental arrangement on account of their widespread use but also due to their anticipated higher and lower creep ductility, respectively. As shown in Fig. 3.13, the grain size in Nimonic 80A and Inconel 718 was 100–200 μm and 30–50 μm, respectively. The microstructure image was obtained through the Bruker ARGUS imaging system using forescattered and backscattered electrons [158]. This system detects the diffracted forescattered signal variation due to orientation changes in a polycrystalline testpiece, offering clear images of the grain boundaries. The specimen gauge length was chosen to be 2 mm and after some experimentation the diameter was fixed at 1.5 mm (Fig. 3.10(f)). The dimension was selected so that the XCT detector allows the X-ray beam to fully penetrate the specimen for optimum capture of the damage accumulation.

Table 3.4 Composition of the alloys studied in wt.-% (Ni-base)

Name	Cr	Al	Ti	Fe	Nb	Co	Mn	Cu	Si	C	B	S
Nimonic 80A	20.0	1.5	2.5	0.2	-	0.14	0.01	0.01	0.03	0.07	0.003	0.002
Inconel 718	18.3	0.6	0.9	18.7	5.2	0.26	0.11	0.08	0.07	0.04	0.04	-

3.4 Results

3.4.1 Rotary control for XCT imaging

Rotation of the specimen is a critical aspect of any CT system. For this reason, experiments were first carried out to prove that the control for this was adequate. A

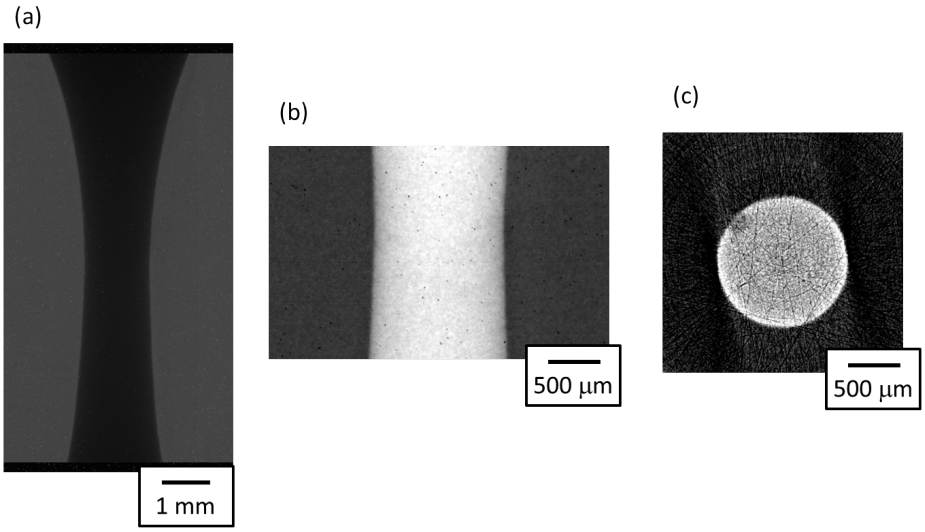


Fig. 3.12 XCT image examples: (a) raw projection image, (b) cropped image of the gauge area after flat-field correction, and (c) calculated sliced image.

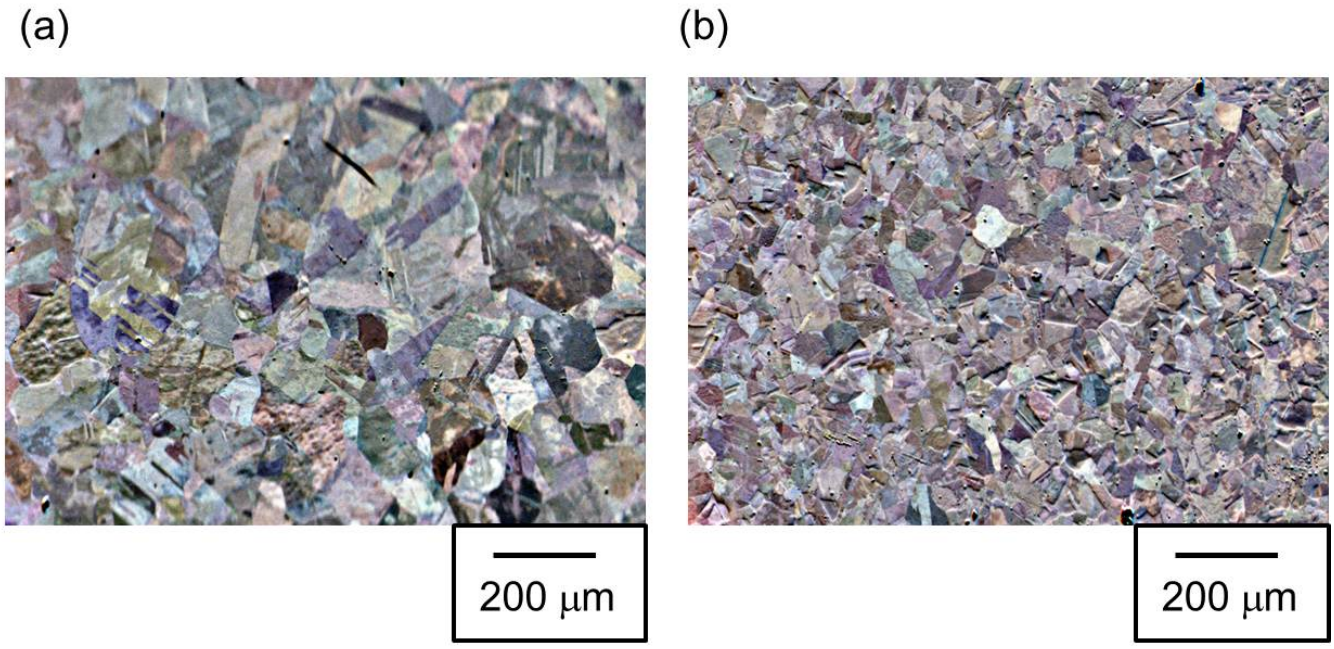


Fig. 3.13 Microstrustures of the Nimonic 80A (a) and Inconel 718 (b) employed in this work.

preliminary tensile testing programme was carried out under both load-controlled and displacement-controlled modes. Fig. 3.14 illustrates some different features which appeared in the corresponding stress - strain curves. As shown in the figure, the stress relaxes in the displacement-controlled mode at the temperature of 800°C, but by way of comparison, the strain increases drastically in the load-controlled mode. In the latter case, the strain increments were abrupt. This made the sample unstable with regard to deformation in the tensile axis direction and resulted in blurred backprojection images, which were unsuitable for the 3D reconstruction process. Furthermore, as the temperature reached 800°C, the applied constant load was clearly too excessive leading to creep fracture in relatively short times. Considering these results, the displacement-controlled mode is thought to be more suitable for the intended *in situ* XCT observations intended in this study. In what follows, displacement-control is used.

3.4.2 True stress - true strain curves, and mapping of local thinning of cross-sections

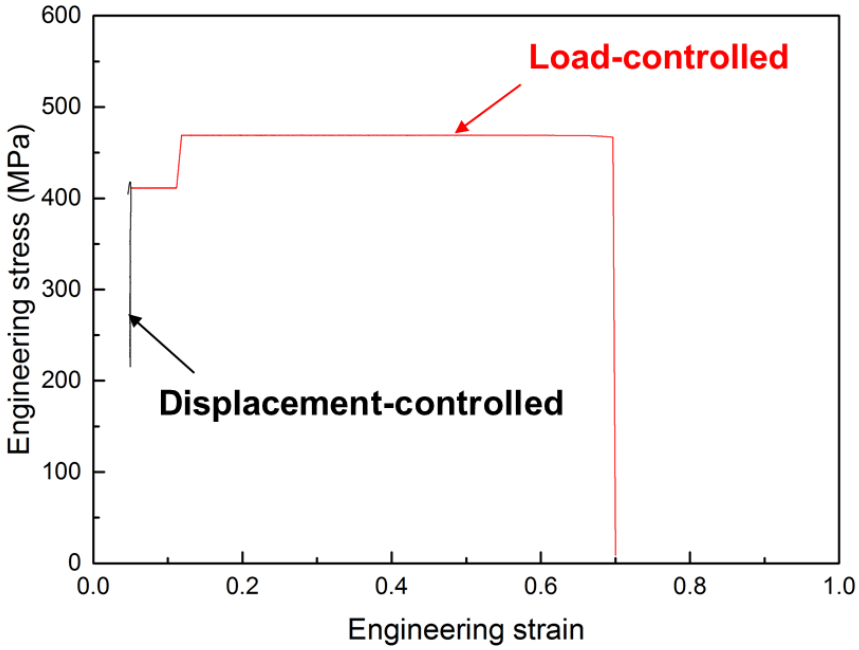


Fig. 3.14 Comparison of stress-strain measurement while rotating the sample with keeping the displacement (displacement-controlled mode) and with keeping the load (load-controlled mode).

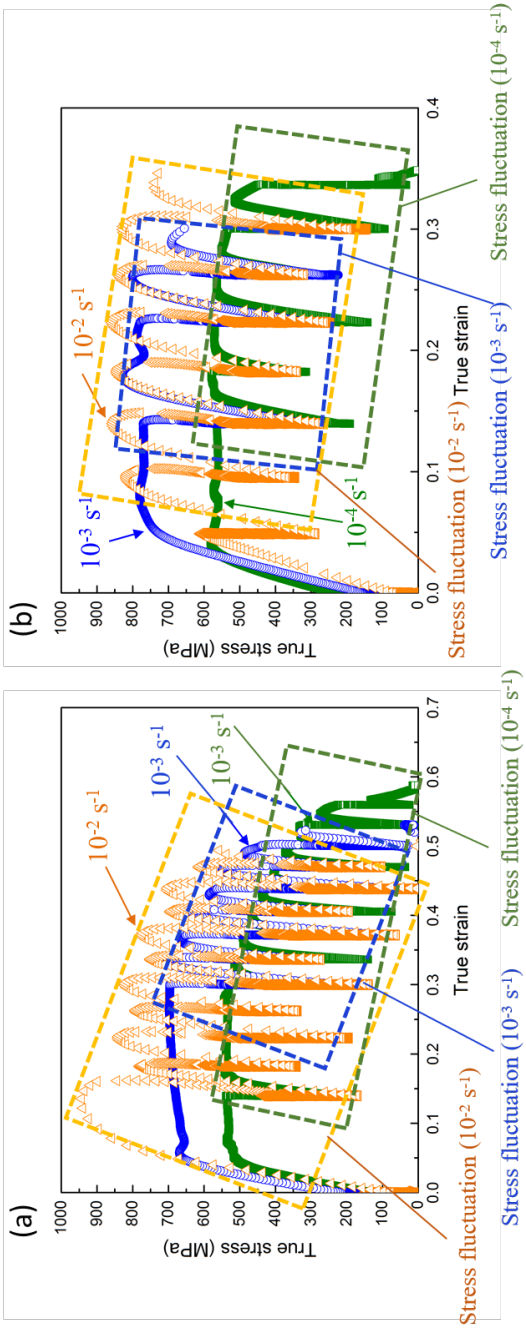


Fig. 3.15 True stress - true strain curves during tensile tests at 800°C for (a) Inconel 718 and (b) Nimonic 80A. For both cases, tensile experiments were carried out with the strain rates from 10^{-4} to 10^{-2} s^{-1}.

The stress-strain curves at 800 °C for the three strain rates employed are illustrated in Fig. 3.15. The stress fluctuation was observed in every case. The stress relaxation caused this behaviour while rotating the testpiece to capture the XCT images sequentially. While rotating in this procedure, the testpiece position (the axial displacement) must be fixed and the applied stress relaxed. The stress fluctuations were observed in both Inconel 718 and Nimonic 80A, and there is a clear tendency of strain rate dependency. In both cases, as a higher strain rate induced higher stress during tensile loading, the range of this stress fluctuation exhibited larger.

Fig. 3.16 and Fig. 3.17 illustrate the cross-section profiles of Inconel 718 and Nimonic 80A during the tensile tests covering the strain rates from 10^{-4} to 10^{-2} s^{-1}. The indicated values – denoted in each profile line – describe the true strain. As indicated, Inconel 718 exhibited a prolonged necking contour prior to the onset of fracture, whilst Nimonic 80A experienced a relatively sudden fracture behaviour indicative of a more brittle behaviour. This was identified consistently for all the applied strain rates, in a consistent fashion. Furthermore, the necking curvature of Inconel 718 showed the smallest when the system was under a lower strain rate 10^{-4} s^{-1} and it became shallower as the strain rate getting higher.

From Fig. 3.16 and Fig. 3.17, the evolution of cross-sectional area of Inconel 718 and Nimonic 80A demonstrated distinctive necking profiles. To take into account the necking profile, the true stress and strain were calculated using the actual diameters from the profile data (Fig. 3.16 and Fig. 3.17). The results are then plotted in Fig. 3.18. In this figure, the average true strain (ε_t, open symbols in fig. 3.18) in the gauge part was calculated as follows,

$$\varepsilon_t = ln(\frac{l_i}{l_0}) \tag{3.3}$$

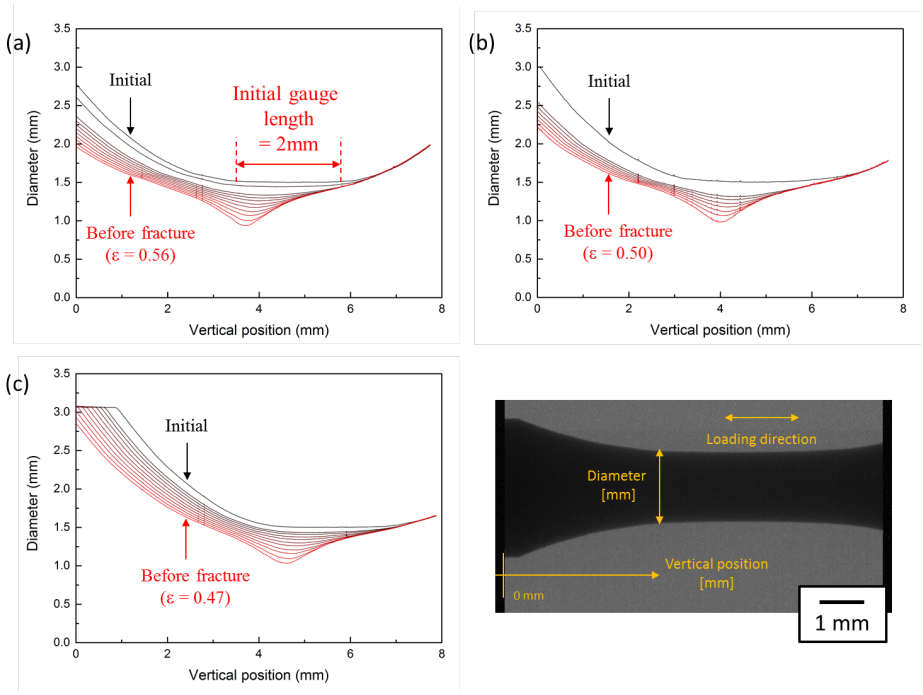


Fig. 3.16 Sample profile curves against the vertical position measured at each step of strain (denoted in the upper right figure legends) during tensile tests at 800°C for Inconel 718 with the strain rate of (a) 10^{-4} s^{-1}, (b) 10^{-3} s^{-1}, and (c) 10^{-2} s^{-1}. Sample profiles are described in terms of diameter on each of vertical point as illustrated in the right XCT image example.

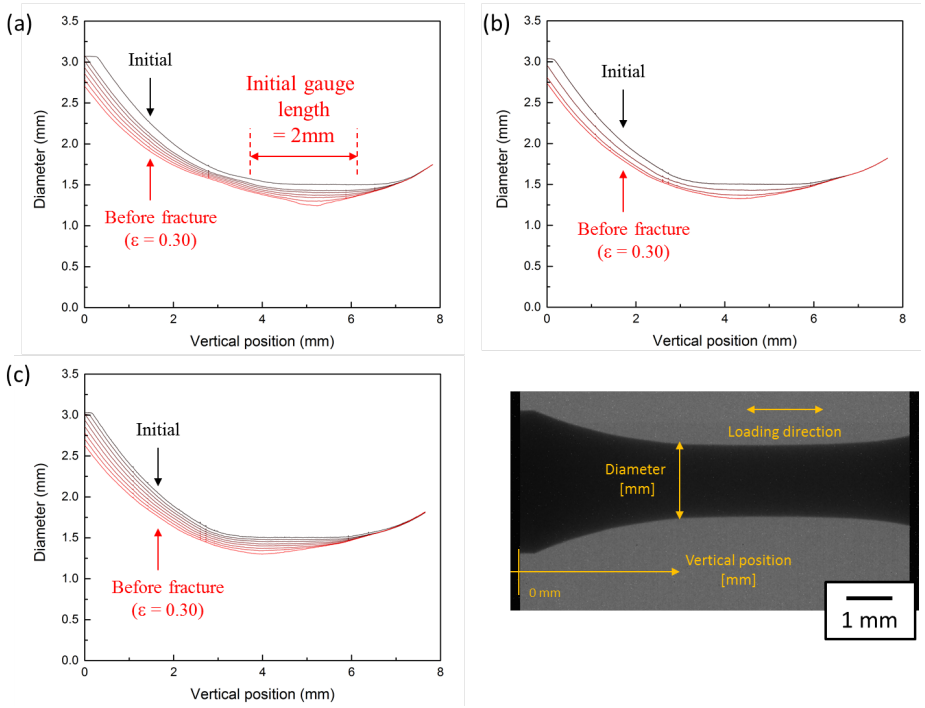


Fig. 3.17 Sample profile curves against the vertical position measured at each step of strain (denoted in the upper right figure legends) during tensile tests at 800°C for Nimonic 80A with the strain rate of (a) 10^{-4} s^{-1}, (b) 10^{-3} s^{-1}, and (c) 10^{-2} s^{-1}. Sample profiles are described in terms of diameter on each of vertical point as illustrated in the right XCT image example.

where l_0 and l_i are initial and current gauge length for each plot obtained from the axial displacement measurement. And the specific true strain at minimum radius (ε_t^{sp}, closed symbols in fig. 3.18) in the necked gauge was calculated from XCT profile results,

$$\varepsilon_t^{sp} = ln(\frac{A_0}{A_i}) = 2 \cdot ln(\frac{d_0}{d_i}) \tag{3.4}$$

where A_0 and A_i are initial and current minimum cross-sectional area in the gauge part for each plot, and d_0 and d_i are initial and current minimum diameters.

As for Inconel 718 in 10^{-4} s^{-1} and 10^{-3} s^{-1} cases, the stress decreased against the increment of strain prior to the onset of fracture. In Nimonic 80A, the stress values were generally more constant for strain rates of 10^{-3} s^{-1} and 10^{-2} s^{-1}, however in 10^{-4} s^{-1}, the stress relaxation was still observed to a degree. The "Cross section" plots in which those data were recalculated from the cross-sectional area without void area showed a little higher than the closed plots, but especially for Inconel 718, the true stress decreased to some extent before fracture. The ductility behaviour is summarised and plotted in Fig. 3.19. Nimonic 80A was generally less ductile with strain at fracture at around 0.3 at the strain rates from 10^{-4} s^{-1} to 10^{-2} s^{-1}. Inconel 718 exhibited more ductile behaviour and the strain at failure increased from less than 0.8 to around 1.0 when the strain rate was decreased from 10^{-2} s^{-1} to 10^{-4} s^{-1}.

3.4.3 XCT results

During the high temperature tensile experiments, backprojection images were captured to allow for subsequent 3D XCT reconstruction so that the damage accumulating behaviour that affects strength could be better understood. Fig. 3.20 and Fig. 3.21 show examples of calculated sliced images and reconstructed 3D images. As shown

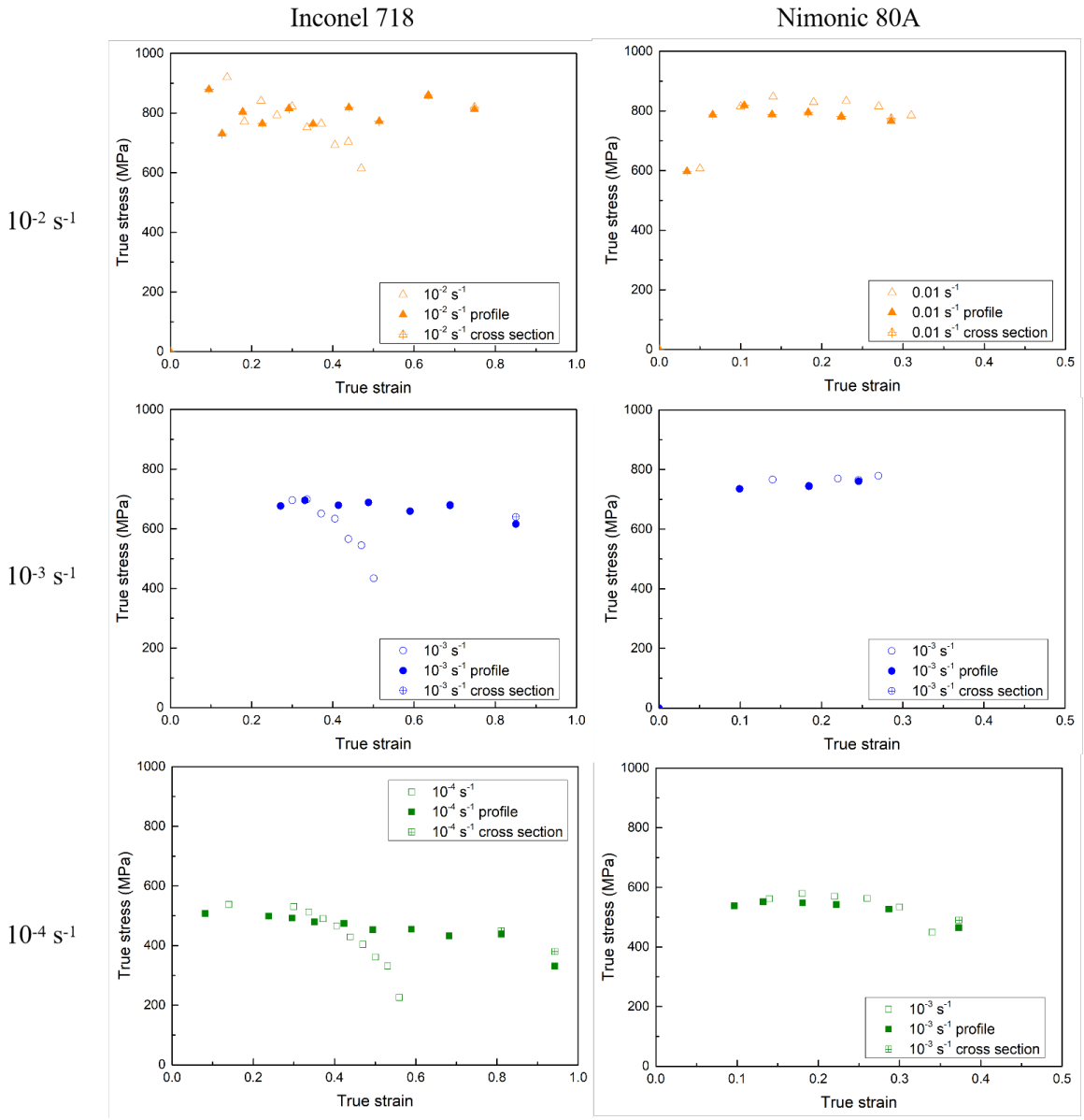


Fig. 3.18 True stress - true strain plots obtained from Fig. 3.15 and recalculated true stress - true strain plots from the necked profile ("profile") and calculated cross-sectional area ("cross section") for Inconel 718 and Nimonic 80A. Open symbols indicate the average true strains calculated from the displacement data. "Profile" plots are true strain calculated from the minimum radius obtained XCT profile analyses. "Cross section" symbols are the plots calculated from the cross-sectional area in which void area were excluded.

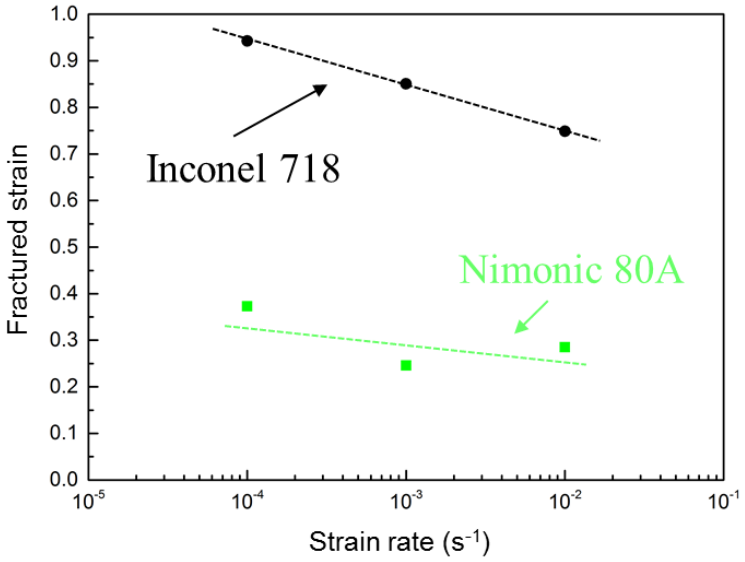


Fig. 3.19 Fractured strain values obtained from Fig. 3.18.

in these figures, the sliced images feature a number of dark features, which could be either real defects or else artefacts. In order to distinguish the voids or cracks from the artefacts, a number of sequential sliced images were compared. If the black patterns can be observed in the same location within the sequential images, those patterns were defined as defects, and *vice versa*.

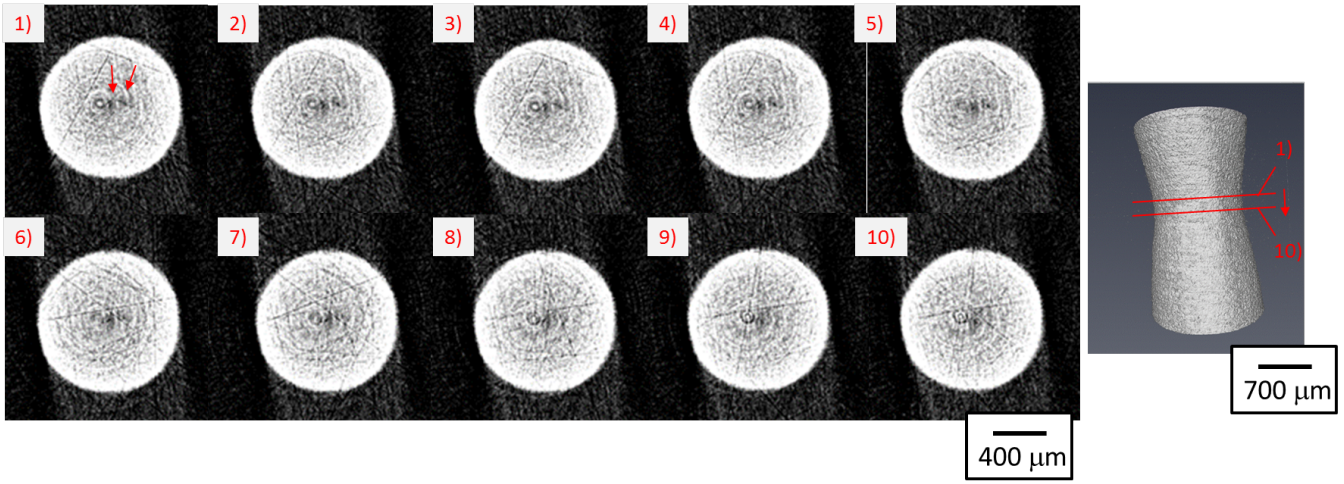


Fig. 3.20 Sequential sliced XCT images and internal voids (indicated by arrows) observed in Inconel 718 at the final imaging step before fracture (10^{-2} s^{-1}).

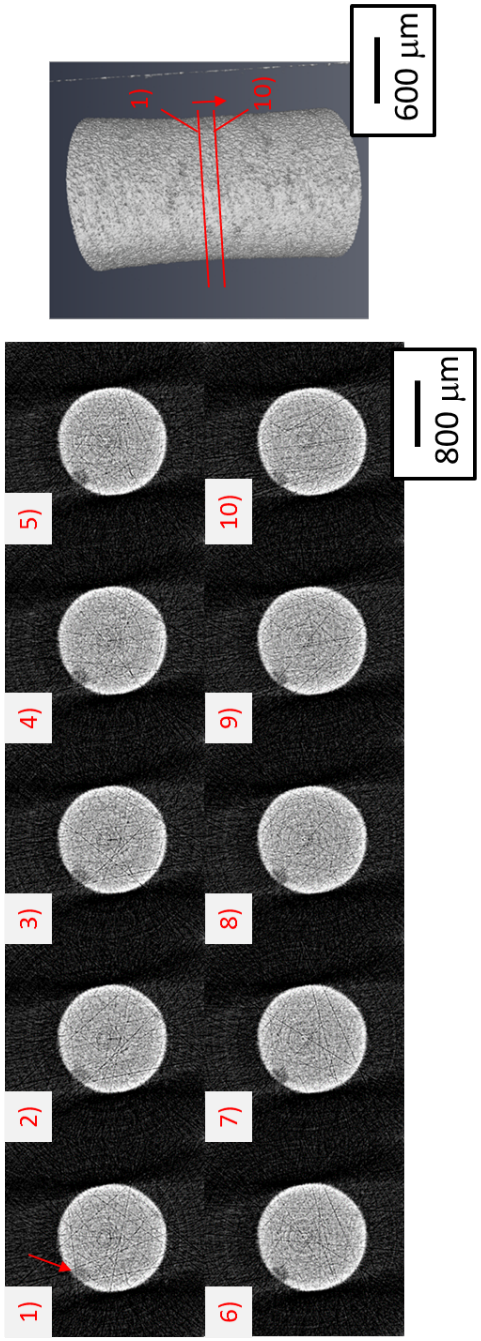


Fig. 3.21 Sequential sliced XCT images and the surface crack (indicated by an arrow) observed in Nimonic 80A at the final imaging step before fracture (10^{-2} s^{-1}).

Fig. 3.22 shows the reconstructed 3D XCT images of both materials just before fracture when tested at strain rates between 10^{-4} and 10^{-2} s^{-1}. Overall, Inconel 718 showed more prolonged necking behaviour than Nimonic 80A whilst Nimonic 80A exhibited more surface cracks than Inconel 718. Surface cracks were observed for all of the three strain rates for Nimonic 80A, while a large crack was observed only in 10^{-4} s^{-1} for Inconel 718. As illustrated by the arrows, in the highest strain rate Nimonic 80A exhibited more cracks than other cases. For Nimonic 80A, the size of cracks observed in 10^{-2} s^{-1} was as small as 30 - 50 μm. The detectable internal voids in Inconel 718 from the sliced images (fig. 3.20) was also 30 - 50 μm. Thus 30 - 50 μm was the minimum defect size that could be observed in this system and the authors believe that this represents the limit of the spatial resolution which can be achieved for the applied nickel-based superalloys. For both grades of superalloys, the surface cracks were larger at the slower strain rates, and the size of cracks before fracture exhibited more than 500 μm.

More detailed features including the damage evolution were revealed by comparing the *in situ* XCT results obtained in several strain steps before the onset of fracture. Fig. 3.23 and Fig. 3.24 show the 3D reconstructed and 2D sliced images of XCT data for Inconel 718 during tensile loading at 10^{-4} and 10^{-2} s^{-1}. In both cases, the results were shown with regard to three steps of the strain before fracture. In both strain rates, the necking behaviour was observed to start prior to the formation of cracks or voids. At 10^{-4} s^{-1}, at $\varepsilon = 0.81$, a surface crack with the size of around 300 μm and the void formation were observed only at the necked region. Those defects grew and coalesced at $\varepsilon = 0.94$, just before the onset of fracture. On the other hand, at 10^{-2} s^{-1}, void formation was observed in many sliced positions against the tensile direction. Those voids started being nucleated at $\varepsilon = 0.64$ and were grown up to 50 - 100 μm in size. The voids observed in different sliced images were enlarged separately without

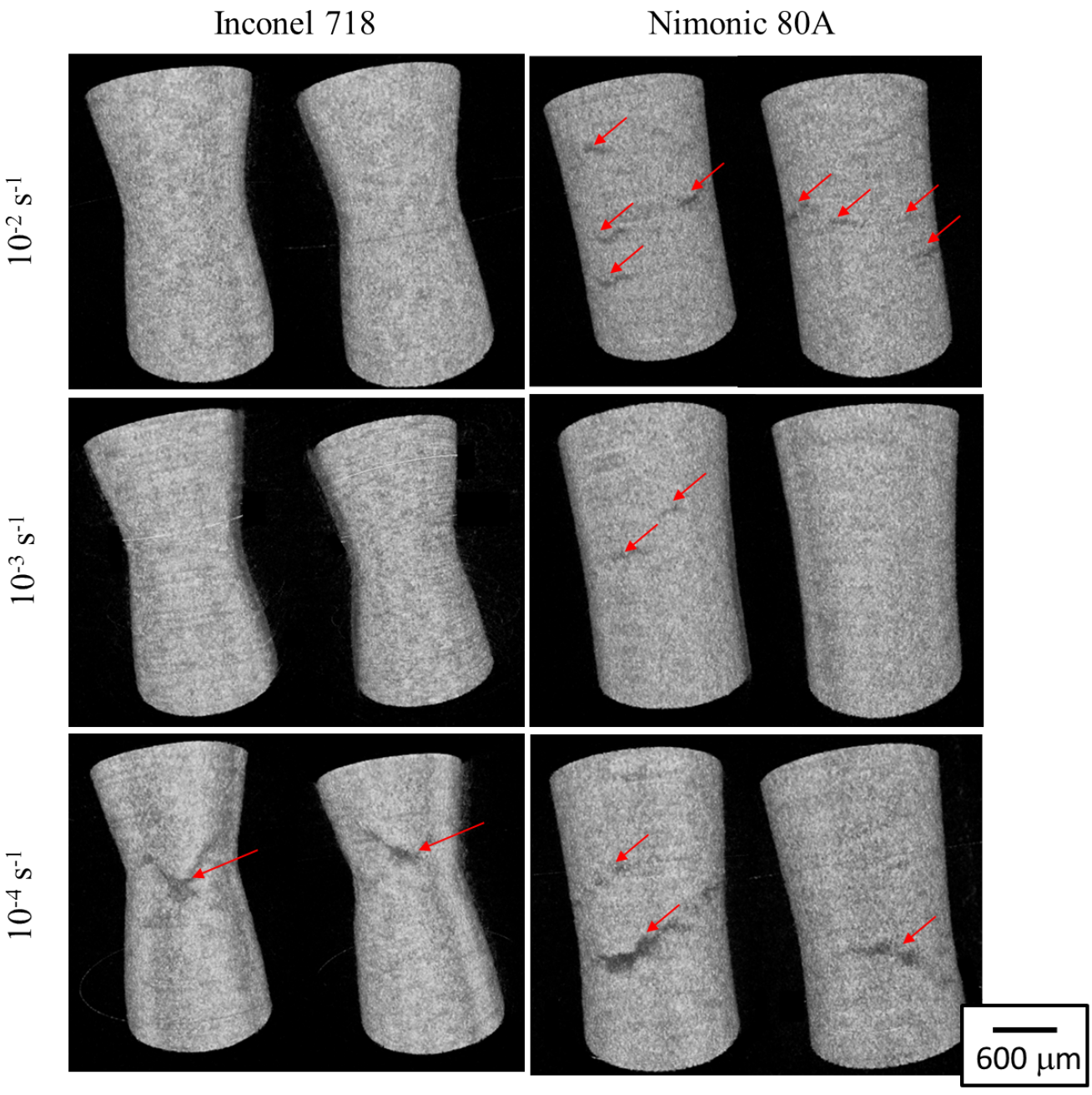


Fig. 3.22 Reconstructed 3D XCT images of Inconel 718 and Nimonic 80A samples at the final imaging step before fracture at 800°C under 10^{-4} to 10^{-2} s^{-1}. Arrows indicate detected surface cracks.

merging into each other. Compared to the slower strain rate, the formation and growth of voids occurred in a rather dispersed fashion and were not concentrated within the necked region.

Similar analyses were also conducted for Nimonic 80A. Fig. 3.25 and Fig. 3.26 show the 3D and 2D images of *in situ* XCT results for Nimonic 80A during the tensile loading in 10^{-4} and 10^{-2} s^{-1} at the three strain stages prior to the onset of fracture. Contrary to Inconel 718, Nimonic 80A exhibited no apparent necking behaviour nor void growth before fracture. Instead, the formation and growth of surface cracks were observed. At 10^{-4} s^{-1}, only two surface cracks with the size of 100 - 200 μm had nucleated at $\varepsilon = 0.29$. They propagated inwards and on the surface along 40 - 50° against the tensile axis. The grown cracks were as large as 500 - 700 μm at $\varepsilon = 0.37$. However, at 10^{-2} /s, as many as 7 crack nucleation events were observed in a wider range of the surface. They were enlarged separately and grew to be 50 - 100 μm. The direction of those cracks was perpendicular to the tensile axis.

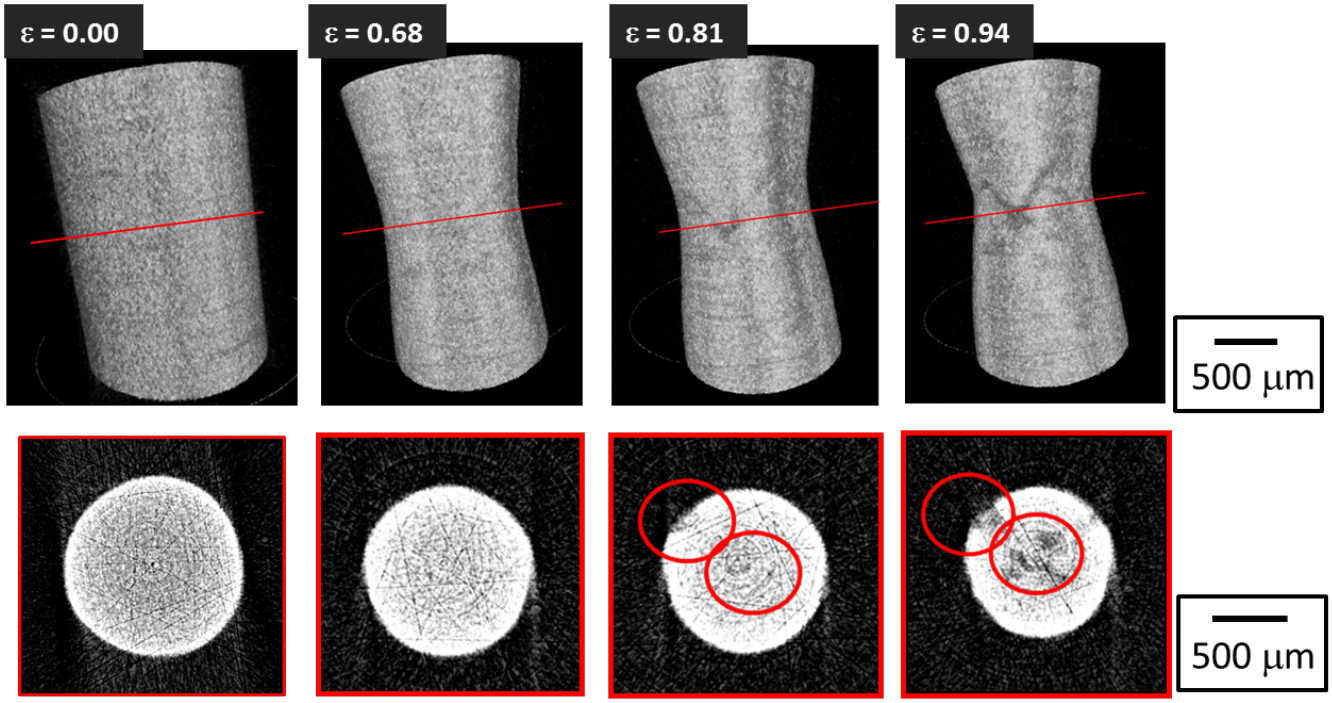


Fig. 3.23 *In situ* XCT results of Inconel 718 in 10^{-4} s^{-1} with true strain obtained from profile data (Fig. 3.16). Circles indicate voids or cracks.

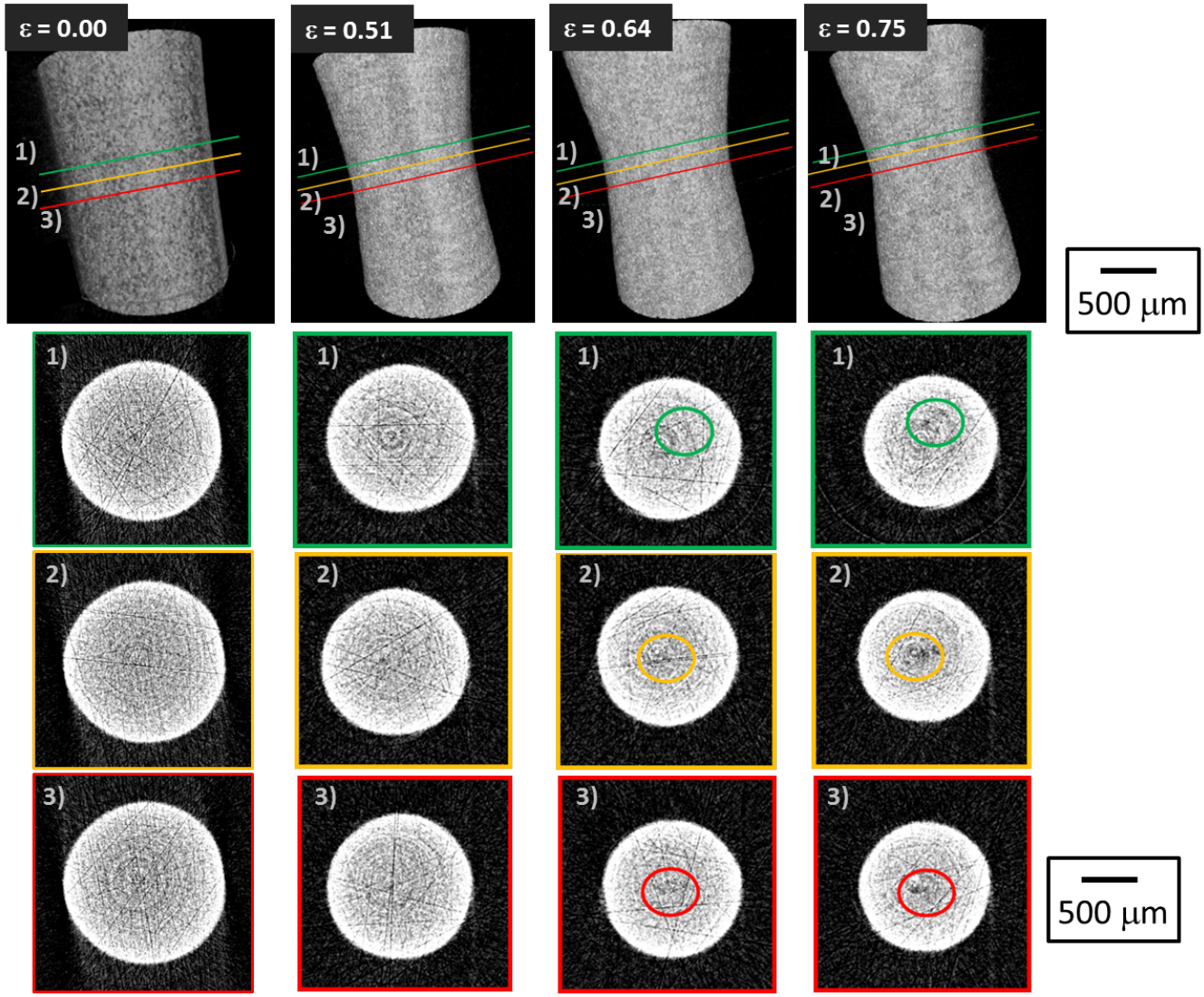


Fig. 3.24 *In situ* XCT results of Inconel 718 in 10^{-2} s^{-1} with true strain obtained from profile data (Fig. 3.16). Circles indicate voids.

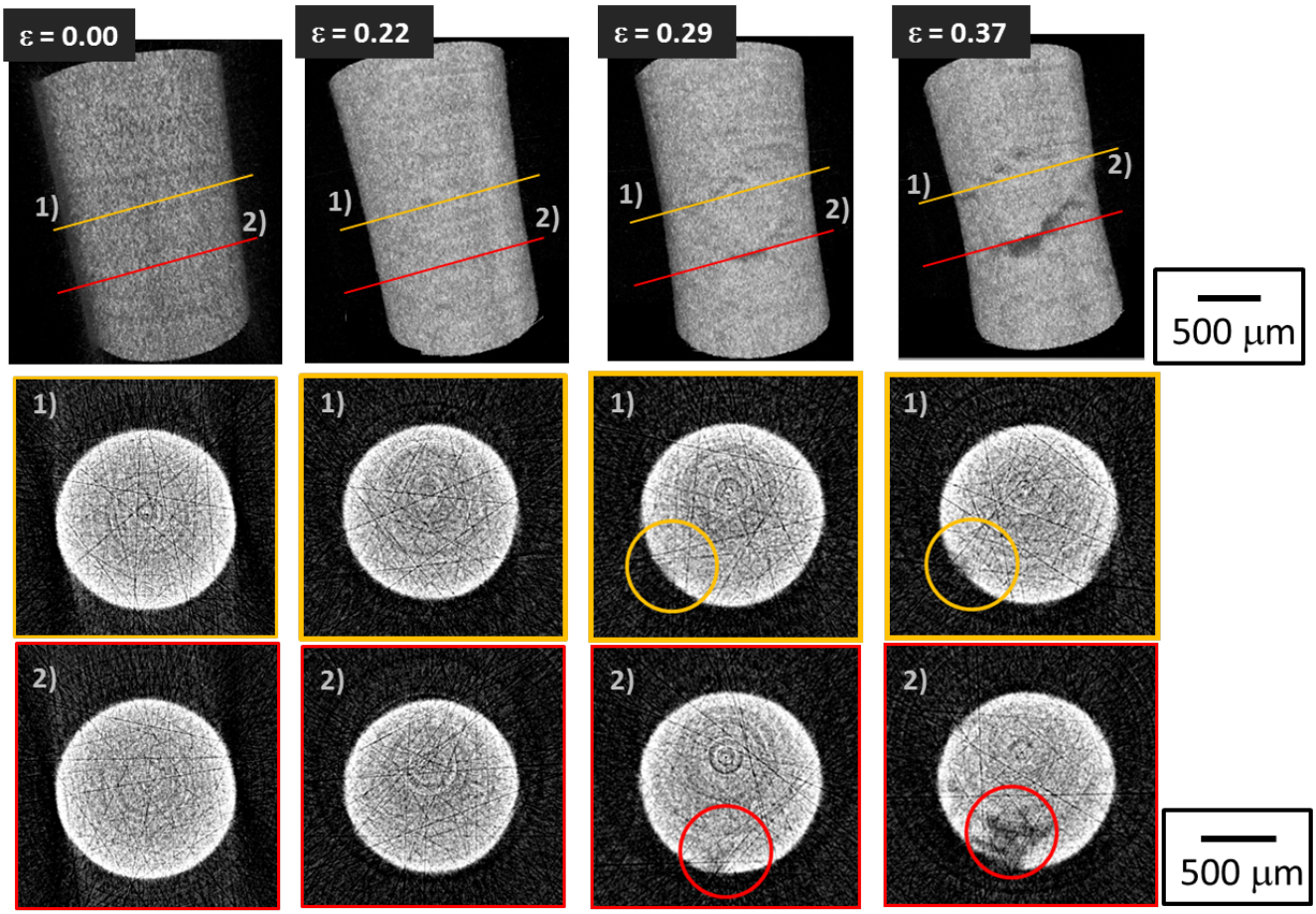


Fig. 3.25 *In situ* XCT results of Nimonic 80A in 10^{-4} s^{-1} with true strain obtained from profile data (Fig. 3.17). Circles indicate voids.

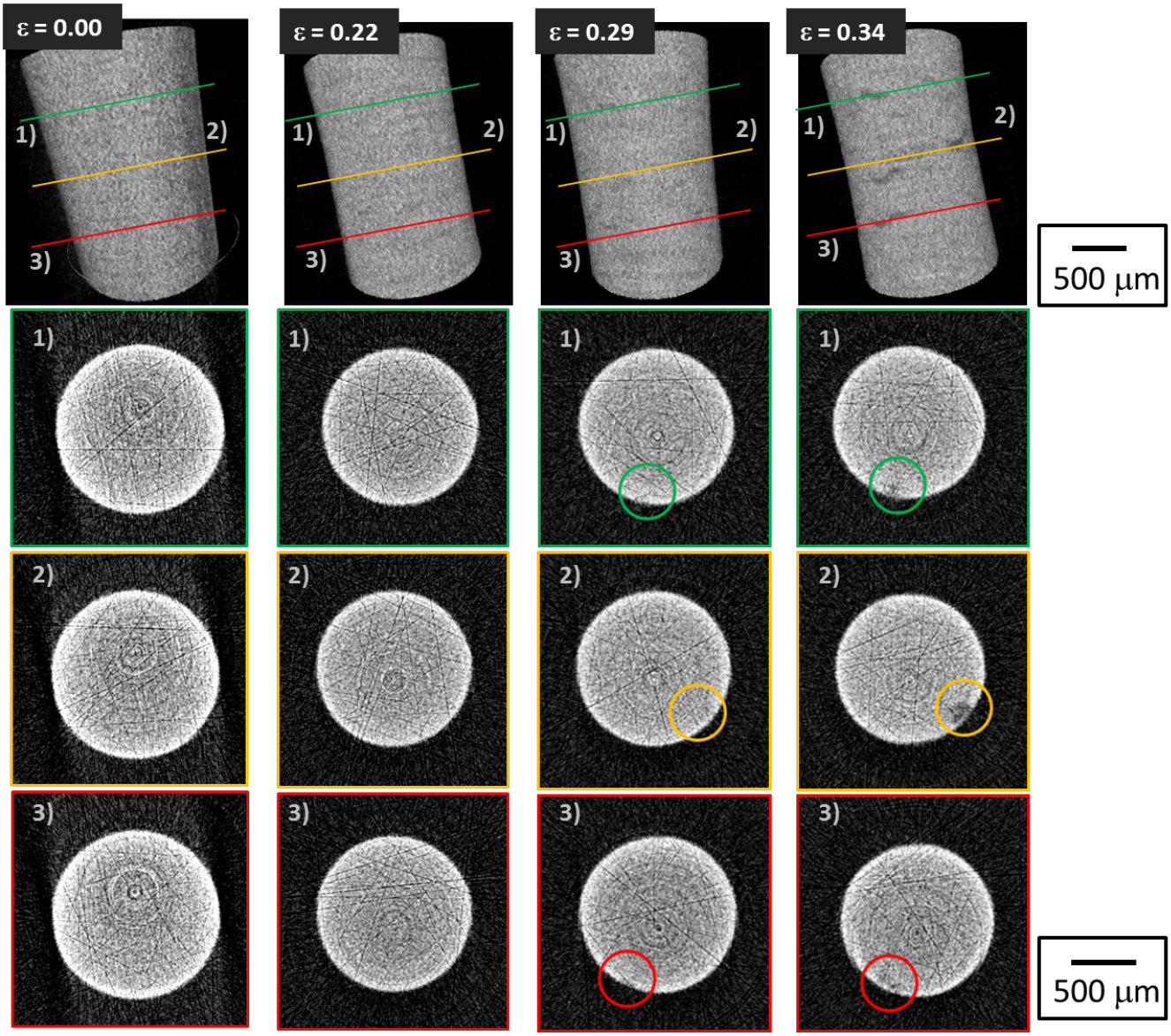


Fig. 3.26 *In situ* XCT results of Nimonic 80A in 10^{-2} s^{-1} with true strain obtained from profile data (Fig. 3.17). Circles indicate voids.

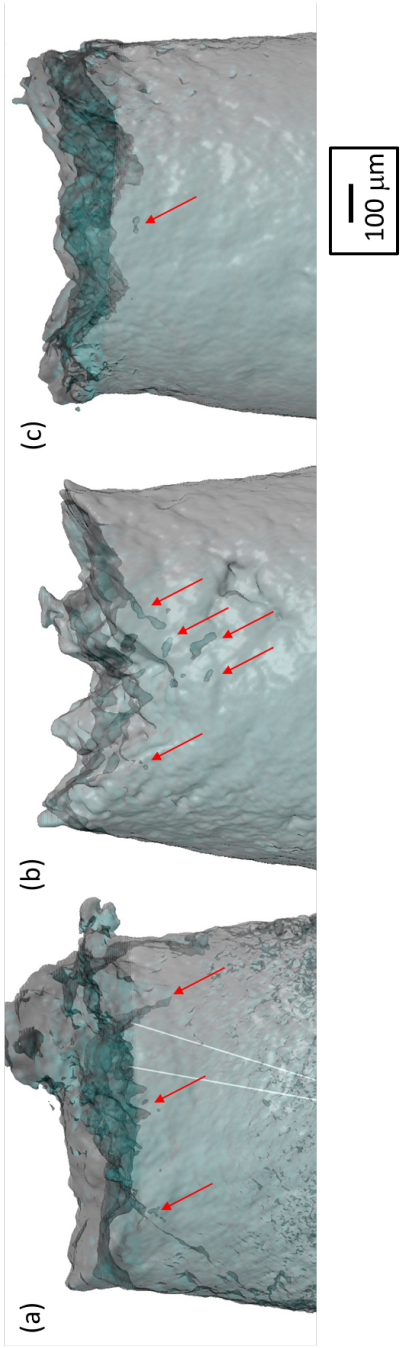


Fig. 3.27 XCT images of Inconel 718 after high temperature tensile tests ((a) 10^{-4} s^{-1}, (b) 10^{-3} s^{-1}, and (c) 10^{-2} s^{-1}). Arrows indicate internal voids.

More detailed features in fractured specimens were examined using *ex situ* XCT observation. Fig. 3.27 illustrates fractured Inconel 718 samples after the tensile tests with the strain rate of 10^{-4} to 10^{-2} s^{-1}. As the arrows illustrated in the figure, fractured samples also showed some internal voids near the fracture surface. Although some differences in the number of voids between these strain rates were observed, the fractured sample at 10^{-2} s^{-1} displayed fewer voids than for the tensile test at *in situ* XCT. Similar analyses were also carried out with Nimonic 80A. Fig. 3.28 shows the XCT image of the Nimonic 80A sample fractured under 10^{-3} s^{-1}. Nimonic 80A did not include any internal voids near the fracture surface.

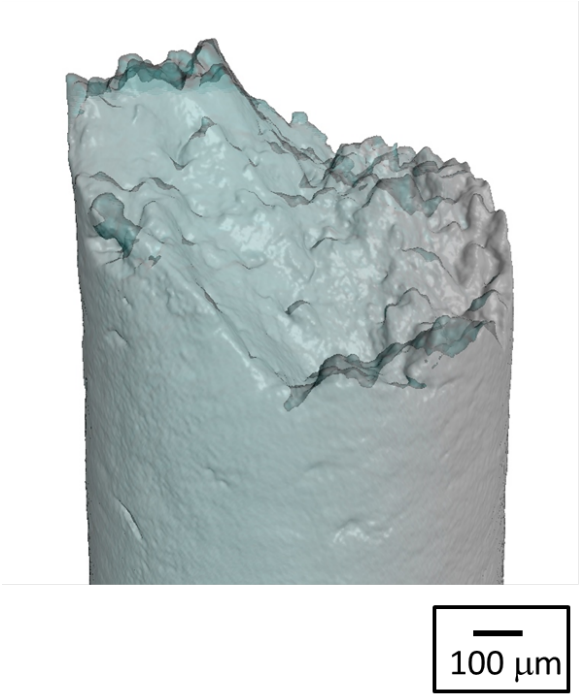


Fig. 3.28 XCT image of Nimonic 80A after high temperature tensile tests (10^{-3} s^{-1}).

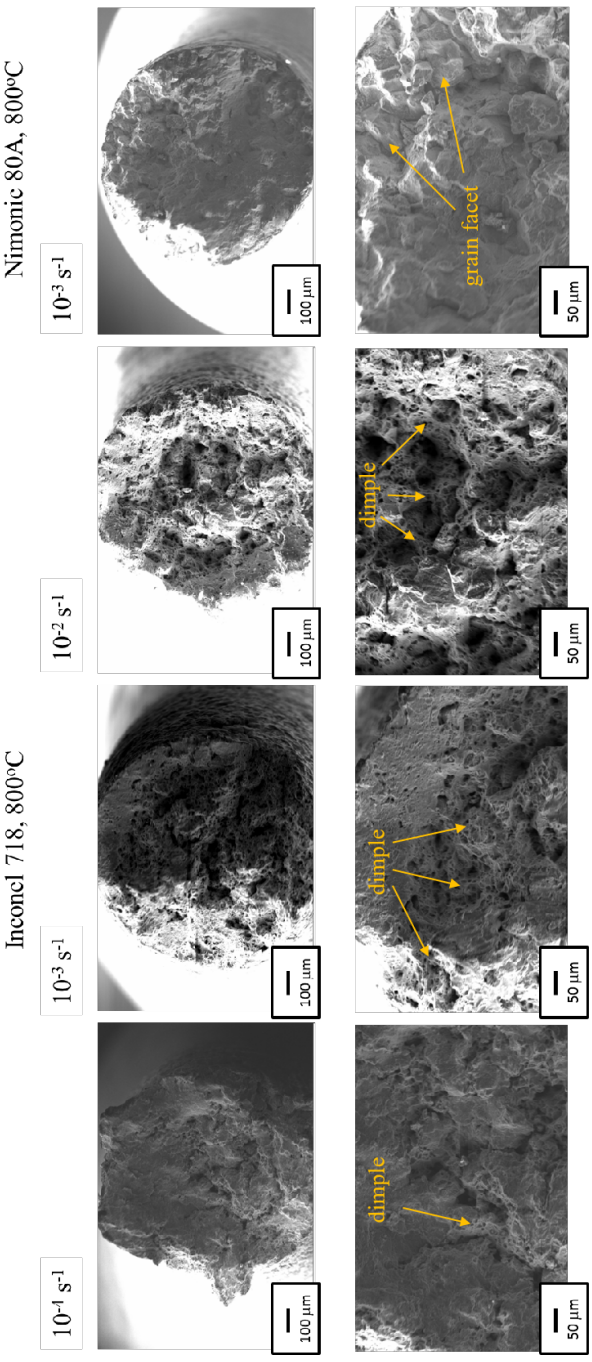


Fig. 3.29 SEM images of fractured surfaces after high temperature tensile tests.

These fracture surfaces were also examined using SEM fractography analyses. Fig. 3.29 illustrates the fracture surfaces of Inconel718 testpieces fractured at 10^{-4} - 10^{-2} s^{-1}, and Nimonic 80A testpiece fractured at 10^{-3} s^{-1}. Inconel 718 fractured surface showed dimple features, which implies fractured void parts as described in other works [159]. At the highest strain rate, more dimples were observed and the fracture surfaces were rougher, which indicated that more voids were generated near the fractured surface before fracture. Comparing these fractography analyses with *ex situ* XCT results mentioned above that in higher strain rate case fewer internal voids were observed, in the strain rate of 10^{-2} s^{-1}, internal voids generated near the necked region during the tensile tests were rapidly grown to coalesce and created the rougher fracture surface. In Nimonic 80A, many grain facets were observed. It indicated that intergranular crack propagations [53] were the main factor of the fracture rather than void growths in grain boundaries. Many of these grain surfaces were observed near the rim rather than the centre of the fractured surface.

3.5 Discussion

3.5.1 On the spatial resolution achieved in the high temperature XCT system

In this study, a new *in situ* XCT system is capable of revealing the time-dependence of the morphological evolution of both internal and external features during specimen testing. Particular novelty arises from the use of high temperature testing using a furnace arrangement; to our best knowledge, there have been very few attempts at doing this before. This feature makes it particularly suitable for the study of nickel-based superalloys for which deformation over significant periods of time is needed. The two

distinct grades IN718 and Nimonic 80A have been used here, tested at strain rates between 10^{-4} and 10^{-2} s^{-1}. Evidently, although alternative techniques such as the 2-dimensional digital image correlation (DIC) method are capable of providing surface information ([160], [161]), these are not suitable for 3-dimensional measurements of the type reported here or else high temperature experiments over extended periods of time.

Tensile testing at 800°C has been used for our verification studies. Evidence has been presented to confirm that external features such as localised thinning/necking and surface cracking can be detected and quantified. But furthermore, the XCT system made it possible to observe the growth of internal defects during the high temperature experiment. One can confirm this succinctly by comparing images obtained in the *in situ* arrangement and those obtained *ex situ* thus taking advantage of the absence of the furnace arrangement which – one might think – cause a compromise on resolution. Fig. 3.30 illustrates several sliced images obtained by *ex situ* and *in situ* XCT of a sample fractured at 10^{-2} s^{-1} under 800°C. *Ex situ* XCT images were obtained at room temperature using a distinct North Star Imaging system that is capable of producing 3D images at a resolution of 5-10 μm. As is apparent, although the *in situ* XCT images during the high temperature tensile test exhibit blurring when compared to the *ex situ* XCT images, the *in situ* XCT system is nonetheless capable of revealing internal defects at a spatial resolution of 30-50 μm.

In practice, the resolution of backprojection XCT images is affected by factors including the image unsharpness (U_g) induced by the focal spot, the movement of the object, and the quality of the detector ([153]). As discussed in the previous section, during the *in situ* XCT observation, the sample was fixed under displacement-controlled mode which thus avoided any effects of creep deformation. Therefore, in this study, any influence of object movement can be confidently ignored as a factor influencing the lack of image sharpness. Assuming that the detector effect could also be eliminated,

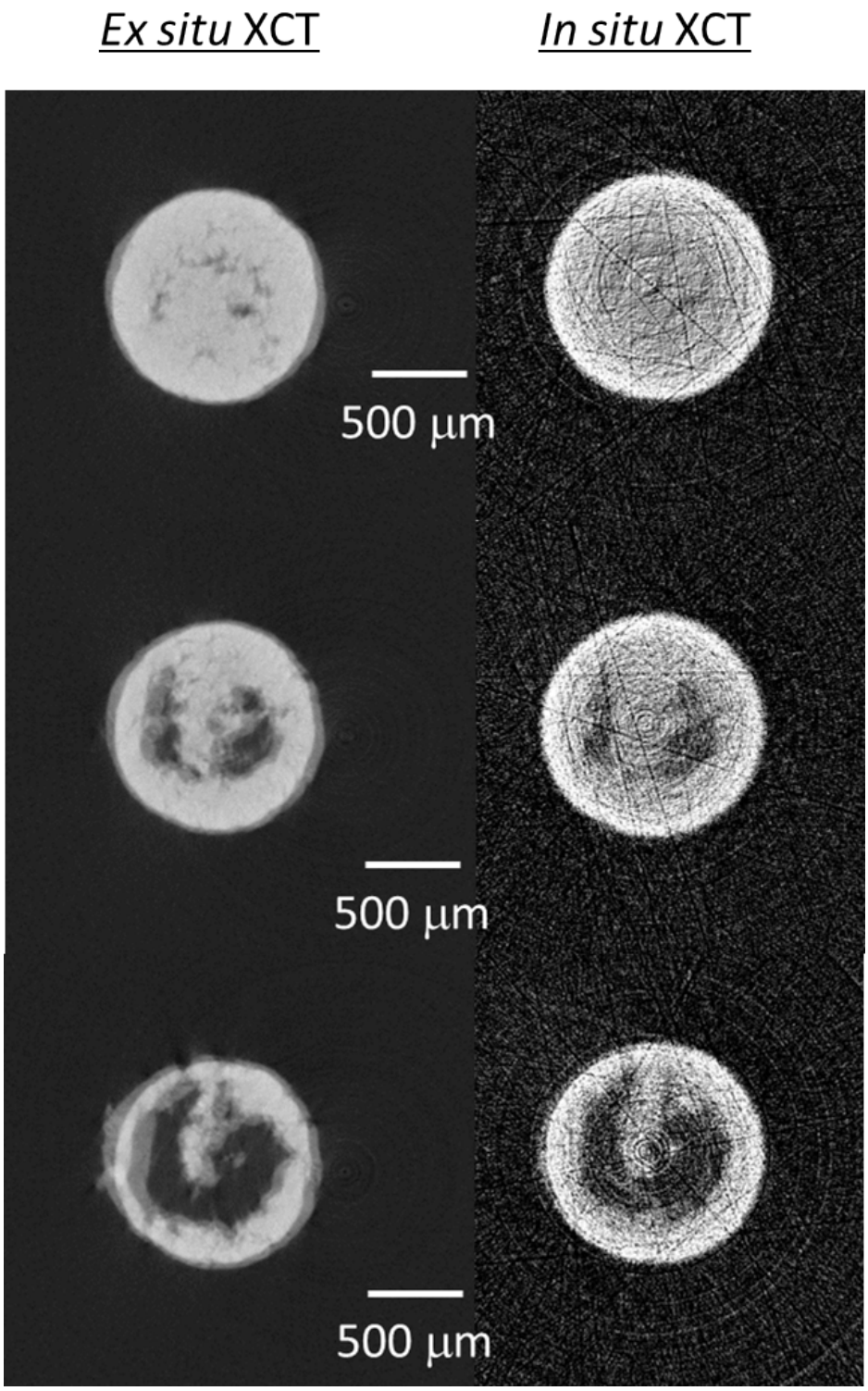


Fig. 3.30 *Ex situ* and *in situ* XCT sliced images of a fractured sample (Inconel 718, 10^{-2} s^{-1})

the major factor limiting resolution is then the focus unsharpness. This value depends upon the distance between the source and the object D, the distance between the detector and the object d, and the focal spot size of the X-ray source F via the following equation: $U_g = F * \frac{d}{D}$. Since the focal spot size in the present system is about 40 μm and the distance from the object to the source and to the detector is similar, the unsharpness is expected to be approximately 40 μm, consistent with the observed results in Fig. 3.30. Although the resolution might be improved in principle by capturing backprojection images with the lower current for a longer time, which might affect the object movement due to the creep fracture which might occur while imaging for longer times at high temperatures.

3.5.2 On internal voids in Inconel 718

As observed in the high temperature tensile tests on IN718, the formation and growth of internal voids were imaged differently depending upon the strain rate employed. In order to quantify the size and distribution of the voids, the Amira software was used to visualise differences between the strain rates. Fig. 3.31 illustrates this quantitative information about voids as distinguished by considering a range of intensity thresholds. As indicated from the sliced images, in the higher strain rate regime, voids are generated along the tensile direction in a rather dispersed fashion. From these 3D maps of voids, void size distribution can be evaluated as a function of distance from the necked region as shown in Fig. 3.32. While at 10^{-4} s^{-1} the voids were found only in the necking region, at 10^{-2} s^{-1} voids were in general smaller and distributed over a wider volume of the gauge. It seems very likely that these internal defects induced the differences in true stress/true strain plots calculated from the necked profiles as shown in Fig. 3.18. The larger voids at the slower strain rate made the actual cross-section area less, thus

contributing to the stress drop before fracturing in the figure. Further improvement for XCT image resolution would offer a more accurate cross sectional area before fracture.

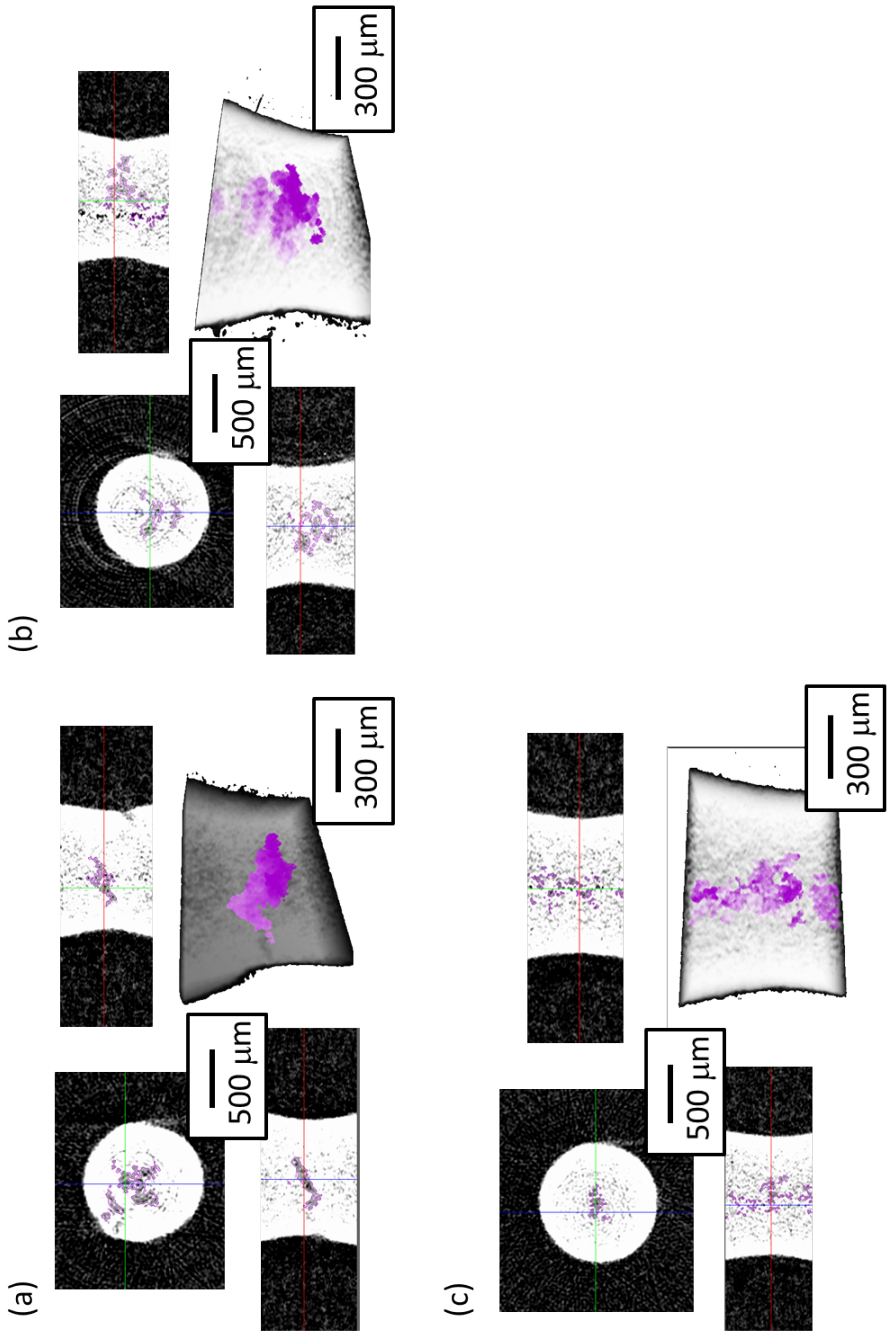


Fig. 3.31 XCT analyses of the voids detected in Inconel 718 before fracture in the strain rate of (a) 10^{-4} s^{-1}, (b) 10^{-3} s^{-1}, and (c) 10^{-2} s^{-1}

According to Hull & Rimmer [162], the stress applied to the void surface increases the diffusion flux needed for void growth. From the profile results in the present study, the necking curve was more apparent and deeper at a slower strain rate. These profile differences can affect the void growth behaviour in the necking part as introduced in other work on ductile materials with a different gauge shape [163]. Hayhurst *et al.* mentioned that in a high triaxial stress field, when the levels of applied load are high, softening due to continuum cavity growth predominates over cavity nucleation [164]. At the slower strain rate, the necked region in the gauge is likely to promote cavity growth more than at the higher strain rate case, due to the necked curvature created.

The stress was concentrated in the necked region at the slower strain rate, which caused the growth of voids to be observed only in that region. On the other hand, at 10^{-2} s^{-1}, the necking curve was comparatively more shallow and the tensile stress affected both the cavity nucleation and the cavity growth over a broader range. Dyson illustrated that the ductility is inversely related to the increase in cavity number per unit strain [165]. Our results are consistent with Dyson's work, since at the higher strain rate in this study, the ductility exhibited lower values than for the slower strain rate. Considering that the higher strain rate induces higher stress during the tensile tests, these cavities were grown rapidly over a broader range at the high strain rate.

3.5.3 On surface cracks in Nimonic 80A

In the case of Nimonic 80A, intergranular cracks were observed on the fractured surface rather than internally. According to the fractography analysis and *ex situ* XCT images of the fractured sample obtained at room temperature, surface cracks originated in an intergranular manner from the rim of the sample gauge. At similar temperature conditions, Sharma et al. [166] mentioned similarly that cracking tended to initiate

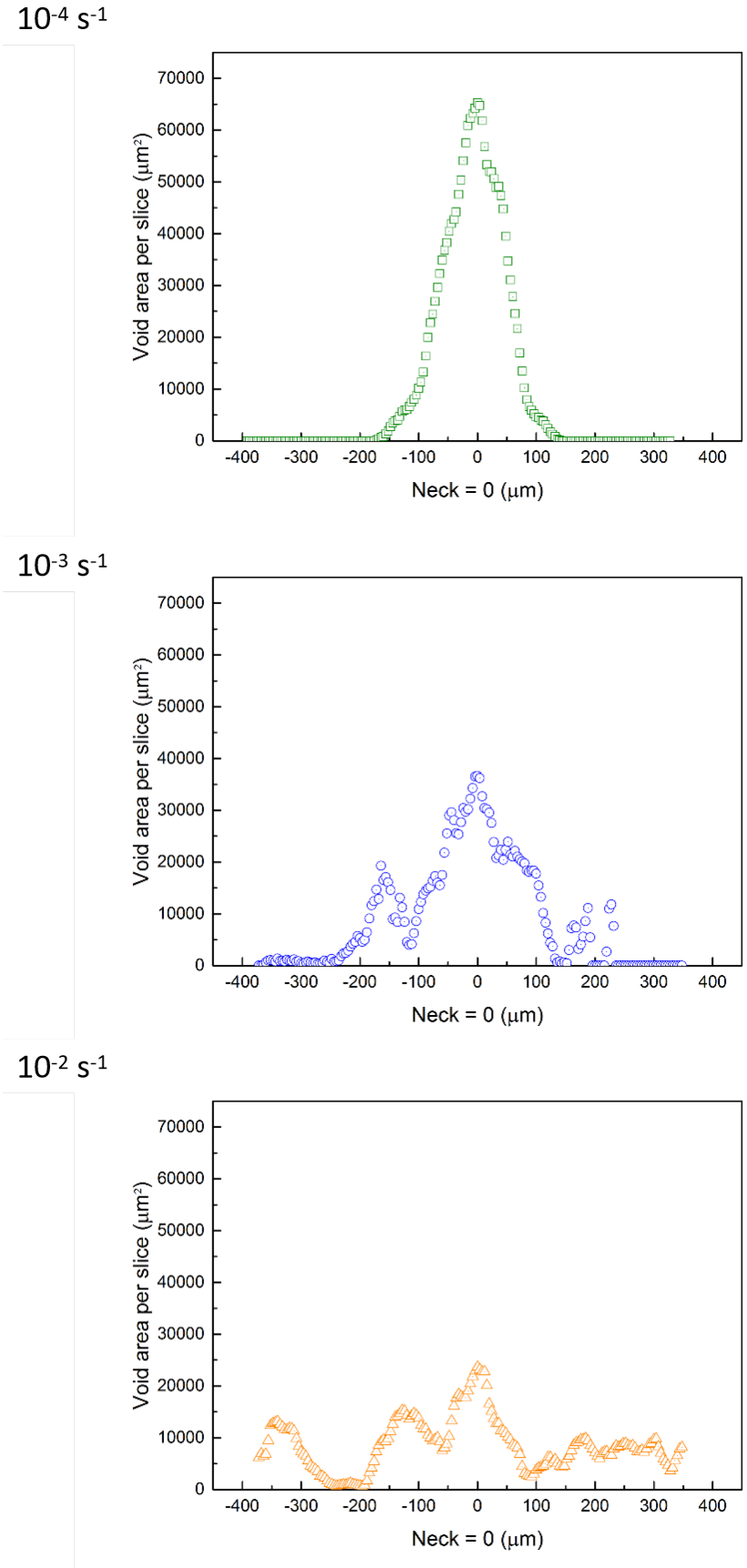


Fig. 3.32 Void size distribution before fracture for Inconel 718 in the strain rate of 10^{-4} s^{-1}, 10^{-3} s^{-1}, and 10^{-2} s^{-1}. Horizontal axis shows the distance from the necked region.

around γ' phases and created intergranular fractured surface, which is consistent with our results. Since Nimonic 80A exhibited less ductility than Inconel 718, one can say that cavity nucleation occurred more favourably than for Inconel 718. Such cavitation can occur preferentially at grain boundaries lying transverse to the tensile direction [30]. Since our results showed that the initiated cracks were largely perpendicular to the tensile direction, tensile cracks were produced by such void coalescence at the grain boundaries. For damage creation with cavity nucleation dominating, other works have also shown that cracks are initially preferentially nucleated at the sample surfaces [164].

Thus Nimonic 80A also exhibited damage accumulation which depended upon the strain rate conditions. At a slower strain rate, a smaller number of the surface cracks were formed and grew to a much larger size, whilst higher strain rates generated a larger number of smaller cracks on the surface. Necking behaviour was not as apparent as Inconel 718, but the slower strain rate in Nimonic 80A also caused a deeper necking profile than the higher strain rate case. Due to the comparatively more necked profile, the tensile stress was concentrated on the necked part at a slower strain rate, resulting in cavity growth and eventually significant cracking in this region.

3.5.4 On the advantage and limitation of the devised system

This paper has presented the details of and performance of an XCT system that is capable of observing void growth and crack generation even at a high temperature as high as 800°C. Such capability was achieved using a radiative furnace and not by means by forms of induction heating emphasised in other works (*e.g.* [87], [88]). Furthermore, the loading capacity of this system is up to 10 kN even at high temperature conditions. This is favourable compared to the other reported works − for example a maximum

load of 2kN at temperatures up to 1750°C [90] or 5kN tensile loading capacity with the temperature limited to 250°C[105]. The devised *in situ* XCT is applicable to a much wider range of experiments and materials than has hereto been possible. The new technique brings with it some significant advantages, which enable our understanding of the strain rate effects on the growth of voids/cracks to be enhanced. The damage accumulation process or mechanical responses from those damages might be clarified more in detail with further investigations. They also include real-time understanding of the damage effects on the creep behaviour, which is impractical by the *ex situ* technique because one cannot predict when the creep curve might start changing [107].

Finally, it is fair to identify some limitations associated with the XCT procedure. Fig. 3.33 compares the obtained stress-strain curves with and without *in situ* XCT – *i.e.* interrupted vs. monotonic loading. Independently of the material employed, when deforming at fast strain rates (10^{-2} s^{-1}), the maximum stress post interruption was lower than the stress values obtained under monotonic loading for the same values of strain. This indicates that some damage occurs during the interruption necessary to rotate the sample for XCT purposes – *i.e.* when deformed without interruption, there was not enough time for damage to occur. It seems likely that this effect is responsible for the lower values of strain-to-failure measured under interrupted experimentation. At slow strain rates (10^{-4} s^{-1}), the behaviour behaved differently. For both materials, the values of stress pre- and post-interruption match those obtained under monotonic loading – in this case, the strain rate was low enough that damage occurs both monotonically and with the interruption needed for XCT. In terms of ductility, Inconel 718 showed similar strain-to-failure independently of the mode of testing. However, for Nimonic 80A, the sample was tended to fracture immediately after surface cracks were observed. In those cases for which fracture was caused by cracks in the surface, the rotation necessary for XCT might conceivably enhance the damage. This is believed

to be responsible for the lower ductility observed when deforming uninterruptedly at low strain rates.

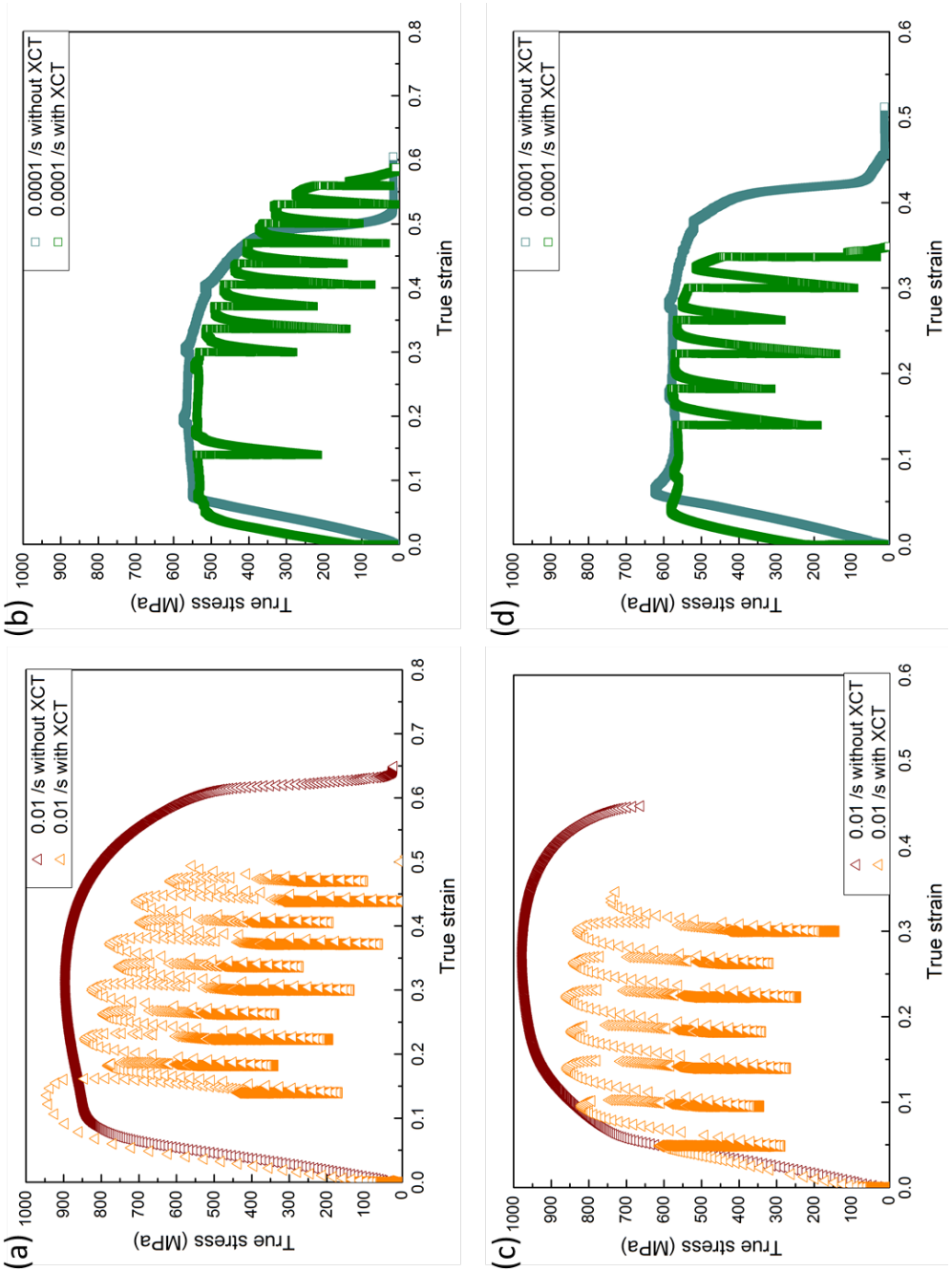


Fig. 3.33 Stress-strain curve in case of with and without XCT procedure. (a) Inconel 718, 10^{-2} s^{-1}, (b) Inconel 718, 10^{-4} s^{-1}, (c) Nimonic 80A, 10^{-2} s^{-1}, (d) Nimonic 80A, 10^{-4} s^{-1}.

3.6 Summary and Conclusions

The design, operation and performance of a laboratory-scale X-ray computed tomography system is described, which is capable of quantifying damage processes arising during the high temperature deformation of nickel-based superalloys. The following specific conclusions can be drawn from this study:

1. The new *in situ* XCT system which uses a laboratory-scale X-ray source has been applied to high temperature tests of the duration of up to 36 hours. The displacement-fixed control for the rotation needed to capture back projection images has been successfully applied for temperatures of at least 800°C and for strain rates in the range 10^{-4} to 10^{-2} s^{-1}.

2. The apparatus allows the collection of backprojection images with resolution sufficient to detect plastic deformation, void growth and crack initiation. Void nucleation and growth were detected with an accuracy of 30 - 50 μm, and this gives an indication of the spatial resolution which can be achieved.

3. Studies on the grades Nimonic 80A and Inconel 718 have been carried out, with the rationale that these are widely used alloys of lesser and greater ductility respectively. For testing at 800°C, Nimonic 80A exhibited surface cracks which are the sites of fracture initiation; for Inconel 718, internal void growth after necking was preferred. In both cases, the XCT system proved to be capable of detecting these failure events.

4. For Inconel 718 at 800°C and higher strain rates, void growth did not occur uniformly; nevertheless, its temporal and spatial distribution could be detected and quantified. Void coalescence was more concentrated within the necked region for slower strain rates. The surface cracks in Nimonic 80A were generated widely

over a wide range of the gauge volume at higher strain rates, whilst the slower strain rate caused fewer larger cracks.

5. At faster strain rates (10^{-2} s^{-1}) at 800°C, interrupted tests show a critical degradation of the maximum stress value in each step when compared to monotonic loading conditions – when deformed monotonically, there is not enough time for damage to occur. At slower deformation rates (10^{-4} s^{-1}) at the same temperature, the stress values pre- and post-interruption overlap those obtained monotonically. This proves that the nature of the damage process is time dependent – thus should be linked to diffusion-assisted forms of damage such as cavitation.

6. Future application of the system will allow for a more detailed quantification assessment of the damage accumulation occurring in these materials, including the statistical distribution and evolution with strain and time.

Chapter 4

Damage Accumulation during High Temperature Deformation of a Superalloy Analysed by *In Situ* Computed Tomography

The devised laboratory-scale X-ray computed tomography (XCT) system enabled to capture of the damage growth in a Ni-based superalloy, Inconel 718, by *in situ*. The newly proposed post-processing method, including beam-hardening correction and spot artefact removing, improved the tomography image resolutions to 30 μm, which got more suitable for quantitative damage analyses. In addition, the careful operation for XCT rotation prevented unintentional damage and focused on the effects of necking on internal void growth. The investigated visualised relations between void growth and necking behaviours during tensile and creep loading at 800°C offered new insights of stress triaxiality effects on cavity growth. Under the same stress state, the ductile void growth was observed more at a slower strain rate than at a higher strain rate.

4.1 Introduction

The developed *in situ* XCT system succeeded in observing internal damage at 800 °C for Ni-based superalloy testpieces, Inconel 718 and Nimonic 80A, as introduced in the previous chapter. The obtained XCT images offered cracks and void growth features larger than 30 - 50 μm. The devised system provided *in situ* XCT observation technique which is capable of quantifying damage processes arising during the high-temperature deformation of nickel-based superalloys. However, some procedures and algorithms still need to be improved. First, interrupted tests for the XCT procedure showed lower tensile stress than the monotonic loading test without the XCT procedure. In this procedure, the testpiece was rotated for XCT with a certain amount of loading being kept, which might affect further damage growth, such as creep damage, under the high temperature condition. Another improvement point is that the XCT image quality was insufficient for the quantitative damage analyses. The obtained XCT images detected cracks and voids by *in situ*, but further image improvements, such as removing speckle/line artefacts and correcting beam hardening [67], would offer clearer images to follow the damage growth quantitatively.

In this chapter, to investigate the grown damage only due to the tensile loading, the chapter 3 procedure was improved to another process where the tensile loading was removed before starting XCT rotation. *In situ* XCT observation was also applied to the creep experiment. This is not only for a new application of *in situ* XCT analyses during a different loading condition but also for the supporting data that might indicate that the remained stress during the XCT procedure employed in Chapter 3 affected creep damage growth. Furthermore, to capture the XCT more clearly, the post-processing method was studied in this Chapter. Obtained damage features were compared with stress conditions, such as stress triaxiality effect on the damage growth [44], [146], [49].

The introduced system in this chapter will investigate the damage growth in Inconel 718 at 800 °C and demonstrate a spatial resolution of better than 50 μm, which is sufficient to allow for new insights into the role of stress triaxiality on cavity growth.

4.2 Experimental Methods

The laboratory-based XCT system with an X-ray source and detector, an all-electric thermo-mechanical testing instrument (Instron E10000), a rotary table and a furnace was used in this work. The detailed experimental setup was described in the previous work [167]. Obtained back projection images were processed by the XCT reconstruction algorithm by implementing the inverse Radon transformation.

4.2.1 Testing machine operation

Tensile and creep test

The tensile and creep tests were conducted at 800°C (Table 4.1). For the tensile test, the target strain rates were 10^{-4}, 10^{-3}, and 10^{-2} s^{-1}, as representative rates in the static strain rate region. For the creep test, two loading conditions were selected; 480 and 566 MPa. These target stresses were close to the remained stresses during the XCT rotation steps for the tensile experiment at 10^{-2} s^{-1} (200 - 600 MPa) in the previous chapter. These creep conditions were designed to investigate whether the remained tensile stress affected creep damage growth during that procedure. Until the tensile stress was reached to these target stresses, the tensile loading was applied at the strain rate of 10^{-3} s^{-1}. These high-temperature experiments employed the electric furnace with a set of quartz windows to secure an unobstructed X-ray beam path. The temperature was monitored in the vicinity of the testpiece in the furnace.

Table 4.1 Tensile and creep test condition.

	Temperature	Strain rate	Target stress
Tensile test	800 °C	10^{-4} s^{-1}	-
Tensile test	800 °C	10^{-3} s^{-1}	-
Tensile test	800 °C	10^{-2} s^{-1}	-
Creep test	800 °C	-	480 MPa
Creep test	800 °C	-	566 MPa

In situ XCT procedure

To capture the 3D XCT images, the testpiece requires rotation for taking X-ray back projection images at every angle. These images are necessary to calculate inverse Radon transformation [168, 61] thus, the images should be captured for 180 or 360 degrees. The testing machine employed in this study has two modes of channel for the operation; axial (displacement and load) and rotational (rotation angle and torque). Within the same channel, operations cannot be carried out simultaneously. For example, it is impossible to control and keep a certain displacement value with the same load. Therefore, while rotating the testpiece, one can keep the same load value or displacement position. In the *in situ* XCT under high temperature, the load-controlled rotation can lead to creep deformation [167]. This kind of control is harmful to taking X-ray images with the object being stable and would generate irrelevant damages. For the XCT rotation procedure, it is better to rotate the testpiece with the displacement remaining the same since the displacement control can lead to stress relaxation during the test.

In this work, the *in situ* XCT experiment was carried out by the two different procedures and compared with the monotonic loading procedure without rotating operations for XCT (Figure 4.1, Table 4.2). In 'Interrupt 1', the crosshead kept the

same axial position before starting the rotation steps (same procedure as Chapter 3). 'Interrupt 2' improved 'Interrupt1' by removing the tensile loading before rotating for XCT. For both *in situ* XCT procedures, the following two points are in mind. (1) While rotating for capturing backprojections, the displacement remained constant. (2) For any rotating operation, the testpiece torque was controlled by precisely adjusting the rotation speed and angle position of both upper and lower flanges so as not to generate torque between them.

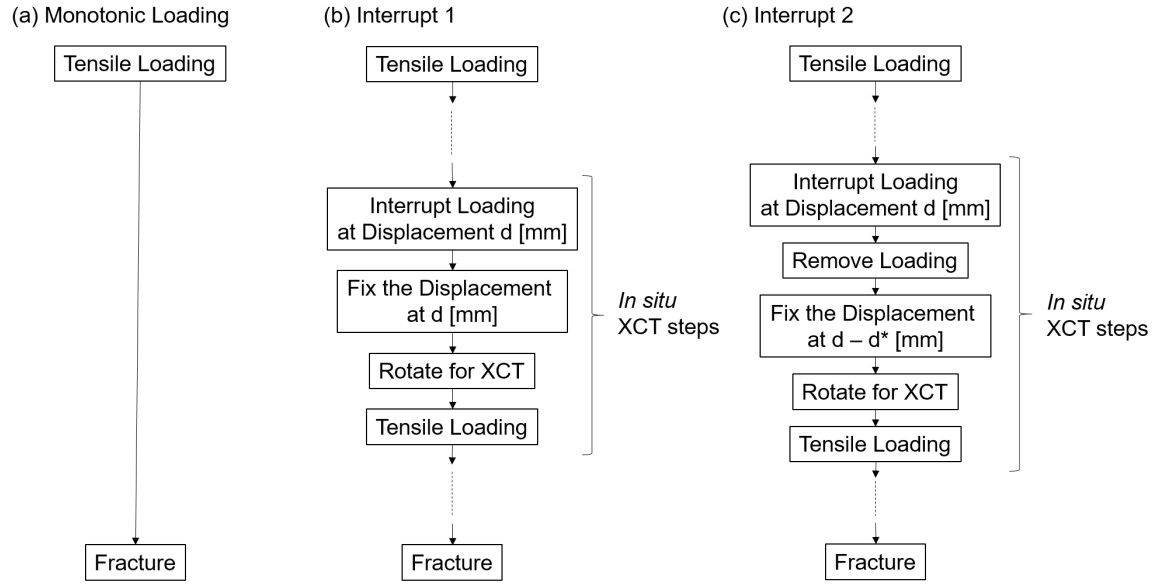


Fig. 4.1 Experimental flow chart for (a) Monotonic loading, (b) Interrupt 1, and (c) Interrupt 2. "d^*" denotes the decreased displacement while relaxing the loading in procedure (c).

Table 4.2 Test conditions for experimental optimisation.

	Loading	Temperature	Strain rate
Monotonic loading	Tensile	800 °C	10^{-4} s^{-1}
Interrupt 1	Tensile	800 °C	10^{-4} s^{-1}
Interrupt 2	Tensile	800 °C	10^{-4} s^{-1}
Monotonic loading	Tensile	800 °C	10^{-2} s^{-1}
Interrupt 1	Tensile	800 °C	10^{-2} s^{-1}
Interrupt 2	Tensile	800 °C	10^{-2} s^{-1}

4.2.2 XCT post processing

Since the poly-energetic type X-ray source was applied in this study, the Beam-hardening effect should be considered before processing the inverse Radon processing [67]. The poly-energetic X-ray is different from the mono-energetic X-ray employed in synchrotron facilities and emit a wide range of energies simultaneously. The backprojection images or reconstructed XCT images are calculated from the X-ray intensities attenuated through the object material. If the mono-energetic X-ray beam passes through the same object material, the attenuation coefficient inside the material would be constant. However, if the poly-energetic beam penetrates the object, the attenuation coefficient would vary depending on the energy: the higher energy beam can penetrate more. If the reconstruction algorithm applies the single attenuation coefficient similarly to the mono-energetic beam case, the inner and outer parts of the sliced object image can be calculated in different intensities. The intensity profile across the reconstructed slice shows concave as shown in Fig. 4.2 [169]. This is called beam hardening effect [67]. The reconstructed artefacts due to this effect can be the obstacle for achieving precise CT imaging, and the correcting methods for the beam-hardening noise need to be considered.

As described in Chapter 3, backprojection images were depicted through the flat field correction (FFC) process and applied to XCT reconstruction. The mono-energetic X-ray source would straightforwardly produce flat-field-corrected (FFC) backprojections and reconstructed XCT images since each pixel intensity just depends on the optical path length. However, the calculated FFC would require further corrections for the beam-hardening effect if the poly-energetic X-ray source were applied.

The beam hardening could be corrected by using pre-hardening filters or post-processing methods [169, 67]. In this work, a 0.5 mm Cu filter was used as the pre-

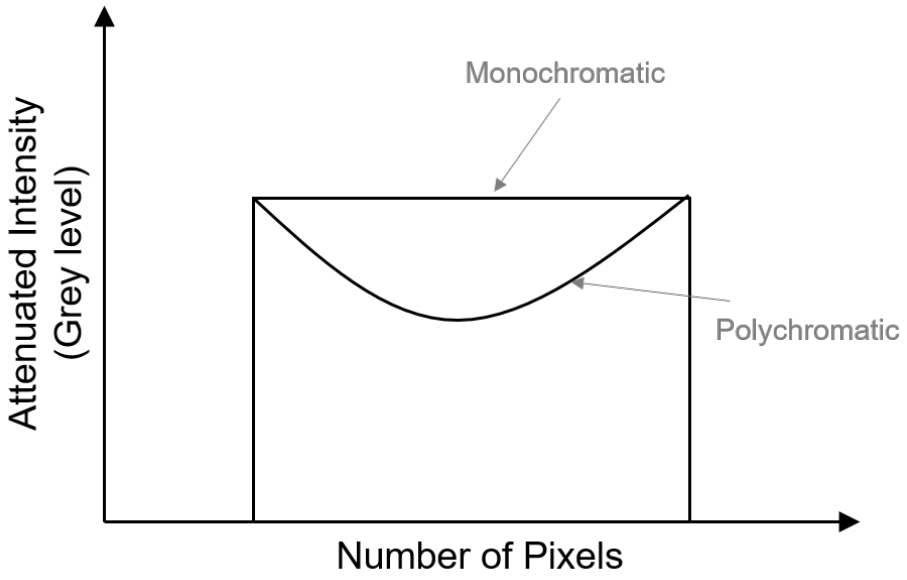


Fig. 4.2 The line profile across the reconstructed slice obtained by a polychromatic X-ray source and monochromatic X-ray source (Adopted from [169]).

hardening filter to reduce the lower energetic X-ray before being severely attenuated through the object. However, if the object material has a high electron density, this filter is insufficient, and the post-processing algorithm was also designed. For a fixed source and detector position in the parallel X-ray beam, let m describe the monoenergetic ray sum under the following condition; (1) source is mono-energetic at energy e, and (2) the attenuation coefficient of the object was independent of the X-ray energy. Let p denote the polychromatic ray sum similarly measured by the detector with the mono-energetic X-ray.

$$m = \int_0^D \mu_{\bar{e}}(z)dz \tag{4.1}$$

$$p = -ln \int_0^E \tau_e exp\Big[- \int_0^D \mu_e(z)dz \Big] de \tag{4.2}$$

where D is the distance from the source to the detector, $\mu_e(z)$ is the linear attenuation coefficient at energy e at a distance z from the detector, E is the highest energy level in the X-ray beam, and τ_e is the probability that a detected X-ray photon is at energy e. In the actual experiment, only the projection data p can be obtained. To estimate the mono-energetic data m, beam hardening correction (BHC) can be applied by performing a polynomial curve fitting between the image data of m and p. As discussed in other works [170, 169, 171], m was approximated by using third degree polynomial function, that is,

$$m = a_0 + a_1 p + a_2 p^2 + a_3 p^3 \tag{4.3}$$

For curve fitting, instead of using mono-energetic ray sum data m, optical path length L for each X-ray [172] penetrated through the cylindrical object was utilised assuming that the X-ray beam was perpendicular to the tensile axis and each cross-section was a circle shape. Since the ray sum, m, is proportional to L for the X-ray beamline, the calculated path from the diameter estimated from a backprojection image was used for fitting by following the following equation.

$$L = A_0 + A_1 p + A_2 p^2 + A_3 p^3 \tag{4.4}$$

After A_0, A_1, A_2, and A_3 were calculated in several object slices along the tensile axis, averaged parameters from those outcomes were utilised to calculate the penetrated path length with beam hardening correction. Assuming that all objects consist of the same material, this optical path length L would be proportional to the actual path length.

Using this correction, X-ray intensities detected in each pixel from the poly-energetic X-ray source were converted to the same intensities expected in the case obtained from

the mono-energetic X-ray beam source. Hence, the calculated L was applicable for inverse Radon transform similarly with mono-energetic XCT images.

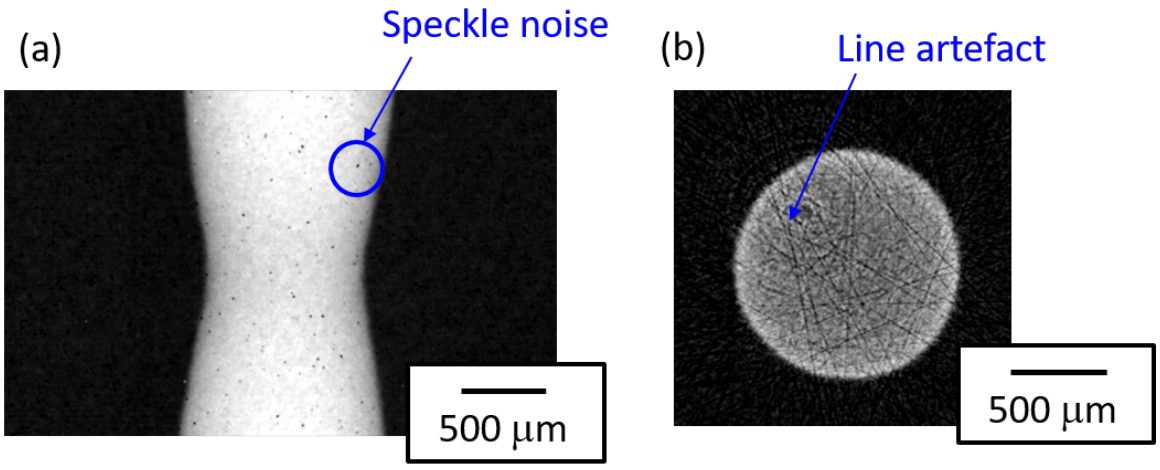


Fig. 4.3 (a) Back projection image with the speckle noises, (b) Reconstructed XCT image with line artefacts due to the speckle noises in back-projections.

The next step is to remove the speckle noises in the backprojection images (Fig. 4.3). These speckles were false signals due to the high power X-ray beams required in the XCT system and could damage the image quality. High power X-ray beam was selected to reduce the exposure time for the detector, but some pixels could not detect the X-ray intensity properly and generate the speckle noise. Speckle patterns in the backprojection images (Fig. 4.3(a)) generate line shape artefact in reconstructed images (Fig. 4.3(b)). To remove these speckles, two steps are required; 1) define the dotted area as the speckle, 2) remove the speckle. Although the speckle noises were displayed as low-intensity pixels in the FFC image, setting the intensity threshold is insufficient to identify those noises from the low-intensity signals due to the actual defects such as voids or cracks. The intensity and the size should define the speckle noises. The dark spots in the FFC image (less FFC values than the object) were defined as the speckle noises if these spots were less than 10 pixels. The detected noise pixels were filled with the averaged value of the adjacent pixels. Then after

smoothing 3×3 pixels, these corrected backprojection images were finally converted to the reconstructed sliced images by employing the inverse Radon transformation coded in MATLAB 2015a. This speckle-removing (SR) process was applied to the XCT images for further quantitative damage analyses.

For visualising the reconstructed 3D images or sliced images, ImageJ [154] or Amira software was used. Corrected XCT images were also compared with XCT results obtained under ambient temperature by a North Star Imaging (NSI) system at 150 kV and a current of 27 μA with a conical X-ray beam and a voxel size of 4.9 μm. The applied reconstruction algorithms were summarised in Table 4.3.

Table 4.3 Experimental conditions in which XCT reconstruction algorithm applied.

Algorithm	Loading	Strain rate	Target stress	Temperature while imaging
FFC	Tensile	10^{-3}, 10^{-2} s^{-1}	-	800 °C
BHC	Tensile	10^{-2} s^{-1}	-	800 °C
SR	Tensile	10^{-2} s^{-1}	-	800 °C
BHC + SR	Tensile	10^{-4}, 10^{-3}, 10^{-2} s^{-1}	-	800 °C
BHC + SR	Creep	-	480 MPa, 566 MPa	800 °C
Ref. NSI system	Tensile	10^{-4} s^{-1}	-	Room Temperature

4.2.3 Stress triaxiality during necking

In this work, the damage growth after necking will be traced by *in situ* XCT. The profiles of necked testpieces can be estimated from XCT data, which is used to calculate stress triaxiality. For a round bar tensile testing, the stress triaxiality (T) in the necked part of the testpiece can be calculated as follows [46].

$$T = \frac{1}{3} + ln(\frac{a^2 + 2aR - r^2}{2aR}) \tag{4.5}$$

where a and R respectively denotes minimum cross-sectional radius in the necked part and necking curvature (please refer to fig. 2.11). r is the radial coordinate from the

centre axis. The minimum radius a was estimated from the XCT image obtained from each strain, whilst R was calculated from the approximated curve of the cross-sectional radius profile obtained from those tomography images. The following fourth-degree polynomial function was applied for this curve fitting by using z as the axial coordinate along the tensile direction,

$$f(z) = p_4 \cdot z^4 + p_3 \cdot z^3 + p_2 \cdot z^2 + p_1 \cdot z + p_0 \tag{4.6}$$

then the radius of curvature at the necking region was calculated as follows. In the following equation, z_0 denotes the point where the cross-sectional radius showed the minimum value ($= a$),

$$R = \left| \frac{1}{\frac{\mathrm{d}^2}{\mathrm{dz}^2} f(z)|_{z=z_0}} \right| = \left| \frac{1}{4 \cdot 3 \cdot p_4 \cdot z_0^2 + 3 \cdot 2 \cdot p_3 \cdot z_0 + 2 \cdot p_2} \right| \tag{4.7}$$

Measured R and a by *in situ* XCT images were substituted to Eq. 4.5 to calculate T, which will be compared with void growth estimated also by *in situ* XCT.

4.2.4 Testing material

For the *in situ* XCT observation, high temperature tensile experiments were conducted for the polycrystalline Ni-based superalloy using IN718 (with composition given in Table 5.2), as a widely-used Ni-based superalloy. IN718 specimens were machined from round bars (NeoNickel Milton Keynes Co, Ltd.), which was solution heat treated at 940 - 1010 °C following air-cooled (AMS5662 bar). As shown in Fig. 4.4, the grain size in IN718 was approximately 30–50 μm. The testpiece gauge length and diameter were 2 mm and 1.5 mm, respectively. The dimensions were selected so that the XCT

detector allows the X-ray beam to fully penetrate the specimen for optimum capture of the accumulated damage.

Table 4.4 Composition of the alloys studied in wt.-% (Ni-base)

Name	Cr	Al	Ti	Fe	Nb	Co	Mn	Cu	Si	C	B	S
IN718	18.3	0.6	0.9	18.7	5.2	0.26	0.11	0.08	0.07	0.04	0.04	-

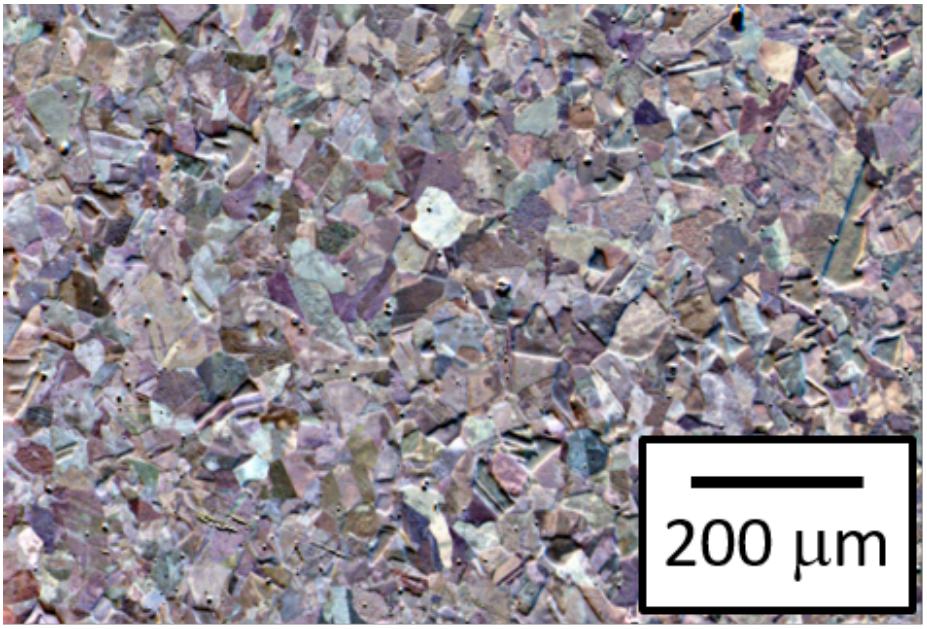


Fig. 4.4 Microstructure image of IN718 employed in this study.

4.2.5 Scanning electron microscopy analyses

Scanning electron microscopy (SEM) was also employed for *post mortem* analyses of the testpieces interrupted during the tensile loading experiment. Tensile specimens were sectioned at the middle position along the loading direction for *post mortem* characterisations. A Zeiss merlin field emission gun scanning electron microscopy (FEG-SEM) was operated at 15 kV to reveal the microstructural features. Multiple

electron images were collected using both secondary electron (SE) and backscattered electron (BSE) detectors for topographical and compositional contrast.

4.3 Results

4.3.1 High temperature tensile experiment for *in situ* XCT

Figure 4.5 and Figure 4.6 show the true strain - true stress curve obtained during the tensile tests at 800 °C. These are the results for the strain rate of 10^{-2} and 10^{-4} s^{-1}, respectively. For XCT observation in each tensile test, two different procedures were applied (fig. 4.1). XCT observation in the case of Interrupt 2 was commenced after the engineering stress was dropped. This is because it was confirmed in our previous work that the damage started growing during the tensile loading after the stress reached the maximum point [167]. While capturing XCT images, the displacement along the tensile axis needs to be fixed then the tensile stress applied to the testpiece was relaxed and decreased. In Interrupt 1, relaxed stress was remained in a certain range; 200 - 600 MPa at 10^{-2} s^{-1} and 100 - 300 MPa at 10^{-4} s^{-1}. Thus, higher stress applied in these steps obviously affected the stress-strain curve and the measured strength exhibited much weaker than the monotonic loading case. The stress-strain curve could change among the different specimens, but for Interrupt 2, both strain rates showed consistent mechanical properties with those obtained during the monotonic loading. These results indicate that the XCT rotation should be operated after removing the applied stress to avoid further damage during the XCT observation.

Another point that should be considered is the time utilised for capturing X-ray backprojections. For each XCT step, accomplishing X-ray backprojections for whole angles required 40 - 60 minutes in the applied lab-scale XCT system. Since Interrupt 1

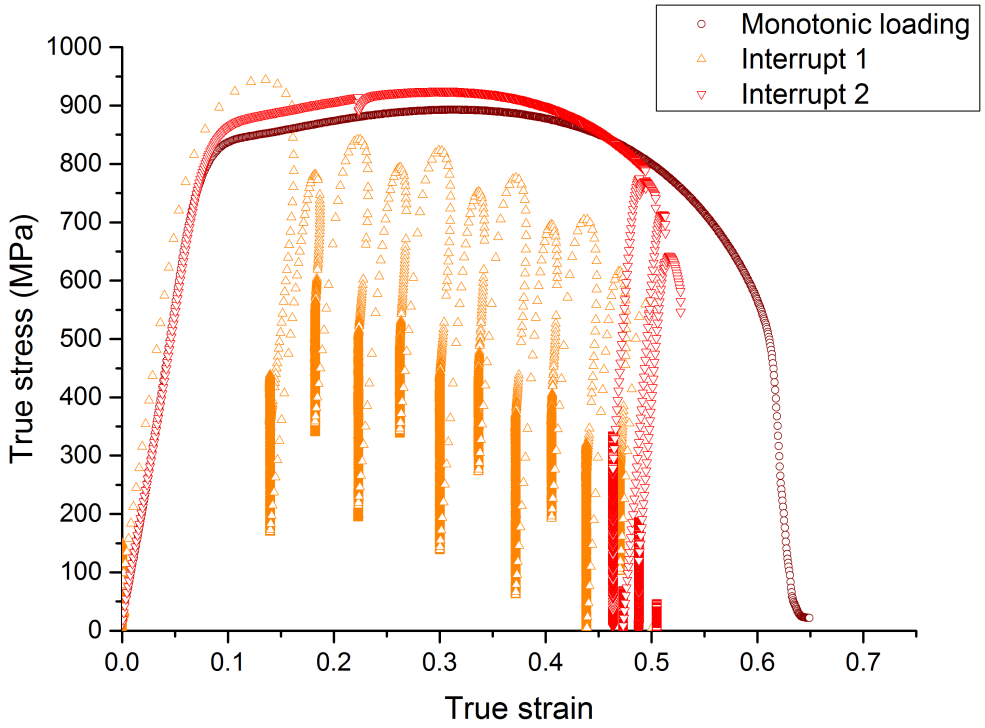


Fig. 4.5 True strain - true stress curve at 10^{-2} s^{-1}. Monotonic loading: Without XCT steps, Interrupt 1: With XCT steps without removing the load before rotation, Interrupt 2: With XCT steps with removing the load before roation.

included much more XCT rotation steps than Interrupt 2, Interrupt 1 required 15 - 20 hours for the whole *in situ* XCT observation, which might have caused the different stress-strain curves from the monotonic loading. If the *in situ* XCT observation was focused on the damage growing, the XCT steps could be limited after the maximum engineering stress to reduce the experiment time. In the slower strain rate (10^{-4} s^{-1}), Interrupt 1 showed higher fractured strain than monotonic loading, whilst Interrupt 2 and monotonic loading case was quite close in the mechanical properties.

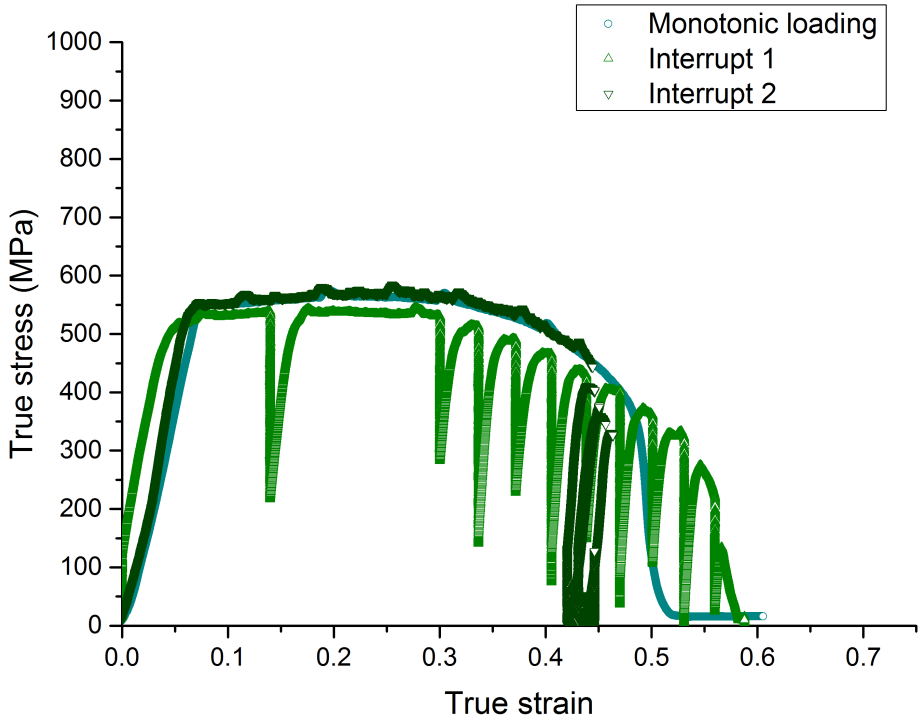


Fig. 4.6 True strain - true stress curve at 10^{-4} s^{-1}. Monotonic loading: Without XCT steps, Interrupt 1: With XCT steps without removing the load before rotation, Interrupt 2: With XCT steps with removing the load before roation.

4.3.2 SEM analyses of the interrupted testpieces

Figure 4.7 depicted microstructures observed by scanning electron microscopy (SEM) of interrupted testpieces during the tensile test at 10^{-2} s^{-1} and 10^{-4} s^{-1}. Even at $\varepsilon = 1.33$ (fig. 4.7(a)(d)), the testpiece deformed at higher strain rate showed fewer number of grown voids. The slowly deformed testpieces (fig. 4.7(b)(c)(e) (f)(h)(i)), on the other hand, possessed grown voids before fracture. Many of these voids were observed on bright second particles (Nb carbides), especially in the case of 10^{-4} s^{-1}.

With strain increment, those voids were enlarged in the necking zone. At $\varepsilon = 0.97$ (fig. 4.7(c)(f)), especially in the minimum cross-section of the necked part, the voids and cavities were grown as much as 20 - 50 μm, which could be observed by *in situ*

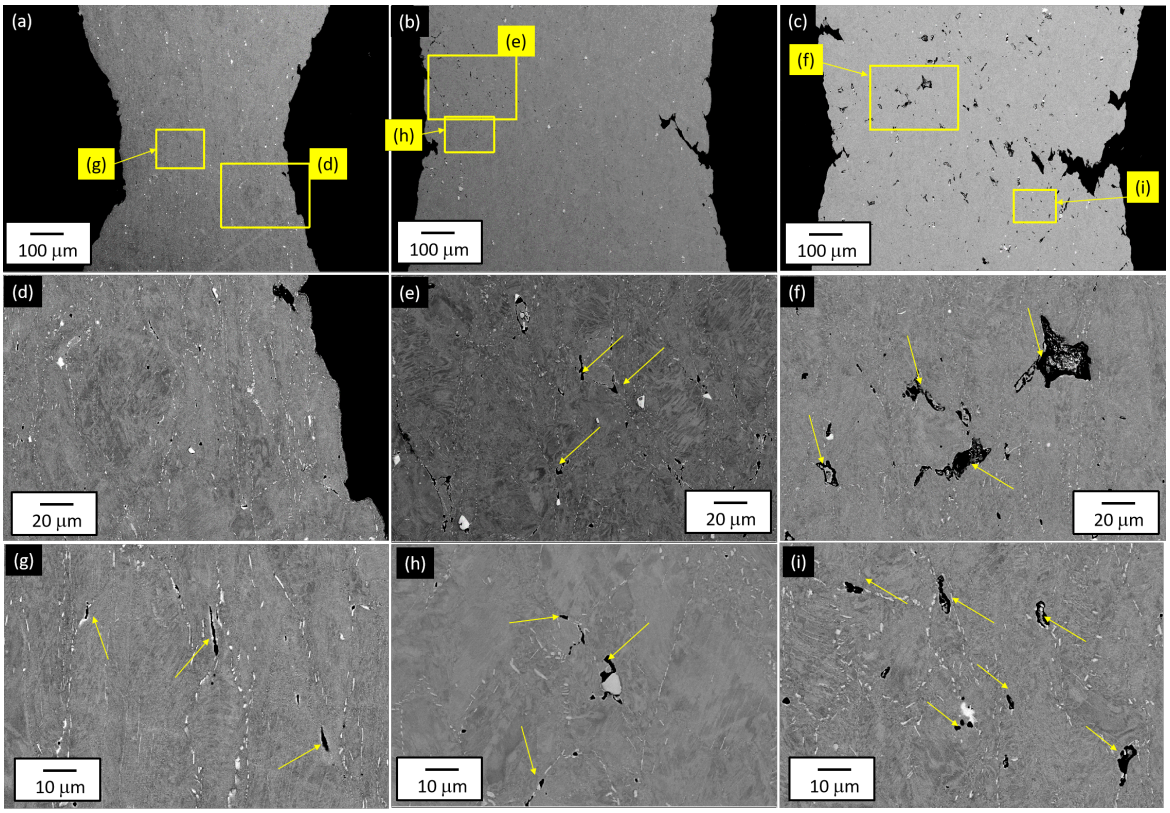


Fig. 4.7 Cross-section microstructure images after the tensile experiment at 10^{-2} s^{-1} ((a),(d), (g) : $\varepsilon = 1.33$) and at 10^{-4} s^{-1} ((b),(e), (h) : $\varepsilon = 0.90$, (c),(f), (i) : $\varepsilon = 0.97$. (d)-(i) are magnified images from (a), (b), and (c), respectively.) Grown voids are marked with arrows.

XCT. The tested pieces at 10^{-4} s^{-1} also possessed surface cracks which inclined 40-45° against the tensile axis and had a zigzag shape.

4.3.3 *In situ* XCT observation

XCT image correction

From backprojection images obtained during *in situ* XCT observation at high temperature, XCT images were reconstructed with those pixel data after FFC was applied. This study's correcting procedures (BH and SR) used flat-field corrected XCT data as original images. Thus, the FFC image was named as the original image.

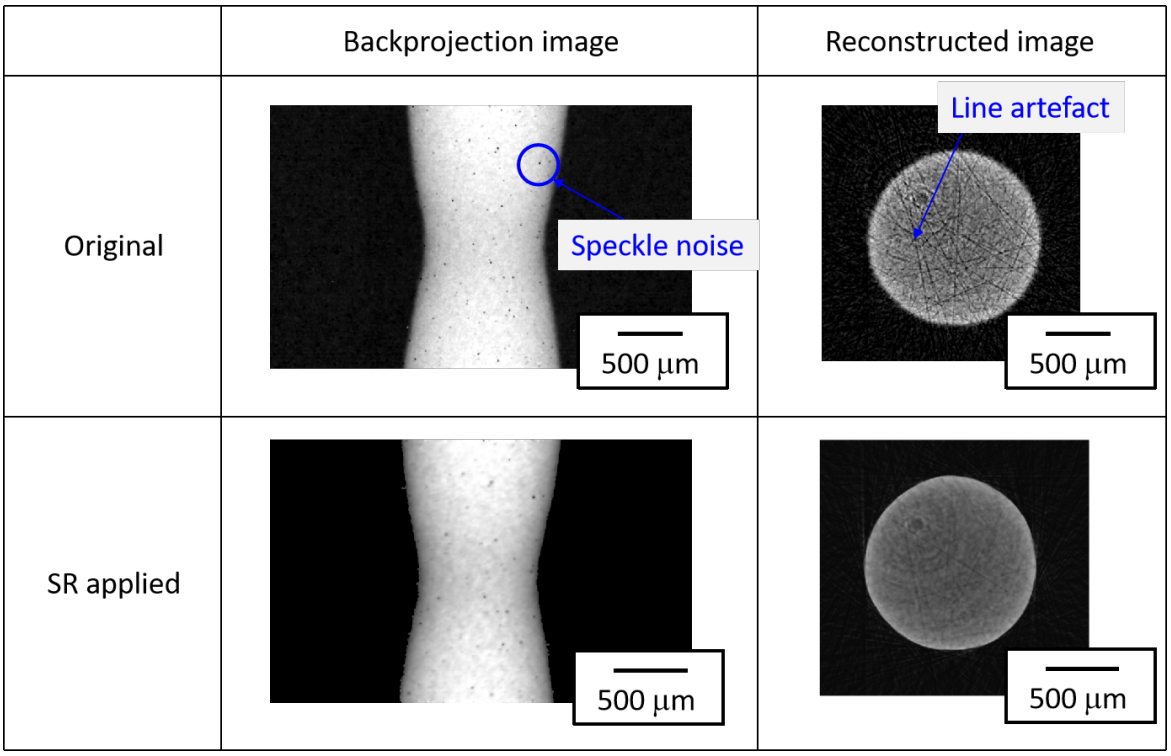


Fig. 4.8 Backprojection images and XCT reconstructed images obtained during high temperature tensile loading before and after speckle-removing correction (SR) applied.

Figure 4.8 shows backprojection and reconstructed images before and after the SR correcting process is applied. Backprojection with speckle noises caused line artefact in reconstructed images, but SR used backprojection images (dark speckle with less than 10 pixels were smoothed) offered reconstructed images with line artefact reduced.

In this study, BH correcting processes were also applied for the quantitative damage analyses from XCT images (fig. 4.9). Without BH correction, the reconstructed images included a dark part in the centre part of the object. The intensity profiles of the cross-section for each corrected image (the cross-section lines were described in fig. 4.9(a)-(d)) were compared in fig. 4.10. The maximum intensity would be displayed as 65536. In the original profile ("Original"), the intensities severely fluctuated, and the intensity value hardly distinguished the defects from artefacts. The fluctuated noises decreased after the speckles were removed ("SR"). However, the intensity difference

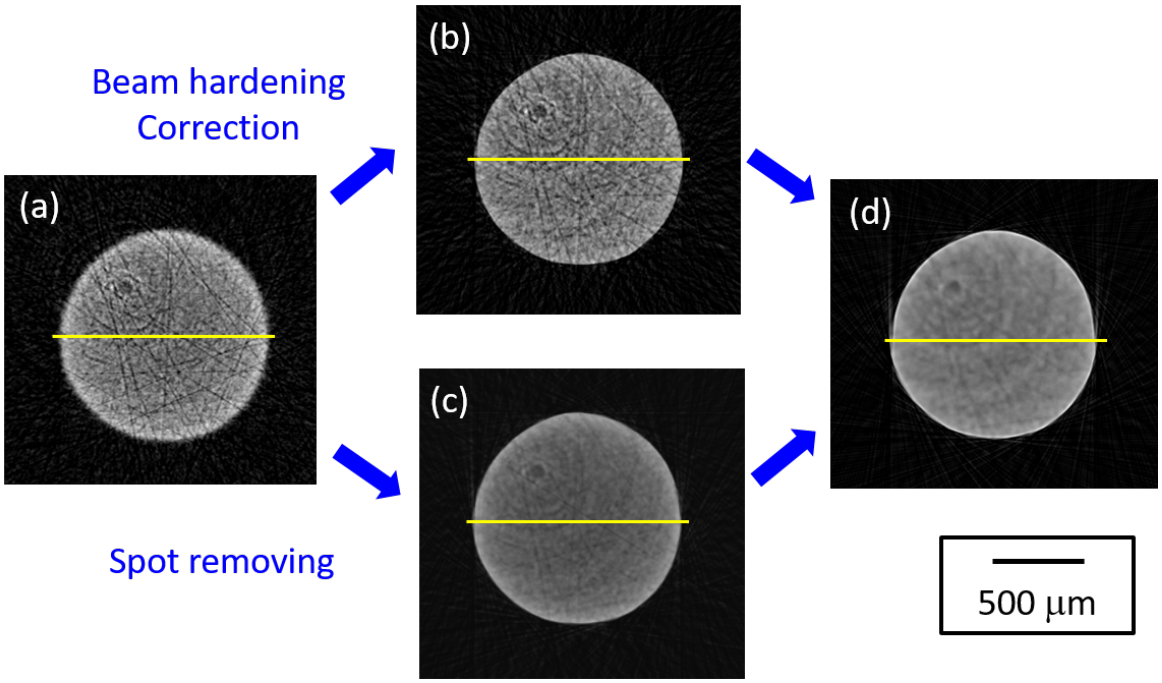


Fig. 4.9 XCT reconstructed images obtained during high temperature tensile loading with (a) flat-field correction (FFC), (b) beam-hardening correction (BHC), (c) speckle-removing correction (SR), and (d) both (b) and (c) (BHC+SR) applied.

between the outer part and inner part of the object still exhibited higher than the inner part intensity. This feature was reported in several literatures ([170], [169]), which also employed poly-energetic X-ray source. In the case of beam-hardening correction applied ("BHC", "BHC+SR"), the intensity profiles were homogeneous compared to the other cases. "BHC+SR" minimised the intensity fluctuations by removing both the beam hardening effect and line artefact noises.

Applying both BH- and SR- correction, the reconstructed XCT image became more suitable for quantitative research on the void distribution. fig. 4.11 shows (a) the original image and (b) the corrected image for the results of *in situ* damage observation at 10^{-3} s^{-1} under 800°C. The small voids (approx. 30 μm) were clearly distinguished from the artefacts after the corrections discussed above. The line figures described the reconstructed images' intensity profiles along the path (a-b). A certain intensity value

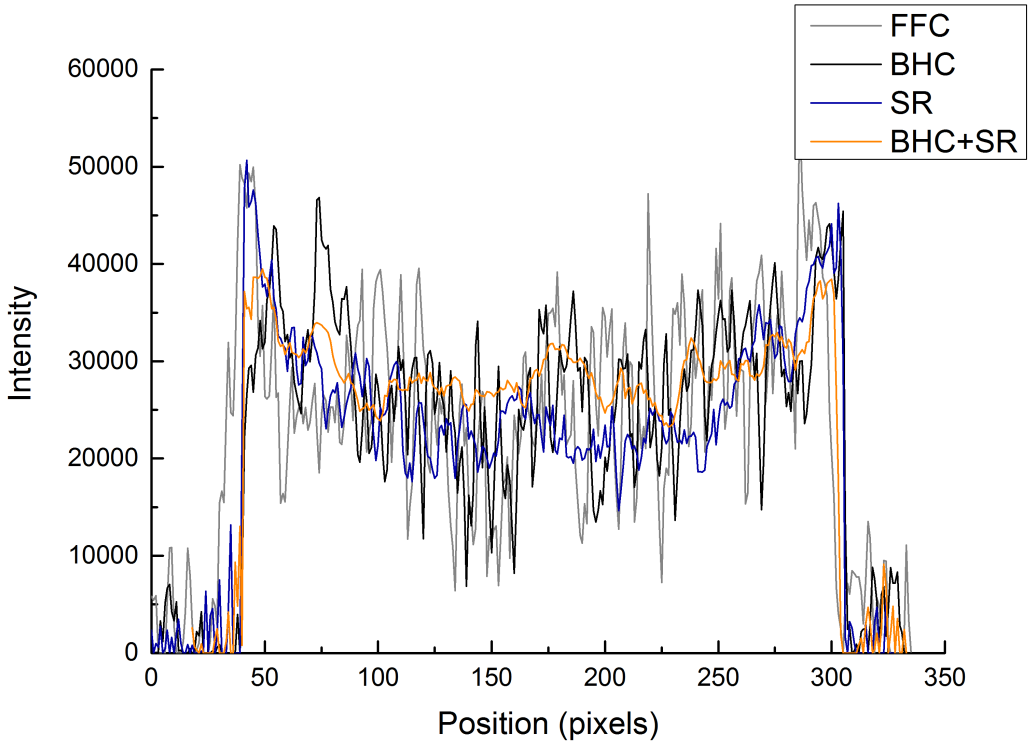


Fig. 4.10 Intensity profiles across the lines described in Fig. 4.9.

needs to be set as a threshold to distinguish defects or damages from artefacts in the sliced images. In that sense, it would be difficult to observe the defects or damages in the original image (a) using the threshold. The original image exhibited the fluctuated intensity with 10000 - 12000 units along the path. Furthermore, the outer part intensity in the sliced image was 50000, twice as much as the centre part. This indicated that the defects in the outer part would not be detected unless the defects would reduce the intensity by more than half and be recognised as black parts. Compared to the original method, those fluctuations were limited in intensity in the corrected image (b) and would not affect capturing defects or damage in the images. In the intensity profile (a-b), the defects around 80 pixels and 240 pixels in position were clearly identified if the threshold intensity were set around 20000. Although the intensity of the outer

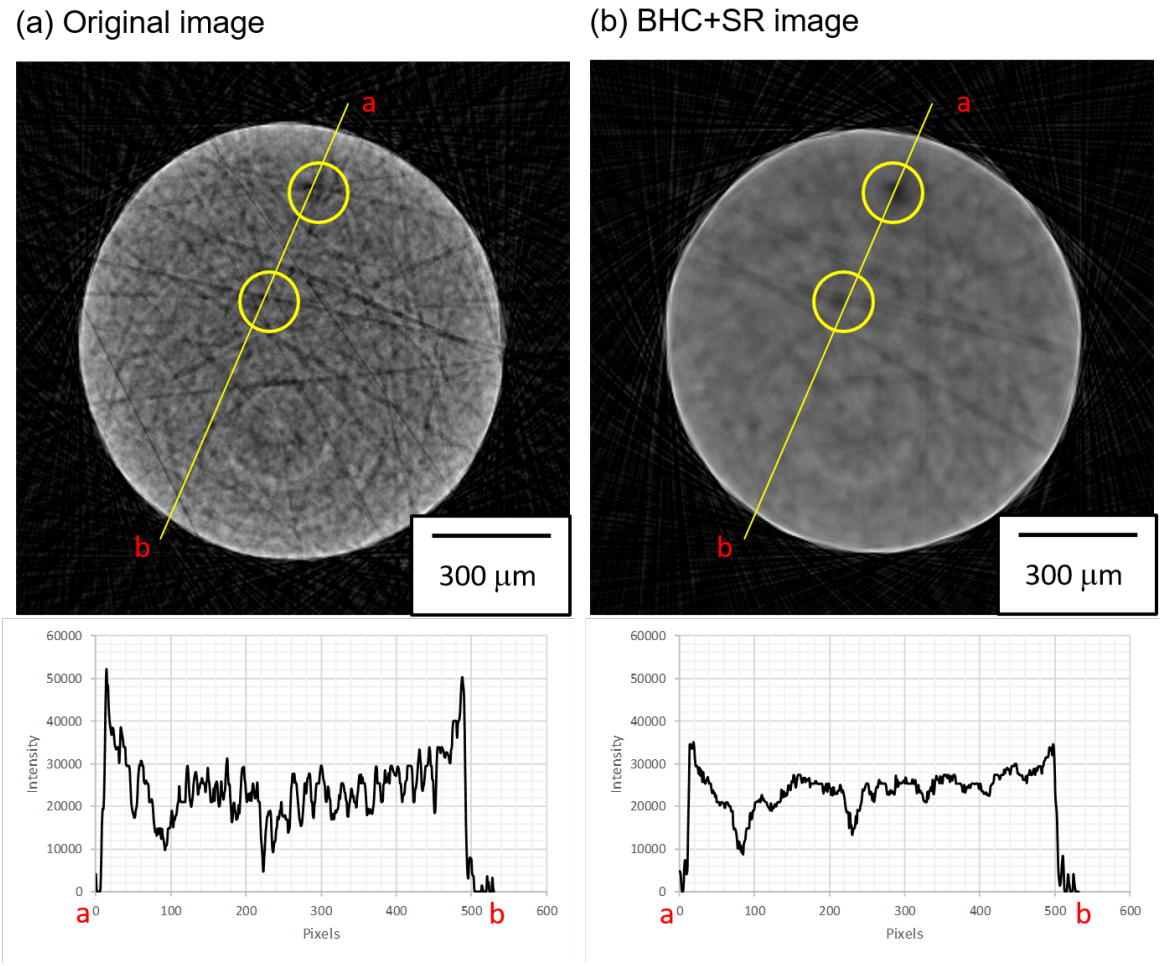


Fig. 4.11 An example of the *in situ* XCT image with (a) FFC and (b) BHC+SR applied. Detected voids in the BHC+SR applied image (b) are marked with circles.

part exhibited slightly higher than the centre part, those intensity differences could hardly affect capturing damage in the specimen surface.

Figure 4.12 is the example of XCT image obtained by *post mortem* and by *in situ* for the same interrupted testpiece during tensile loading at 10^{-4} s^{-1}. The *post mortem* image was captured for the testpiece removed from the loading machine when the strain reached $\varepsilon = 0.9$ after the *in situ* XCT was imaged. The *post mortem* image was detected under room temperature and with an X-ray detector set closed to the testpiece and produced a high resolved image. Compared to these images, it was confirmed that

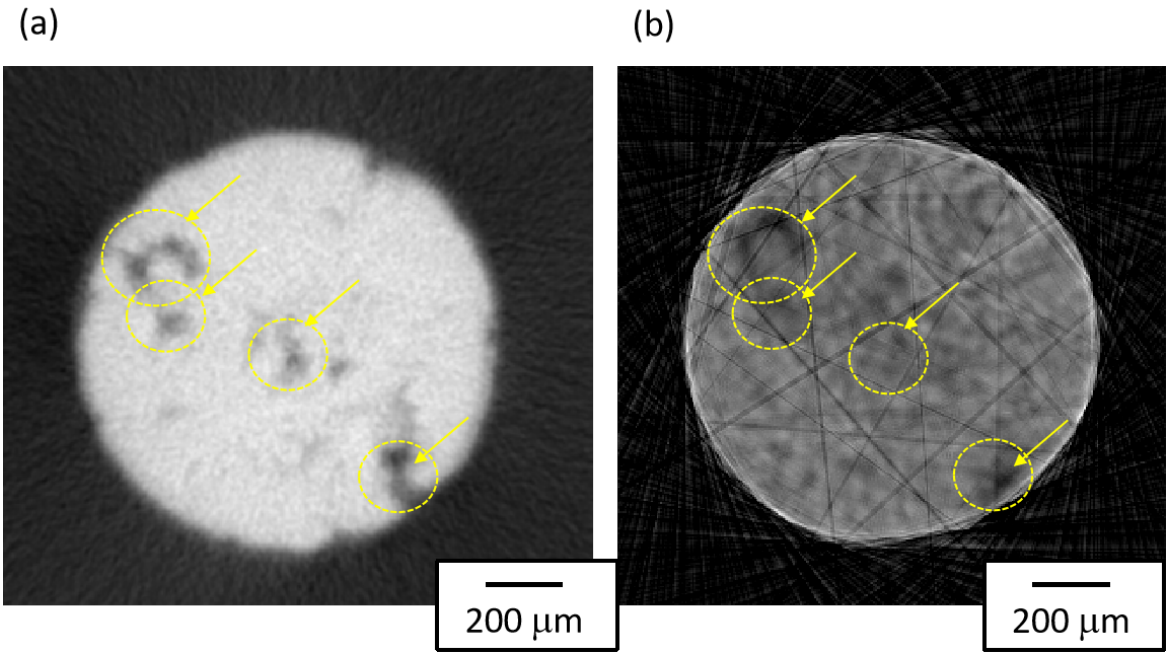


Fig. 4.12 XCT image of the interrupted testpiece (IN718) during 800 °C tensile test at 10^{-4} s^{-1} obtained by (a) *post mortem* and by (b) *in situ*. Detected voids are marked with arrows.

small voids from the size of 30 μm were detected in the *in situ* XCT system, which shows the image resolution obtained with the introduced post-processing methods.

In situ **XCT images during tensile deformation**

Figure 4.13 and Figure 4.14 are the sequential *in situ* XCT images obtained during tensile loading. The true strains described in these figures were calculated from obtained XCT images of necked part. The stress-strain curves at 10^{-4} s^{-1} and at 10^{-2} s^{-1} are shown in fig. 4.6 and fig. 4.5, respectively. The 'Interrupt 2' XCT images include less number of noises, which enabled to identify the defects more clearly from artefacts or noises. But generally at 10^{-4} s^{-1}, in both methods, voids were grown similarly and caused fracture.

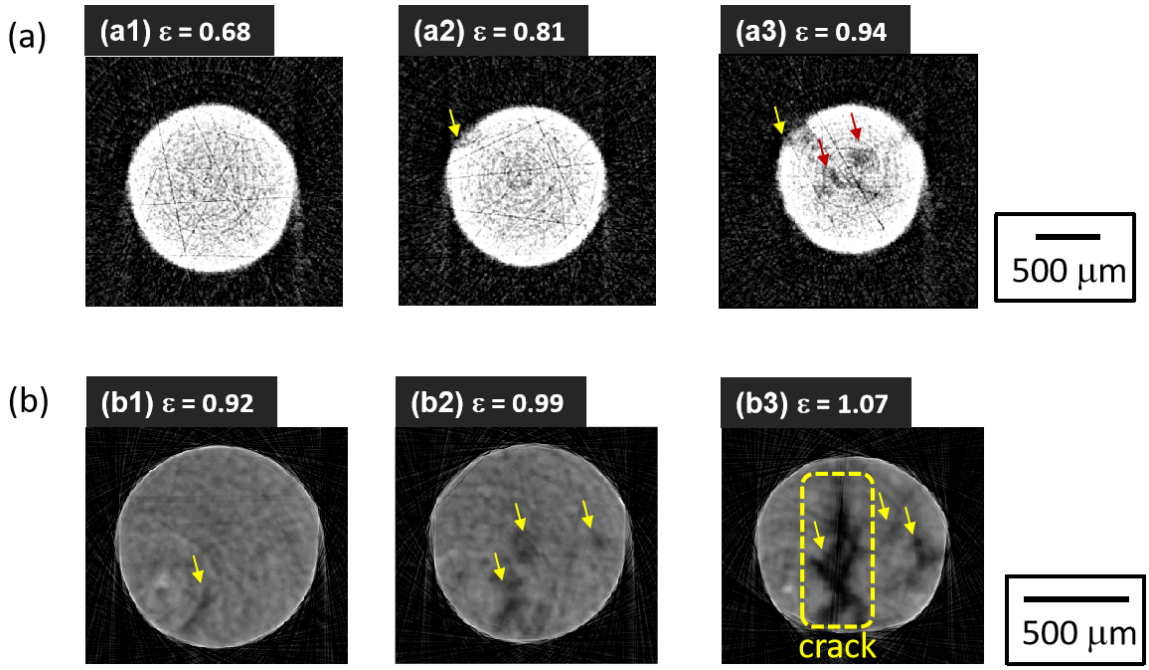


Fig. 4.13 *In situ* XCT images sequentially captured during tensile loading at 10^{-4} s^{-1} (800 °C) by (a) Interrupt1 method ((a1) $\varepsilon = 0.68$, (a2) $\varepsilon = 0.81$, (a3) $\varepsilon = 0.94$) and (b) Interrupt2 method ((b1) $\varepsilon = 0.92$, (b2) $\varepsilon = 0.99$, (b3) $\varepsilon = 1.07$). Voids and cracks are marked with arrows.

On the other hand, at 10^{-2} s^{-1}, the damages in 'Interrupt 1' and 'Interrupt 2' are observed differently. 'Interrupt 1' showed some voids before fracture, but 'Interrupt 2' did not exhibit any voids or defects. 'Interrupt 2' showed a smaller cross-section area than 'Interrupt 1' or the case of slower strain rate, which indicates that the 10^{-2} s^{-1} case showed more severe necking than those conditions. The ductile fracture without void growth enhanced the necking behaviour.

Void fraction of tensile deformed testpieces at several strain rates

The XCT image analyses detected voids or defects generated during the tensile deformation. It is difficult to determine whether the void formation or the necking comes first from the studies. However, this *in situ* XCT analysis enables us to follow the changes of void size and distribution and necking profile from the same testpiece. Later,

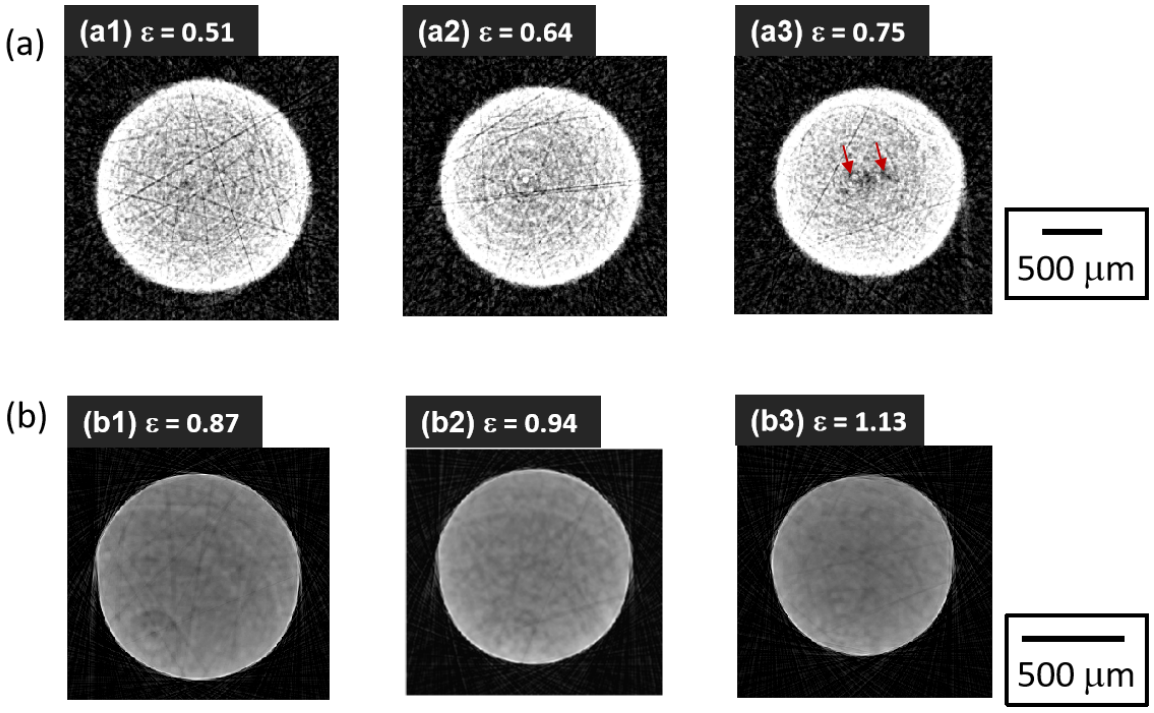


Fig. 4.14 *In situ* XCT images sequentially captured during tensile loading at 10^{-2} s^{-1} (800 °C) by (a) Interrupt1 method ((a1) $\varepsilon = 0.51$, (a2) $\varepsilon = 0.64$, (a3) $\varepsilon = 0.75$) and (b) Interrupt2 method ((b1) $\varepsilon = 0.87$, (b2) $\varepsilon = 0.94$, (b3) $\varepsilon = 1.13$). Voids are marked with arrows.

it will be discussed how the voids were grown by the strain rates and the stress state due to the necking profiles. Plots shown in fig. 4.15 showed the examples of the testpiece necking profile and defect sizes or distribution inside the testpiece. The radius of the sliced round bar and grown void volume inside the necked part plotted along the tensile direction. Horizontal coordinate indicates the position along the tensile axis of the specimen, and the plots for the cross-sectional radius and the void volume were located against this axial position. Each sliced area was regarded as a circle shape, so the radius value was estimated from the cross-sectional testpiece area in each of the sliced images. The minimum radius indicates the necking part after the ductile deformation, whose position also showed a high volume of the defect or void especially for the case of lower strain rate (fig. 4.15(a)). The figure shows that the void was grown inside the specimen differently against the strain rates. Since the different strain rates

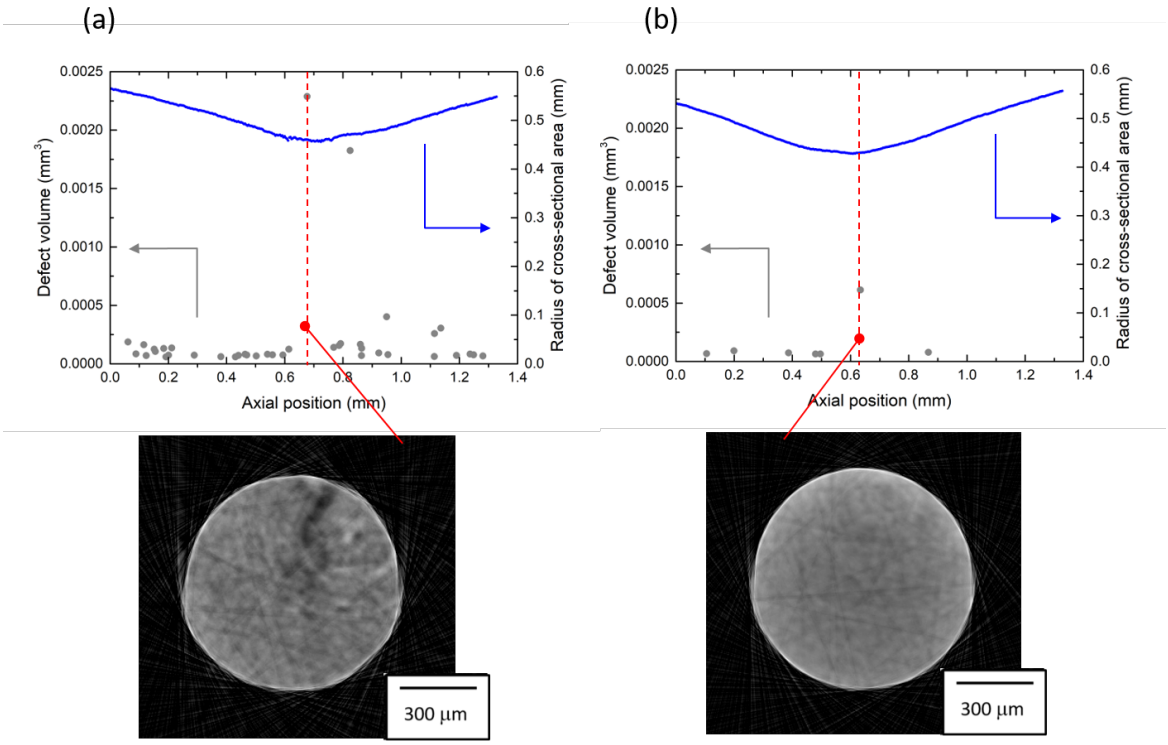


Fig. 4.15 Examples of calculated values of the radius of sliced specimen and void volume along the axial position ((a) : 10^{-4} s^{-1}, $\varepsilon = 0.99$, (b) : 10^{-2} s^{-1}, $\varepsilon = 1.12$).

induced the other necking behaviour, which might have affected the stress triaxiality before fracture, this void volume was compared with the stress state in each deforming condition. The employed true strain values in the following section will be calculated from the necked part XCT images.

Effect of stress triaxiality during necking

Figure 4.16 shows the curvature radius plotted against the minimum radius of cross-sectional area calculated from each XCT image of deformed testpieces until fracture at a strain rate of 10^{-4} to 10^{-2} s^{-1}. This figure indicates that the heavily necked testpiece also exhibited a small necking curvature. Although a higher strain rate (10^{-2} s^{-1}) induced a smaller necking radius than a lower strain rate, the correlation between

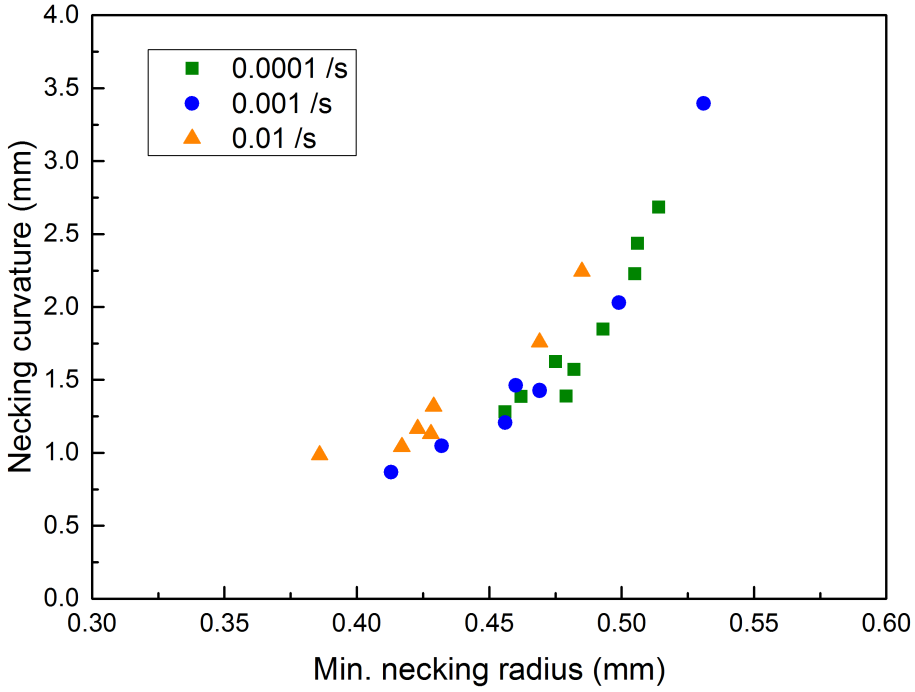


Fig. 4.16 Minimum radius of the cross-sectional area and curvature radius at the necked region calculated from XCT images.

these two necking parameters was similar among the applied strain rate range in this experiment.

The obtained R and minimum necking radius (cross-sectional radius) a were used to calculate stress triaxiality by equation (4.5). Fig. 4.18 shows the correlation between these two parameters. For each strain step, the calculated triaxiality and the size of grown voids or defects were also compared in fig. 4.17.

As shown in fig. 4.18, the fractured strain plots for 10^{-3} s^{-1} and 10^{-4} s^{-1} were lower than those for 10^{-2} s^{-1} at the same stress triaxiality level. The plots for 10^{-3} s^{-1} and 10^{-4} s^{-1} were on the similar trends between the triaxiality and true strain. The reason why the deformed testpieces at 10^{-2} s^{-1} remained being strained even at high stress triaxiality can be assumed from the results shown in fig. 4.17. Compared to

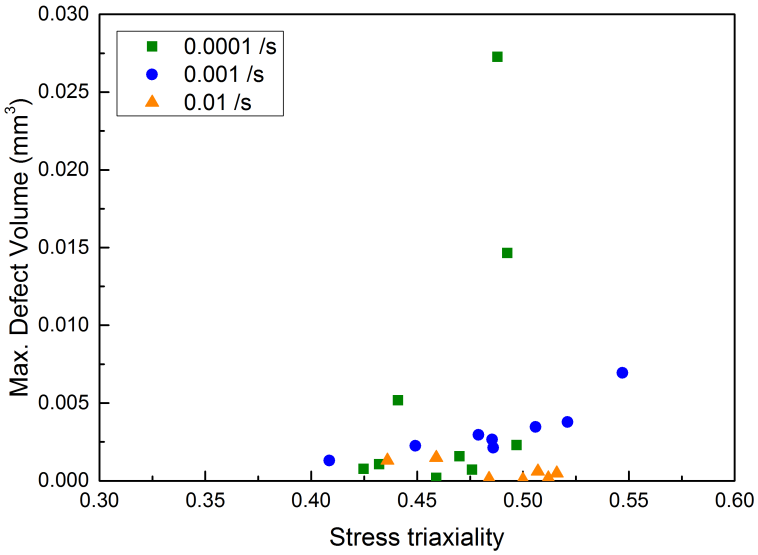


Fig. 4.17 Stress triaxiality and maximum defect size inside the necked region.

10^{-3} s^{-1} or 10^{-4} s^{-1}, the deformed testpieces at 10^{-2} s^{-1} obviously exhibited less size and amounts of defects. The difference of grown void size between higher and lower strain rates was also observed from the SEM analyses in fig. 4.7. It is indicated that the void growth and coalescence in slower strained testpieces lowered fracture strain.

In situ XCT observation during creep test

Similarly, during creep loading, the sequential damage growth and deformation behaviour were captured by *in situ* XCT at 800°C. Figure 4.19 describes the obtained creep strain curve in this experiment. In this observation, the transition of the creep strain rate from the second stage to the third stage triggered the *in situ* XCT algorithm to start capturing back-projection images by rotating the testpiece. As shown in fig. 4.19, after transiting to the third stage, the strain curve showed the sudden drop followed by constant strain value, which indicates that the rotation for XCT was carried out after the tensile loading was removed. During this step, *in situ* observations were

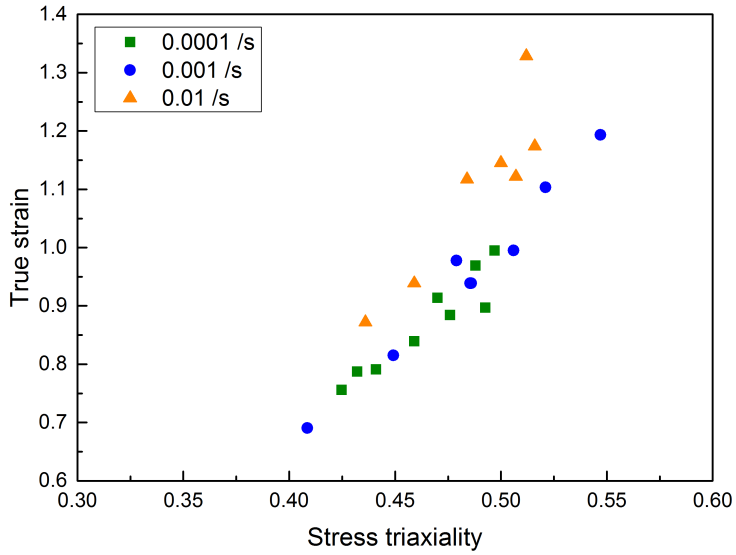


Fig. 4.18 Stress triaxiality and true strain obtained from Fig. 4.16.

successfully implemented with the testpiece displacement remaining constant at the certain creep strain level as described in the 'Interrupt2' method in tensile loading experiments. Fig. 4.20 shows the XCT sliced images obtained by *in situ* after reached $\varepsilon = 0.3$ under 566 MPa and $\varepsilon = 0.27$ under 480 MPa. These are the last *in situ* XCT images before fracture. Under 566 MPa loading at 800 °C, the grown creep voids in IN718 were not detected as clearly as under 480 MPa. The time required for the creep fracture could be estimated by excluding the time for XCT rotation during these experiments. Under 480 MPa and 566 MPa, the testpiece was fractured after 18 hours and 3.3 hours, respectively.

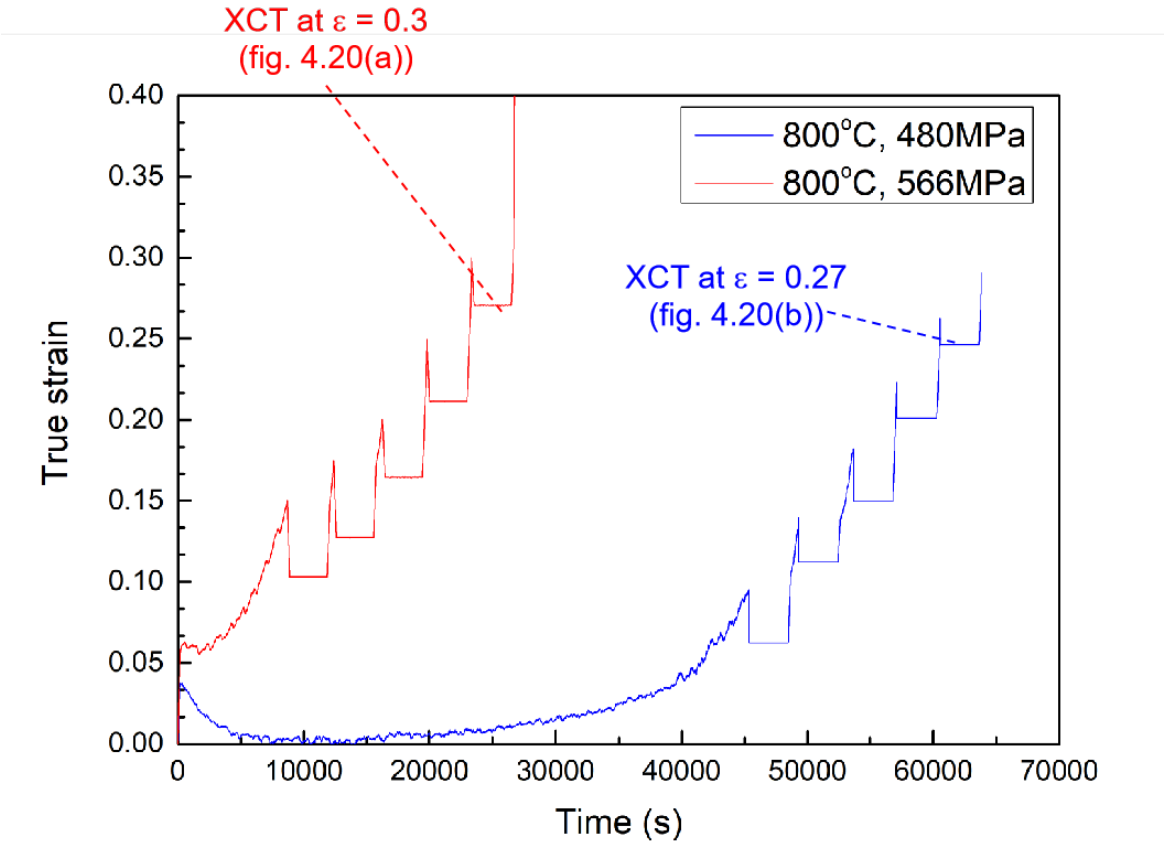


Fig. 4.19 True strain curve of IN718 under creep loading of 566 MPa and 480 MPa at 800°C.

4.4 Discussion

4.4.1 Post-processing method for *in situ* XCT images

The BHC and SR combined method offered highly resolved XCT images even under high temperatures compared to the previous work. It is obviously confirmed from sequentially obtained *in situ* XCT (*e.g.* fig. 4.13). Beam-hardening effect induces higher intensity in the outer part or rims of the cross-section for the employed superalloy, but the corrected images flattened that intensity in the whole section. As the intensity values were included within 25000 - 40000 in the whole cross-section, the defects that could be identified with the threshold around 20000 in intensity were now observed in

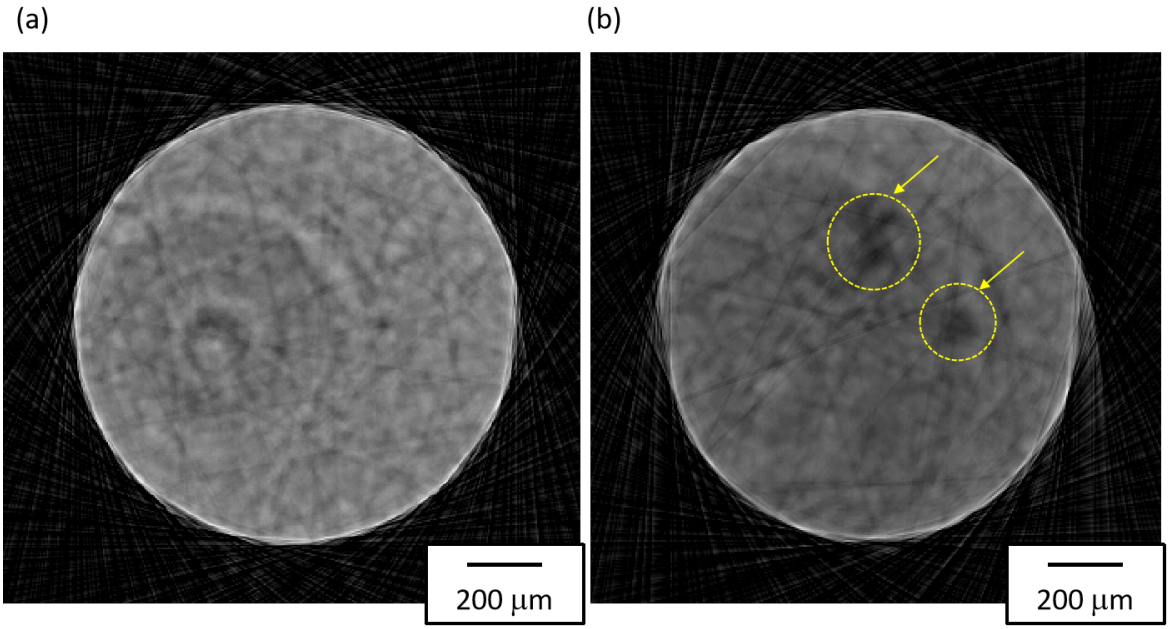


Fig. 4.20 *In situ* XCT image of IN718 obtained at (a) $\varepsilon = 0.3$ under 566 MPa and at (b) $\varepsilon = 0.27$ under 480 MPa during the creep test in 800°C. Detected grown voids are marked with arrows.

the whole section. Furthermore, this image correction made it possible to quantitatively analyse the defect size and distribution against the loading direction. As the diameter of the testpiece would be different along this direction, one could not count the defect area by clarifying with the same threshold value for each section. This is because the Beam-hardening effect would more severely affect the thicker metal part due to its attenuation effect [173][174]. Especially for necked testpieces, it is important to discuss the distribution of voids or defects or their growing behaviour against the different parts in diameter. The devised image correction method offered sufficient resolution of XCT images to follow the growth of defects.

4.4.2 Damage during the tensile deformation

For the ductile fracture, many of the reports suggested that the stress triaxiality affected damage growth and the fractured strain [175][176]. Teng and Wierzbicki [177]

introduced two basic failure mechanisms: void growth and shear decohesion, which were based on the assumption that the material includes nucleated voids from the beginning of the deformation process. Barsoum et al. [178][179] demonstrated that these mechanisms could be described as failure by intervoid necking and intervoid shearing. However, since those voids were not always nucleated at the early stage of the deformation [180], Noell et al.[49] proposed the damage models in a wider prospect that seven different mechanisms can control the ductile fracture and these mechanisms act in concert or compete for each other during the damage growth. The seven mechanisms consist of intervoid necking, intervoid shearing, void sheeting, the Orowan alternating slip, necking to a point, single-plane catastrophic shear, and multi-plane catastrophic shear. The ductile damage can be grown depending on the stress triaxiality state. If the triaxiality is more than 1/3, the damage growth tends to select 'intervoid necking' or 'necking to a point'. According to the report, the damage growth with void nucleation, growth, and coalescence would choose 'intervoid necking', whilst void-free rupture would follow 'Necking to a point'. In this work, the stress triaxialities after the damage growth started were calculated as higher than 1/3. At 10^{-4} and 10^{-3} s^{-1}, the void growth was observed, but no void was captured at 10^{-2} s^{-1} rate until the testpiece ruptured. The fracturing testpiece at 10^{-2} s^{-1} exhibited more severe necking than the slower strain rates, which was consistent with the damage type described above. In this study, under 800°C, it was confirmed that 10^{-2} s^{-1} induced 'necking to a point' type rupture, whilst 10^{-4} and 10^{-3} s^{-1} followed 'intervoid necking'.

Noell et al. discussed the competition between void-based (intervoid necking) and void-free (necking to a point) fracture mechanisms depending on microstructure, but the results in our work showed strain rates also affected void-based or void-free fracture. Void nucleation sites were often compared with the distribution of second-phase particles [181][182] or sometimes thought to be related to deformation-induced

dislocation boundaries [183]. As shown in Fig. 4.7(d)-(i), since the higher strain rate induced plastic deformation, voids seemed to be nucleated by grain boundaries and independently on second particle distribution, whilst in the slower strain rate case, void growth was observed adjacent to second particles. As shown in Fig. 4.17, under the same stress triaxiality, voids tend to grow larger in the slower strain rate.

Under a uniaxial tension strain rate ($\dot{\varepsilon}$), considering that a spherical void of radius R_0, Rice and Tracey [175] stated that the incompressible velocity field could be split into three parts: (1) a velocity field resulting in a uniform strain rate, (2) a spherically symmetric velocity field regarding a volume change of the void without changing the shape, and (3) a velocity field which changes the void shape without changing its volume. Using the averaged radial velocity on the void boundary $\dot{R}$ under these velocity fields assumed, the damage growth rate D of the spherical void of radius R_0 can be expressed as,

$$D = \dot{R}/(\dot{\varepsilon} \cdot R_0) \tag{4.8}$$

They reported that it becomes larger with the stress triaxiality increase. To plot the damage growth data obtained in this work against the stress triaxiality, the D value in each strain rate was calculated from the void radius evaluated from the XCT images. (Note that $\dot{R}$ can be determined by the radius change and the time between two steps in which XCT was captured. 3 XCT steps would produce 2 data of $\dot{R}$ and a corresponding plot of D. The tensile test in which only the two XCT images were visualised would produce only one plot, and this evaluation need to be followed with the same testpiece.) Fig. 4.21 shows D parameter against the stress triaxiality which was re-calculated using the obtained results in this work (from Fig. 4.17 and Eq. 4.8). At the slower strain rate, D increased with the stress triaxiality similarly in the plot reported by Rice

and Tracey[175], however, with increasing the strain rate, this trend behaved differently. It can be estimated from the microstructure analyses in this work (Fig. 4.7) that under the higher strain rate, the voids tend to be nucleated in dislocation boundaries and the slower strain rate induced the void nucleation adjacent to the second particles. Since the nucleation site depends on the local dislocation density [184], the higher strain rate induced dispersed nucleation site due to the higher dislocation density than slower strain rate. On the other hand, diffusive chemical reactions at the slower strain rate affected the void nucleation and growth behaviour adjacent to second particles. It can also be assumed that the tensile stress was concentrated on the resulting voids, which caused the void growth under the high stress triaxiality. Under 800°C, at 10^{-3} s^{-1}, IN718 possessed both mechanisms for void nucleation and growth, which showed intermediate trends between 10^{-2} and 10^{-4} s^{-1} in triaxiality-D plots.

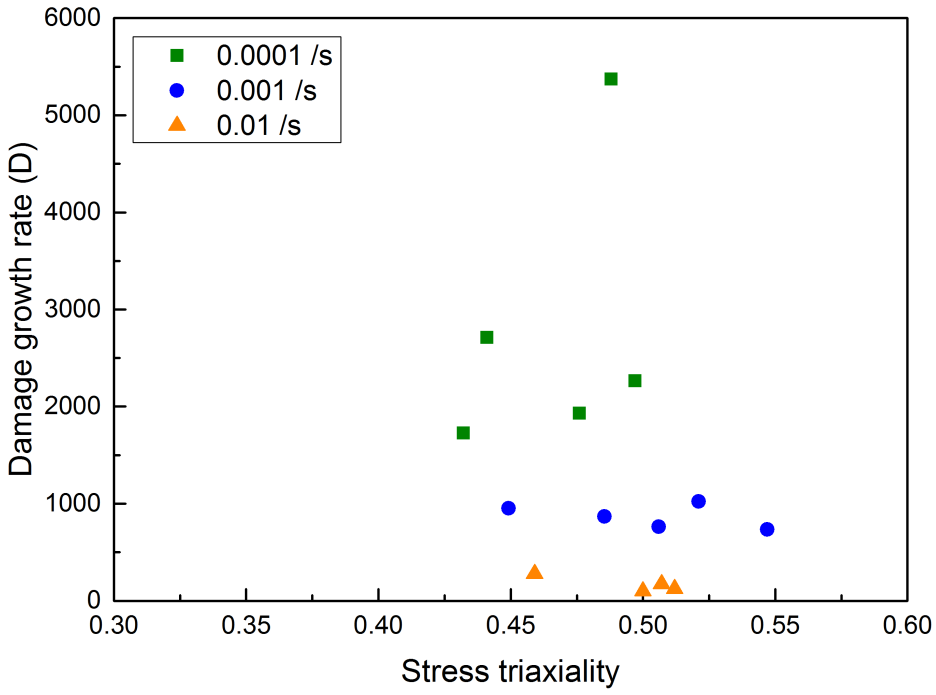


Fig. 4.21 Stress triaxiality and damage growth rate.

4.4.3 Damage generated due to XCT operation

In the *in situ* XCT observation in this study, the testpiece was rotated for capturing back-projection images under the axial loading removed. Compared to the stress applied during the rotation without the loading removed ('Interrupt 1' in fig. 4.5 or fig. 4.6), the rotation with the applied loading had some effect on decreasing the testpiece mechanical strength. As indicated in the 'Interrupt 1' results, since the loading was not removed in this case, during the XCT rotation, the testpiece experienced respectively 200 - 600 MPa and 100 - 300 MPa for 10^{-2} s^{-1} and 10^{-4} s^{-1} cases. The creep test results implied that 480 -566 MPa was sufficient loading for creep void growth and creep fracture in less than 18 hours. Considering the time required for the 'Interrupt 1' XCT procedure (up to 10 hours) and loading fluctuation during the XCT rotation within 200 - 600 MPa, one can assume that the creep voids were generated during the rotation step, which caused the following creep fracture. This can be presumed from the result that none of the 'Interrupt 2' at 10^{-2} s^{-1} exhibited void growth until its fracture, as the 'Interrupt 2' mode started XCT rotation after the loading was totally removed. It is now indicated that the 'Interrupt 2' method would be more suitable for the *in situ* damage observation during tensile deformation.

4.5 Summary and Conclusions

A laboratory-scale *in situ* XCT system is optimised, and postprocessing methods to reconstruct XCT images are described. Quantitatively, the method evaluates the damage growth arising in a nickel-based superalloy, IN718, during tensile and creep deformation at high temperatures. The following specific conclusions can be drawn from this study:

1. The improved mechanical procedure for *in situ* XCT observation has been developed for high temperature experiments, which succeeded in capturing void growth during tensile deformation along with the recorded stress-strain curve. Carefully removing the loading while rotating the testpiece limited the further damage due to this mechanical operation.

2. The newly developed post-processing method for tomography images employed the beam-hardening correction and spot-removing algorithm. The corrected images offered sufficient resolution, – approximately 30 μm –, to clarify the difference of void growth in the testpiece gauge during the tensile deformation among its strain rate.

3. The *in situ* observed XCT images succeeded in capturing the necking behaviour and the internal void growth during creep deformation at 800 °C. For the first time, the void growth during the third stage creep was captured by *in situ* at high temperature.

4. The *in situ* XCT during the tensile deformation at 800 °C clearly observed the difference of damage accumulation behaviour at 10^{-4} s^{-1} to 10^{-2} s^{-1}. Slower strain rate enhanced the ductile void growth, whilst higher strain rate induced the necking to a point fracture.

5. The stress state change of the testpiece during necking was calculated from the deformed profiles sequentially obtained by *in situ* XCT. Comparing them with the internal damage growth, under the high stress triaxiality, the ductile void growth was observed more at a slower strain rate than at a higher strain rate.

6. The devised *in situ* observation system could clarify the dominant damaging factors during tensile deformation, such as stress triaxiality, or loading time, from

the complicated damage growth at high temperature, which enables to predict of its fracture mode.

Chapter 5

In situ XCT and Acoustic Emission Diagnostics of High Temperature Deformation of Nickel-based Superalloy

Summary This study employs the laser-based Acoustic Emission (AE) technique to investigate AE behaviours during damage growth and plastic deformation in Ni-based superalloy at high temperatures. Laser Doppler Vibrometer (LDV) successfully enables to detection of AE signals from the testpiece surface vibration in a contactless manner during tensile and creep loading at 800°C, which simulates the service conditions inside the jet engine. In this research, *in situ* XCT is also applied to observe the damage growth inside the testpiece during such loading conditions to understand the mechanical effects on the induced AE characteristics. The quantitative AE and 3D XCT image analyses of deformation status and damage growth revealed that the plastic strain rate correlates with the amplitude and energy of generated elastic waves, and

the development of internal defects affect the AE median frequency. The present study offers a better understanding of detecting and predicting the damage growth and failure during the high-temperature loading experiment.

5.1 Introduction

In previous chapters, the developed *in situ* XCT system captured grown voids and surface cracks in the testpieces with tensile load applied at high temperatures. Post-processing detected these defects from the size of 30 - 50 μm by removing artificial noises. As the accompanied experimental arrangements such as the electric furnace and cooling systems work correctly up to 800°C and 10000 N loading, this system can be applied to on-time damage observation during any kinds of high temperature loading experiments within these temperature and loading ranges.

In this system, capturing XCT started by intentionally interrupting the loading procedure when the testpiece displacement exceeded the threshold value. However, it is quite challenging to precisely follow the growth of voids and cracks. In many cases, the first shot of *in situ* XCT captured huge grown damages, mainly because there are few means which can inform the initiation of these damages.

One possible tool for detecting damage initiation at high temperatures is a non-destructive testing method. Acoustic Emission (AE) has challenged to inform mechanical degradation by quantifying the acoustic signals which related to the damage status of the object materials (e.g. [115], [116]).

In most AE studies, the wave parameters, such as energy, frequency, and amplitude, were applied to quantitative analyses correlated with the size and mode of fracture or plastic deforming behaviours. The AE signals were normally detected *via* piezoelectric

ceramics (*e.g.* PZT (Lead zirconate titanate)) sensors which were directly attached to testpieces (*e.g.* [185] [186] [138]). PZT AE sensors are widely accepted, but there are some limitations of the attachable designs of testpieces and thermal conditions where these sensors are available [143]. Especially for high-temperature testing, the ceramics sensors must be attached apart from the deformed, fractured or heated part of the testpieces, which may affect the signal analyses. Therefore, quantitative AE analyses in high-temperature experiments are difficult using PZT sensors.

Recently, the Laser-Doppler vibrometer (LDV) method has been introduced to detect AE signals without sensors attached to the object surface. The LDV can capture the testpiece surface vibration as an AE signal feature by detecting Doppler shift in wavelength of reflected laser due to the surface velocity [187], [188]. This method overcame the difficulties with the PZT ceramics sensors. The detector can record the AE signals directly without obstacles between source and sensors and evaluate its quantitative parameters even from the object testpiece's deformed, fracturing or heated part.

This chapter employs the LDV method to detect AE signals from the object Ni-based superalloy during tensile and creep loading at high temperatures. The calculated AE wave parameters are correlated with the plastic deformation, the accumulated damage or defects during the high-temperature testing observed by *in situ* XCT system developed in previous chapters. Thus the AE signals are discussed as the damage growth indicator.

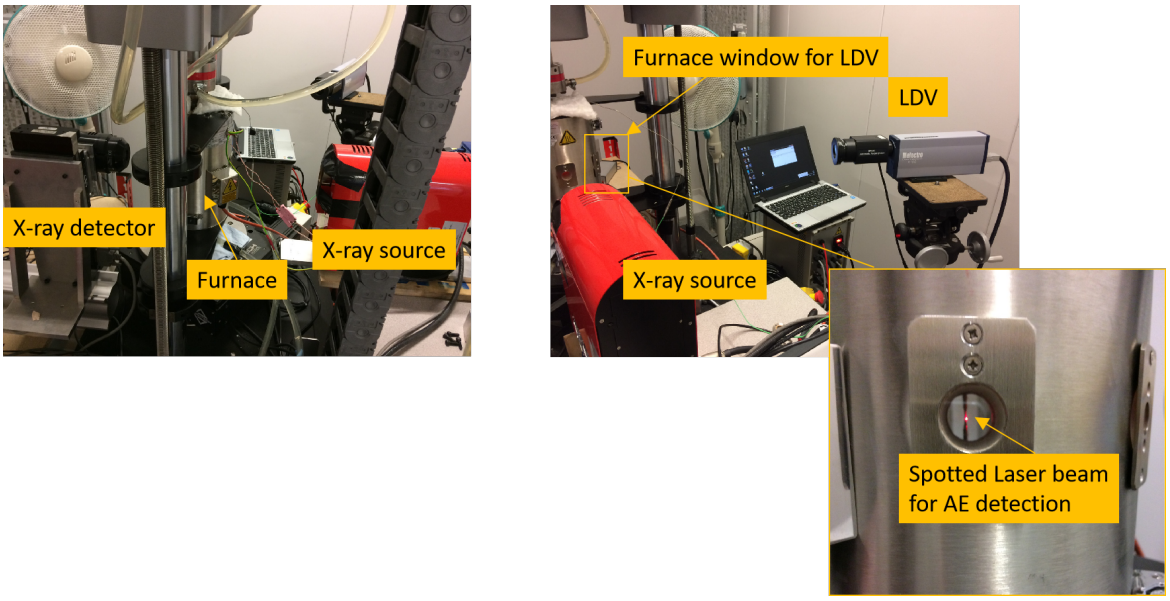


Fig. 5.1 Experimental setup of LDV and high-temperature XCT system. Laser beam from LDV was emitted and the reflected beam was observed through the furnace window.

5.2 Experimental Methods

5.2.1 Preparation for experiment

The employed LDV emitted a laser beam and detected the reflected laser from the object through the furnace window. Figure 5.1 described the LDV set-up placed with the high-temperature XCT system developed in chapters 3 and 4. The LDV system utilises the He-Ne laser to spot the object and captures the subtle variation of the reflected beam from the original. This variation can be generated in case the reflected energy was insufficient to compare with the original beam (Fig. 5.2(c)), in case the reflected signal included the radiant light (Fig. 5.2(d)), and in case the reflected signal experienced Doppler-shift due to the object surface vibration (Fig. 5.2(e)). To remove the false signal described in fig. 5.2(c) in this AE measurement, the LDV detecting direction was aligned with the right angle against the tensile axis so that the reflected

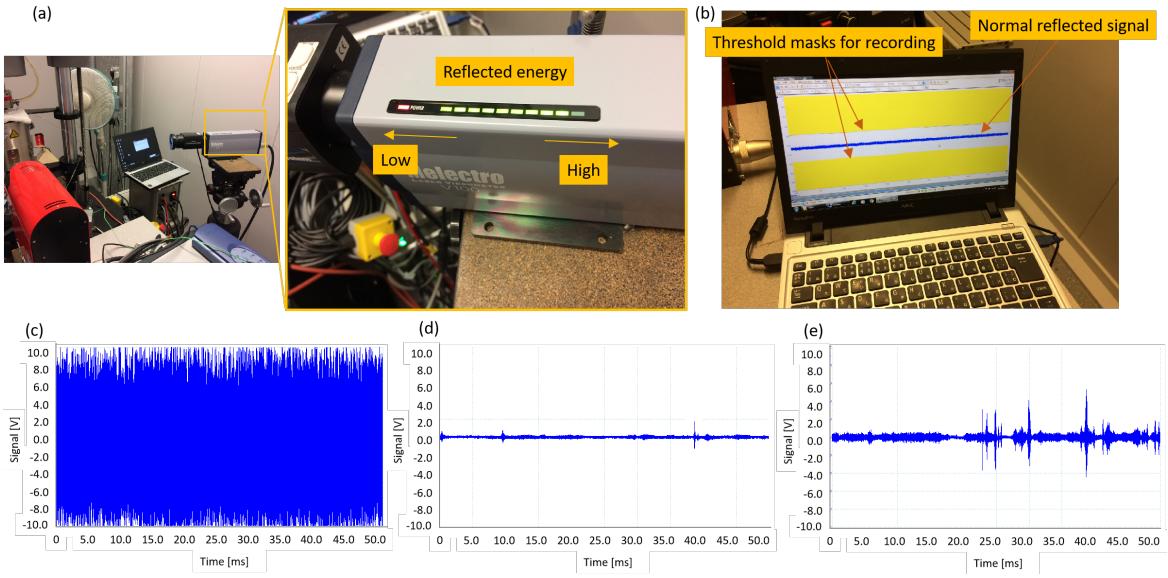


Fig. 5.2 (a) Detected laser energy indicator in the LDV machine (fig. 5.1), (b) a normal signal observed from the furnace window, (c) a false signal when the detected laser energy was insufficient, (d) a false signal due to the radiant light captured at high temperature, and (e) an example of detected signal with Doppler-shifted.

beam could be detected with sufficient energy (fig. 5.2(a)). Another false signal (fig. 5.2(d)) was unrecorded by setting the threshold. The preliminary experiment confirmed the false radiant light signals at 800°C was lower than 2[V] in this system. Thus, the signals with peaks of more than 2[V] were employed for the AE analyses in this study. A detected example of Doppler-shifted signal is illustrated in fig. 5.2(e). While in the experiment, any signals cannot be recorded unless the maximum amplitude exceeds the threshold (fig. 5.2(b)).

All of the raw signal data was recorded by the Picoscope 5000 system with the '.psdata' form. The '.psdata' form was converted to '.csv' to compute these data. The csv data were then applied for the Fast-Fourier transform (FFT) algorithm calculating in MATLAB to give a periodogram $G(f_k)$ for each pulse as follows:

$$G(f_k) = \frac{1}{f_c \cdot N}|V_k|^2 \tag{5.1}$$

$$V_k = \sum_{n=0}^{N-1} V_n exp(-i\frac{2\pi kn}{N}) \tag{5.2}$$

where f_c is a maximum frequency of analysis (900kHz in this study), determined by the following equation,

$$f_c = \frac{1}{2} \cdot \frac{1}{\Delta\tau_s} \tag{5.3}$$

with the sampling interval $\Delta\tau_s$. The factor $\frac{1}{2}$ is used for eliminating the aliasing errors as described in other works [123]. $G(f_k)$ is the power spectral density function for the frequency f_k which is utilised for AE parameter calculation in the following sections. The examples of colour contour maps of detected AE signals were illustrated in figure 5.3. The contour figure indicates the value of $G(f)$.

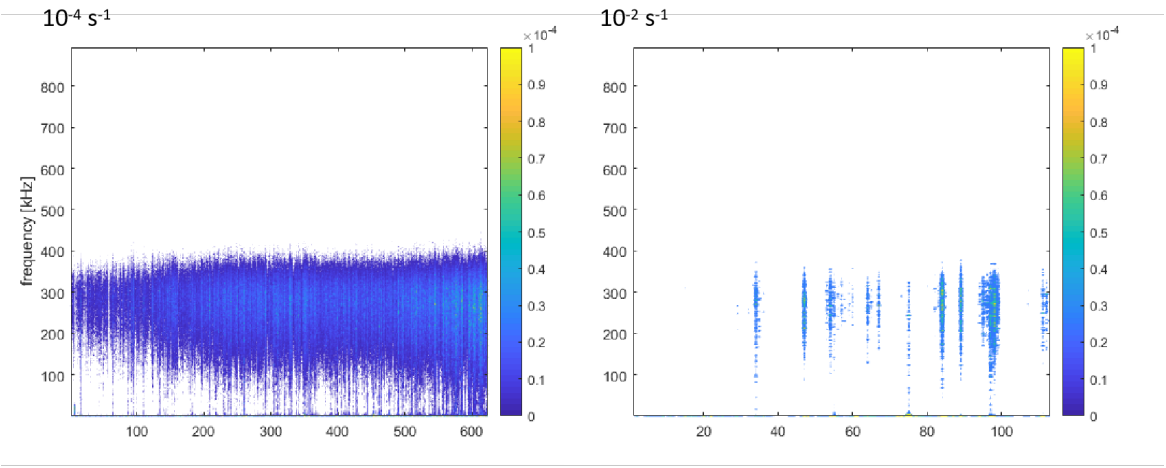


Fig. 5.3 Colour contour maps of $G(f)$ after calculated by FFT.

5.2.2 Testing system

The *in situ* XCT system for high temperature testing was developed in chapters 3 and 4. In this study, LDV was combined with *in situ* XCT system as an AE detector. The employed LDV (V100(H), Kyoritsu Electric Corporation) captured AE signals through

a quartz window attached within the electric furnace during tensile or creep loading (Fig. 5.4). This LDV is a velocity-sensitive Laser interferometer that detects the surface vibration originating from the internal AE elastic waves [143]. The He-Ne Laser beam from the LDV was focused and exposed at the testpiece gauge area, precisely the same part where the XCT was observed, during the loading applied. The output voltage was proportional to the surface velocity with a coefficient of 0.1 m/s/V. Only the signals with the amplitude voltage above 2 V were recorded and used in this study to remove the background noises. The AE signals were continuously monitored every 50 ms and recorded when any part of the signal amplitude exceeded 2 V, which is supposed to be the highest voltage of background noises. The maximum amplitude of the signal in 50 ms was defined as the amplitude of each AE wave (Fig. 5.5). AE waveforms were recorded by the wave memory (Picoscope 5000) with a sampling rate of 1 GS/s. The duration for recording one AE signal requires approximately one second.

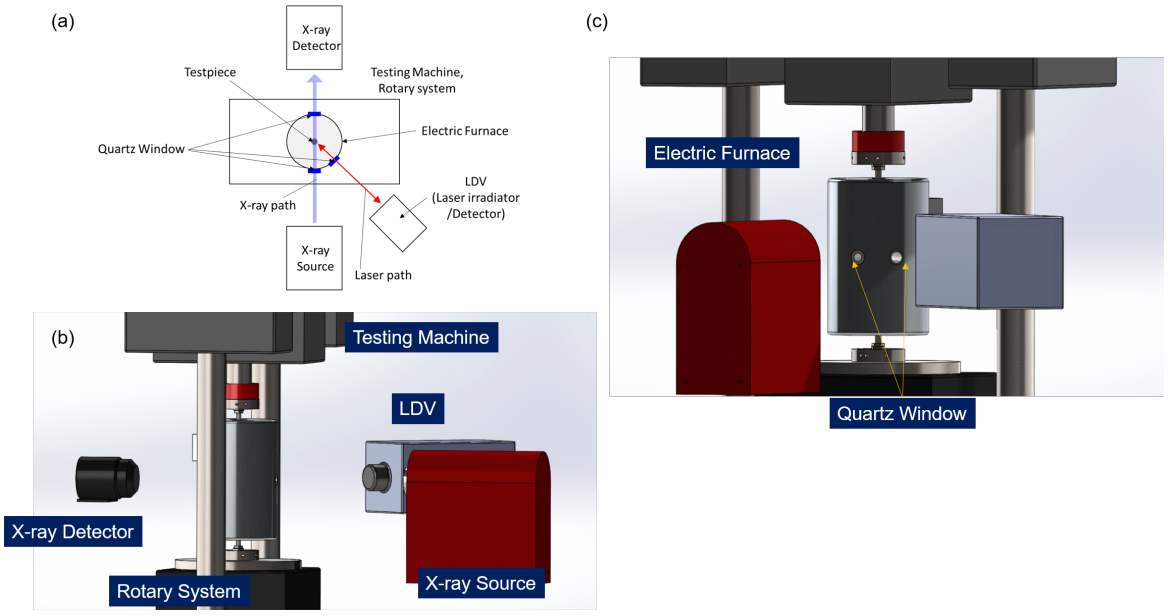


Fig. 5.4 Experimental setup of AE and *in situ* XCT setup during high temperature mechanical testing. (a) 2D sketch of top view; (b) 3D sketch of side view; (c) 3D sketch from X-ray source side.

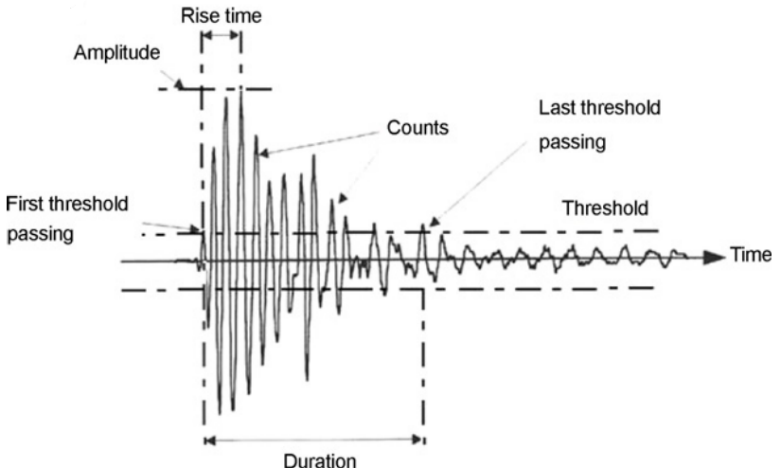


Fig. 5.5 Main acoustic characteristic parameters in a typical waveform signal [119].

AE energy (E) and median frequency (f_m) were calculated using Eq.(5.4) and Eq.(5.5) respectively from the recorded original signal, and compared with mechanical results and XCT observations. AE energy was evaluated using signal amplitude in V unit and frequency in Hz. 1 V shows 0.1 m/s velocities of the testpiece surface vibration. The energy unit is set as an arbitrary unit which is equivalent to V^2s^{-1}.

$$E = \int_{f_{min}}^{f_{max}} G(f)\mathrm{d}f \tag{5.4}$$

$$\int_{0}^{f_m} G(f)\mathrm{d}f = \int_{f_{min}}^{\infty} G(f)\mathrm{d}f \tag{5.5}$$

$G(f)$ in these equations is the power spectral density function, calculated by fast Fourier transformation of the obtained AE data [123] [124] [112]. For statistical analyses of AE signals, amplitude distribution analyses were employed [133],

$$\log_{10} N(A) = a - b \log_{10} A \tag{5.6}$$

where N is the number of cumulative AE signals whose peak amplitudes exceed A, and a and b are constants. The parameter b, called "b-value", is known to have some physical implications; when a deformation proceeds with a small number of large steps, a large amount of high-amplitude AE waves are induced, which leads to the small b-value [9].

AE signals were detected during *in situ* XCT procedure as follows. First, the testpiece was fixed along the loading axis inside the electric furnace and heated up to 800°C. Two thermocouples attached to the testpiece fixers observed the averaged temperatures as the testpiece temperature to control the furnace temperature. After the testpiece temperature reached 800°C, tensile loading was applied to the testpiece. In the case of the tensile test, the tensile loading was applied at strain rates of 10^{-4}, 10^{-3}, and 10^{-2} s^{-1}. After the engineering stress exhibited maximum, if the true strain reached 0.42, the loading was removed, and the XCT procedure was commenced as described in the previous chapter. The tensile loading was again applied after all the projection images were captured, if the true strain reached 0.44 (0.02 more than the last strain), the loading was removed again, and the next XCT started to be captured. These XCT and AE observations were carried out to compare the growth of voids or cracks and plastic deformation with detected acoustic signals. The procedure was repeated until failure and started from more than 0.42 or just before fracture in some cases to investigate damage growth and acoustic signals limited to the fracturing stage. In the tensile test, XCT started to be observed after the stress decreasing and the applicable strain range until fracture was determined, so 0.02 was chosen as the straining step. For the creep test, the tensile loading was applied at the rate of 10^{-3} s^{-1} until the stress was reached to the two targets creep stresses, 480 MPa and 566 MPa, and the same loading conditions remained until the true strain earned 0.15 and 0.10, respectively. Then the loading was removed, and XCT observation was

carried out. These strains to start XCT observation was chosen because over these strains third creep stage began, and the strain rate increased. The creep loading was again applied, and if the true strain reached 0.05 more than the previous step, the same XCT procedure was started again. For capturing X-ray backprojection images, a microfocus X-ray source by Hamamatsu Photonics – of capacity 150 kV and 500 μA – and an SCMOS X-ray detector by Photonic Science were employed. These were aligned precisely vertical to the testing specimen's tensile axis. Then, the step went back to the loading phase and repeated the above procedure. The experimental conditions were summarised in Table 5.1.

During this experiment, AE signals were continuously detected by the LDV. Still, in this study, all of the signals employed in AE analyses were captured during the tensile loading for the tensile test and during the target creep stress for the creep experiment. Any AE signals recorded during XCT steps, removing the load, or reloaded until the previous displacement point was released for the analyses.

Table 5.1 Experimental Conditions

	Temperature	Strain rate	Target Stress	XCT observed
Tensile test	800°C	10^{-4} s^{-1}	—	$\varepsilon > 0.42$
Tensile test	800°C	10^{-3} s^{-1}	—	$\varepsilon > 0.42$
Tensile test	800°C	10^{-2} s^{-1}	—	$\varepsilon > 0.42$
Creep test	800°C	—	480 MPa	$\varepsilon > 0.15$
Creep test	800°C	—	566 MPa	$\varepsilon > 0.10$

5.2.3 Testing materials

In this work, Inconel 718 was used as the exemplar polycrystalline nickel-based superalloys of composition given in Table 5.2. Inconel 718 testpieces were machined from round bars (NeoNickel Milton Keynes Co, Ltd.), which was solution heat treated at 940 - 1010 °C following air-cooled (AMS5662 bar). Prepared grain size in Inconel 718

was 40-50 μm. The testpiece gauge length and the diameter were 2 mm and 1.5 mm, respectively. The dimension was selected so that the XCT detector allows the X-ray beam to fully penetrate the specimen for optimum capture of the damage accumulation [167].

Table 5.2 Composition of the alloys studied in wt.-%

Name	Ni	Cr	Al	Ti	Fe	Nb	Co	Mn	Cu	Si	C	B
Inconel 718	55.7	18.3	0.6	0.9	18.7	5.2	0.26	0.11	0.08	0.07	0.04	0.04

5.3 Results

5.3.1 AE and XCT analyses during high temperature tensile deformation

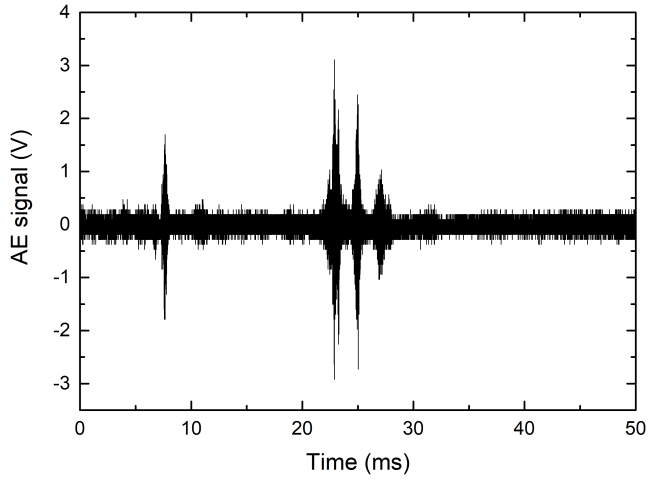


Fig. 5.6 Detected AE sample during tensile loading at 10^{-4} s^{-1}.

Figure 5.6 shows an example of the detected AE signals during tensile loading. Some parts of the signal amplitude exceeded 2 V within 50 ms (8 ms, 22 ms, 25 ms, and 27 ms) thus this 50 ms wave signal was detected as an AE signal. If any parts of the wave signal do not exceed 2 V, the signal would be recognised as background noise and removed in this detecting system.

Figure 5.7 depicted stress - strain curves with the AE energy plots at 10^{-4}, 10^{-3}, and 10^{-2} s^{-1}. The stress values exhibited higher at a higher strain rate. In every strain rate case, the true stress had a maximum around the true strain of 0.4 and decreased over that strain. The decrease of the true stress could be attributed to the internal damage growth. The fluctuated stress-strain curve over 0.4 in true strain indicated the relieved stress during *in situ* XCT observation. The obtained XCT images will be compared later with the AE signals detected in these strain ranges before fracture. These results indicated that large deformation and damage growth in a single step might have induced high energy AE bursts at the higher strain rate case. Overall, AE signals detected during tensile loading increased from 0.2 in true strain and a higher strain rate induced higher energy signals.

For more quantitative analyses of these detected signals, those AE parameters such as energy, frequency, and amplitude were calculated and compared with strain rates during plastic deformation. Averaged energy and frequency parameters of detected AE signals were plotted against strain rates (fig. 5.8). Considering the acoustic signals were emitted from an undamaged and damaged object, the detected AE signals before and after 0.4 were analysed as the different signal groups. As shown in fig. 5.8, between 0.1 and 0.4 in true strain, the averaged AE energy increased against the strain rate. The tendency was more apparent over 0.4. On the other hand, the trend against the strain rate was more apparent until 0.4 in true strain rather than fracturing stage for the median frequency. In the former case, the averaged median frequency decreased

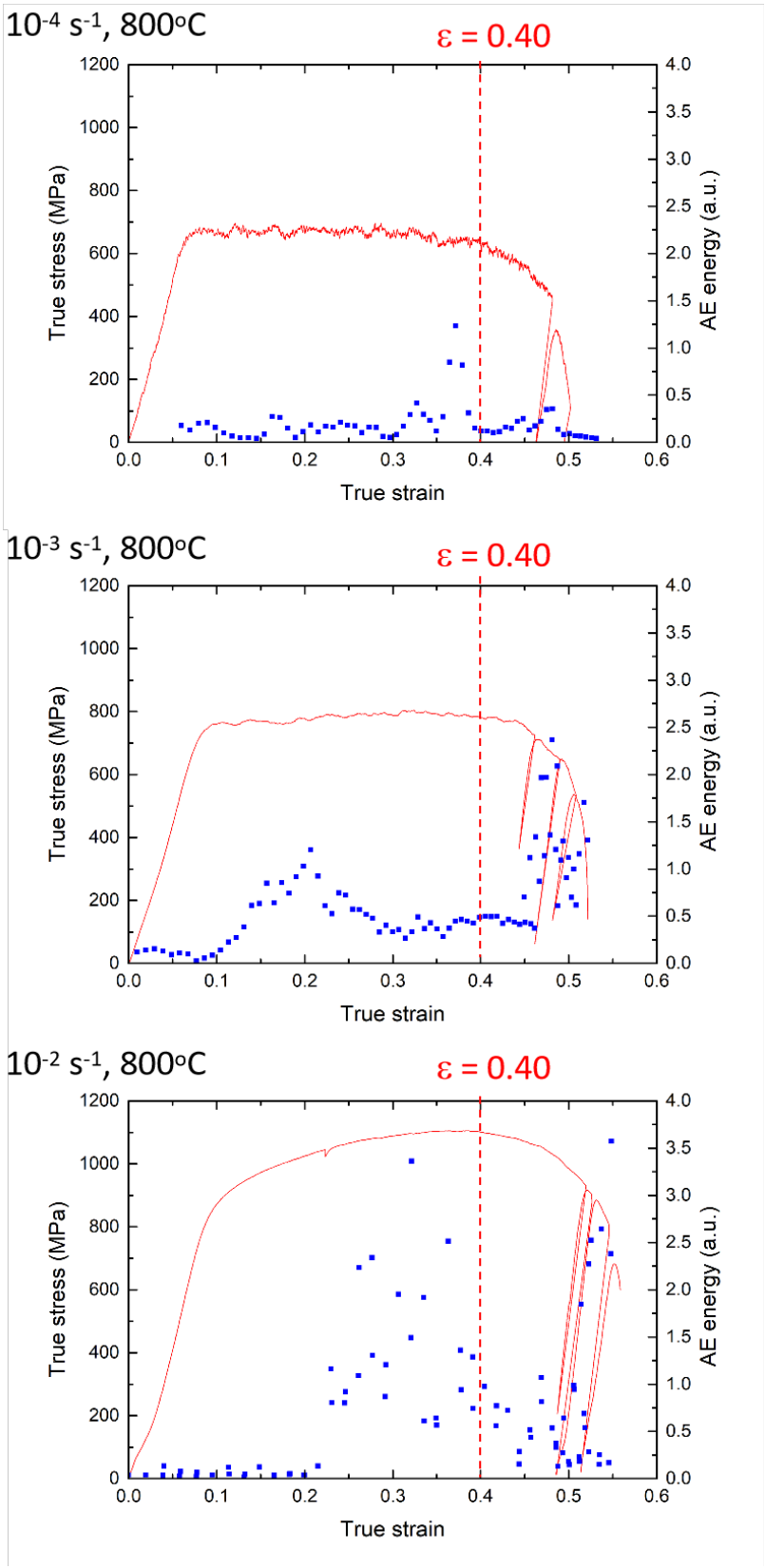


Fig. 5.7 True stress and true strain curve and detected AE energy plots at 10^{-4} s^{-1}, at 10^{-3} s^{-1}, and at 10^{-2} s^{-1} at 800°C. Red line and blue plot denotes stress-strain curve and AE energy, respectively.

with increasing the strain rate, and in the latter case, the frequency values were almost same regardless of the strain rate. The frequency values fluctuated at 10^{-4} s^{-1}, as the error bars enlarged compared to other rates or before 0.4 in true strain.

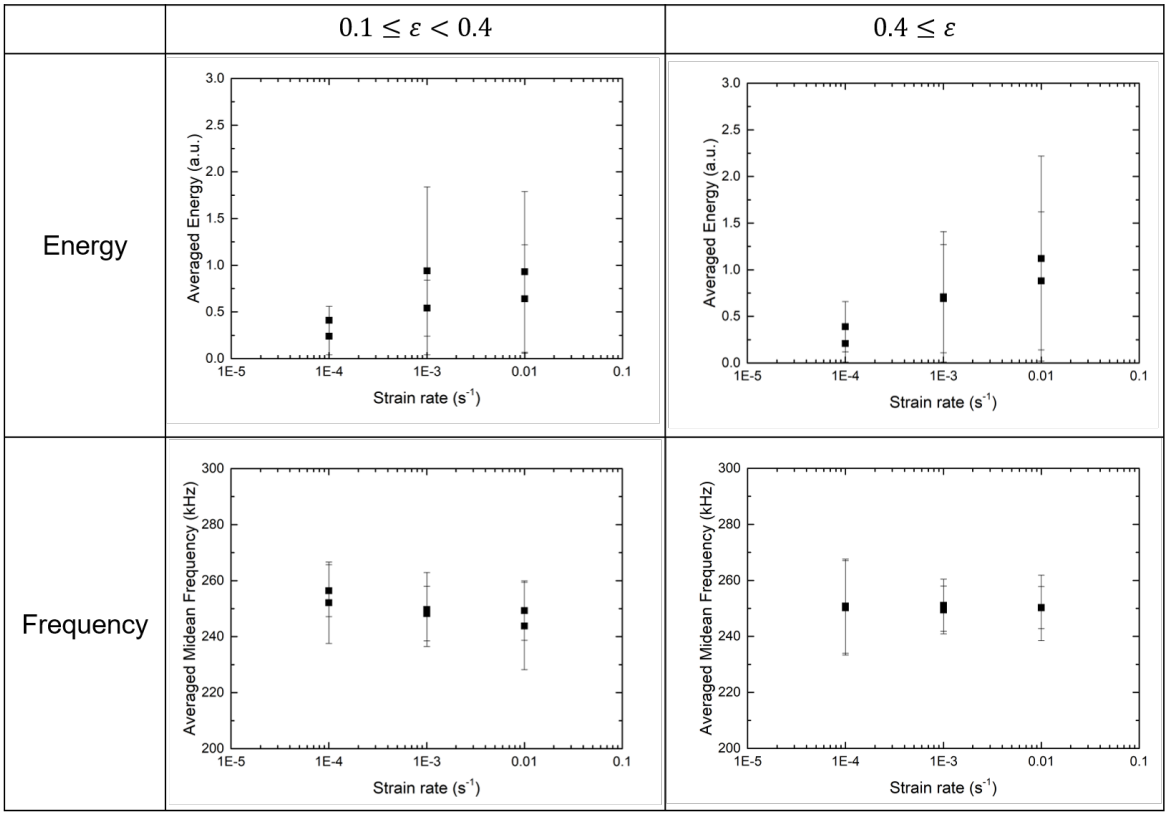


Fig. 5.8 Averaged energy and median frequency of detected AE signals during tensile loading at 800°C.

Fig. 5.9 - 5.11 illustrated the examples of XCT images observed by *in situ* over 0.4 in true strain. The green coloured regions exhibited defects and image noises, defined as lower than 30 % of maximum intensity. At 10^{-2} s^{-1}, the green voxels remained small, which indicated that the void growth was limited during tensile loading, and plastic deformation was the predominant damaging factor. On the other hand, at 10^{-3} s^{-1} and at 10^{-4} s^{-1}, the growth of defects was observed, which led to the internal void growth, void coalescence, or inter-void cracking. Compared to these XCT analyses with the AE data above, damaged objects affect the frequency range generated by AE

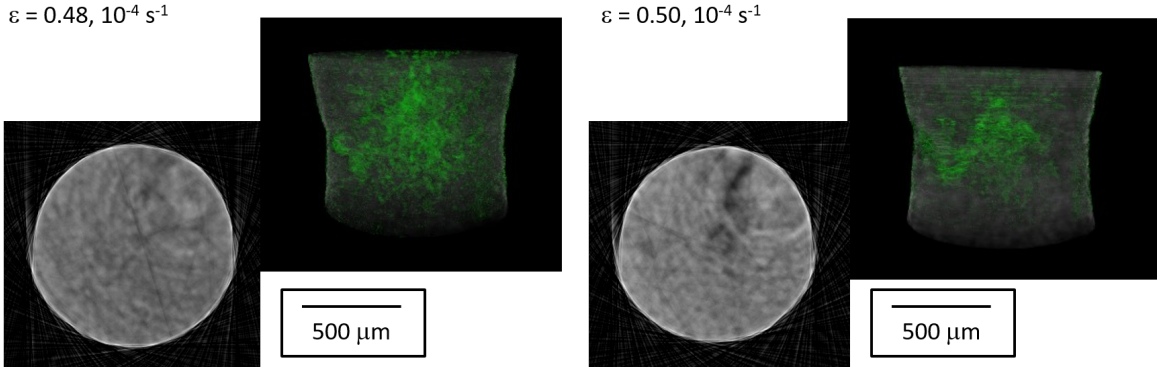


Fig. 5.9 *In situ* XCT images captured at $\varepsilon = 0.48$ and 0.50 during tensile loading at 10^{-4} s^{-1} at 800°C.

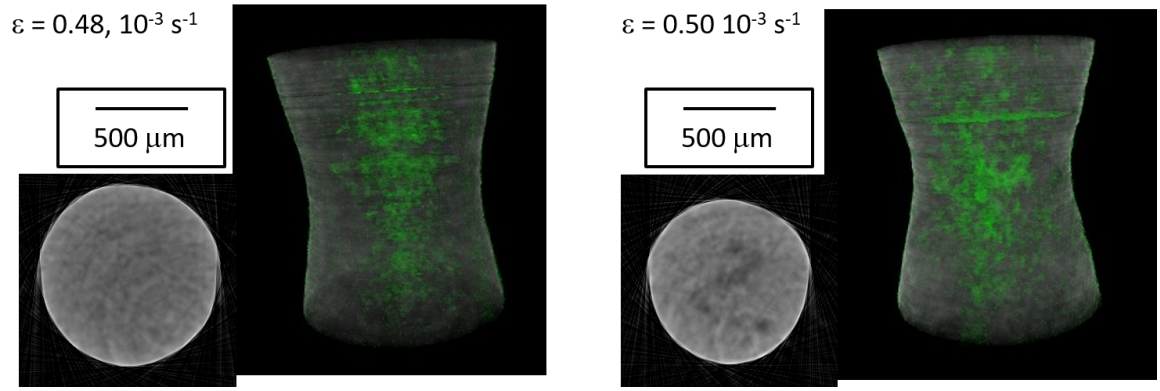


Fig. 5.10 *In situ* XCT images captured at $\varepsilon = 0.48$ and 0.50 during tensile loading at 10^{-3} s^{-1} at 800°C.

signals. At 10^{-3} s^{-1} and at 10^{-4} s^{-1}, the testpiece included more grown voids and generated AE signals in a wider range of frequency (or in a lower frequency range) than during plastic deformation at 10^{-2} s^{-1}.

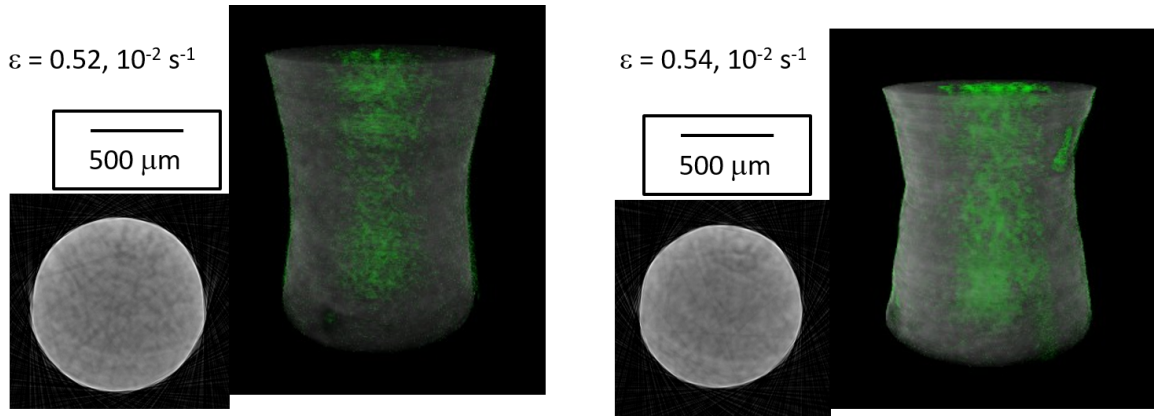


Fig. 5.11 *In situ* XCT images captured at $\varepsilon = 0.52$ and 0.54 during tensile loading at 10^{-2} s^{-1} at 800°C.

The AE amplitude distributions were obtained at each strain rate for 0.1 - 0.4 in true strain and over 0.4 (Fig. 5.12). In every case, the tensile tests were repeated twice. The AE data in each case was plotted in those two strain ranges. As the strain rate increased, the total cumulative AE events decreased from 1000 - 3000 at 10^{-4} s^{-1} to 30 - 100 at 10^{-2} s^{-1}. This is because recording an AE signal required approximately one second; thus higher strain rate limited the number of signals detected. The distribution shapes were different among these strain rates. 10^{-4} s^{-1} and 10^{-2} s^{-1} seemed to follow the power-law (Eq. 5.6) as approximate linear curves for those log-log plots in the figures were fitted with a determination coefficient (R2) of nearly 0.9 or more. On the other hand, the R2 values were much less in the 10^{-3} s^{-1} case than others and the plots followed rather a Weibull function [133]. The difference in distribution shapes was observed in both strain ranges. This behaviour will be discussed in the discussion part.

The b-value in Eq. (5.6), the slope of the approximate curve, was lower in the distributions over 0.4 than until 0.4 in true strain in every case (Fig. 5.12). The AE bursts with higher amplitude were generated more over the strain of 0.4 until fracture, which attributed to the released energy due to large cracks or large scale deformation.

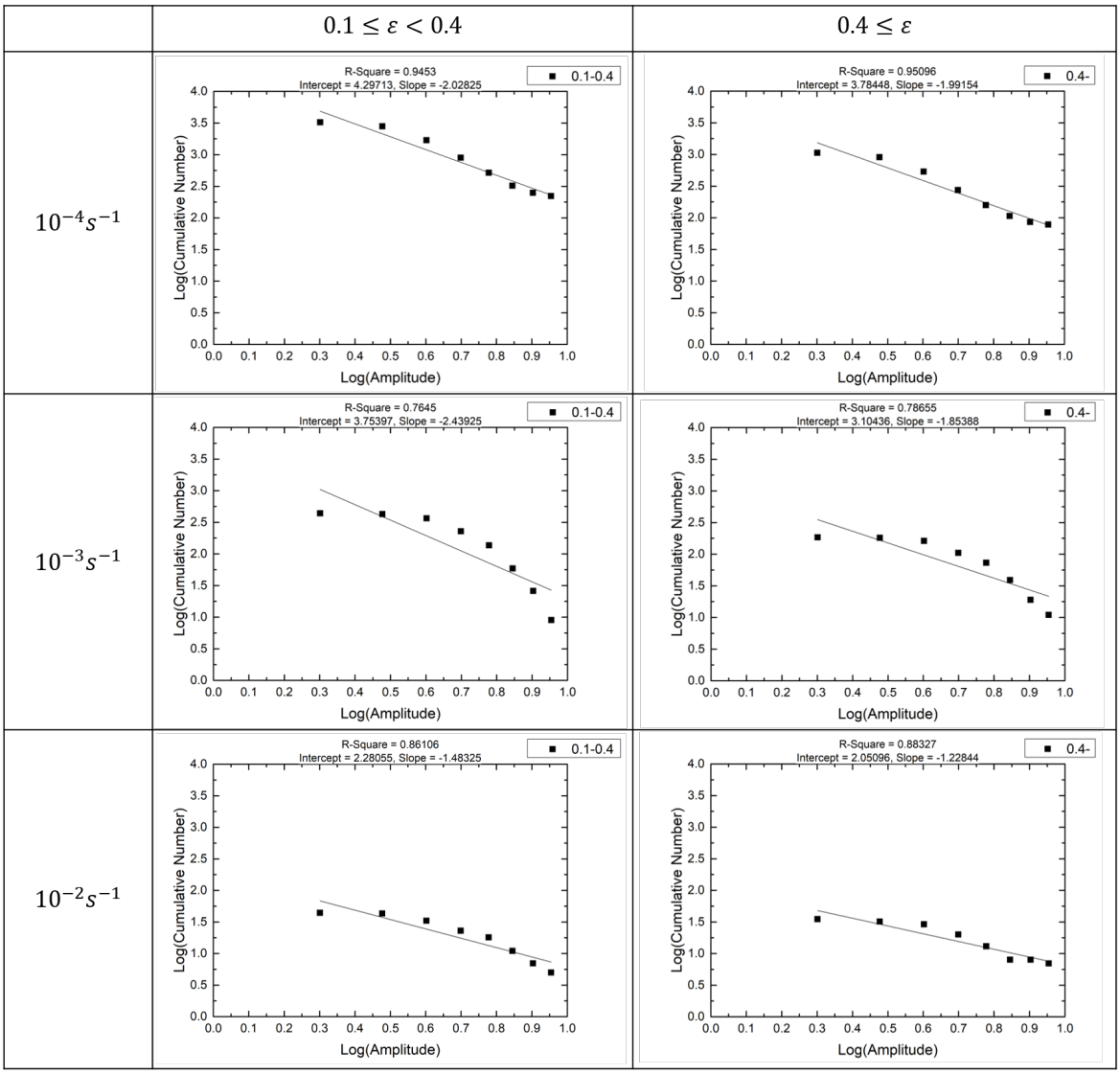


Fig. 5.12 Amplitude distribution at 10^{-4} s^{-1}, 10^{-3} s^{-1}, and 10^{-2} s^{-1} during tensile loading at 800°C less and greater than 0.4 in true strain.

5.3.2 AE and XCT analyses during high temperature creep loading

AE signals were detected by *in situ* also during creep loading of 480 MPa and 566 MPa under 800°C. *In situ* XCT images started being observed when the object true strain exceeded 0.15, from which the testpiece started third-stage creep where the strain rate drastically increased. In the following section, the detected AE signals were studied after XCT *in situ* observation commenced.

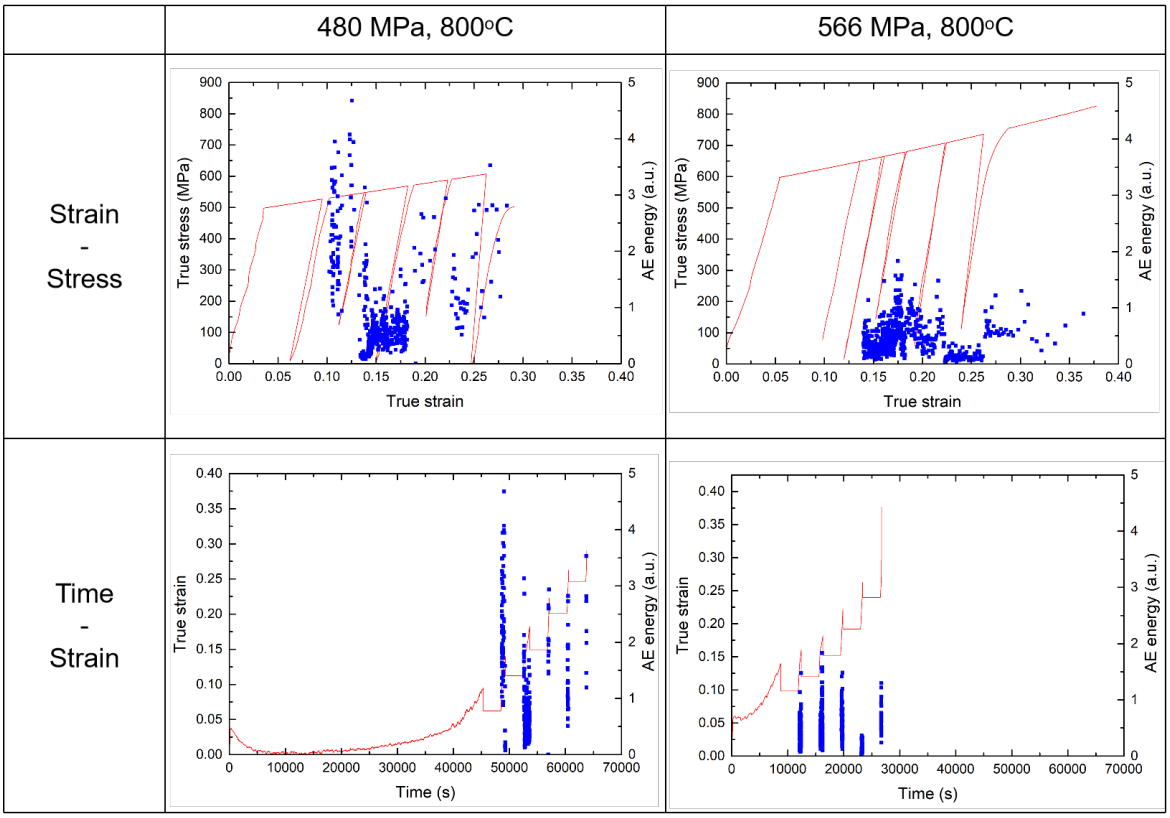


Fig. 5.13 True Strain - True Stress, AE Energy plot and Time - True Strain, AE Energy plot during creep loading of 480 MPa and 566 MPa at 800 °C.

Figure 5.13 shows the stress - strain curve and creep curve under the creep loading of 566 MPa and 480 MPa at 800°C. This study focused on AE signals recorded after the third-creep stage started. The fluctuated strain data after the third-creep phase

were due to the stress-relaxed steps for *in situ* XCT observation. Both cases included five times XCT observations until fracture. Overall, AE signals were generated with higher energy and lower frequency range in the lower creep loading case.

AE signals detected in creep loading steps between XCT steps were plotted against the calculated strain rate in each loading step (Fig. 5.14). As the strain rate increased and the fracture approached, averaged AE energy increased and median frequency decreased. Overall, the error bars in AE energy plots were larger in 480 MPa than in 566 MPa. The median frequency calculated from these signals also had some differences between these two creep conditions.

Under these creep loading conditions, *in situ* XCT images were captured along with detecting AE signals. Fig. 5.15 shows the tomography images before fracture in those creep conditions. Visible defect size in this XCT system was over 30 μm, as suggested in our previous chapter. The reconstructed 3D images in Fig. 5.15 exhibited green voxels, which includes both defects and artefacts. But from the sliced image at e=0.30, 480 MPa showed two defects in the pointed region. The lower creep loading case is supposed to generate more creep void than the higher loading condition. Referring to the deformation mechanism map of IN718 [189], at 800°C, both 480 MPa and 566 MPa were located in the 'Recovery by dislocation climb' area. This indicated that both conditions induced dislocation climb by lattice-diffusion. It is supposed that lower creep loading, under 480 MPa, offered sufficient time for void growth than under 566 MPa as observed in XCT analyses.

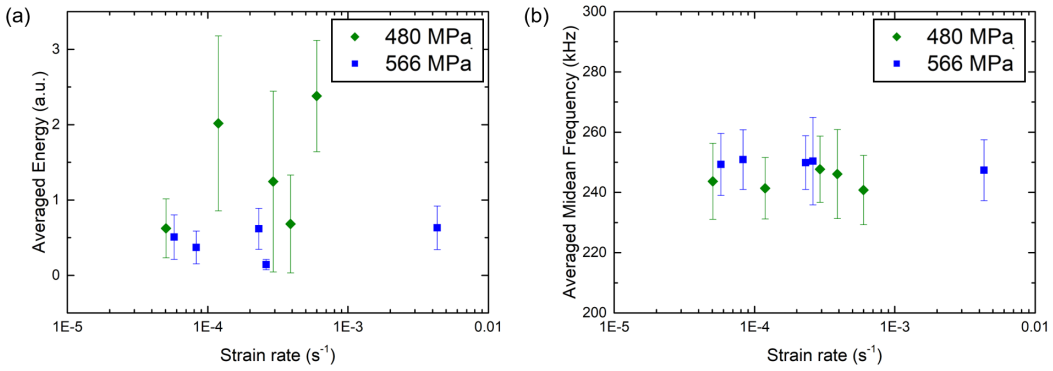


Fig. 5.14 Averaged energy (a) and median frequency (b) of detected AE signals during creep loading at 800°C.

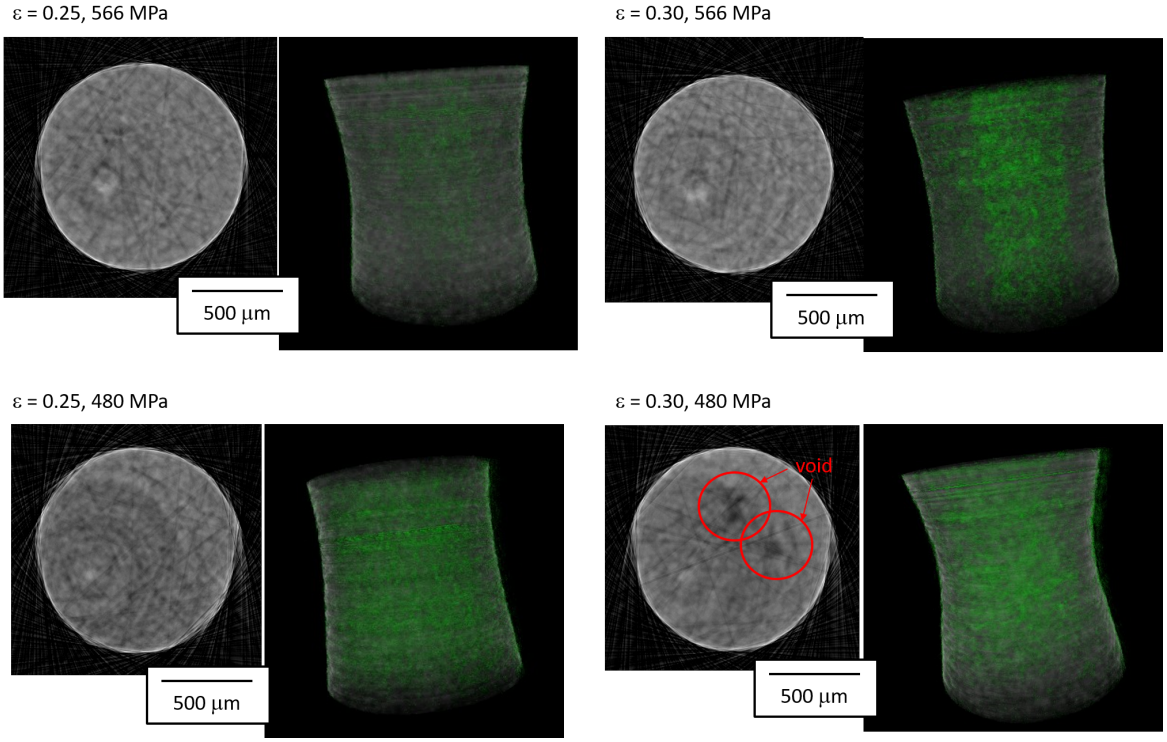


Fig. 5.15 *In situ* XCT images captured at $\varepsilon = 0.25$ and 0.30 under 480 MPa and 566 MPa at 800°C.

5.3.3 Defect volume effect on AE parameters

Since the low-intensity voxels with the size of over 30 μm were identified as defects from artefacts, those voxels volumes were calculated as defect volume. The threshold of the intensity can be referred to in chapter 4. Fig. 5.16 shows the results for tensile tests at 800°C and Fig. 5.17 is for creep tests. For tensile tests, the frequency fluctuated between 230 kHz and 260 kHz and higher energy AE tended to be generated in lower frequency range. Higher tensile strain rate generated higher energy AE waves. Compared to the averaged defect volume, which was calculated from the *in situ* XCT images, the AE signals burst from the object with larger defects decreased their median frequency. Similarly, 480 MPa induced high energy AE waves during the creep tests in the lower frequency range. Additionally, the testpiece during creep loading was affected by the size of inner defects, as 480 MPa generated larger defects, and most of the AE signals burst in a lower frequency range than those in 566 MPa. But the frequency range was not fluctuated compared to the tensile loading case. These results show that both strain rates and defects affect AE median frequency and wave energy.

5.4 Discussion

5.4.1 Plastic deformation and AE parameters

It was confirmed that this LDV system could detect the AE signals from the testpiece by observing its surface vibration without attaching any piezoelectric sensors directly. This method successfully offered the acoustic information during the testpiece deforming or being damaged even at as high as 800°C. The AE parameters, such as amplitude, frequency, and energy, were calculated for each signal from the surface vibration.

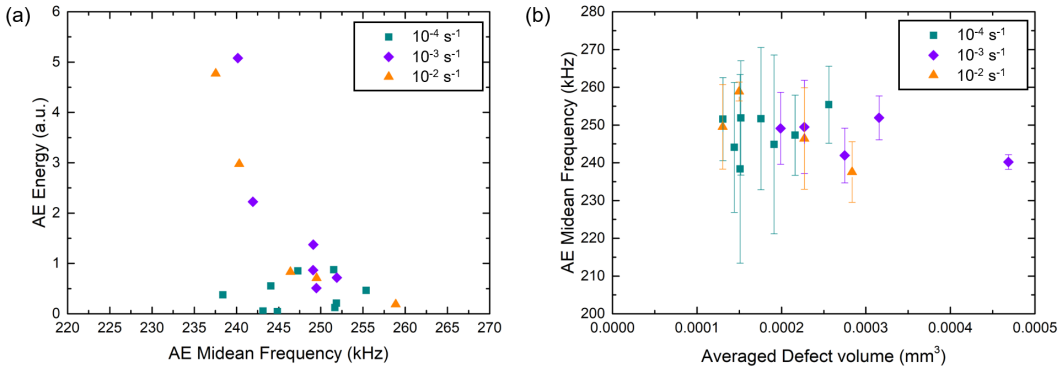


Fig. 5.16 (a) Frequency - Energy plot and (b) defect volume - frequency plot during tensile tests at 800°C.

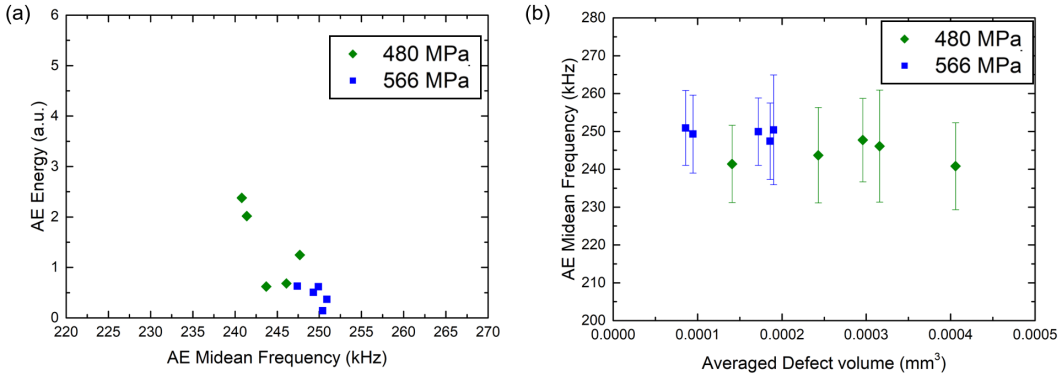


Fig. 5.17 (a) Frequency - Energy plot and (b) defect volume - frequency plot during creep tests at 800°C.

Within this same AE detecting system, those wave parameters were comparable among the several loading conditions under the same signal coefficient of 0.1 m/s/V.

The averaged AE energy was correlated with the strain rate during the high temperature tensile loading. The energy increased with the strain rate and towards fracture, which indicates that the released acoustic energy was relevant to the size of the plastic deformation. These results in the high-temperature experiment were consistent with some works obtained at a lower temperature, which is applicable for piezoelectric sensors [122], [131]. A similar tendency was also observed during creep loading. The averaged AE energy increased against the calculated strain rate between the XCT steps. But the trend at 480 MPa and 566 MPa creep loading behaved differently, which will be discussed in the next section. Furthermore, one can deduce from this result that the released acoustic energy due to tensile or creep loading affects the parameters of detected signals, such as amplitude and power.

During the laser observations at 800°C, the heated testpiece surface could emit radiant light with a wavelength around 630 nm, which is close to the wavelength of the He-Ne laser employed in the presented LDV system. However, since the AE energy changed proportionally against the strain rate, the AE signals due to the radiant light from the testpiece surface at 800°C did not exceed the threshold, 2 V, and were successfully removed. Therefore, the obtained results could be treated and discussed similarly with the reported findings studied by piezoelectric sensors.

The AE amplitude distribution at each strain rate was compared during tensile loading. As discussed in the results section, for both before and over the true strain of 0.4, the strain rate 10^{-4} and 10^{-2} s^{-1} cases showed the power-law correlations in log(Amplitude) - log(Cumulative Number) plots. This indicated that in these two strain rate conditions, the amplitude distribution followed Eq. (5.6). Only the mediate

strain rate case exhibited different correlations, which seemed the Weibull function [133].

If strain rates mainly affected the number of detected AE events because of being overlapped by high amplitude events [190], 10^{-2} case needed to show the Weibull distribution as 10^{-3} case did, but 10^{-2} showed similar distribution to 10^{-4}. These results indicated that the strain rate was not the main factor controlling this distribution. From the XCT results, at 10^{-2}, the testpiece fractured due to plastic deformation, while at 10^{-3} and at 10^{-4} void growth was observed. Some works using steel materials showed the distribution was affected by cracking path, brittle or ductile fracture [9]. But in our study, the difference was observed from the early stage of tensile loading (0.1 - 0.4 in true strain). 10^{-3} might have induced both plastic deformation and cavitation at grain boundaries, which could differently cause the shearing mode. These acoustic signals might be related to twinning behaviour, as some works reported[191]. This requires further investigations in a future study.

When deformation proceeds in a large number of small steps, small AE signals dominate the distribution, and the b-value becomes large [9]. Overall, the results showed a higher b-value at 0.1 - 0.4, which indicated that the deformation proceeded in more significant steps at over 0.4 in true strain towards fracture than at 0.1 - 0.4.

Detected AE signals possessed the energy values, which are negatively correlated with the median frequency. This is consistent with the results obtained by the conventional AE detecting methods[124], [192]. The AE waves observed in this study are supposed to be generated in a similar damaging form considering Vinogradov *et al.*'s work evaluating AE signals in several alloys, including steels, Fe-Ni, and Mg alloy, detected by piezoelectric sensors attached to the testpiece during tensile loading at room temperature to 100°C. They claimed that AE clusters could be divided into several groups, which originates from different damaging mechanisms such as dislocation slip

and twinning [128], [112], [129]. Their study used steel material, dislocation slips, or twining in γ phase generated AE waves in the low-frequency range, 200 - 300 [kHz], and martensite transformation in α phase induced high-frequency signals in over 500 [kHz]. As all of the AE signals obtained in our results were generated in the lower frequency range, the damaging mechanism mainly affecting detected signals supposed to be the slips or twins in the primary phase, γ phase, in Inconel 718. Since the signals did not include the burst type (short rise time and high amplitude signals) both during tensile loading and during creep loading, most of the AE signals generated in these conditions did not attribute to the inclusion fracture [121].

5.4.2 Damage effect on AE parameters

It was challenging to evaluate AE features directly from the deforming object by the conventional method (piezoelectric sensors) (*e.g.* [132]). This was because the attaching condition to the object could become unstable, and the resonant frequency could vary due to the object deformation. Thus very few studies on the AE analyses have addressed the damaged objects. However, in this study, the subtle changes in the AE median frequency of the detected signal were successfully observed from the fracturing Inconel 718 by LDV system at 800°C.

During tensile loading at 800°C, some frequency changes were observed. The calculated frequency decreased against the strain rate during plastic deformation. The frequency was lower before fracture than in the earlier plastic deformation stage. Considering these data and the frequency plots against the averaged defect volume calculated from *in situ* XCT, the frequency seemed to decrease as the inner defect size increased or in case the AE energy increased. However, the correlation with these parameters exhibited differently. While the AE data obtained at 10^{-4} to 10^{-2} s^{-1}

followed the same tendency between energy and frequency, the correlation of median frequency with the inner defect volume was weak. In the case of tensile loading, the AE frequency is supposed to be affected by deforming speed or plastic deforming behaviour rather than the damage in the object testpiece.

On the other hand, although the energy was less correlated with the calculated strain rate during creep loading at the same temperature, the frequency had a quite strong correlation with averaged defect volume. Both under 480 MPa and 566 MPa, the frequency followed the same trend decreasing against the defect volume. This result indicates that median frequency in the creeping loading was affected predominantly by the defect or damage in the testpiece. Combined with *in situ* XCT analyses, the critical AE wave characteristics, energy and frequency, were linked to the damaging features during two kinds of mechanical loading at 800°C.

5.4.3 AE signals as fracture indicators

As discussed above, the LDV system was successfully applied to AE observation during a high-temperature mechanical loading experiment. The detected AE data were also available in the study on the fracture mode utilising some conventional AE analysing methods. The amplitude distribution analyses indicated that the b-value in the distribution could lead to the deformation speed becoming larger. The AE energy was found to be correlated with the strain rate. Furthermore, AE frequency had correlations with the AE energy and the generated defect volume inside the object testpiece. At least, the object with a larger void volume is supposed to emit the low-frequency AE signals. Continuously monitoring these AE parameters will inform when the object is damaged in a particular form before fracture, which can trigger the XCT to start to be captured. Combined with *in situ* XCT image information,

dynamic and statistical mechanical modelling in a wide range of temperature and loading conditions will be available in future.

5.5 Summary and Conclusions

Non-contact AE detector combined with *in situ* XCT technique was successfully developed to investigate generated acoustic signals as the indicators of the damage accumulation in the Ni-based superalloy during loading at high temperature. The following specific conclusions can be drawn from this study:

1. The LDV detector could detect AE signals generated from the testpiece surface during high temperature testings. The non-contact AE detector successfully captured the acoustic features from the vibration of the testpiece surface *via* laser interferometer, which was applied to the evaluation of generated AE in the Ni-based superalloy during tensile or creep loading at 800°C.

2. The developed AE - XCT combined system allowed the investigation of the correlation between the damage growth and plastic deformation and AE features: Energy, Frequency, and Amplitude distribution utilising *in situ* observation of AE and 3D XCT images. During the plastic deformation, a slower strain rate tended to induce lower energy AE bursts that were supposed to generate minor damage or plastic deformation.

3. The *in situ* 3D sequential XCT data observing the defect growth were correlated with the calculated features of AE detected simultaneously. AE energy increased with the strain rate, indicating that the deforming speed affected the released acoustic energy. AE median frequency change was affected by the defect growth

or the defect size in the object. These acoustic features were observed during both tensile loading and creep loading at 800°C.

4. For the first time in this field, detected AE features were correlated with the damage growth or mechanical behaviours in the Ni-based superalloy during loading at high temperatures. More meticulous observation will be required to understand the detailed damage effects on acoustic parameters for the induced internal defect information under high temperature conditions. Such techniques would be applied for triggering *in situ* XCT observation and more accurate NDT methods.

Chapter 6

Conclusions and Future Work

6.1 Conclusion

The presented work developed the novel *in situ* XCT system to diagnose the damage accumulation in Ni-based superalloys during high temperature tensile and creep loading, which was later combined with a laser-based AE detector for a better understanding of the initiation of failure. This novel technique enables to observe and analyse of the plastic deformation and damage accumulation induced during high temperature mechanical loading which is the simulated environment during actual service in the engine part. The *in situ* observation techniques during high temperature experiments will factorise the damage mechanisms, such as stress triaxiality state, plastic strain rate, and oxygen-induced damage. Furthermore, XCT-AE combined system can offer precise understandings of acoustic information related to the damage accumulation in Ni-based superalloy, and develop new NDT techniques to diagnose the existing internal damage and remaining material life.

Chapter 3 described the design, operation and performance of a laboratory-scale XCT system, which was capable of quantifying damage processes arising during the high temperature deformation of nickel-based superalloys, Nimonic 80A and Inconel 718. This new *in situ* XCT system was applied to a high temperature tensile experiment of the duration of up to 36 hours. The displacement-fixed rotation control was employed to capture X-ray back projection images from the whole angles for temperatures of at least 800°C and for strain rates between 10^{-4} and 10^{-2} s^{-1}. The obtained tomography images offered sufficient resolution, with an accuracy of 30 μm, to detect plastic deformation, void growth and crack initiation. Studies on Nimonic 80A and Inconel 718 have been carried out, with the rationale that these are widely used alloys of lesser and greater ductility, respectively. At 800°C, Nimonic 80A exhibited surface cracks which are the sites of fracture initiation; for Inconel 718, internal void growth after necking was preferred. In both cases, the XCT system proved to detect these failure events. Those were confirmed differently against the strain rate. At faster strain rates (10^{-2} s^{-1}) at 800°C, interrupted tests show a critical degradation of the maximum stress value in each step when compared to monotonic loading conditions – when deformed monotonically, there is not enough time for damage to occur. At slower deformation rates (10^{-4} s^{-1}) at the same temperature, the stress values pre- and post-interruption overlap those obtained monotonically. This proves that the nature of the damage process is time dependent – thus should be linked to diffusion-assisted forms of damage such as cavitation.

In chapter 4, the laboratory-scale *in situ* XCT system presented in chapter 3 was optimised and corrected post-processing methods for XCT reconstruction were described. The method quantitatively evaluated the damage growth arising in a nickel-based superalloy, Inconel 718 (IN718), during tensile and creep deformation at high temperatures. The improved mechanical procedure for *in situ* XCT succeeded

in capturing void growth during tensile deformation along with the recorded stress-strain curve. Carefully removing the loading while rotating the testpiece limited the further damage due to this mechanical operation for XCT. The newly developed post-processing method for tomography images utilised the beam-hardening correction and spot-removing algorithm. The corrected images successfully removed beam-hardening noises and imaging artefacts, which offered sufficient resolution to quantitatively identify the size and distributions of damages by setting the intensity threshold. The obtained images exhibited approximately 30 μm resolution to capture void growth in the testpiece gauge during the tensile deformation. For the first time, the void growth during the third stage creep was captured by *in situ* at high temperature. The *in situ* XCT during the tensile deformation at 800 °C clearly observed the difference of damage accumulation behaviour at 10^{-4} s^{-1} to 10^{-2} s^{-1}. Slower strain rate enhanced the ductile void growth, whilst higher strain rate induced the necking to a point fracture. The stress state change of the testpiece during necking was calculated from the deformed profiles sequentially obtained by *in situ* XCT. Comparing them with the internal damage growth, under the high stress triaxiality, the ductile void growth was observed more at a slower strain rate than at a higher strain rate. The devised *in situ* observation system and post-processing method offered the visual information which can correlate the damage growth and the deformation from the same testpiece with the applied stress and strain rate conditions.

Finally, in chapter 5, a non-contact AE detector combined with *in situ* XCT technique was successfully developed to investigate generated acoustic signals as the indicators of the damage accumulation in the Ni-based superalloy during loading at high temperature. The LDV detector could detect surface vibration due to AE signals inside the testpiece during high temperature experiments. The non-contact AE detector successfully captured the acoustic features, which was evaluated to relate with

generated damage in the Ni-based superalloy during tensile or creep loading at 800°C. The developed *in situ* AE - XCT observation system enabled to correlate visualised information of the damage growth and plastic deformation to AE features: Energy, Frequency, and Amplitude distribution. The *in situ* 3D sequential XCT observation of the defect growth was correlated with the analysed features of AE signals detected simultaneously. During the plastic deformation, a slower strain rate induced lower energy AE bursts and the energy increased with the strain rate. This result indicated that the deforming speed affected the released acoustic energy. AE median frequency change was affected by the defect growth and the defect size in the object. These acoustic features were observed during both tensile loading and creep loading at 800°C. For the first time in Ni-based superalloy studies, AE features were correlated with the damage growth and mechanical behaviours at high temperatures. More meticulous observation will lead to understanding damage effects on acoustic parameters, which can predict the remained life under high temperature conditions.

Overall this work on *in situ* XCT and AE diagnostics for observing damage accumulation in Ni-based superalloys have provided beneficial insights regarding (i) the development of a novel experimental system for *in situ* XCT observation under a wide range of service conditions, (ii) the improvement of XCT operation and image processing for quantitative damage analyses, and (iii) the development of AE detecting methods to investigate NDT damage analyses and XCT triggering techniques. The research presented is valuable, and is more widely applicable to the *in situ* damage observation of Ni-based superalloys and other types of alloys under the simulated severe conditions.

6.2 Future Work

The presented research focuses on designing the experimental setup of the XCT system and post-processing methods for *in situ* damage observation in Ni-based superalloys during high temperature loading. The devised system offers clear visual information with a resolution of 20 - 30 μm to observe internal void growth and crack propagations. The *in situ* observations along with controlled loading conditions offer insights into the effects of strain rates and stress triaxiality on the ductile fracture behaviour. The LDV system combined with XCT observations sheds light on the possibilities to detect acoustic emissions as a damage indicator, which can determine when to start *in situ* XCT observations of the internal damage. The topics below for further work arise from this study:

(1) Damage observation at a temperature which simulates service conditions.

(2) Microstructural analyses of the grain boundaries, twinning regions, and voids.

(3) Application of more complex loading conditions such as fatigue loading at elevated temperatures.

Regarding the first topic, this XCT system should also be applied to the observation of damage generated under room temperature loading conditions and typical operating temperature conditions of Ni-based superalloys, such as 650°C. In this thesis, the developed system challenged the maximum temperature of 800°C to expand the range of the experimental environment and to simulate severe operating conditions. The lower temperature condition is readily applicable to the *in situ* XCT observation. This will enable damage analyses in Ni-based superalloys closer to the actual service environment, which is beneficial to derive guidelines for the design of new superalloy grades. Furthermore, especially for the LDV, the noise due to the radiant light can be

significantly reduced under such lower temperatures. This would enable AE features to be more precisely correlated to visualised information, and to provide a damage detecting system with LDV that can start the XCT algorithms at the point of damage initiation.

For the second point, microstructural analyses will be needed for deepening the discussion in this thesis. As described in chapter 4, in the SEM observation of IN718 after the tensile experiment, formed and grown voids were found around the grain boundaries and near the carbide particles. These features appeared differently for the cases tested under 10^{-4} s^{-1} to 10^{-2} s^{-1}, which was used for the further discussion of the damage mechanisms by referring to other works. Similar analyses for N80A testpieces and other pieces tested under creep loading will better understand the damage mechanisms. Furthermore, in chapter 5, some of the detected AE signals were thought to have a relation with the microstructural features, such as twinning, which XCT cannot identify. Future work on the microstructural analyses could enable the correlation of AE signals to the micro-damage that could not be discovered only by the XCT system.

For the last point, Chapters 3 and 4 described the improvements for the mechanical algorithms during the XCT step so as not to generate unexpected damage. This design was mainly intended to prevent damage while rotating the testpiece. This improved *in situ* XCT observation procedure is also applicable for fatigue loading conditions. An example of a trial experiment is given in Figure 6.1, which shows the preliminary results of the damage observation in Nimonic 80A during fatigue loading with a stress range between 88 MPa and 878 MPa (1 Hz) at a frequency of 1 Hz at room temperature. The figure shows the propagated cracks observed after 50970, 51470, and 51970 cycles. The testpiece employed in this observation had no pre-cracks, but the experiment shows the loading condition was sufficient to capture the cracking point in this object. This trial

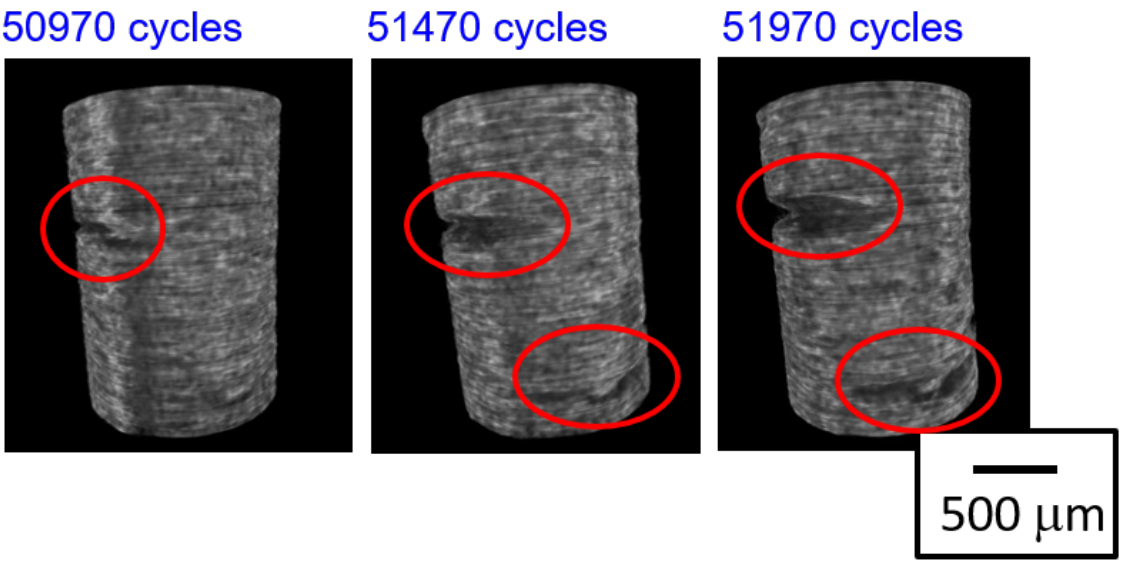


Fig. 6.1 The fatigue crack propagation under the stress range between 88 MPa and 878 MPa (1 Hz) in Nimonic 80A at room temperature.

experiment set the strain threshold to start the XCT above 0.4. In future work, this XCT starting algorithm can be combined with AE signals as mentioned above. These results and devised *in situ* XCT setup for the damage observation can be employed for further works under more complicated and accurately simulated operating conditions.

References

[1] T. M. Pollock, Alloy design for aircraft engines, Nature Materials 15 (2016) 809–815. doi:10.1038/nmat4709.

[2] N. Blyth, Examination of a filed cfm56-3c-1 turbofan engine - boeing 737-476, vh-tjn, technical analysis report 3/01 (reference be/200000023) (2001).

[3] D. Cooper, D. King, Report on the accident to boeing 737-237 series 1 (g-bgjl) at manchester international airport on 22nd august 1985 (1988).
URL http://www.aaib.gov.uk/cms_resources.cfm?file=/8-1988G-BGJL.pdf

[4] R. C. Reed, The Superalloys, Cambridge University Press, 2006. doi:10.1017/CBO9780511541285.

[5] S. R. Stock, Recent advances in x-ray microtomography applied to materials, International Materials Reviews 53 (2008) 129–181. doi:10.1179/174328008X277803.

[6] G. Requena, P. Cloetens, W. Altendorfer, C. Poletti, D. Tolnai, F. Warchomicka, H. P. Degischer, Sub-micrometer synchrotron tomography of multiphase metals using kirkpatrick-baez optics, Scripta Materialia 61 (2009) 760–763. doi:10.1016/j.scriptamat.2009.06.025.
URL http://dx.doi.org/10.1016/j.scriptamat.2009.06.025

[7] M. A. Azeem, P. D. Lee, A. B. Phillion, S. Karagadde, P. Rockett, R. C. Atwood, L. Courtois, K. M. Rahman, D. Dye, Revealing dendritic pattern formation in ni, fe and co alloys using synchrotron tomography, Acta Materialia 128 (2017) 241–248. doi:10.1016/j.actamat.2017.02.022.

[8] B. Muralikrishnan, M. Shilling, S. Phillips, W. Ren, V. Lee, F. Kim, X-ray computed tomography instrument performance evaluation, part i: Sensitivity to detector geometry errors, Journal of Research of the National Institute of Standards and Technology 124 (2019) 1–16. doi:10.6028/jres.124.014.

[9] A. A. Pollock, Acoustic emission - 2. acoustic emission amplitudes, Non-Destructive Testing 6 (1973) 264–269. doi:10.1016/0029-1021(73)90074-1.

[10] K. Ono, Acoustic emission in materials research – a review, J. Acoustic Emission 29 (2011) 284–308.
URL http://www.ndt.net/article/jae/papers/29-284.pdf

[11] D. J. Crudden, A. Mottura, N. Warnken, B. Raeisinia, R. C. Reed, Modelling of the influence of alloy composition on flow stress in high-strength nickel-based superalloys, Acta Materialia 75 (2014) 356–370. doi:10.1016/j.actamat.2014.04.075.

[12] S. Miller, Advanced materials mean advanced engines, Interdisciplinary Science Reviews 21 (1996) 117–129.

[13] M. Dareck, C. Edelstenn, T. Ender, Flightpath 2050 europes vision for aviation (2011). doi:10.2777/50266.

[14] C. S. Giggins, F. S. Pettit, Oxidation of ni-cr alloys between 800 and 1200 deg c, Transactions of the Metallurgical Society of AIME 245 (1969) 2495–2507.

[15] R. Jarrett, J. Tien, Effects of cobalt on structure, microchemistry and properties of a wrought nickel-base superalloy, Metallurgical and Materials Transactions 11 (1982) 1021–1032.

[16] H. Roth, C. Davis, R. Thomson, Modeling solid solution strengthening in nickel alloys, Metallurgical and Materials Transactions A 28 (1997) 1329–1335. doi:10.1007/s11661-997-0268-2.

[17] T. M. Pollock, S. Tin, Nickel-based superalloys for advanced turbine engines: Chemistry, microstructure and properties, Journal of Propulsion and Power 22 (2006) 361–374. doi:10.2514/1.18239.

[18] D. Furrer, H. Fecht, Ni-based superalloys for turbine discs, JOM 51 (1999) 14–17. doi:10.1007/s11837-999-0005-y.

[19] W. D. Summers, E. Alabort, P. Kontis, F. Hofmann, R. C. Reed, In-situ high-temperature tensile testing of a polycrystalline nickel-based superalloy, Materials at High Temperatures 33 (2016) 338–345. doi:10.1080/09603409.2016.1180857.
URL http://dx.doi.org/10.1080/09603409.2016.1180857

[20] C. T. Sims, W. C. Hagel, The Superalloys, John Wiley and Sons Inc, 1972.

[21] R. A. Ricks, A. J. Porter, R. C. Ecob, The growth of precipitates in nickelbase superalloys, Acta Metallurgica 31 (1983) 43–53.

[22] G. P. Sabol, R. Stickler, Microstructure of nickel-based superalloys, Physica Status Solidi (b) 35 (1969) 11–52.

[23] H. E. Collins, Relative stability of carbide and intermetallic phases in nickel-base superalloys, 1968, pp. 171–198.

[24] C. T. Sims, N. S. Stoloff, W. C. Hagel, Superalloys II, Wiley, 1987.

[25] D. Raabe, M. Herbig, S. Sandlöbes, Y. Li, D. Tytko, M. Kuzmina, D. Ponge, P. P. Choi, Grain boundary segregation engineering in metallic alloys: A pathway to the design of interfaces, Current Opinion in Solid State and Materials Science 18 (2014) 253–261. doi:10.1016/j.cossms.2014.06.002.

[26] E. C. Guo, F. J. Ma, The strengthening effect of niobium on ni-cr-ti type wrought superalloy (1980). doi:10.7449/1980/superalloys_1980_431_438.

[27] B. Reppich, Some new aspects concerning particle hardening mechanisms in precipitating ni-base alloys i. theoretical concept, Acta Metallurgica 30 (1982) 87–94.

[28] H. J. Frost, M. F. Ashby, Deformation-Mechanism Maps, The Plasticity and Creep of Metals and Ceramics, Pergamon Press, 1982.
URL https://engineering.dartmouth.edu/defmech/

[29] R. L. Coble, A model for boundary diffusion controlled creep in polycrystalline materials, Journal of Applied Physics 34 (1963) 1679–1682. doi:10.1063/1.1702656.
URL http://aip.scitation.org/doi/10.1063/1.1702656

[30] M. E. Kassner, T. A. Hayes, Creep cavitation in metals, International Journal of Plasticity 19 (2003) 1715–1748. doi:10.1016/S0749-6419(02)00111-0.

[31] W. D. Jenkins, T. G. Digges, C. R. Johnson, Creep of high-purity nickel, Journal of Research of the National Bureau of Standards 53 (1954) 329–352.

[32] K. Ankit, N. Prasad, Simulation of creep cavity growth in inconel 718 alloy, Materials Science and Engineering A 528 (2011) 4209–4216. doi:10.1016/j.msea.2011.02.012.
URL http://dx.doi.org/10.1016/j.msea.2011.02.012

[33] M. C. Rezende, L. S. Ara??jo, S. B. Gabriel, J. Dille, L. H. de Almeida, Oxidation assisted intergranular cracking under loading at dynamic strain aging temperatures in inconel 718 superalloy, Journal of Alloys and Compounds 643 (2015) S256–S259. doi:10.1016/j.jallcom.2014.12.279.
URL http://dx.doi.org/10.1016/j.jallcom.2014.12.279

[34] A. Thomas, M. El-Wahabi, J. M. Cabrera, J. M. Prado, High temperature deformation of inconel 718, Journal of Materials Processing Technology 177 (2006) 469–472. doi:10.1016/j.jmatprotec.2006.04.072.

[35] B. Max, B. Viguier, E. Andrieu, J. M. Cloue, A re-examination of the portevin-le chatelier effect in alloy 718 in connection with oxidation-assisted intergranular cracking, Metallurgical and Materials Transactions A: Physical Metallurgy and Materials Science 45 (2014) 5431–5441. doi:10.1007/s11661-014-2508-6.

[36] E. Andrieu, B. Max, B. Viguier, Oxidation assisted intergranular cracking in alloy 718 : Effects of strain rate and temperature, AerospaceLab (2015) 1–7.

[37] L. Fournier, D. Delafosse, T. Magnin, Oxidation induced intergranular cracking and portevin-le chatelier effect in nickel base superalloy 718, Materials Science and Engineering A 316 (2001) 166–173. doi:10.1016/S0921-5093(01)01224-2.

[38] Y. C. Lin, K. K. Li, H. B. Li, J. Chen, X. M. Chen, D. X. Wen, New constitutive model for high-temperature deformation behavior of inconel 718 superalloy, Materials and Design 74 (2015) 108–118. doi:10.1016/j.matdes.2015.03.001.
URL http://dx.doi.org/10.1016/j.matdes.2015.03.001

[39] J. Davis, Tensile testing second edition, 2004.

[40] G. H. Edward, M. F. Ashby, Intergranular fracture during power-law creep, Acta Metallurgica 27 (1979) 1505–1518. doi:10.1016/0001-6160(79)90173-1.

[41] A. C. F. Cocks, M. F. Ashby, On creep fracture by void growth, Progress in Materials Science 27 (1982) 189–244. doi:10.1016/0079-6425(82)90001-9.

[42] J. Kumar, A. Kumar, V. Kumar, Ambient and high temperature in situ damage evolution in nickel based in 718 super alloy, Materials Science and Engineering A 528 (2011) 4009–4013. doi:10.1016/j.msea.2011.01.111.
URL http://dx.doi.org/10.1016/j.msea.2011.01.111

[43] K. Chen, J. Dong, Z. Yao, Creep failure and damage mechanism of inconel 718 alloy at 800–900 °c, Metals and Materials International (2019) 1–15doi:10.1007/s12540-019-00447-4.

[44] M. Algarni, Y. Bai, Y. Choi, A study of inconel 718 dependency on stress triaxiality and lode angle in plastic deformation and ductile fracture, Engineering Fracture Mechanics 147 (2015) 140–157. doi:10.1016/j.engfracmech.2015.08.007.
URL http://dx.doi.org/10.1016/j.engfracmech.2015.08.007

[45] K. Nahshon, J. W. Hutchinson, Modification of the gurson model for shear failure, European Journal of Mechanics, A/Solids 27 (2008) 1–17. doi:10.1016/j.euromechsol.2007.08.002.

[46] P. W. Bridgman, Studies in large plastic flow and fracture, Harvard University Press, 1952.
URL https://doi.org/10.4159/harvard.9780674731349

[47] Y. Bao, Dependence of ductile crack formation in tensile tests on stress triaxiality, stress and strain ratios, Engineering Fracture Mechanics 72 (2005) 505–522. doi:10.1016/j.engfracmech.2004.04.012.

[48] Y. Bao, T. Wierzbicki, On fracture locus in the equivalent strain and stress triaxiality space, International Journal of Mechanical Sciences 46 (2004) 81–98. doi:10.1016/j.ijmecsci.2004.02.006.

[49] P. J. Noell, J. D. Carroll, B. L. Boyce, The mechanisms of ductile rupture, Acta Materialia 161 (2018) 83–98. doi:10.1016/j.actamat.2018.09.006.
URL https://doi.org/10.1016/j.actamat.2018.09.006

[50] C. Sims, A history of superalloy metallurgy for superalloy metallurgists, Superalloys 1984 (1984) 399–419.

[51] T. Gibbons, B. Hopkins, Creep behaviour and microstructure of ni-cr base alloys, Metal Science 18 (1984) 273–280.

[52] W. Hermann, M. Fahrmann, H.-G. Sockel, Determination of the gamma-prime-solvus temperature of two commercial wrought ni-base superalloys by thermal expansion measurements (2004).

[53] R. Sunulahpašić, M. Oruč, Effect of temperature on mechanical properties and type of fracture of superalloys nimonic 80a., Uticaj temperature na mehanička svojstva i tip loma superlegure Nimonic 80A. 50 (2011) 155–158.

[54] B. Geddes, H. Leon, X. Huang, Superalloys : Alloying and Performance, ASM International, 2010.

[55] R. B. Frank, C. G. Roberts, J. Zhang, Effect of nickel content on delta solvus temperature and mechanical properties of alloy 718, 7th International Symposium on Superalloy 718 and Derivatives (2010) 725–736.

[56] J. W. Brooks, P. J. Bridges, Metallurgical stability of inconel 718, Superalloys 1988 Symposium (1988) 33–42doi:10.7449/1988/Superalloys_1988_33_42.

[57] D. Keiser, Idaho national engineering laboratory a review of the physical metallurgy of alloy 718 (1976).

[58] J. Radon, On the determination of functions from their integrals along certain manifolds, Berichte über die Verhandlungen der Sächsische Akademie der Wissenschaften 69 (1917) 262–277. doi:10.1109/TMI.1986.4307775.

[59] S. Stock, X-ray microtomography of materials, International Materials Reviews 44 (1999) 141–164. doi:10.1179/095066099101528261.

[60] J. Elliott, P. Anderson, G. Davis, S. Dover, S. Stock, T. Breunig, A. Guvenilir, S. Antolovich, Application of x-ray microtomography in materials science illustrated by a study of a continuous fiber metal matrix composite, Journal of X-Ray Science and Technology 2 (1990) 249–258. doi:10.3233/XST-1990-2402.

[61] B. Gustafsson, Mathematics for computer tomography, Physica Scripta T61 (1996) 38–43. doi:10.1088/0031-8949/1996/T61/006.
URL http://stacks.iop.org/1402-4896/1996/i=T61/a=006?key=crossref.ab8f254dda5dc9b4daa451f66b12751e

[62] P. J. Withers, X-ray nanotomography, Materials Today 10 (2007) 26–34. doi:10.1016/S1369-7021(07)70305-X.

[63] S. Midgley, N. Schleich, Dual-energy x-ray analysis using synchrotron computed tomography at 35 and 60kev for the estimation of photon interaction coefficients describing attenuation and energy absorption, Journal of Synchrotron Radiation 22 (2015) 807–818. doi:10.1107/S1600577515004579.

[64] J. Y. Buffiere, E. Maire, J. Adrien, J. P. Masse, E. Boller, In situ experiments with x ray tomography: An attractive tool for experimental mechanics, Proceedings of the Society for Experimental Mechanics, Inc. 67 (2010) 289–305. doi:10.1007/s11340-010-9333-7.

[65] J. H. Kinney, M. C. Nichols, X-ray tomographic microscopy (xtm) using synchrotron radiation, Annual Review of Materials Science 22 (1992) 121–152. doi:10.1146/annurev.ms.22.080192.001005.
URL http://www.annualreviews.org/doi/pdf/10.1146/annurev.ms.22.080192.001005

[66] R. A. Brooks, G. D. Chiro, Beam hardening in x-ray reconstructive tomography, Physica Medica 21 (1976) 390–398. doi:10.1088/0031-9155/21/3/004.
URL http://dx.doi.org/10.1016/j.ejmp.2012.03.005

[67] G. T. Herman, Correction for beam hardening artefacts in computerised tomography., Physics in Medicine Biology 24 (1979) 81–106. doi:10.1118/1.594429.
URL http://www.ncbi.nlm.nih.gov/pubmed/22388427

[68] B. M. Patterson, K. C. Henderson, P. J. Gibbs, S. D. Imhoff, A. J. Clarke, Laboratory micro- and nanoscale x-ray tomographic investigation of al-7 at.structures, Materials Characterization 95 (2014) 18–26. doi:10.1016/j.matchar.2014.06.004.
URL http://dx.doi.org/10.1016/j.matchar.2014.06.004

[69] E. Maire, P. J. Withers, Quantitative x-ray tomography, International Materials Reviews 59 (2014) 1–43. doi:10.1179/1743280413Y.0000000023.

[70] F. Beckmann, R. Grupp, A. Haibel, M. Huppmann, M. Nöthe, A. Pyzalla, W. Reimers, A. Schreyer, R. Zettler, In-situ synchrotron x-ray microtomography studies of microstructure and damage evolution in engineering materials, Advanced Engineering Materials 9 (2007) 939–950. doi:10.1002/adem.200700254.

[71] A. Guvenilir, T. Breunig, J. Kinney, S. Stock, Direct observation of crack opening as a function of applied load in the interior of a notched tensile sample of al-li 2090, Acta materialia 45 (1997) 1977–1987. doi:10.1016/S1359-6454(96)00311-4.

[72] L. Feldkamp, L. Davis, J. Kress, Practical cone-beam algorithm, Journal of the Optical Society of America 1 (1984) 612–619.

[73] M. D. Michiel, J. M. Merino, D. Fernandez-Carreiras, T. Buslaps, V. Honkimäki, P. Falus, T. Martins, O. Svensson, Fast microtomography using high energy synchrotron radiation, Review of Scientific Instruments 76 (2005). doi:10.1063/1.1884194.

[74] N. Limodin, L. Salvo, M. Suéry, M. DiMichiel, In situ investigation by x-ray tomography of the overall and local microstructural changes occurring during partial remelting of an al-15.8 wt.3177–3191. doi:10.1016/j.actamat.2007.01.027.

[75] N. Limodin, J. Réthoré, J. Y. Buffière, A. Gravouil, F. Hild, S. Roux, Crack closure and stress intensity factor measurements in nodular graphite cast iron using three-dimensional correlation of laboratory x-ray microtomography images, Acta Materialia 57 (2009) 4090–4101. doi:10.1016/j.actamat.2009.05.005.

[76] S. Terzi, J. A. Taylor, Y. H. Cho, L. Salvo, M. Suéry, E. Boller, A. K. Dahle, In situ study of nucleation and growth of the irregular -al/-al5fesi eutectic by 3-d synchrotron x-ray microtomography, Acta Materialia 58 (2010) 5370–5380. doi:10.1016/j.actamat.2010.06.012.

[77] D. Tolnai, P. Townsend, G. Requena, L. Salvo, J. Lendvai, H. P. Degischer, In situ synchrotron tomographic investigation of the solidification of an almg4.7si8 alloy, Acta Materialia 60 (2012) 2568–2577. doi:10.1016/j.actamat.2012.01.024.

[78] F. Eckermann, T. Suter, P. J. Uggowitzer, A. Afseth, A. J. Davenport, B. J. Connolly, M. H. Larsen, F. D. Carlo, P. Schmutz, In situ monitoring of corrosion processes within the bulk of almgsi alloys using x-ray microtomography, Corrosion Science 50 (2008) 3455–3466. doi:10.1016/j.corsci.2008.09.015.

[79] S. P. Knight, M. Salagaras, A. M. Wythe, F. D. Carlo, A. J. Davenport, A. R. Trueman, In situ x-ray tomography of intergranular corrosion of 2024 and 7050 aluminium alloys, Corrosion Science 52 (2010) 3855–3860. doi:10.1016/j.corsci.2010.08.026.
URL http://dx.doi.org/10.1016/j.corsci.2010.08.026

[80] C. F. Martin, C. Josserond, L. Salvo, J. J. Blandin, P. Cloetens, E. Boller, Characterization by x-ray micro-tomography of cavity coalescence during superplastic deformation, Scripta Materialia 42 (2000) 375–381. doi:10.1016/S1359-6462(99)00355-3.

[81] N. Limodin, L. Salvo, E. Boller, M. Suéry, M. Felberbaum, S. Gailliègue, K. Madi, In situ and real-time 3-d microtomography investigation of dendritic solidification in an al-10 wt.2300–2310. doi:10.1016/j.actamat.2009.01.035.

[82] H. Zhang, H. Toda, P. C. Qu, Y. Sakaguchi, M. Kobayashi, K. Uesugi, Y. Suzuki, Three-dimensional fatigue crack growth behavior in an aluminum alloy investigated with in situ high-resolution synchrotron x-ray microtomography, Acta Materialia 57 (2009) 3287–3300. doi:10.1016/j.actamat.2009.03.036.
URL http://dx.doi.org/10.1016/j.actamat.2009.03.036

[83] C. Landron, E. Maire, O. Bouaziz, J. Adrien, L. Lecarme, A. Bareggi, Validation of void growth models using x-ray microtomography characterization of damage in dual phase steels, Acta Materialia 59 (2011) 7564–7573. doi:10.1016/j.actamat.2011.08.046.

[84] H. Toda, E. Maire, S. Yamauchi, H. Tsuruta, T. Hiramatsu, M. Kobayashi, In situ observation of ductile fracture using x-ray tomography technique, Acta Materialia 59 (2011) 1995–2008. doi:10.1016/j.actamat.2010.11.065.

[85] N. Limodin, A. E. Bartali, L. Wang, J. Lachambre, J. Y. Buffiere, E. Charkaluk, Application of x-ray microtomography to study the influence of the casting microstructure upon the tensile behaviour of an al-si alloy, Nuclear Instruments and Methods in Physics Research, Section B: Beam Interactions with Materials and Atoms 324 (2014) 57–62. doi:10.1016/j.nimb.2013.07.034.
URL http://dx.doi.org/10.1016/j.nimb.2013.07.034

[86] A. Isaac, F. Sket, W. Reimers, B. Camin, G. Sauthoff, A. R. Pyzalla, In situ 3d quantification of the evolution of creep cavity size, shape, and spatial orientation using synchrotron x-ray tomography, Materials Science and Engineering A 478 (2008) 108–118. doi:10.1016/j.msea.2007.05.108.

[87] S. Terzi, L. Salvo, M. Suéry, E. Boller, In situ x-ray microtomography characterization of the entrapped liquid formed during partial remelting of a cold-rolled al-8 wt.doi:10.1016/j.scriptamat.2008.12.042.

[88] M. Suery, S. Terzi, B. Mireux, L. Salvo, J. Adrien, E. Maire, Fast in situ x-ray microtomography observations of solidification and semisolid deformation of al-cu alloys, Jom 64 (2012) 83–88. doi:10.1007/s11837-011-0219-7.

[89] B. Cai, S. Karagadde, L. Yuan, T. J. Marrow, T. Connolley, P. D. Lee, In situ synchrotron tomographic quantification of granular and intragranular deformation during semi-solid compression of an equiaxed dendritic al-cu alloy, Acta Materialia 76 (2014) 371–380. doi:10.1016/j.actamat.2014.05.035.

[90] H. A. Bale, A. Haboub, A. A. MacDowell, J. R. Nasiatka, D. Y. Parkinson, B. N. Cox, D. B. Marshall, R. O. Ritchie, Real-time quantitative imaging of failure events in materials under load at temperatures above 1,600°c, Nature Materials 12 (2012) 40–46. doi:10.1038/nmat3497.
URL http://www.nature.com/doifinder/10.1038/nmat3497

[91] P. M. Mummery, B. Derby, P. Anderson, G. Davis, J. C. Elliott, X-ray microtomography of damage in particle-reinforced metal matrix composites, Journal De Physique 3 (1993) 1857–1860.

[92] J. Kastner, B. Harrer, G. Requena, O. Brunke, A comparative study of high resolution cone beam x-ray tomography and synchrotron tomography applied to fe- and al-alloys, NDT and E International 43 (2010) 599–605. doi:10.1016/j.ndteint.2010.06.004.
URL http://dx.doi.org/10.1016/j.ndteint.2010.06.004

[93] J. Baruchel, J. Y. Buffiere, P. Cloetens, M. D. Michiel, E. Ferrie, W. Ludwig, E. Maire, L. Salvo, Advances in synchrotron radiation microtomography, Scripta Materialia 55 (2006) 41–46. doi:10.1016/j.scriptamat.2006.02.012.

[94] S. Titarenko, V. Titarenko, A. Kyrieleis, P. J. Withers, A priori information in a regularized sinogram-based method for removing ring artefacts in tomography, Journal of Synchrotron Radiation 17 (2010) 540–549. doi:10.1107/S0909049510010964.

[95] E. M. A. Anas, S. Y. Lee, M. K. Hasan, Removal of ring artifacts in ct imaging through detection and correction of stripes in the sinogram, Physics in Medicine and Biology 55 (2010) 6911–6930. doi:10.1088/0031-9155/55/22/020.

[96] T. Hirano, K. Usami, Y. Tanaka, C. Masuda, I. Introduction, In situ x-ray ct under tensile loading using synchrotron radiation, J. Materials Research Society 10 (1995) 381–386.

[97] A. Guvenilir, S. Stock, High resolution computed tomography and implications for fatigue crack closure modelling, Fatigue Fracture of Engineering Materials Structures 21 (1998) 439–450.

[98] J. Y. Buffiere, E. Maire, P. Cloetens, G. Lormand, R. Foug??res, Characterization of internal damage in a mmcp using x-ray synchrotron phase contrast microtomography, Acta Materialia 47 (1999) 1613–1625. doi:10.1016/S1359-6454(99)00024-5.

[99] T. Nakayama, F. Yuse, Y. Tsubokawa, J. Matsui, Direct observations of cracks and voids in structural materials by x-ray imaging using ultra-bright synchrotron radiation, ISIJ International 43 (2003) 589–596.

[100] H. Toda, I. Sinclair, J.-Y. Buffière, E. Maire, T. Connolley, M. Joyce, K. Khor, P. Gregson, Assessment of the fatigue crack closure phenomenon in damage-tolerant aluminium alloy by in-situ high-resolution synchrotron x-ray microtomography, Philosophical Magazine 83 (2003) 2429–2448. doi:10.1080/1478643031000115754.
URL http://dx.doi.org/10.1080/1478643031000115754

[101] H. Toda, K. Uesugi, A. Takeuchi, K. Minami, M. Kobayashi, T. Kobayashi, Three-dimensional observation of nanoscopic precipitates in an aluminum alloy by microtomography with fresnel zone plate optics, Applied Physics Letters 89 (2006) 1–4. doi:10.1063/1.2359288.

[102] E. Maire, S. Zhou, J. Adrien, M. Dimichiel, Damage quantification in aluminium alloys using in situ tensile tests in x-ray tomography, Engineering Fracture Mechanics 78 (2011) 2679–2690. doi:10.1016/j.engfracmech.2011.07.004.

[103] Y. Shen, T. F. Morgeneyer, J. Garnier, L. Allais, L. Helfen, J. Cr??pin, Three-dimensional quantitative in situ study of crack initiation and propagation in aa6061 aluminum alloy sheets via synchrotron laminography and finite-element simulations, Acta Materialia 61 (2013) 2571–2582. doi:10.1016/j.actamat.2013.01.035.

[104] S. Dezecot, J.-Y. Buffiere, A. Koster, V. Maurel, F. Szmytka, E. Charkaluk, N. Dahdah, A. E. Bartali, N. Limodin, J.-F. Witz, In situ 3d characterization of high temperature fatigue damage mechanisms in a cast aluminum alloy using synchrotron x-ray tomography, Scripta Materialia 113 (2016) 254–258. doi:10.1016/j.scriptamat.2015.11.017.

[105] L. Saucedo-Mora, T. Lowe, S. Zhao, P. D. Lee, P. M. Mummery, T. J. Marrow, In situ observation of mechanical damage within a sic-sic ceramic matrix composite, Journal of Nuclear Materials 481 (2016) 13–23. doi:10.1016/j.jnucmat.2016.09.007.
URL http://dx.doi.org/10.1016/j.jnucmat.2016.09.007

[106] J. Y. Buffiere, E. Ferrie, H. Proudhon, W. Ludwig, Three-dimensional visualisation of fatigue cracks in metals using high resolution synchrotron x-ray micro-tomography, Materials Science and Technology 22 (2006) 1019–1024. doi:10.1179/174328406X114135.

[107] J. B. le Graverend, J. Adrien, J. Cormier, Ex-situ x-ray tomography characterization of porosity during high-temperature creep in a ni-based single-crystal superalloy: Toward understanding what damage is, Materials Science and Engineering A 695 (2017) 367–378. doi:10.1016/j.msea.2017.03.083.
URL http://dx.doi.org/10.1016/j.msea.2017.03.083

[108] R. Jiang, D. J. Bull, D. Proprentner, B. Shollock, P. A. S. Reed, Effects of oxygen-related damage on dwell-fatigue crack propagation in a p/m ni-based superalloy: From 2d to 3d assessment, International Journal of Fatigue 99 (2017) 175–186. doi:10.1016/j.ijfatigue.2017.03.003.
URL http://dx.doi.org/10.1016/j.ijfatigue.2017.03.003

[109] C. Scruby, H. Wadley, J. Sinclair, The origin of acoustic emission during deformation of aluminium and an aluminium-magnesium alloy, Philosophical Magazine A 44 (1981) 249–274. doi:10.1080/01418618108239532.

[110] J. Baram, M. Rosen, On the nature of the thermoelastic martensitic phase transformation in au-47.5 at.Metallurgica 30 (1982) 655–662. doi:10.1016/0001-6160(82)90114-6.

[111] C. H.R. Caceres, Bertorello, Acoustic emission during non-homogeneous flow in al-mg alloys, Scripta METALLURGICA 17 (1983) 1115–1120.

[112] M. Linderov, C. Segel, A. Weidner, H. Biermann, A. Vinogradov, Deformation mechanisms in austenitic trip/twip steels at room and elevated temperature investigated by acoustic emission and scanning electron microscopy, Materials Science and Engineering A 597 (2014) 183–193. doi:10.1016/j.msea.2013.12.094.
URL http://dx.doi.org/10.1016/j.msea.2013.12.094

[113] E. Vives, J. Ortin, L. Manosa, I. Rafols, R. Perez-Magrane, A. Planes, Distributions of avalanches in martensitic transformations, Physical Review Letters 72 (1994) 1694–1697.

[114] S. Weissner, F. E. Talke, Load/unload measurements using laser doppler vibrometry and acoustic emission, Tribology International 33 (2000) 367–372. doi:10.1016/S0301-679X(00)00054-2.

[115] M. Mohammad, S. Abdullah, N. Jamaludin, O. Innayatullah, Predicting the fatigue life of the sae 1045 steel using an empirical weibull-based model associated to acoustic emission parameters, Materials and Design 54 (2014) 1039–1048. doi:10.1016/j.matdes.2013.09.021.
URL http://dx.doi.org/10.1016/j.matdes.2013.09.021

[116] C. Ennaceur, A. Laksimi, C. Hervé, M. Cherfaoui, Monitoring crack growth in pressure vessel steels by the acoustic emission technique and the method of potential difference, International Journal of Pressure Vessels and Piping 83 (2006) 197–204. doi:10.1016/j.ijpvp.2005.12.004.

[117] J. Cuadra, P. A. Vanniamparambil, D. Servansky, I. Bartoli, A. Kontsos, Acoustic emission source modeling using a data-driven approach, Journal of Sound and Vibration 341 (2015) 222–236. doi:10.1016/j.jsv.2014.12.021.
URL http://dx.doi.org/10.1016/j.jsv.2014.12.021

[118] R. W. B. Stephens, A. A. Pollock, Waveforms and frequency spectra of acoustic emissions, The Journal of the Acoustical Society of America 50 (1971) 904–910. doi:10.1121/1.1912715.
URL http://asa.scitation.org/doi/10.1121/1.1912715

[119] S. Didier-Laurent, H. Idrissi, L. Roué, In-situ study of the cracking of metal hydride electrodes by acoustic emission technique, Journal of Power Sources 179 (2008) 412–416. doi:10.1016/j.jpowsour.2007.12.073.

[120] C. B. Scruby, H. N. Wadley, K. L. Rusbridge, Origin of acoustic emission in alznmg alloys ii: Copper-containing quaternary alloys, Materials Science and Engineering 59 (1983) 169–183. doi:10.1016/0025-5416(83)90165-9.

[121] M. Lugo, J. B. Jordon, M. F. Horstemeyer, M. A. Tschopp, J. Harris, A. M. Gokhale, Quantification of damage evolution in a 7075 aluminum alloy using an acoustic emission technique, Materials Science and Engineering A 528 (2011) 6708–6714. doi:10.1016/j.msea.2011.05.017.
URL http://dx.doi.org/10.1016/j.msea.2011.05.017

[122] E. D. Merson, P. N. Myagkikh, G. V. Klevtsov, D. L. Merson, A. Vinogradov, Effect of fracture mode on acoustic emission behavior in the hydrogen embrittled low-alloy steel, Engineering Fracture Mechanics 210 (2019) 342–357. doi:10.1016/j.engfracmech.2018.05.026.
URL https://doi.org/10.1016/j.engfracmech.2018.05.026

[123] A. Vinogradov, M. Nadtochiy, S. Hashimoto, S. Miura, Acoustic emission spectrum and its orientation dependence in copper single crystals, Materials Transactions 36 (1995) 496–503.

[124] A. Vinogradov, A. Lazarev, Continuous acoustic emission during intermittent plastic flow in -brass, Scripta Materialia 66 (2012) 745–748. doi:10.1016/j.scriptamat.2012.01.053.
URL http://dx.doi.org/10.1016/j.scriptamat.2012.01.053

[125] A. A. Shibkov, M. A. Zheltov, M. F. Gasanov, A. E. Zolotov, A. A. Denisov, M. A. Lebyodkin, Dynamics of deformation band formation investigated by high-speed techniques during creep in an almg alloy, Materials Science and Engineering A 772 (2020) 138777. doi:10.1016/j.msea.2019.138777.
URL https://doi.org/10.1016/j.msea.2019.138777

[126] A. Vinogradov, E. Vasilev, M. Seleznev, K. Máthis, D. Orlov, D. Merson, On the limits of acoustic emission detectability for twinning, Materials Letters 183 (2016) 417–419. doi:10.1016/j.matlet.2016.07.063.
URL http://dx.doi.org/10.1016/j.matlet.2016.07.063

[127] A. Vinogradov, S. Hashimoto, S. Miura, Effect of grain boundary on acoustic emission during plastic deformation of copper-aluminum bicrystals, Acta Materialia 44 (1996) 2883–2890.

[128] R. Takeda, Y. Kaneko, D. L. Merson, A. Vinogradov, Cluster analysis of acoustic emissions measured during deformation of duplex stainless steels, Materials Transactions 54 (2013) 532–539. doi:10.2320/matertrans.MBW201203.

[129] A. Vinogradov, D. Orlov, A. Danyuk, Y. Estrin, Effect of grain size on the mechanisms of plastic deformation in wrought mg-zn-zr alloy revealed by acoustic emission measurements, Acta Materialia 61 (2013) 2044–2056. doi:10.1016/j.actamat.2012.12.024.
URL http://dx.doi.org/10.1016/j.actamat.2012.12.024

[130] S. Kawai, Y. Yoshida, H. Asano, S. Miura, M. Kobayashi, J. ichi Shibano, Acoustic emission response of magnesium alloy during cyclic and creep tests, Materials Science and Engineering A 668 (2016) 120–124. doi:10.1016/j.msea.2016.05.057.
URL http://dx.doi.org/10.1016/j.msea.2016.05.057

[131] S. V. Panin, A. V. Byakov, I. V. Vlasov, P. O. Maruschak, F. Berto, A. Vinogradov, Acoustic emission study on the effect of notch shape and temperature on elastic energy release during impact testing of 17mn1si pipe steel, Engineering Fracture Mechanics 210 (2019) 288–299. doi:10.1016/j.engfracmech.2018.05.021.
URL https://doi.org/10.1016/j.engfracmech.2018.05.021

[132] D. Martelo, D. Sampath, A. Monici, R. Morana, R. Akid, Correlative analysis of digital imaging, acoustic emission, and fracture surface topography on hydrogen assisted cracking in ni-alloy 625+, Engineering Fracture Mechanics 221 (2019) 106678. doi:10.1016/j.engfracmech.2019.106678.
URL https://doi.org/10.1016/j.engfracmech.2019.106678

[133] K. Ono, M. Yamamoto, Anisotropic mechanical and acoustic emission behavior of a533b steels, Materials Science and Engineering 47 (1981) 247–263. doi:10.1016/0025-5416(81)90051-3.

[134] I. S. Colombo, I. G. Main, M. C. Forde, Assessing damage of reinforced concrete beam using b-value analysis of acoustic emission signals, Journal of Materials in Civil Engineering 15 (2003) 280–286. doi:10.1061/(ASCE)0899-1561(2003)15:3(280).

[135] H. N. G. Wadley, C. B. Scruby, J. H. Speake, Acoustic emission for physical examination of metals, International Metals Reviews 25 (1980) 41–64. doi:10.1179/imtr.1980.25.1.41.
URL http://www.tandfonline.com/doi/full/10.1179/imtr.1980.25.1.41

[136] B. Gutenberg, C. F. Richter, Earthquake magnitude, intensity, energy, and acceleration, Bulletin of the Seismological Society of America 32 (1942) 163–191. doi:10.1785/0120160029.
URL http://www.bssaonline.org/cgi/content/abstract/66/3/639

[137] X. Q. Ma, M. Takemoto, Quantitative acoustic emission analysis of plasma sprayed thermal barrier coatings subjected to thermal shock tests, Materials Science and Engineering A308 308 (2001) 101–110. doi:10.1016/S0921-5093(00)01985-7.

[138] E. Maire, V. Carmona, J. Courbon, W. Ludwig, Fast x-ray tomography and acoustic emission study of damage in metals during continuous tensile tests, Acta Materialia 55 (2007) 6806–6815. doi:10.1016/j.actamat.2007.08.043.

[139] A. Y. Vinogradov, V. A. Khonik, Kinetics of shear banding in a bulk metallic glass monitored by acoustic emission measurements, Philosophical Magazine 84 (2004) 2147–2166. doi:10.1080/14786430410001678217.

[140] B. T. Kishi, T. Ohira, Dynamic crack growth during pop-in fracture in 7075 aluminum alloy, Transactions of the Japan Institute of Metals 24 (1983) 255–263.

[141] K. Ito, M. Enoki, Acquisition and analysis of continuous acoustic emission waveform for classification of damage sources in ceramic fiber mat, Materials Transactions 48 (2007) 1221–1226. doi:10.2320/matertrans.I-MRA2007850.
URL http://joi.jlc.jst.go.jp/JST.JSTAGE/matertrans/I-MRA2007850?from=CrossRef

[142] A. Vinogradov, V. Patlan, S. Hashimoto, Spectral analysis of acoustic emission during cyclic deformation of copper single crystals, Philosophical Magazine A 81 (2001) 1427–1446. doi:10.1080/01418610108214356.

[143] M. Watanabe, M. Enoki, T. Kishi, Fracture behavior of ceramic coatings during thermal cycling evaluated by acoustic emission method using laser interferometers, Materials Science and Engineering A 359 (2003) 368–374. doi:10.1016/S0921-5093(03)00394-0.

[144] U. Krupp, W. Kane, J. a Pfaendtner, L. Xinyu, C. Laird, C. J. M. Jr, Oxygen-induced intergranular fracture of the nickel-base alloy in718 during mechanical loading at high temperatures, Materials Research 7 (2004) 35–41. doi:10.1590/S1516-14392004000100006.
URL papers3://publication/uuid/563B46BF-1CB0-464F-A597-39D2F44C3AC9

[145] L. Wang, S. Wang, X. Song, Y. Liu, G. Xu, Effects of precipitated phases on the crack propagation behaviour of a ni-based superalloy, International Journal of Fatigue 62 (2014) 210–216. doi:10.1016/j.ijfatigue.2013.10.006.
URL http://dx.doi.org/10.1016/j.ijfatigue.2013.10.006

[146] X. Wang, G. Han, C. Cui, S. Guan, T. Jin, X. Sun, Z. Hu, The dependence of portevin–le châtelier effect on the precipitates in a wrought ni-base superalloy, Metallurgical and Materials Transactions A: Physical Metallurgy and Materials Science 47 (2016) 5994–6003. doi:10.1007/s11661-016-3718-x.

[147] A. A. N. Nemeth, D. J. Crudden, D. E. J. Armstrong, D. M. Collins, K. Li, A. J. Wilkinson, C. R. M. Grovenor, R. C. Reed, Environmentally-assisted grain boundary attack as a mechanism of embrittlement in a nickel-based superalloy, Acta Materialia 126 (2017) 361–371. doi:10.1016/j.actamat.2016.12.039.

[148] B. F. Dyson, D. E. Henn, The effect of room temperature pre-strain on grain boundary cavitation in nimonic 80a, Journal of Microscopy 97 (1973) 165–170. doi:10.1111/j.1365-2818.1973.tb03771.x.

[149] J. Komenda, P. Henderson, Growth of pores during the creep of a single crystal nickel-base superalloy, Scripta Materialia 37 (1997) 1821–1826. doi:10.1016/S1359-6462(97)00341-2.

[150] R. C. Reed, D. C. Cox, C. M. F. Rae, Damage accumulation during creep deformation of a single crystal superalloy at 1150 c, Materials Science and Engineering A 448 (2007) 88–96. doi:10.1016/j.msea.2006.11.101.

[151] A. Srivastava, A. Needleman, Phenomenological modeling of the effect of specimen thickness on the creep response of ni-based superalloy single crystals, Acta Materialia 61 (2013) 6506–6516. doi:10.1016/j.actamat.2013.07.028.
URL http://dx.doi.org/10.1016/j.actamat.2012.06.043

[152] M. Ferrucci, R. K. Leach, C. Giusca, S. Carmignato, W. Dewulf, Towards geometrical calibration of x-ray computed tomography systems - a review (9 2015). doi:10.1088/0957-0233/26/9/092003.

[153] B. Nielsen, Resolution, unsharpness and mtf, Department of Medicine and Care Radio Physics Report, Universitetet i Linkoping, ISSN 0348-7679 39 (1980) 1–18. doi:10.1017/CBO9781107415324.004.

[154] C. A. Schneider, W. S. Rasband, K. W. Eliceiri, Nih image to imagej: 25 years of image analysis, Nature Methods 9 (2012) 671–675. doi:10.1038/nmeth.2089.
URL http://dx.doi.org/10.1038/nmeth.2089

[155] T. Sjöberg, S. Marth, J. Kajberg, H. Åke Häggblad, Experimental characterisation of the evolution of triaxiality stress state for sheet metal materials, European Journal of Mechanics, A/Solids 66 (2017) 279–286. doi:10.1016/j.euromechsol.2017.07.013.

[156] K. Genovese, L. Cortese, M. Rossi, D. Amodio, A 360-deg digital image correlation system for materials testing, Optics and Lasers in Engineering 82 (2016) 127–134. doi:10.1016/j.optlaseng.2016.02.015.
URL http://dx.doi.org/10.1016/j.optlaseng.2016.02.015

[157] L. Pan, I. Scheibli, M. B. Henderson, B. A. Shollock, Asymmetric creep deformation of a single crystal superalloy, Acta Metallurgica and Matreialia Materialia 43 (1995) 1375–1384.

[158] A. Day, T. E. Quested, A comparison of grain imaging and measurement using horizontal orientation and colour orientation contrast imaging, electron backscatter pattern and optical methods, Journal of Microscopy 195 (1999) 186–196.
URL https://onlinelibrary.wiley.com/doi/abs/10.1046/j.1365-2818.1999.00571.x

[159] Y. C. Lin, J. Deng, Y. Q. Jiang, D. X. Wen, G. Liu, Effects of initial delta phase on hot tensile deformation behaviors and fracture characteristics of a typical ni-based superalloy, Materials Science and Engineering A 598 (2014) 251–262. doi:10.1016/j.msea.2014.01.029.

[160] K. Sato, Q. Yu, J. Hiramoto, T. Urabe, A. Yoshitake, A method to investigate strain rate effects on necking and fracture behaviors of advanced high-strength steels using digital imaging strain analysis, International Journal of Impact Engineering 75 (2015) 11–26. doi:10.1016/j.ijimpeng.2014.07.001.
URL http://dx.doi.org/10.1016/j.ijimpeng.2014.07.001

[161] M. Algarni, Y. Choi, Y. Bai, A unified material model for multiaxial ductile fracture and extremely low cycle fatigue of inconel 718, International Journal of Fatigue 96 (2017) 162–177. doi:10.1016/j.ijfatigue.2016.11.033.
URL http://dx.doi.org/10.1016/j.ijfatigue.2016.11.033

[162] D. Hull, D. E. Rimmer, The growth of grain-boundary voids under stress, Philosophical Magazine 4 (1959) 673–687. doi:10.1080/14786435908243264.
URL http://www.tandfonline.com/doi/abs/10.1080/14786435908243264

[163] A. A. Benzerga, J. Besson, A. Pineau, Anisotropic ductile fracture: Part i: Experiments, Acta Materialia 52 (2004) 4623–4638. doi:10.1016/j.actamat.2004.06.020.

[164] D. R. Hayhurst, J. Lin, R. J. Hayhurst, Failure in notched tension bars due to high-temperature creep: Interaction between nucleation controlled cavity growth and continuum cavity growth, International Journal of Solids and Structures 45 (2008) 2233–2250. doi:10.1016/j.ijsolstr.2007.11.026.

[165] B. F. Dyson, M. McLean, Particle-coarsening, 0 and tertiary creep, Acta Metallurgica 31 (1983) 17–27. doi:10.1016/0001-6160(83)90059-7.

[166] K. K. Sharma, D. Banerjee, S. N. Tewari, Effect of reverse-aging treatment on the microstructure and mechanical properties of nimonic alloys, Materials Science and Engineering 104 (1988) 131–140. doi:10.1016/0025-5416(88)90414-4.

[167] K. Kageyama, F. Adziman, E. Alabort, T. Sui, A. M. Korsunsky, R. C. Reed, In situ diagnostics of damage accumulation in ni-based superalloys using high temperature computed tomography, Metallurgical and Materials Transaction A 49 (2018) 4274–4289. doi:10.1007/s11661-018-4737-6.

[168] A. G. Lindgren, P. A. Rattey, The inverse discrete radon transform with applications to tomographic imaging using projection data, Advances in Electronics and Electron Physics 56 (1981) 359–410. doi:10.1016/S0065-2539(08)60427-8.
URL http://www.sciencedirect.com/science/article/pii/S0065253908604278

[169] K. Arunmuthu, M. Ashish, T. Saravanan, J. Philip, B. P. C. Rao, T. Jayakumar, Simulation of beam hardening in x-ray tomography and its correction using linearisation and pre-filtering approaches, Insight: Non-Destructive Testing and Condition Monitoring 55 (2013) 540–547. doi:10.1784/insi.2012.55.10.540.

[170] V. S. V. M. Vedula, P. Munshi, An improved algorithm for beam-hardening corrections in experimental x-ray tomography, NDT and E International 41 (2008) 25–31. doi:10.1016/j.ndteint.2007.06.002.

[171] R. A. Ketcham, R. D. Hanna, Beam hardening correction for x-ray computed tomography of heterogeneous natural materials, Computers and Geosciences 67 (2014) 49–61. doi:10.1016/j.cageo.2014.03.003.
URL http://dx.doi.org/10.1016/j.cageo.2014.03.003

[172] S. S. Titarenko, a. G. Yagola, Ring artefact suppression in real-time x-ray tomography, Moscow University Physics Bulletin 65 (2010) 65–67. doi:10.3103/S0027134910010157.
URL http://www.springerlink.com/index/10.3103/S0027134910010157

[173] K. Rajendran, M. F. Walsh, N. J. A. de Ruiter, A. I. Chernoglazov, R. K. Panta, A. P. H. Butler, P. H. Butler, S. T. Bell, N. G. Anderson, T. B. F. Woodfield, S. J. Tredinnick, J. L. Healy, C. J. Bateman, R. Aamir, R. M. N. Doesburg, P. F. Renaud, S. P. Gieseg, D. J. Smithies, J. L. Mohr, V. B. H. Mandalika, A. M. T. Opie, N. J. Cook, J. P. Ronaldson, S. J. Nik, A. Atharifard, M. Clyne, P. J. Bones, C. Bartneck, R. Grasset, N. Schleich, M. Billinghurst, Reducing beam hardening effects and metal artefacts in spectral ct using medipix3rx, Journal of Instrumentation 9 (2014) P03015. doi:10.1088/1748-0221/9/03/P03015.
URL http://stacks.iop.org/1748-0221/9/i=03/a=P03015

[174] F. E. Boas, D. Fleischmann, Ct artifacts: causes and reduction techniques, Imaging in Medicine 4 (2012) 229–240. doi:10.2217/iim.12.13.
URL http://www.futuremedicine.com/doi/abs/10.2217/iim.12.13

[175] J. Rice, D. Tracey, On the ductile enlargement of voids in triaxial stress fields, Journal of the Mechanics and Physics of Solids 17 (1969) 201–217. doi:10.1016/0022-5096(69)90033-7.
URL http://linkinghub.elsevier.com/retrieve/pii/0022509669900337

[176] J. W. Hancock, A. C. Mackenzie, On the mechanisms of ductile failure in high-strength steels subjected to multi-axial stress-states, Journal of the Mechanics and Physics of Solids 24 (1976) 147–160. doi:10.1016/0022-5096(76)90024-7.

[177] X. Teng, T. Wierzbicki, Evaluation of six fracture models in high velocity perforation, Engineering Fracture Mechanics 73 (2006) 1653–1678. doi:10.1016/j.engfracmech.2006.01.009.

[178] I. Barsoum, J. Faleskog, Rupture mechanisms in combined tension and shear-experiments, International Journal of Solids and Structures 44 (2007) 1768–1786. doi:10.1016/j.ijsolstr.2006.09.031.

[179] I. Barsoum, J. Faleskog, Micromechanical analysis on the influence of the lode parameter on void growth and coalescence, International Journal of Solids and Structures 48 (2011) 925–938. doi:10.1016/j.ijsolstr.2010.11.028.
URL http://dx.doi.org/10.1016/j.ijsolstr.2010.11.028

[180] A. Ghahremaninezhad, K. Ravi-Chandar, Ductile failure behavior of polycrystalline al 6061-t6, International Journal of Fracture 174 (2012) 177–202. doi:10.1007/s10704-012-9689-z.

[181] K. Spencer, S. F. Corbin, D. J. Lloyd, The influence of iron content on the plane strain fracture behaviour of aa 5754 al-mg sheet alloys, Materials Science and Engineering A 325 (2002) 394–404. doi:10.1016/S0921-5093(01)01481-2.

[182] A. Ghahremaninezhad, K. Ravi-Chandar, Ductile failure in polycrystalline ofhc copper, International Journal of Solids and Structures 48 (2011) 3299–3311. doi:10.1016/j.ijsolstr.2011.07.001.
URL http://dx.doi.org/10.1016/j.ijsolstr.2011.07.001

[183] N. Hansen, R. F. Mehl, New discoveries in deformed metals, Metallurgical and Materials Transactions A: Physical Metallurgy and Materials Science 32 (2001) 2917–2935. doi:10.1007/s11661-001-0167-x.

[184] D. Teirlinck, F. Zok, J. D. Embury, M. F. Ashby, Fracture mechanism maps in stress space, Acta Metallurgica 36 (1988) 1213–1228. doi:10.1016/0001-6160(88)90274-X.

[185] T. Kishi, H. Tanaka, R. Horiuchi, Y. Obata, K. Aoki, Acoustic emission peak of bauschinger effect, Scripta Metallurgica 9 (1975) 1023–1026. doi:10.1016/0036-9748(75)90272-0.

[186] A. Vinogradov, A. Lazarev, M. Linderov, A. Weidner, H. Biermann, Kinetics of deformation processes in high-alloyed cast transformation- induced plasticity/twinning-induced plasticity steels determined by acoustic emission and scanning electron microscopy: Influence of austenite stability on deformation mechanisms, Acta Materialia 61 (2013) 2434–2449. doi:10.1016/j.actamat.2013.01.016.
URL http://dx.doi.org/10.1016/j.actamat.2013.01.016

[187] M. Watanabe, T. Okabe, M. Enoki, T. Kishi, Evaluation of in situ fracture toughness of ceramic coatings at elevated temperature by ae inverse analysis, Science and Technology of Advanced Materials 4 (2003) 205–212. doi:10.1016/S1468-6996(03)00032-9.

[188] K. Ito, S. Ohmata, K. Kobayashi, M. Watanabe, S. Kuroda, M. Enoki, Crack monitoring during plasma spraying of ceramic coatings by non-contact acoustic emission method, Materials Transactions 51 (2010) 1272–1276. doi:10.2320/matertrans.M2010004.

[189] A. Malmelöv, M. Fisk, A. Lundbäck, L. E. Lindgren, Mechanism based flow stress model for alloy 625 and alloy 718, Materials 13 (2020) 1–17. doi:10.3390/ma13245620.

[190] M. Minozzi, G. Caldarelli, L. Pietronero, S. Zapperi, Dynamic fracture model for acoustic emission, European Physical Journal B 36 (2003) 203–207. doi:10.1140/epjb/e2003-00336-7.

[191] C. Kienl, P. Mandal, H. Lalvani, C. M. Rae, Role of the secondary phase during high-temperature compression of ati 718plus®, Metallurgical and Materials Transactions A: Physical Metallurgy and Materials Science 51 (2020) 4008–4021. doi:10.1007/s11661-020-05837-7.

[192] A. Vinogradov, I. S. Yasnikov, D. L. Merson, Phenomenological approach towards modelling the acoustic emission due to plastic deformation in metals, Scripta Materialia 170 (2019) 172–176. doi:10.1016/j.scriptamat.2019.06.011. URL https://doi.org/10.1016/j.scriptamat.2019.06.011